EXPERIMENTAL & NUMERICAL INVESTIGATION OF POOL BOILING ON ENGINEERED SURFACES WITH INTEGRATED THIN-FILM TEMPERATURE SENSORS

A Dissertation

by

VIJAYKUMAR SATHYAMURTHI

Submitted to the Office of Graduate Studies of
Texas A&M University
in partial fulfillment of the requirements for the degree of

DOCTOR OF PHILOSOPHY

December 2009

Major Subject: Mechanical Engineering

EXPERIMENTAL & NUMERICAL INVESTIGATION OF POOL BOILING ON ENGINEERED SURFACES WITH INTEGRATED THIN-FILM TEMPERATURE SENSORS

A Dissertation

by

VIJAYKUMAR SATHYAMURTHI

Submitted to the Office of Graduate Studies of
Texas A&M University
in partial fulfillment of the requirements for the degree of

DOCTOR OF PHILOSOPHY

Approved by:

Chair of Committee,	Debjyoti Banerjee
Committee Members,	Jerald A. Caton
	Nagamangala K. Anand
	Hamn-Ching Chen
Head of Department,	Dennis O'Neal

December 2009

Major Subject: Mechanical Engineering

ABSTRACT

Experimental & Numerical Investigation of Pool Boiling on Engineered Surfaces with Integrated Thin-film Temperature Sensors. (December 2009)

Vijaykumar Sathyamurthi, B.E. (Hons.), Nagpur University; M.S., Texas A&M University

Chair of Advisory Committee: Debjyoti Banerjee

The objective of this investigation is to measure and analyze surface temperature fluctuations in pool boiling. The surface temperature fluctuations were recorded on silicon surfaces with and without multi-walled carbon nanotubes (MWCNT). Novel Thin Film Thermocouples (TFT) are micro-fabricated on test substrates to measure surface temperatures. A dielectric liquid refrigerant (PF-5060) is used as test fluid. Both nucleate and film boiling regimes are investigated for the silicon test substrates. Dynamics of nucleate boiling is investigated on the CNT coated substrates. High frequency temperature fluctuation data is analyzed for the presence of determinism using non-linear time series analysis techniques in TISEAN© software. The impact of subcooling and micro/nano-scale surface texturing using MWCNT coatings on the dynamics of pool boiling is assessed. Dynamic invariants such as correlation dimensions and Lyapunov spectrum are evaluated for the reconstructed attractor. A non-linear noise reduction scheme is employed to reduce the level of noise in the data. Previous investigations in pool boiling chaos, reported in literature were based on temperature measurements underneath the test surface consisting of single or few active nucleation sites. Previous studies have indicated the presence of low-dimensional behavior in nucleate boiling and high-dimensional behavior in CHF and film boiling. Currently, there is no study detailing the effects of multiple nucleation sites, subcooling and surface texturing on pool boiling dynamics.

The investigation comprises of four parts: i) in situ micro-machining of Chromel-alumel (K-type) TFT, ii) calibration of these sensors, iii) utilizing these sensors in pool boiling experiments iv) analysis of these fluctuations using techniques of non-linear time series analysis. Ten TFT are fabricated on a rectangular silicon surface within an area of $\sim$ 3.00 cm $\times$ 3.00 cm. The sensing junctions of the TFT measure 50 μm in width and 250 nm in depth. Surface temperature fluctuations of the order of i) 0.65-0.93 ℃ are observed near ONB ii) 2.3-6.5 ℃ in FDNB iii) 2.60-5.00 ℃ at CHF and iv) 2.3-3.5 ℃ in film boiling.

Investigations show the possible presence of chaotic dynamics near CHF and in film-boiling in saturated and subcooled pool boiling. Fully developed nucleate boiling (FDNB) is chaotic. No clear assessment of the dynamics could be made in the onset of nucleate boiling (ONB) and partial nucleate boiling (PNB) regimes due to the effects of noise. However, the frequency spectra in these regimes appear to have two independent frequencies and their integral combinations indicating a possible quasi-periodic bifurcation route to chaos. The dimensionality in FDNB, at CHF and in film-boiling is lower in saturated pool boiling as compared to values in corresponding regimes in subcooled pool boiling.

Surface temperature fluctuations can damage electronic components and need to be carefully controlled. Understanding the nature of these fluctuations will aid in deciding the modeling approach for surface temperature transients on an electronic chip. Subsequently, the TFT signals can be employed in a suitable feedback control loop to prevent the occurrence of hotspots.

To my (late) grandmother Dr. S. Hymavathi (M.B.B.S., D.C.H., PhD)

ACKNOWLEDGMENTS

First and foremost, I acknowledge the mental and financial support rendered by my loving parents, Mr. Rajagopal Sathyamurthi & Mrs. Suryapraba Sathyamurthi. If not for their financial support and constant encouragement in the first year of my graduate education, I would not have been at this stage. I thank my sister for her encouragement and support. I thank all my teachers here at A&M as well as those back home in India for helping me achieve my educational goals.

Additionally, I thank my grandparents Prof. S. Srinivasan, (Principal & Head & Prof. of Physics (Retd.), Hindu College) and Dr. S. Hymavathi for their constant encouragement in this endeavor. I dedicate this dissertation to the memory of my grandmother, Dr. S. Hymavathi who passed away on May, 05, 2009. It was her ardent wish to see me graduate with a Ph.D. Special thanks to my grandfather, Prof. S. Srinivasan, for the various discussions concerning my research and life in general and for egging me on '*...to strive, to seek, to find and not to yield* - Ulysses'.

Special thanks are due to Dr. Sai C. Lau for providing me with the opportunity to be a teaching assistant for three semesters, thus providing invaluable experience. His emphasis on meticulous planning and thoroughness helped me in my research activities. I thank Mr. Ysidoro Ramirez & Mr. Brian Bachmeyer, for the assistance rendered during various stages of my graduate study. I thank my former lab mates and mentors, Dr. Hee Seok Ahn and Dr. Sangwon Lee, for teaching me good experimental practices. I owe a debt of gratitude to my current friends, Mr. Satish Karra, Mr. Shriram Srinivasan, Mr. Saradhi Koneru, Mr. Praveen Mokkapatti, Mr. Auviur Nandagopalan and Dr. Anshul Kaushik for their invaluable company. I thank all my lab mates, current as well as former, for putting up with me!

I especially thank the following individuals:

1. Dr. Marylene Palard & Mr. Johnny Johnson at the MERC-NNIN center at UT-Austin for taking the time to train me on the CHA.

2. Mr. Navdeep Singh for allowing me to eat his lunch daily for the last 10 months!

3. Mr. Brandon J. Mabe, for the many intellectually stimulating discussions and for proof-reading my dissertation.

To Dr. Banerjee, I owe a debt that I cannot repay. I thank him for his financial support that enabled us to execute this work. I cannot thank him enough for the exposure he gave me in terms of sending me to conferences and training workshops. The greatest gifts he gave me are the research problem that is the subject of this study and for teaching me to be independent in my research. I believe that the qualities that have been imbued in me during the course of my research will last a lifetime. I wish him the best. I also thank members of my committee, Dr. N. K. Anand, Dr. Jerald A. Caton & Dr. H. C. Chen for their guidance. I thank Dr. N. K. Anand for the direction provided through his questioning in my preliminaries. It has helped me tremendously in identifying and addressing several shortcomings of the study and in making it more comprehensive. I thank Dr. Caton both as a teacher and as a member of my committee, for I benefitted from his tutelage in MEEN-615 in Spring-2005. I also thank Dr. J. C. Han for his heat transfer courses, they taught me a lot.

The pleasurable, chaotic torment that this research problem has given me over the past three years will remain etched in my memory for a lifetime. What seemed to be a simple problem led me down paths I never envisioned traveling. To this end I recall the following words of Swami Vivekanand (The Complete Works of Swami Vivekananda by Swami Vivekananda Volume 2, Practical Vedanta and other lectures, 'The Way to Blessedness-The Open Secret' Delivered at Los Angeles, Calif., 5th January 1900):

"Whichever way we turn in trying to understand things in their reality, if we analyze far enough, we find that at last we come to a peculiar state of things, seemingly a contradiction: something which our reason cannot grasp and yet is a fact. We take up something- we know it is finite; but as soon as we begin to analyze it, it leads us beyond our reason, and we never find an end to all its qualities, its possibilities, its powers, its relations. It has become infinite."

NOMENCLATURE

Greek Symbols

α	Thermal diffusivity
β	Fraction of surface occupied by solid
δ	Thickness/difference
ϵ	Neighborhood size
θ	Contact Angle
κ	Seebeck Coefficient (μV/K)
ρ	Density (kg/m^3)
σ	Surface Tension (N/m) or standard deviation
τ	Optimal delay time
φ	The Heaviside step function
ϕ	Contact angle
χ	Fraction of false nearest neighbors
Υ	Electric Field (μV/m)
ω	Relative uncertainty (%)

Roman Symbols

A	Area (m^2)

C	Correlation sum
c	Specific heat of liquid (J/kgK)
D	Dimension/Diameter
g	Acceleration due to gravity (m/s^2)
h	Convective heat transfer coefficient (W/m^2K) or enthalpy (KJ/kgK)
I	Mutual information between X and Y (bits)
k	Thermal conductivity (W/mK)
L	Length scale
N	Number/Number of vectors
P	Pressure within bulk liquid (Pa) or Probability density
q''	Heat flux (W/cm^2)
r	Radius (m)
T	Temperature (K)
V	Electric potential/e.m.f (V)
W	Width (m)
x	Position (m)
x	Vector (boldface) or its component (subscript)
y	Vector (boldface) or its component (subscript)

Subscripts

b	Bubble
C	Correlation dimension
c	Cavity
crit	Critical
Cu	Copper
ev	Evaporation
f	Fraction
fg	Liquid-vapor region
fnn	False nearest neighbors
H	Hausdorff dimension
h	Heater
h=2r_c	Top of bubble
I	Information dimension
i, j, k	Indices
l	Liquid phase
lo	Capillary
max	Maxiumum/peak
maxog	Maximum for other geometries
mlay	Microlayer

nc	Natural convection
p	Constant pressure/pressure
sat	Saturated state
ϕ_{Si}	Smooth silicon surface
s	Rough surface/solid
sup	Wall superheat, superheat
blt	Boundary layer thickness
v	Vapor phase
w	Within liquid phase, wafer, wall
XY	Measurements of two quantities denoted by X & Y

Other Symbols

∞	Bulk/Ambient

TABLE OF CONTENTS

CHAPTER Page

LIST OF TABLES

TABLE Page

LIST OF FIGURES

FIGURE Page

FIGURE Page

FIGURE Page

FIGURE Page

FIGURE Page

FIGURE Page

FIGURE Page

FIGURE Page

CHAPTER I

INTRODUCTION TO THE STUDY

A. Background

Boiling occurs when a liquid, in contact with a heated surface, changes to a vapor state. It is commonly encountered in process engineering applications, annealing of metals and other materials, and in boiling water reactors. Pool boiling refers to boiling in a quiescent liquid maintained at a constant temperature. The maximum temperature variation within the liquid phase is confined to a thin, unsteady thermal boundary layer located in vicinity of the solid heater. Because of the nucleation process, vigorous mixing of the liquid occurs especially at high heat fluxes. This leads to variations in surface temperature as a consequence of rupturing of the thermal boundary layer. At low heat fluxes, active nucleation sites are few and sparsely distributed. Consequently, the heater surface temperature is a function of the spatial location and time at low heat fluxes. At high heat fluxes, the heater surface temperature may be strongly dependent on time and position. The measurement and characterization of the nature of these surface temperature variations is the focus of the present study. The nature of the temporal dependence of surface temperatures is elucidated using techniques of non-linear time series analysis.

Between 1950 and 1980, significant number of studies in pool boiling focused on estimating averaged heat transfer rates for process engineering applications. Correlations developed in the last seven decades typically deal with estimation of a temporally averaged heat transfer coefficient. These correlations were for the greater

---

The dissertation follows the style of *Elsevier International Journal of Heat and Mass Transfer*.

part, concerned with estimation of averaged heat fluxes rather than prediction of local surface temperature fluctuations. The emergence of high performance computing, light emitting diodes and lasers have resulted in high density heat loads requiring enhanced cooling. Other applications include, electronic chips, data-centers, telecommunications, cooling of chips in automotive applications, phased array radars and advanced avionics. The ever decreasing form factor of electronic chips coupled with increasing heat loads ($\sim$ 100 W/cm^2) necessitates the development of new measurement techniques and models capable of measuring and predicting transient surface temperatures and heat fluxes for the purposes of improving system reliability and control.

Spatial temperature differentials of the order of a few degrees are of little concern in process equipment. However, electronic components have to adhere to strict operating temperature ranges. Hotspots can ruin or degrade the component. The importance of dynamic temperature fluctuations on performance of electronic chips has been emphasized recently (Ref. [1]). Nearly 90% of existing thermal model models for chip cooling applications (convective air/liquid cooling and liquid immersion cooling) are steady-state models [1]. The PROFIT (Prediction of Temperature Gradients Influencing the Quality of Electronic Products) program, aimed at improving the quality of thermal data and methods used in design of electronic components, has placed emphasis on the need for accurate surface temperature measurments. Surface temperature measurements on IC chips can be employed to detect structural integrity of the circuit or solder layers in the package [2]. Laser thermoreflectometer, scanning thermal microscopes etc. have been proposed for this purpose. However, these devices cannot provide realtime measurements under actual device operating conditions given the bulky nature of these thermal probes. Thin film thermocouples (TFT) provide a more viable alternative as they can be manufactured insitu.

Additionally, the manufacturing process for TFT can be easily integrated in the IC manufacturing stage.

In the 1990's it was realized that convective cooling with air as the working fluid would be incapable of providing sufficient cooling to emerging thermal management needs and applications. Pool boiling and spray cooling are two attractive options for cooling such devices. The former has the additional advantage of not requiring any moving parts thus reducing cost of operation. Most liquids suitable for such applications are dielectric fluorocarbons with very low latent heat. Therefore, these devices must operate in the high-heat flux regime of the boiling curves. A higher component temperature due to presence of hotspots lowers the operation frequency. Additionally, it results in higher leakage power, leads to increased thermal mechanical stress, causes faster degradation of material property and reliability thereby affecting system life. As the number of cores in a processor increases, the power distribution is expected to be more uniform with an even distribution of hotspots [3]. A successful implementation of pool boiling for such applications requires a thorough understanding of the underlying physics to develop predictive tools. Predicting onset of nucleation, creating surfaces with consistent onset of nucleation at a particular temperature, enhancing critical heat fluxes, development of models capable of predicting transient surface temperature fluctuations and instituting a feedback control mechanism are some of the key areas requiring attention. Engineered surfaces have to some extent addressed the first and second concerns. Development of predictive models for surface temperature fluctuations however, is largely unexplored. The first step in developing predictive tools therefore involves understanding the dynamics of surface temperature fluctuations in controlled pool boiling experiments.

The importance of measuring surface temperatures with adequate spatial and temporal resolution in pool boiling systems to improve understanding at a fundamen-

tal level has recently gained emphasis [4], [5]-[8]. In a numerical study by Banerjee and Dhir [9], temperature fluctuations of the order of 10 - 20K were identified during growth and departure of a bubble in boiling of water. Kenning et al. [10] employed liquid crystal thermography on the underside of a thin stainless steel plate, to measure temperature fluctuations in pool boiling of water. Extensive spatial and temporal variations in temperature ($\sim$ 30K) was observed. However, the liquid crystals had a frequency response of only 200Hz with associated noise issues that precluded thorough application of non-linear time-series analysis tools. In both studies, the need for an array of temperature sensors with very low time constants, located on the boiling surface was clearly highlighted.

In 1892, Henri Poincaré, realized that Hamiltonian systems may possess characteristics of random systems such as unpredictability. Nearly eight decades passed before Lorenz encountered similar features in dissipative convection. The system investigated by Lorenz comprised of three simplified, coupled, first-order non-linear differential equations derived from the Navier-Stokes and energy balance equations. Irregular behavior was observed despite well-defined initial conditions. Thus, chaos theory was born. Despite the seemingly irregular characteristics of deterministic chaotic systems, short-term predictions of system variables is possible. With the advent of high-power computing and simultaneous development of the mathematical theory of fractals, it is now possible to characterize chaotic systems. Deterministic chaos is commonly encountered in Rayleigh-Benard convection, motion of a double pendulum, various electronic oscillators, chemical reactions, population dynamics and weather patterns to name a few. Chaotic dynamics has also been observed in operation of Boiling Water Reactors (BWR). Geometrical patterns (attractors) characterizing various states of the BWR system has been reconstructed for various operating scenarios using measured velocity, pressure and temperature fluctuations [11]. The

reconstruction of attractors in these cases is important to differentiate between stable and unstable operating regimes.

In the past three decades, understanding of deterministic (temporally) chaotic systems in terms of routes to chaos and its universal characteristics has improved tremendously. Characterization of experimental time-series and determination of chaotic behavior through the time record of a few system variables however, is still in its infancy. Concepts of ergodicity such as information and entropy are now used to analyze time series data thus providing a new, richer perspective. A successful application of these techniques requires high quality experimental data. This is especially true of chaotic systems possessing many active degrees of freedom or dimensions. With increase in the number of dimensions, the requirements on resolution of the measurement probes increases. In order to access smaller measurement scales, the probes need to be more sensitive and yet less susceptible to noise. The disparities in the length and time scales [12] that exist in different pool boiling regimes further complicates measurements. For instance equation (1.1) gives the expression for evaluating the capillary length.

$$L_{lo} = \sqrt{\frac{\sigma}{g\left(\rho_l - \rho_v\right)}} \tag{1.1}$$

For instance, in nucleate boiling, the characteristic length, given by (1.1) and the total heat flux is dominated by the contribution from the microlayer [4]. The bubble size and frequency of departure varies throughout the nucleate boiling regime and is different for each of the three regimes. Furthermore, near CHF the Taylor instability wavelength determines the spacing of the vapor columns [4]. Therefore, the development of new measurement techniques capable of resolving temperature fluctuations at smaller length and time scales is crucial for the development of sound predictive models. The developed measurement techniques must possess adequate

spatio-temporal resolution to resolve the various thermo-hydraulic features that exist at disparate scales in pool boiling.

Various regimes can be distinguished in a system depending on the the relation between the system size (L_c) and the characteristic correlation length (ξ_{corr}). The correlation length is the same as the basic [13] instability length λ for points away from a critical point and in the absence of dynamically significant defect. In systems with $\xi_{corr} \geq \mathrm{L}_c$, the fluctuations are spatially correlated and a few modes are sufficient to describe the dynamics. For systems with $\mathrm{L}_c >> \xi_{corr}$, and many active modes a statistical approach is valid. Systems which are intermediate are more difficult to describe. Therefore, near CHF and in film-boiling, the correlation length may be related to the Taylor instability wavelength. For nucleate boiling, the correlation length may be assumed equal to the capillary length (L_{lo}). Therefore, in a pool boiling experiment, the test surface may be large compared to the capillary length in nucleate boiling and small compared to the Taylor instability wavelength in FDNB, at CHF and in film-boiling. Thus, a statistical model of nucleate boiling may be valid for a practical application provided the characteristic length is significantly greater than the capillary length scale and there are many active modes. At intermediate length scales both models may be applicable. The device size in electronic cooling applications is typically of the order of a few centimeters or less. At smaller length scales, restriction of the spatial modes may result in only a few active modes or degrees of freedom. Therefore, there is a possibility for the system to be described using a deterministic approach. Alternatively, the dimensionality of nucleate boiling even for a few sites may be very high. High-dimensional systems can be described by stochastic equations. For instance, Kitron et al. [14] modeled nucleation site interactions using a stochastic approach. Mallozi et al. [15] investigated the site-seeding theory of Judd et al. [16] using a stochastic model. Their results matched closely with experiments

of Judd and Chopra [17] confirming the site seeding theory. The presence or absence of chaotic dynamics in pool boiling, if established, would serve as guide in choosing an appropriate time-series modeling approach.

The above review clearly highlights the need to study the dynamics of surface temperature fluctuations in saturated and subcooled pool boiling using sensors that afford enhanced spatial and temporal resolution. Micro-machined thin-film nano-thermocouples are employed in this study to acquire surface temperature fluctuation data in the nucleate and film boiling regimes. The nano-thermocouples ensure minimal interference with the thermal and hydrodynamic phenomena while providing superior transient response and spatial resolution. As a part of this investigation, the impact of liquid subcooling, surface texturing and substrate material on the surface temperature fluctuations is assessed using techniques of non-linear time series analysis.

B. Motivation

The motivation behind this study is to determine and classify the dynamics of pool boiling processes. The variation of dynamics with heat flux as the control parameter is investigated. The dynamics of boiling is assessed in terms of invariants such as dimensions and Lyapunov exponents. The results of this study is expected to serve as a guide and lead to development of suitable models for surface temperature fluctuations in boiling. These models can be employed to develop suitable control strategies for surface temperature fluctuations in electronic chip cooling applications. Clear presence of deterministic dynamics, routes to chaos or chaotic dynamics if established, can provide useful physical insights that can be used to model surface temperatures in pool boiling for practical applications. At the very least, onset of chaotic behaviour

can be predicted as a function of control parameter if one of the classic routes to chaos is exhibited by the system.

C. Hypothesis

Hydrodynamics of pool boiling is governed by the non-linear Navier-Stokes equations whereas the energy exchange process is essentially dissipative. Coupling of hydrodynamic phenomena with energy as well as mass transport lead to surface temperature variations causing high frequency surface temperature fluctuations [18]. It is possible that surface temperature fluctuations in boiling are deterministic and possibly chaotic, therefore monitoring surface temperature fluctuations at a given location can provide information on the nature and dynamics of the non-linear coupled parameters during boiling experiments.

D. Problem Statement

Does a pool boiling system possess chaotic dynamics? Previous studies involving a single nucleation site [19], few nucleation sites (Refs. [20], [21]) or on small surfaces conclusively verified the presence of chaos in pool boiling systems. The primary goal of the present study is to experimentally measure surface temperature fluctuations using novel thin-film nano-thermocouples. The temperature fluctuation data is analyzed to assess the dynamics of a pool boiling system. The second aim is to determine the impact of subcooling on boiling dynamics. Lastly, a preliminary study of impact of surface texturing on the dynamics of boiling is conducted.

E. Significance of Study

This study will contribute to existing literature in pool boiling chaos. Available data on chaotic dynamics of pool boiling is sparse. Many of these studies have been conducted on small wires or on surfaces with a single or a few (2 - 3) nucleating cavities. The effect of subcooling and surface texturing on the dynamics of pool boiling has not been analyzed in literature. This study is expected to make the following contributions.

1. This is the first study conducted to assess the impact of subcooling on the dynamics of pool boiling.

2. This is one of the first studies involving application of non-linear time-series analysis techniques to surfaces with multiple nucleation sites.

3. The approach employed in this study can be extended to arrays of thin film sensors to analyze spatial and temporal temperature variations

4. The results of this study can be used to implement a suitable feedback loop to monitor and regulate surface temperature fluctuations which can be the subject of a future study.

F. Nature of the Study

This study comprises of two parts:

1. In the first part, pool boiling experiments were conducted to acquire surface temperature fluctuation data.

2. In the second part, the experimental data was analyzed using time-series techniques.

The experiments were conducted in a constant heat flux type apparatus. PF-5060 was used as the test fluid in all experiments. Thin film thermocouples (TFT) were micromachined on silicon substrates measuring 450 μm in thickness. Experiments were conducted over silicon substrates with TFT, with and without MWCNT. Contact angle measurements were performed on the substrates using an FTA-188 goniometer. The test fluid wetted all surfaces very well. The TFT were calibrated insitu in air using a calibrated wire-bead thermocouple as reference. High frequency, quasi-steady state surface temperature measurements were acquired during the tests.

The high frequency surface temperature measurements were analyzed using the TISEAN© software package. Higher dimensional vectors were constructed from the measured, scalar, temperature time-series using a delay embedding technique. Phase plots were generated to visualize the attractor geometry in nucleate and film boiling. Invariants such as correlation dimension and Lyapunov exponents were evaluated.

G. Research Questions

This study aims to address the following questions:

1. Are surface temperature fluctuations on heater surfaces in pool boiling deterministic?

2. Are the surface temperature fluctuations chaotic? If so, what are the values of various quantifiers such as dimensions and Lyapunov exponents?

3. Does subcooling and texturing impact the dynamics of boiling and hence surface temperature fluctuations?

H. Theoretical Framework

Various notions of dimensions are employed in this study. Non-linear time-series analysis of the data is conducted to determine the class of dynamics. An introduction to elementary concepts of fractals and chaos theory is therefore in order.

1. Fractals & dimensions

Irregular, non-smooth, non-differentiable functions and sets were treated as pathological cases by mathematicians until the first half of the twentieth century. However, these sets abound in nature for e.g. ferns, trees, clouds etc. Mathematical examples include the Cantor set, Sierpinski triangle and Peano curve. Mandelbrot [22] realized this and created a generalized framework to describe the rich geometrical aspects of these objects which he termed 'fractals'. In doing so, he generalized the notion of dimensions. Fractal theory propounded that dimensions can be real positive fractional numbers and not just a positive whole number. Most mathematical fractals show the following characteristics [22]:

1. self-similarity i.e. a part of the fractal is similar to the whole
2. structure at arbitrarily fine scales
3. a generator which on recursive application results in the fractal
4. inability to be described in terms of classical geometry for e.g. locus of points satisfying some geometric criterion
5. Classical measures such as length, area and volume cannot be applied to these objects

Natural fractals do not show exact self-similarity and structure at arbitrarily length scales close to the mean free path of molecules. Additionally, they possess different self-similarities at different scales and are therefore called 'multifractals'.

There are many notions of 'dimension' that can be applied to characterize fractals such as, box-counting dimension, Hausdorff dimension, self-similarity dimension etc. The Hausdorff dimension and the box-counting dimension are the most important. The former due to its ability to be defined for any set and the latter for its ease in computational evaluation. These are described in what follows.

From [22], the Hausdorff measure is defined before defining the Hausdorff dimension.

1. If A is a non-empty subset of the n-dimensional Euclidean space $\Re^n$
2. | A | = supremum {| x-y |:x, y $\in A$}
3. If $\{A_i\}$ is a finite collection of sets of diameter of at most ξ, covering B i.e. $B \subset \bigcup_{i=1}^{\infty} A_i$
4. If $0 <$ | A_i| $\leq \xi$, $\forall$ i, then $\{A_i\}$ is a ξ - cover of B.
5. If B $\subset \Re^n$ and s is a non-negative number for $\xi > 0$

$$H^s_\xi(B) = \textit{infimum}\{\sum_{i=1}^{\infty}|A_i|^s : A_i \textit{ is a } \xi - \textit{cover of } B\} \tag{1.2}$$

$$H^s(B) = \lim_{\xi \to 0} H^s_\xi(B) \tag{1.3}$$

The Hausdorff-Besicovitch dimension is then

$$dim_H B = \textit{infimum}\{s : H^s(B) = 0\} = \textit{supremum}\{s : H^s(B) = \infty\} \tag{1.4}$$

$$H^s(B) = \begin{cases} \infty \ if \ s \ < dim_H B \\ 0 \ if \ s \ < dim_H B \end{cases} \tag{1.5}$$

The above limit generally exists for any B subset of $\Re^n$, though a limiting value of 0 or ∞ can be found. $H^s(B)$ is the Hausdorff measure of B. The box-counting dimension exists if the lower and upper box counting dimensions defined below exist.

$$dim_L B = \lim_{\xi \to 0} \frac{log N_\xi(B)}{-log \xi} \tag{1.6}$$

$$dim_U B = \lim_{\xi \to 0} \frac{log N_\xi(B)}{-log \xi} \tag{1.7}$$

where, N_ξ(B) is the smallest number of sets of diameter at most ξ, which cover a non-empty bounded set B $\subset \Re^n$. While the box-counting dimension lends itself to computer implementation for low-dimensional objects, it is computationally intensive to evaluate and assign a box-counting dimension for high-dimensional objects. It is necessary to use various notions of dimensions in order to characterize the geometrical patterns encountered in chaotic dynamical systems. Physically, the dimensions can be used to determine a qualitative picture of the dynamics involved such as (periodic, multiply-periodic, chaotic, etc.). Based on the classification of dynamics, simplified difference models can be developed on the attractor geometry. These models can be employed for prediction and forecasting. In order to describe the geometries encountered in experimental chaotic dynamical systems, an alternative strategy needs to be devised. This is discussed in the following section.

2. Chaos & time-series analysis

Chaos is a feature exhibited by systems with non-linearities for specific parameter values. Not all systems with non-linearities will exhibit chaotic dynamics for all parameter values. A chaotic system usually possesses the following properties:

i) it is topologically transitive, i.e. has a dense orbit,

ii) has sensitive dependence on initial conditions,

iii) it is expansive and has a dense set of periodic points

Chaotic dynamical systems generally possess strange attractors. Strange attractors are those geometrical patterns that characterize the final state of the dissipative system [23]. The characterization of geometrical aspects of these strange attractors serves as a measure of the number of parameters required to describe the system. Strange attractors are found to possess fractal geometry and hence are characterized by fractal dimensions.

However, these are difficult to estimate computationally for dimensions greater than two. Grassberger and Proccacia [24] suggested the use of a new measure called 'correlation dimension'. Correlation dimensions can be evaluated with ease compared to the Hausdorff dimension. The correlation between points $\{\overrightarrow{Y}\}_{i=1}^{N} \equiv \{\overrightarrow{Y}(t+i\tau)\}_{i=1}^{N}$ of a long time-series attractor is considered and a quantity known as a 'correlation integral' is evaluated. In order to estimate the correlation dimension, the correlation integral defined below is evaluated first:

$$C(\epsilon, N) \equiv \lim_{N\to\infty} \frac{1}{N^2} \sum_{i,j=1}^{N} \varphi\left(\epsilon - |\overrightarrow{Y_i} - \overrightarrow{Y_j}|\right) \equiv \int_0^{\epsilon} d^d\epsilon' c(\overrightarrow{\epsilon'}) \propto e^{\eta} \tag{1.8}$$

where, φ is the Heaviside step function and η is closely related to the Hausdorff dimension D_H. The correlation dimension is obtained in the limit of infinite data as follows:

$$D_C = \lim_{\epsilon\to 0} \lim_{N\to\infty} \frac{\partial ln C(\epsilon, N)}{\partial ln \epsilon} \tag{1.9}$$

The following relation between the correlation 'dimension' D_C, information dimension D_I and Hausdorff dimension D_H was proved [24]:

$$D_C \leq D_I \leq D_H \tag{1.10}$$

The information dimension is defined as:

$$D_I = \lim_{\epsilon \to 0} \frac{\langle \ln p_\epsilon \rangle_\mu}{\ln \epsilon} \tag{1.11}$$

In order to evaluate the aforementioned dimensional measures, a high frequency measurement of one variable is sufficient, provided "enough" transient data is available.

The goals of time series analysis are [25]: i) characterization ii) modeling iii) forecasting. The goal of characterization is to determine properties of a system such as the number of degrees of freedom or the randomness. Modeling aims to accurately describe the long term behavior of the system whereas forecasting is concerned with short-term predictions. Common linear time series models involve i) the use of past values in predicting the future such as in Moving Average (MA) models ii) the use of past values and controlled input or error in case of Autoregressive (AR) models or iii) a combination of both such as in ARMA models. Selecting the model order is of crucial importance as increasing the model order will result in overfitting. Overfitting leads to poor prediction and increased model complexity.

These linear models fail in case of deterministic non-linear systems possessing a few degrees of freedom and exhibiting a broadband power spectrum. Linear ARMA models can show a broadband spectra only in the presence of an external noise input. The embedding approach to forecasting is very similar to the AR model in that, both seek to determine a predictive function based on time-lagged vectors. A global AR/linear model represents the geometrical structure in a hyperplane whereas, state-space forecasting involves recognition of the underlying geometrical structure and then representing it [25]. Once the number of time-lagged components exceeds the minimum embedding dimension required to embed the attractor geometry, the attractor geometry remains unchanged. Characterization of the geometry plays a vital role in recognizing the presence of excessive noise or non-stationarities in the data.

If low-dimensional dynamics is determined, the next step involves modeling of the hypersurface geometry capable of interpolating between measured points and distinguishing noise from system dynamics [25].

As mentioned above, the first task in state-space forecasting is the recovery of attractor geometry. It has been shown by Sauer (Ref. [26]) that the time-series measurement of single physical quantity can be utilized to recreate the attractor geometry by forming vectors in higher dimensional spaces using time-delay embedding. The reconstructed attractor can then be characterized and used for forecasting. Mathematically, the value of the time-lag or optimal delay should not affect the estimates for correlation dimensions and Lyapunov exponents. Practically however, this is not the case. Experimental time series are always corrupted with noise. Furthermore, the limited resolution of measuring instruments limits access to finer scales. Additionally, it is not possible to acquire and analyze an infinitely long dataset. Estimation of invariants in theory, requires an infinitely long, noise-free dataset. Such being the case, the choice of the delay affects the structure of the reconstructed attractor. Approximately seventeen different procedures exist for determination of the optimal delay. The most widely used approach is based on the mutual information concept.

After attractor reconstruction using delays, the second step is characterization of the attractor in terms of invariants. Attractor dimension and Lyapunov exponents are two key invariant quantities. The latter measures the rate of divergence or contraction of nearby trajectories. Onset of chaotic dynamics results in a positive Lyapunov exponent. Presence of a clear attractor dimensionality and positive Lyapunov exponents implies chaotic dynamics. Therefore, existence of invariants is informative in discerning the class of dynamics present in the system, consequently dictating the modeling approach. The validity of characterizing the system with invariants is assessed by surrogate data tests. The surrogate data sets are generated by

assuming various hypotheses about the class of system dynamics. Certain quantities for e.g. higher order autocorrelations are evaluated for the original and surrogate data sets. If the value of the quantity for the original data set differs significantly from that for the surrogates, then the hypotheses assumed in generating surrogates is false. After validation, the next step involves prediction and developing suitable models. Common approaches involve local or global models using linear, polynomial or radial basis functions.

I. Scope & Limitations

The present study is limited to non-linear analysis of temperature fluctuations at a specific location. Temperature fluctuations measured by multiple thermocouples are not combined to generate higher dimensional phase spaces. Prediction and forecasting are not a part of this study. The experimental temperature fluctuation data is available only for nucleate and film pool boiling for all test cases.

J. Overview of Dissertation

Previous studies have shown presence of significant spatio-temporal fluctuations in pool boiling. It is necessary to acquire and analyze this spatio temporal temperature fluctuation for successful application of pool boiling to electronics cooling. Previous studies in boiling literature have claimed the presence of chaotic dynamics in systems with a single or a few nucleation sites. Furthermore, preliminary review of chaos literature shows the need for acquiring time-series data of one or more variables with sufficient temporal resolution to reconstruct the attractor for non-linear time-series analysis. This requires the development of novel sensors. Therefore, thin film thermocouples have been employed in this study to analyze the dynamical nature of

pool boiling systems.

Chapter II begins with an overview of pool boiling heat transfer. Previous work pertaining to enhancement of pool boiling heat transfer rates using engineered surfaces is reviewed and summarized. This is done with a view to understand and highlight the impact of surface characteristics on the boiling process. Chaotic dynamics in bubbling, a phenomenon closely associated with nucleate boiling, is reviewed with a view to understanding the dynamics of nucleate boiling. Results of studies concerning dynamics of boiling on surfaces with a single, few or multiple nucleation sites is summarized. The limitations of these studies with regard to data acquisition and analysis are identified. The working principle of thermocouples is briefly discussed. Additionally, literature concerning thin film temperature sensors and time-series analysis is reviewed briefly.

Chapter III describes the experimental methodology. Details of the test fluid employed, steps involved in fabrication of the thin film temperature sensors, synthesis of Multi-walled Carbon Nanotubes and characterization of the textured surface are elucidated. In Chapter IV, the data analysis procedure and associated concepts are described. In Chapter V, the pool boiling curves and results of the non-linear analysis is presented and analyzed. Chapter VI, discusses the results of the non-linear statistical analysis for the textured surfaces. Chapter VII summarizes the results of this study and presents several suggestions for future work in this area.

CHAPTER II

REVIEW OF LITERATURE

A. Purpose of this Review

The present review is intended to serve the following purposes:

1. Provide an overview of Pool Boiling Heat Transfer Research
2. Identify recent trends in boiling research such as boiling on engineered surfaces
3. Review current surface temperature measurement techniques
4. Review current state of the art in boiling chaos research and identify areas needing additional research

B. Overview of Pool Boiling Heat Transfer & Prior Research

Boiling is a first-order phase transition process characterized by drastic changes in thermo-physical properties and very high rates of heat transfer across a sharp interface. Thermodynamically, a first order phase change process occurs at a constant temperature. In practice however, this can be achieved by infinitesimally slow heating. In practical applications, the liquid is in contact with the heating surface and heterogeneous nucleation occurs. The nearly isothermal phase change process is confined to a thin layer between the vapor bubbles (or void fractions) and the liquid phase. Temperature variation within the liquid phase occurs close to the wall in a thin thermal boundary layer which is continually disrupted by the departing vapor bubbles. Pool boiling involves hydrodynamic and thermal interactions between the heating surface, the liquid and the vapor phases of the fluid. The heater surface temperature varies spatially primarily due to the presence/absence, activation/deactivation of nucleation

sites, and variations in convection currents. Temporal variations in the heater surface temperature at a specific location can occur due to variations in bubble departure frequencies, bubble sizes and the associated variations in convection currents as well as latent heat.

The high rates of heat transfer in pool boiling processes are attributed to the enhanced convection currents generated by the motion of the bubbles and the latent heat involved in the change of phase. Pool boiling is commonly encountered in process industry equipment [27]. The parameter of interest in these applications is the average heat transfer coefficient. Surface temperature and its fluctuation is relatively of less importance.

Investigations by [28],[29] and [30] elucidated various features of the classical pool boiling curve. The classical pool boiling curve is obtained for well-wetted surfaces with large characteristic dimensions exceeding the capillary length scale (in nucleate boiling).

In 1934, Nukiyama [30] while investigating the heat transferred by a metal to a boiling liquid plotted the heat flux as a function of the wall superheat. This was the first representation of pool boiling heat transfer data in the form of a boiling curve encompassing the nucleate and film boiling regimes in scientific literature. Additionally, this was the first instance in which the critical heat flux and Leidenfrost points were experimentally attained. Wires made of iron, nickel, nichrome and platinum were used in these experiments. The metallic test wires formed a leg of a Wheatstone bridge circuit. The surface temperatures of the wires were determined by balancing the resistance. In earlier studies, Austin [30] proposed that the heat transfer rate in pool boiling increased asymptotically with wall superheat without a limit. Nukiyama's seminal work contradicted this theory. Faber and Scorah [31], experimentally investigated the relationship between the heat flux and wall superheat in

the nucleate, transition and film regimes at different pressures. They were the first to apply Newton's law of cooling to characterize the heat transfer coefficient along boiling curve at different superheat. The impact of surface roughness on the heat transfer coefficients was analyzed in that study.

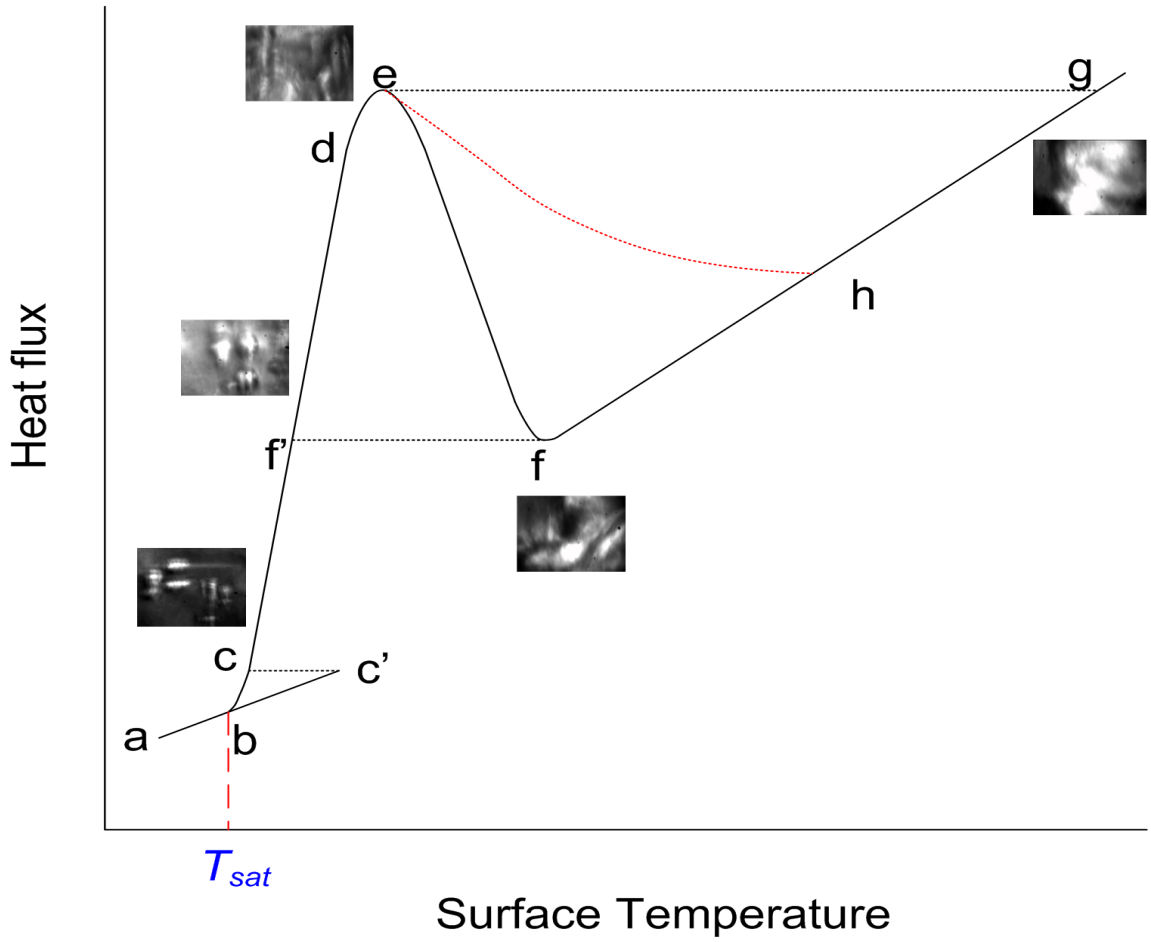

Fig. 1.: The classical pool boiling curve

Figure 1 shows a typical pool boiling curve with stills from high-speed movies acquired during the tests conducted in this study. At very low wall superheat (a - b) heat transfer occurs by natural convection. At 'b', the surface temperature equals

the 'boiling point' or the saturation temperature of the liquid at the corresponding pressure and inception of boiling occurs. This is termed as the *'onset of nucleate boiling'* in pool boiling literature. At this stage, a small increase in wall superheat results in a large increase in heat flux. The boiling curve thus rises sharply beyond 'b'. Sometimes, especially in the case of very smooth well-wetted surfaces, inception fails to occur at 'b'. Instead, natural convection prevails despite the increase in wall superheat. In these cases, the boiling curve follows the natural convection curve up to a point 'c'. At 'c', there is an onset of nucleation causing a sudden decrease in the surface temperature as shown by the dashed line c-c$'$. Hsu [4] proposed that an embryo will become a bubble provided it was surrounded by superheated liquid all around. Hsu arrived at the following expression for the wall superheat required to cause inception:

$$\frac{T_{h=2r_c} - T_{l\infty}}{T_{sat}(P_{liq}) - T_{l\infty}} = \frac{3.2\sigma T_{sat}(P_l)}{\rho_l h_{fg} \delta_t (T_{sat}(P_l) - T_{l\infty})(1 - 2r_c/\delta_{blt})} \tag{2.1}$$

Wang and Dhir [32] proposed the following relation for wall superheat required for incipience based on vapor-liquid interfacial instability analysis:

$$T_{sup} = \frac{2\sigma T_{sat}}{\rho_v h_{fg} r_c} K_{max} \tag{2.2}$$

$$K_{max} = \begin{cases} 1 \text{ if } \theta_w \leq 90^\circ \\ Sin(\theta_w) \text{ if } \theta_w > 90^\circ \end{cases} \tag{2.3}$$

After incipience, the bubble begins to grow. This may be due to i) evaporation around the entire interface ii) or evaporation of a thin microlayer between the bubble interface and the heater iii) convection currents created by marangoni effects within the microlayer. Further increase in surface temperature results in a rapid rise in heat flux due to activation of additional nucleation sites. This is called Partial Nucleate

Boiling (PNB). This is depicted in the figure by the curve c′ - d. Bubbles are discrete in this regime and do not merge in the vertical direction. The increase in the number of active cavities with wall superheat is given by the following expression [32]:

$$N_c \sim \delta T^{n_1} \tag{2.4}$$

The constant n_1 lies between 4 and 6 for water boiling on various surfaces [32]. The proportionality constant varies with surface roughness. The heat transfer rate in the nucleate boiling regime is given as [32]:

$$q = \frac{K^2}{2}(\sqrt{\pi k_l \rho_l c_{pl} f}) D_b^2 N_a \Delta T + \left(1 - \frac{K^2}{2} N_a \pi D_b^2\right) \overline{h}_{nc} \Delta T + \overline{h}_{ev} \Delta T N_a \frac{\pi}{4} D_b^2 \tag{2.5}$$

'K' is a proportionality constant.

The region (d - e), is characterized by the merging of bubbles in the vertical direction initially followed by lateral merger subsequently. This regime is termed *'the regime of slugs and columns'* in some references. It is more commonly known as *'fully developed nucleate boiling'* (FDNB). Increase in surface temperature results in increased vapor formation and flow rates. This results in increased vapor drag on the liquid flowing toward the surface between the vapor columns. This causes a decrease in the liquid flow rate toward the surface. Hence, the vapor stems spread on the surface and merge together. This process eventually reaches a critical point wherein the heat transfer rate is maximum. This point is known as *'critical heat flux'* (CHF) and is the point of maximum heat transfer rate. Nucleate boiling encompasses all the aforementioned regimes with the exception of CHF. Hydrodynamic models, bubble packing models and microlayer evaporation models have been put forth to explain phenomenon of CHF. Kutateladze [32], employed dimensional analysis to obtain an equation for the CHF in terms of dimensionless groups. Zuber [32], obtained a similar estimate by assuming that CHF occurred because of Kelvin-Helmholtz instability of

the jets. The following expression was proposed by Zuber [32]:

$$q''_{max} = C\rho_v h_{fg} \sqrt[4]{\frac{\sigma g(\rho_l - \rho_v)}{\rho_v^2}} \sqrt{\frac{\rho_l + \rho_v}{\rho_l}} \left[\frac{\rho_l(16-\pi)}{\rho_l(16-\pi)+\rho_v\pi}\right] \tag{2.6}$$

The constant C as obtained by Zuber was $\frac{\pi}{24}$. Subsequently, this was modified Lienhard and Dhir [32] for large horizontal plates ($L_{char} \geq 3.0\lambda_{Tay}$) and a variety of well-wettin fluids. For other geometries, the relation for peak heat flux is modified as:

$$q''_{maxog} = f\left(\frac{W}{L_{lo}}\right) q''_{max} \tag{2.7}$$

As the characteristic, dimensionless length defined by the ratio of heater width to the capillary length scale decreases, the function f increases. For large heaters, this value of f tends to one [32]. Values of CHF predicted by hydrodynamic models exceed the experimentally observed values by as much as 55% [32]. Furthermore, visual observations reveal the presence of large mushroom type bubbles rather than vapor jets. This led Haramura and Katto [32] to postulate their microlayer evaporation model. However, the microlayer evaporation model is inconsistent with experimental observations and is unable to explain the effect of wettability on CHF. Surface texturing, wettability, geometry, material, size, subcooling, flow velocity, heating method, gravity, all affect the CHF. For instance, CHF is higher in case of well-wetted surfaces. Heaters with low thickness show a lower CHF compared to predictions of the hydrodynamic theory. Surface texturing, wettability, geometry, material, size, subcooling, flow velocity, heating method, gravity, all affect the CHF. For instance, CHF is higher in case of well-wetted surfaces. Thin heaters show a lower CHF compared to predictions of the hydrodynamic theory [32].

The impact of porous coatings on pool boiling heat transfer has received significant attention. Porous coatings may be broadly classified as consolidated and

unconsolidated. In the latter case, the particles are not constrained and can undergo self-organization to form vapor escape paths at high heat fluxes. Porous coatings impact the nucleate boiling process by providing additional nucleation sites, which can be activated at low wall superheats Ref. [33]. Additionally, porous media enhance the surface area, decrease instability wavelengths, influence bubble departure diameters and frequencies, and provide additional paths for the liquid to reach the surface under the influence of capillary pressure. Typically, smaller particles lead to early inception of boiling because of the difficulty in removing entrapped gases in the interstitial voids. At higher heat transfer rates however, there is no perceptible heat transfer enhancement and the boiling curves for surfaces with porous coatings collapse onto the pool boiling curve for uncoated surfaces. For surfaces with small particles ($\sim$ 10 - 100μm), capillary effects and particle drag forces are dominant [33]. Some models for predicting peak heat fluxes in porous media are reviewed in ref. [33]. An approach proposed in Ref. [34] may be applicable to pool boiling over carbon nanotube coated surfaces. The model assumes the presence of fine capillaries supplying liquid to larger 'chimneys'. A force balance applied to the liquid and vapor phases yields an expression for the maximum heat transfer rate. A more recent work ref. [35], modified the hydrodynamic theory to account for the CHF phenomenon. Two liquid choking limits were proposed and the lower of these limits was postulated to result in CHF.

A slight increase in surface temperature at CHF results in a vapor blanket covering the entire surface. Depending on the application or the type of experimental setup (constant temperature or constant heat flux), the system may either reach film boiling after passing through the transition boiling regime or alternatively, it may directly proceed to burnout in the absence of any interruption to the power supply. Transition boiling (e - f) is characterized by rapid and severe changes in surface temperatures

and local heat fluxes. Violent vapor explosions occur in the transition boiling regime resulting in repeated wetting and dewetting of the surface. Subsequent increases in surface temperature in the transition boiling regime results in decrease in heat flux due to the gradual stabilization of the vapor film resulting in fewer 'explosive' events.

As the surface temperature is increased further, another critical phenomenon is encountered resulting in a second inflection in the pool boiling curve. This local minimum in heat flux is termed as 'Leidenfrost point'. The Leidenfrost point marks the onset of film boiling wherein the entire heater surface is covered by a vapor blanket. Subsequent increase in surface temperature results in increase in heat transfer rates. However, the increase in heat transfer rates are not as high as those encountered in the nucleate boiling regime. The contribution to the total heat transfer rate by radiative and convective modes increases as surface temperature is increased in the film boiling regime.

The transition boiling regime cannot be sustained in constant heat flux equipment. Any increase in surface temperature at the CHF results in the system directly proceeding to the corresponding point (point with the same heat flux as at CHF) in the film boiling regime. This often results in damage to the equipment and is termed as 'burnout'.

C. Boiling heat transfer enhancement - Prior Research

1. Micro-engineered surfaces

The impact of surface texturing on heat transfer enhancement and subcooling on pool boiling heat transfer rates has been the subject of numerous studies. Research in this field is focused in three main areas:

1. promoting consistent onset of nucleate boiling at low wall superheat levels for

electronics cooling

2. enhancing nucleate boiling

3. enhancing critical heat flux

The occurrence of ONB and enhancement nucleate boiling heat transfer can be achieved by creation of re-entrant type cavities with poorly wetted walls. Nucleate boiling heat transfer can be enhanced by roughening the surface or by impregnating the surface with artificial nucleation cavities Ref. [36]. Re-entrant cavities promote nucleation by vapor trapping and evaporation within. Consequently, liquid convection is increased resulting in enhanced heat transfer rates. Although roughening a surface increases pool boiling heat transfer rates, the performance of the surface deteriorates with time. Long term stability of nucleation sites is an important parameter in developing commercially viable surfaces for enhanced nucleate boiling heat transfer.

An enhanced structure consisting of six layers of grooved copper plates capable of being stacked was employed by Ramaswamy and co-workers [37]. They used this structure to investigate the effects of sub-cooling, pressure and height on its boiling performance. They observed that an increase in subcooling and pressure caused an increase in the heat transfer rate. The effect of varying pore size and pitch on boiling performance was investigated in the same study. An increase in pore size and reduction in pitch augmented the heat transfer rate. Coursey et al. [38] investigated the performance of graphite foam in nucleate boiling at various chamber pressures, working fluids and liquid levels. They concluded that heat fluxes approaching 50 W/cm^2 were attainable with wall temperatures maintained below 85 ℃ .

Li et al. [39] studied pool boiling of water over copper surfaces with and without copper nano-rods. Significant enhancement in pool boiling heat transfer rates was observed. The pool boiling curves shifted to the left i.e. lower wall superheats were

required to sustain a given level of heat flux on the surface with nano-rods compared to the plain surface. The magnitude of peak heat fluxes however, were relatively constant ($\sim$140 - 160 W/cm^2). Many bubbles of smaller diameter were observed on the nano-rod coated surface compared to the plain surface. This was similar to the photographic observations of Sathyamurthi et al. (Ref. [40]) for boiling over MWCNT coated surfaces. The increased nucleation was attributed to the micro-scale defects with the nano-scale pores between the nano-rods acting as 'feeders' to the larger cavities. Aging of the test surface caused a decrease in heat transfer rates but these were higher than the heat transfer rates over the plain copper surface. Bubble release frequencies were $\sim$ 2 - 4 times the release frequencies of the plain surface which varied from $\sim$ 2 to 30 Hz for wall superheats ranging from $\sim$ 0 to 25 K. Bubble departure diameters however, were 2.5 to 3.5 times higher for the plain surface.

Chang et al. [41] investigated the impact of microporous coatings on pool boiling heat transfer rates using FC-72 as the working fluid. Five different coatings ranging between 3 μm and 50 μm in size were evaluated. Three coating materials comprised of aluminum (1 - 20 μm), copper (1 - 50 μm) and diamond (8 -12 μm) powders with brushable ceramic as binder and methylethylketone as the carrier. The other two coating materials were diamond (8 - 12 μm) and silver (3 - 10 μm) with Omegabond as the binder and alcohol as the carrier. All five coatings showed similar heat transfer rates ($\sim$ 30 W/cm^2) at CHF with the excess temperature ranging between 10 and 20 ℃ . Therefore, a heat transfer enhancement of 200 % was obtained over that shown by a reference surface. Additionally, the microstructured surfaces showed early incipience of boiling (ONB) at significantly lower heat flux levels ($\sim$ 0.2 - 0.4 W/cm^2) and at significantly lower excess temperatures ($\sim$ 2.5 - 9 ℃). By contrast, corresponding heat flux at boiling incipience was 3 W/cm^2 and the excess temperature was 45 ℃ for the reference surface. One of the obstacles in employing phase change cooling

of electronic components is the high excess temperatures required to initiate the incipience of boiling. This study demonstrates, that microporous surfaces can be employed to lower incipience.

Honda et al. [42] studied pool boiling of FC-72 over three micro-fabricated surfaces (10 mm ×10 mm × 0.5 mm). Three different surfaces, two consisting of micro pin fins (50 μm× 50μm×60 μm, 100 μm pitch) with and without sub-micron scale roughness (32nm) and a third surface with sub-micron scale roughness of 25 nm and no pin fins. Experiments were conducted at subcooling levels of 0, 3, 25 and 45 K. The micro-pin fins enhanced the heat transfer in the nucleate boiling regime and in increasing CHF. The chip with sub-micron scale roughness showed an increase in heat transfer rates at low heat fluxes whereas the chips with micro-pin fins enhanced heat fluxes in the high heat flux regime. Photographic observations revealed the presence of vapor trapping between the micro-pin fins after bubble departure leading to enhanced nucleation rates and possibly, higher heat transfer rates. Critical heat flux was observed to increase linearly with subcooling. Heat transfer rates at CHF were 1.8 - 2.3 times the CHF for a smooth surface, similar to the increase in surface area of 2.2 times for the micro-fabricated surfaces.

2. Boiling on CNT coated surfaces

M. Endo and others [43]-[45] CNT were the first to produce and analyze carbon nanotubes (CNT) using high resolution electron microscopy in 1975. The rolled-up lamellar sheets of 'carbon fibers' produced by pyrolysis of Benzene and Ferrocene at 1000 ℃ were analyzed. Single walled and multi-walled carbon nanotubes (SWCNT and MWCNT) were imaged in this study. In 1991, S. Iijima [46] reported the formation of microtubules of graphitic carbon. Capped, needle-like MWCNT 4-30 nanometers in diameter and 1 μm in length were produced by using D.C. arc dis-

charge evaporation in an inert argon filled chamber. CNT have inspired numerous research activities due to their interesting physical properties. Physical properties of CNT are highly dependent on its length, diameter and chirality. The thermal properties of CNT are dependent upon its phonon dispersion relation and phonon density states [47]. Phonons are quantized vibration modes occurring in crystalline materials. The thermal conductivity of CNT varies with temperature and the phonon mean free paths. The estimation of thermal conductivity of SWCNT has been the subject of numerous studies and is a subject of debate. CNT may possess high thermal conductivity values (3000 - 6000 W/mK) according to studies([48] -[51]). However, another study [52] shows thermal conductivity of CVD-grown MWCNT possess thermal conductivities of the order of 25 W/mK. However, these MWCNT were grown by CVD at temperatures as low as $\sim$ 600 K resulting in many defects. It must be mentioned here, that the MWCNT used in this study are made using a similar technique and similar temperatures. Therefore, it is reasonable to expect similar thermal properties for the CNT used in this study. Crystalline, defect-free CNT are produced at elevated temperatures of the order of 1100 K or more.

The impact of CNT on pool boiling heat transfer rates has been the subject of few studies. Independent investigations by Ahn et al. [53] and Ujereh et al. [54] were amongst the first in this area. Ujereh et al. [54] reported a 60 % enhancement at CHF employing silicon substrates covered with multi-walled carbon nanotubes (MWCNT) of 30 nanometer diameter and 20 - 30 microns length with FC-72 as the working fluid. The study was restricted to the nucleate boiling regime. Impact of CNT on film-boiling heat transfer rates and the impact of sub-cooling were not a part of the study. Almost simultaneously, Ahn et al. [53] reported a 25 - 28 % enhancement in heat transfer (within the heating block) at CHF using two silicon substrates coated with MWCNT 9 μm and 25 μm in height with PF-5060 as the working fluid. The 25

μm tall CNT surface showed a 57% increase in heat transfer rates at the Leidenfrost point while the 9 μm tall CNT substrate showed no perceptible enhancement in the film-boiling regime. The impact of sub-cooling was the subject of another study by Ahn and co-workers [40]. Pool boiling experiments were conducted using PF-5060 as the working fluid on silicon substrates with (9 μm and 25 μm) and without nanotubes. The enhancement in heat flux was weakly dependent on the height of the MWCNT layer in the nucleate boiling regime. The enhancement in heat transfer rates for nanotube coated substrates decreased with increase in subcooling. This was attributed to the change in morphology of the bubbles with increase in subcooling. Additionally, the nucleation site density increased on the nanotube coated surfaces compared to the bare substrate. In nucleate boiling, MWCNT coated substrates yielded higher wall heat fluxes under saturated and subcooled conditions compared to a bare silicon surface. The 25 μm tall MWCNT array augmented CHF by $\sim$ 2% compared to a bare silicon surface under saturated and 10 ℃ subcooling. In the film boiling regime, the heat flux was sensitive to the height of the MWCNT coating. For Type-B MWCNT (25 μm height) the wall heat flux values were enhanced under saturated ($\sim$ 62%), 5 ℃ subcooling ($\sim$ 62 % - 124 %), 10 ℃ subcooling conditions ($\sim$ 66 % - 148%), (compared to control experiments performed on a bare silicon surface). However, for Type-A MWCNT (9 μm thickness) the wall heat flux values are similar to the corresponding values for the bare silicon surface during film boiling, for low subcooling. At high subcooling the film boiling heat flux values were enhanced significantly and by similar magnitudes for both bare silicon and Type-A MWCNT coated heaters.

Additional details of these and other studies are summarized in Table I. Clearly, surface texturing affects pool boiling heat transfer rates. Porous surfaces for instance, bring capillary forces into play.

Table I.: Studies on boiling over textured surfaces

Author	*Substrate & Geometry*	*Feature Size & Test Condition*	*Liquid*	ΔT_{sup}	q''_{max}
Ramaswamy et al. [37]	6 grooved copper plates, 1.1 cm^2	90 - 320 μm width Pitch 0.5 - 2.1 mm $\Delta T_{sub} = 0$, P = 1atm.	FC-72	4 - 30K	50 W/cm^2
Coursey et al. [38]	18mm (H)×13mm ×13mm (D) Graphite	T_{cond} = 23, 43.5 ℃	PF-5060, PF-5050	-30 - 60K 0 - 90K	75 W/cm^2 65 W/cm^2
Li et al. [39]	Copper	40 - 50nm (ϕ), 450nm (H) $\Delta T_{sub} = 0$, P = 1atm.	Water	1 - 20K	150 W/cm^2
Chang et al. [41]	12.7mm (ϕ) copper	1 - 50μm	FC-72 $\Delta T_{sub} = 0$, P = 1atm.	2.5 - 25K	30 W/cm^2
Honda et al. [42]	Silicon, 10×10 ×0.5mm^3	30×60μm^2, 30×120μm^2, 30×200μm^2, 50×60μm^2	FC-72	-40 - 20K	80 W/cm^2

Table I. Continued.

Author	*Substrate & Geometry*	*Feature Size & Test Condition*	*Liquid*	ΔT_{sup}	q''_{max}
	with square micro-fins	$50\times200\mu m^2$, $50\times270\mu m^2$ ΔT_{sub} = 0, 3, 25, 45K			
Liter & Kaviani [35]	Copper disk, ϕ = 5.08 cm	Copper microspheres uniform, single or double modulated, 0.6 - 1.2 mm ΔT_{sub} = 0K	Pentane	1 - 22K	76.2 W/cm^2
Ujereh & Mudawar [54]	Silicon 12.7mm×12.7mm	Carbon nanotubes $\phi \sim$ 50nm, 20-30μm (H) ×400μm Fully coated, Island ΔT_{sub} = 0K	FC-72	1 - 12K 4 - 30K	17 W/cm^2 14 W/cm^2
Sathyamurthi et al. [40]	Silicon 5.9cm×3.2cm×450μm	Carbon nanotubes $\phi \sim$ 16nm, 9μm, 25μm (H), Fully coated	PF-5060	0 - 20K 4 - 30K	14.3 W/cm^2 18.4 W/cm^2-

Table I. Continued.

Author	*Substrate & Geometry*	*Feature Size & Test Condition*	*Liquid*	ΔT_{sup}	q''_{max}
Mitrovic [55]	Cavities arranged in hexagons	Artificial cavities $\phi \sim 180$ μm, 120μm deep $\Delta T_{sub} = 0$, P = 1atm.	R-11	0 - 20K	20 W/cm^2
Mitrovic [55]	Copper tube 18mm$\times$180mm 1×10^4, 1×10^7/cm^2	Micro-pins $\phi \sim 1$ - 25 μm, 10 - 100 μm deep $\Delta T_{sub} = 0$	R-141b	0 - 15K	15 W/cm^2

D. Related Topics: Chaos & Non-linear Dynamical Phenomena in Boiling

In the past three decades alternative approaches to understanding pool boiling mechanisms has emerged. It has been suggested that a pool boiling system is dissipative and chaotic [21]-[57]. Pool boiling is characterized by the formation and departure of bubbles and associated convection in the nucleate boiling regime. In FDNB and at CHF, vertical and lateral coalescence of bubbles occur. In the film boiling regime, the surface is blanketed by a vapor film. Chaotic dynamics has been observed in bubbling of a gas from orifices submerged in a liquid medium. This has important implications for the nucleate boiling, FDNB and possibly CHF. Bubbling of gases through submerged orifices mimic cavities present on surfaces in pool boiling. Therefore, dynamical behavior of bubbling may provide important clues about the dynamics of bubble departure in pool boiling. Studies pertaining to bubbling from submerged orifices and boiling chaos are reviewed in the following section.

1. Chaos in bubbling from submerged orifices

Zhang and Shoji [58] investigated bubbling from a capillary orifice submerged in a pool of water. Compressed air was forced through the orifice at flow rates ranging from 100 cc/min - 2000 cc/min. Four distinct regimes were observed:

1. isolated/single bubble regime
2. interference regime, where the newly formed bubble interacted with the wake left behind by the previous bubble
3. collision regime, where the newly formed bubble assumed an ellipsoidal shape and touched the previous ascending bubble

4. coalescence regime, where the newly formed bubble merged with the previously formed bubble

Period -1, 2 and 3 behvior was observed in this experiment. Balance of forces led to a theoretical model for the bubble emissions and a set of criteria for determining transition from one regime to another. Tufaile and Sartorelli [59] investigated the chaotic behavior of bubbling of air from a submerged nozzle, placed in a water/glycerine solution for three different conditions. In the first case, a hypodermic syringe was connected to a capacitive air reservoir without the needle. Because of bubbling, the pressure within the capacitive reservoir decreased. A bifurcation diagram showed the evolution from a chaotic state at high pressure to a period-1 state at low pressures. In the second case, a needle was attached to the syringe. Only period-2 behavior was observed followed by a period-1 behaviors. In the third case, the air pressure was fixed and sound wave amplitude was used as a control parameter. Bifurcations were observed from a fixed point to a limit cycle and finally chaotic attractors through a flip bifurcation. Positive Lyapunov exponents ranging from 0.25 - 0.75 were estimated indicating the presence of chaotic dynamics. In another study by the same authors, [60] observed the existence of a henon like attractor in bubbling of air through a water/glycerol mixture.

Cieslinski and Mosdorf [61] investigated bubbling of air through three different glass nozzles submerged in distilled water. They used a photo-acoustic technique to measure the bubble departure rates. Changes from a periodic to a chaotic state was observed as the air flow rate was varied. Attractors were reconstructed for different nozzles and different flow rates. Correlation dimensions were found to vary from 2-6 for the rarer part of the attractor and from 7-12 for the denser part.

Clearly, from the aforementioned studies that bubbling progresses from a low-dimensional, periodic state to a higher dimensional chaotic state through a series of bifurcations. It is reasonable to expect an analogous behavior in the nucleate boiling regime with heat flux being the controlling parameter instead of the flow rate. Thus, nucleation from a single site in pool boiling should progress from a periodic state at low heat fluxes to a chaotic state at high heat fluxes through a series of bifurcations. Bubble merger in the vertical direction is indeed observed at high heat fluxes in pool boiling. Studies of chaos in boiling from a capillary tube, single and multiple nucleation sites are reviewed in the following section.

2. Dynamics of boiling: Single or few nucleation sites

There are very few studies pertaining to the dynamics of pool boiling on a surface with many active nucleation sites. The studies mentioned in the previous section investigated bubbling from a single nozzle/orifice. A non-uniform temperature distribution exists within a pool boiling system comprising of the heater, the liquid and the vapor phases. Because of the non-uniformity in temperature distribution and motion of the liquid, a pool boiling system is in thermal and mechanical non-equilibrium [62]. Kenning [10], measured temperature variations of the order of 4 - 30K over a distance of a few millimeters during boiling of water on a stainless steel plate coated with thermochromic liquid crystals. Development of predictive tools for surface temperature fluctuations is vital for applications such as electronic cooling [63]. Many parameters affect the boiling process such as heater surface characteristics, the type of fluid and the spatio-temporal variations of solid-liquid-vapor interfaces [5] to name a few. These parameters lead to additional spatial and temporal fluctuations of surface temperature.

Acharya et al. [56] studied boiling in a glass capillary tube. The capillary

tube mimicked the cavities present on a heating surface in practice. A differential thermocouple arrangement with an amplifier was used to measure the time intervals between successive bubble emissions. The average frequency of bubbling increased with increase in heat flux. One-dimensional return maps of the time intervals between successive bubble emissions were used to study the transitions from the periodic state. Bifurcations from the periodic state to period-2 and period-3 were observed with increase in the control parameter i.e. the heat flux. The presence of period-3 implies the presence of chaos [64]. Indeed, seemingly random behavior was observed with an increase in heat flux. The depth of penetration of the vapor interface within the cavity was theoretically estimated and its impact on the dynamics of bubbling was explained.

Shoji and Takagi [19] investigated saturated boiling of water on copper surfaces with single conical, cylindrical and re-entrant type cavities. At low heat transfer rates (1.69 and 1.88 W), periodic behavior was observed with correlation dimensions of 0.94 and 1.80 for a conical cavity of 50μm diameter. At higher heat flux levels of 1.98 and 2.73 W, correlation dimensions were 2.28 and 2.31 respectively. Correlation dimensions of the order of 0.49 - 1.36 was observed for heat flux levels of 2 - 2.67 W and cavity diameter of 100μm. The phase plots fig. 2 were traingular in shape with a 'ball' like substructure at higher heat transfer rates. Positive Lyapunov exponents were estimated for all but one heat flux level (100μm cavity, 2 W heat transfer rate). The authors concluded the presence of chaotic dynamics from these quantifiers. It is however, well-established, that chaos is not possible in flow systems in dimensions less than two. It is therefore, very likely that the estimated dimensions and Lyapunov exponents in some of the test cases are spurious.

In [20], temperature fluctuations under a single nucleation site and the thermo-hydraulic interaction between two nucleating sites was measured. The temperature

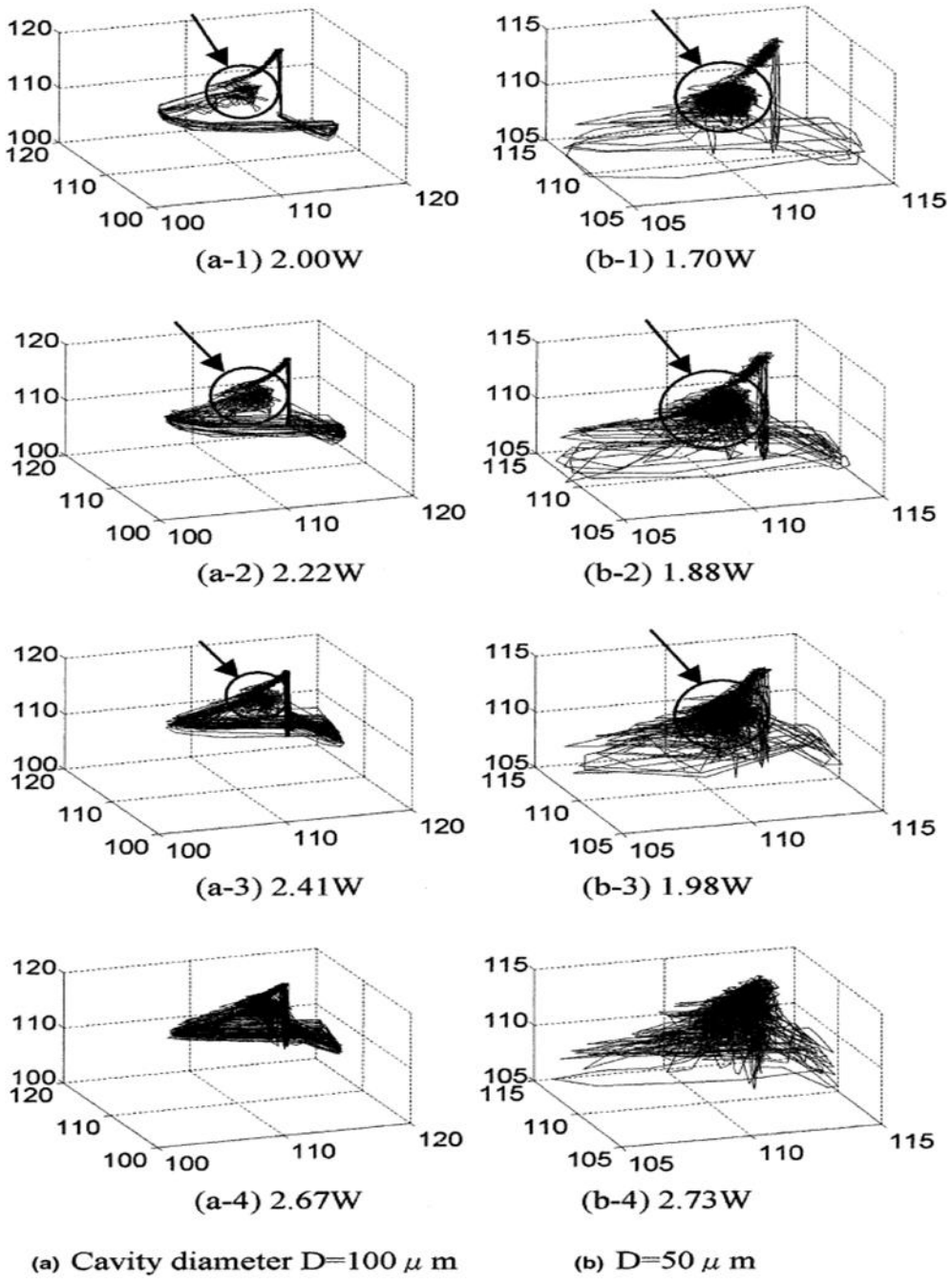

Fig. 2.: Phase plots for nucleation from a single conical cavity.

Reprinted from International Journal of Heat and Mass Transfer, Vol. 44 (14), M. Shoji, Y. Takagi, Bubbling features from a single artifical cavity, (2001), with permission from Elsevier.

fluctuations under a single nucleation site for three different heat flux levels was plotted with time. The fluctuations appear to be periodic, multiply periodic or quasiperiodic from the temperature time-series plots and the phase plots. However, the authors claimed the presence chaotic dynamics based on a positive maximal Lyapunov exponent ($\sim$ 32 bits/s) and a fractal dimensionality ($\sim$ 3.7). The positive Lyapunov exponent in this case could be an artifact of noise in the system. Yasui and Shoji (Ref. [21]) studied the 'complexity' of boiling on a surface with a single nucleation site. Spatio-temporal temperature fluctuations were measured along the center line of the cavity. Non-linear analysis indicated that the 'complexity' was low at the bubble base but increased in regions beyond the bubble base periphery. This was attributed to the bulk liquid motion, micro-convection currents and/or due to heat transfer at the bubble meniscus. The presence of thermal and hydraulic interactions between neighboring nucleation sites in pool boiling gives rise to additional phenomena such as site activation and deactivation. These interactions can also cause departure from the period doubling route to chaos and can influence the number of degrees of freedom of the system. The effect of multiple ($\sim$2-3) nucleation sites was the subject of studies by Mosdorf and Shoji [65], Zhang and Shoji (Refs. [66], [67]). The effect of site spacing on the dynamics of surface temperature fluctuations was investigated in [20]. The distance between two nucleation sites was varied and the thermal fluctuations were recorded. Phase plots were reconstructed for different wall superheat values and inter-site spacings. It was found that the temperature fluctuations became more 'complex' for certain site spacings. The correlation dimensions were observed to vary from 4 - 12 depending on the heat flux and site spacing. Zhang and Shoji [57] selected twin cavities of 10 μm diameter and 80 μm depth and kept the size of the cavity constant while varying the spacing from 1.0 to 8.0 mm. Bubble sizes were typically of the order of 2.4 mm in diameter. The spacing to bubble diameter ratio

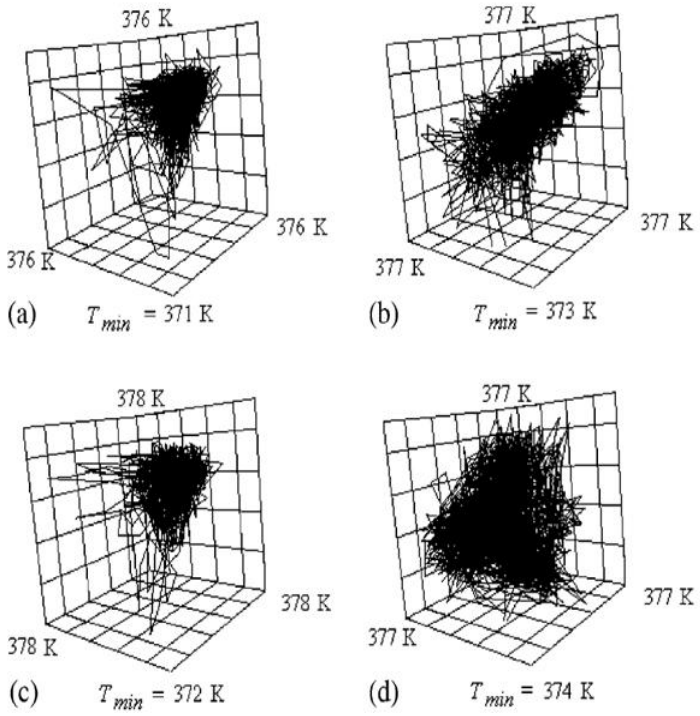

Fig. 3.: Phase plots for nucleation from two cavities with different spacing.

Reprinted from International Journal of Heat and Mass Transfer, Vol. 47 (6-7), R. Mosdorf, M. Shoji, Chaos in nucleate boiling - non-linear analysis and modelling, (2004), with permission from Elsevier.

was thus 0.3 to 3.3. It was observed that as the spacing decreased the bubble diameter decreased and departure frequency increased and heat transfer was enhanced. Three modes of interaction were identified. They were, the hydrodynamic interaction, the thermal interaction and the horizontal and vertical bubble coalescence. Based on the intensity, competition and dominance relationships four interaction regimes were identified. Additionally, the attractors were plotted (fig. 3) for different nucleation site spacing. For site spacing below a particular value, thermal and hydrodynamic interactions were significant. Consequently, the attractor had a “wool - ball” shape indicative of a dimensionality greater than three.

While the aforementioned studies helped in understanding the dynamics of nucleate boiling, they were limited to a single nucleation site. Additionally, most of the aforementioned studies were confined to the low heat flux nucleate boiling regime. The collective behavior of multiple nucleation sites, located randomly on a surface is important in many commercial applications. More importantly the possibility of using chaotic dynamics to obtain a predictive tool needs to be analyzed. The location of these sites is unknown a priori and results in numerous thermo-hydraulic interactions. The large amount of thermo-hydraulic interactions may lead to high-dimensional or stochastic behavior. If the dimensions are too high, the system behaves similar to a stochastic system anyway. It is also possible that the collective behavior of the interactions is relatively simple. This is similar to thermodynamic systems which consists of many atoms but have only a few normal modes.

Many different techniques have been used in literature to obtain a time-series record of variables in pool boiling. The most common variable, measured in these studies was the surface temperature. Shoji et al. [68] used micro-thermocouples located 0.1mm from the heated surface to obtain high-frequency ($\sim$ 1 kHz)temporal surface temperature measurements. Ellepola and Kenning [69] used copper plates 0.05 and 0.1 mm thick coated with liquid crystal on the underside to obtain simultaneous spatio-temporal temperature data under pool boiling conditions. Due to thermal inertia, they were limited to acquiring data at 200 Hz. Due to high levels of noise in the video recordings, singular value decomposition was used to reconstruct the attractor. Other studies by Shoji et al. have (Refs. [67], [66], [65] and [19]) employed radiation thermometers to obtain temperature-time records. Despite many studies, evidence of chaotic dynamics in pool boiling systems is sketchy at best.

Shoji [70] investigated the dynamics of pool boiling over short wires with water as the working fluid. The correlation dimension was determined to identify the presence

of chaos in saturated pool boiling. The diameter of the wires used in that study was similar to the size of bubbles and thus the classical pool-boiling curve was not obtained. Surface temperature was estimated using the electrical resistance method by employing a specially designed circuit. Temperature fluctuations of the order of 70 K were observed in film boiling. The Fourier spectra was broad banded indicating the possible presence of chaotic dynamics. Lyapunov exponents were estimated and positive exponents were determined.

Phenomenological model equations have often been used to describe systems [71]-[73].The model equations have the same linear instabilities as the experimental system but are analytically or numerically more tractable than the physical models. Qualitative models have been proposed based on non-linear dynamics approach to explain pool boiling phenomena. Yanagita (Refs. [74],[75]) developed a coupled map lattice (CML) approach to simulate boiling. CML is a useful tool for aiding understanding of the qualitative nature of complex spatio-temporal systems. Using this technique, Yanagita succeeded in explaining boiling modes and transition from nucleate to film boiling. Yanagita assumed that thermal convection, phase change, bubble formation and departure were the fundamental dynamic processes involved in pool boiling. However, the study replicated homogeneous nucleation which seldom occurs in practice. Furthermore, boiling phase-change occurred at surface temperatures below the saturation temperature and finally, the film boiling mode was not strictly realized in this study.

Shoji [76], modified Yanagita's approach to include effects of heterogeneous nucleation and Taylor instability. While these models reproduced the qualitative features of the entire pool boiling curve, the Fourier spectra were inconsistent with experimental observations of a previous study by Shoji et al. [70]. In that study [70], the Fourier spectrum near CHF showed a significant concentration of power (≥ 0.2) at frequen-

cies ranging from 0-100 Hz and a peak at 190 Hz but the Fourier spectra obtained using CML approach showed insignificant power at frequencies ranging from 0-90 Hz (≤ 0.125). Furthermore, in the experimental study, significant concentration of power in the 20-30 Hz range was observed whereas in the CML approach showed concentration of power at frequencies in excess of 250 Hz. This is unrealistic, as it implies that bubbles depart at frequencies of 250 Hz in the film boiling regime. Additionally, it is well-known from the photographic studies of Westwater, that bubble departure frequency in film boiling is much slower than that at CHF and fully-developed nucleate boiling. However, the Fourier spectra of the CML studies shows a peak at 100 Hz and additional peaks with lower power for frequencies in excess of 100 Hz and less than 200 Hz at CHF. This implies that bubbles depart much more slowly near CHF as compared to film boiling thus contradicting experimental observations.

Ellepola and Kenning [69], developed a simplified model for the interaction between two nucleation sites using a lumped thermal capacitance approach and showed the presence of non-linear switching behavior. Similar models for multiple nucleation sites were developed by Mosdorf et al. [77]-[81].

Simulations of nucleation from multiple sites have been conducted recently [82], to investigate the on-off switching behavior of multiple nucleation sites. Nelson and Bejan [83], have proposed a self-organizing principle within pool boiling. Chai and coworkers have discussed the complexity, nonequilibrium and random nature of boiling by analyzing the nonlinear processes of boiling [21]. Chai and Shoji [84] proposed a set of criterion for the transition of boiling modes using concepts of non-equilibrium thermodynamics. However, in that study the bubbles were assumed to be in a state of equilibrium and a dynamical equation for bubble growth was derived by minimization of a Gibbs potential. It is well-known that bubble growth is not well-approximated by equilibrium criteria except, possibly for ONB. Furthermore, a Gibbs functional or

free-energy is not defined in many non-equilibrium situations [13]. Thus, the scope of applicability of the aforementioned criteria is rather restricted.

Since the publication of the aforementioned studies in chaotic dynamics of boiling, new theories and rigorous tests have been devised to test for the presence of non-linear dynamics in experimental systems. Since the publication of [70], many different techniques to estimate dimensions and establish the existence of determinism have been established. Qualitative techniques such as false nearest neighbor tests and visual techniques such as recurrence plots and space-time separation plots have been established in chaos literature [85]. Establishing the presence of chaotic dynamics in an experimental system is an involved task and requires careful, unbiased interpretation. It is always possible to determine a correlation sum from a time-series data. However, the 'correlation dimension' determined using this sum may not be a dimension at all. A correlation dimension may be assigned only if the space-scale vs. correlation sum plot shows a clear saturation in slopes. Examples abound in literature with false claims of correlation dimensions and chaos.

Any experimental system has a noise component which biases the correlation dimension estimate. Depending on the relative magnitude of noise and the strength of the signal in the system, it may or may not be possible to identify the presence of non-linear dynamics (assuming chaos is present). Therefore, special attention needs to be paid to the design of the experimental system. The level of planning that goes into designing an experiment determines its success and quality of data obtained. Poor quality data, improper functioning and generally too many problems in setting up experiments are indicative of very poor foresight, planning and/or execution. This is especially true of experiments conducted to investigate the presence of chaotic dynamics. Spatio-temporal chaos and high-dimensional chaos present additional problems in terms of accessibility of scales and resolution in the presence of noise. These issues

Table II.: Studies on boiling chaos

Author	*Details of study*	*Summary*
Mosdorf [77]	$\frac{\partial T}{\partial t} - \nabla T = 0$, y = 0, T = T_0 q(t)= C$\frac{k_s}{\Delta\delta}T_{sat}\sqrt{\frac{T-T_{sat}}{T_{sat}}}$ if T $\geq$ T_c, t = τ_1 else q(t)= Constant if T < T_c, t = τ_2	 D_c = 2-3, T_0=380K
Shoji et al. [70]	Water boiling on two wires: ϕ 80μm×0.8mm(L), ϕ 100μm×2mm(L), sampling $\sim$ 50kHz	 D_c = 6.1 (ONB), 8.7* (CHF), 3.2 (FB), 6.5 (Transition)
Shoji et al. [65]	i) Copper surface, 0.1mm(T)×ϕ 10mm 1 central cavity of conical, cylindrical, reentrant type ϕ 50μm or 100μm, 30μm or 50μm (D) ii) Silicon surface, 0.2mm(T)×ϕ 15mm 1 central cylindrical cavity ϕ 5μm - 100μm, 20μm - 80μm (D) iii) Silicon surface, 0.2mm(T)×ϕ 15mm 2 cylindrical cavities, ϕ 10μm, 80μm (D)	D_c = 3 - 7, Low dim. chaos D_c = 3 - 8, Lyapunov exp. 27 - 40 bits/s Shallow cavities shows greater complexity S $\downarrow\rightarrow$ D_{dep} $\downarrow$, f_{dep} $\uparrow$

Table II. Continued.

Author	*Details of study*	*Summary*
	spacing (S): 1, 2, 3, 4, 6 and 8mm	
Ellepola et al. [86]	Copper 25mm×20mm×0.1mm, q = 20 W/cm^2 Liquid crystal thermography, 200Hz video camera	Lyapunov exponents $\sim$ 6, D_{embed} 3 - 6
Mosdorf et al. [87]	8-silicon microchannels with 186μm (ϕ_{hyd})× 30mm (L) Cases 1a), b): Liquid/two-phase alternating flow, q = 13.5, 16.6W/cm^2, m = 14.6, 12.7gm/cm^{2}s Continuous two-phase flow, q = 18.8W/cm^2, m = 11.9gm/cm^2 Case 3: Liquid/two-phase/vapor alternating flow, q = 22.6W/cm^2, m = 11.2gm/cm^{2}s	D_c = 1.1, 2.25, 5.2, 6 Lyapunov Exponents $0.254^{+0.036}_{-0.024}$, $0.046^{+0.036}_{-0.016}$, $0.126^{+0.064}_{-0.046}$, $0.054^{+0.076}_{-0.034}$
Biserni et al. [88], [89]	Vapotron effect, finned aluminum plate 32 fins, 7mm high, 3mm thick, 2mm pitch	

Table II. Continued.

Author	*Details of study*	*Summary*
	Temperature 40Hz, in first and a central cavity P = 1200, 1400, 1600 W, $\dot{m}$ = 0.026 kg/s P = 1600W, $\dot{m}$ = 0.050, 0.096 kg/s Modeling approach: NARMAX with Multilayer Perceptron neural networks	D_{emb} = 8, 10, 8; D_{loc} = 6, 5, 6; D_{Lyap} = 5.57, 4.48, 5.76 D_{emb} =9, 10; D_{loc} = 5, 6 D_{Lyap} = 4.21, 5.64 2 - 3 positive Lyapunov exponents, 0.006 - 0.083

will be addressed as part of this study. Table II summarizes key findings of various studies in boiling chaos.

E. Thin-film Temperature Sensors

Most studies in pool boiling report 'wall' temperature measurements based on thermocouples placed some distance underneath the boiling surface or using other indirect measurements such as the resistance method. Pool boiling is characterized by significant spatial and temporal variations of surface temperature (Ref. [90]). In electronic chip cooling applications, a local hot-spot could damage the entire device. Therefore, an accurate estimation of surface temperature map in pool boiling is necessary to establish suitable control. In the aforementioned study, the surface temperatures for the various test surfaces were determined indirectly using correlations and interpolations. While, these are fairly accurate, actual surface temperature measurements for CNT coated surfaces and bare test surfaces would aid in a more representative comparison. Therefore, measuring surface temperatures with adequate spatial and temporal resolution in pool boiling systems has recently gained emphasis [6], [7]. As mentioned above, disparities in length and time scales exist in pool boiling processes in different regimes. Micro-fabrication has become a key technology enabler and has made micro and nanoscale devices a possibility. The small spatial scales of thin-film sensors can provide the necessary spatio-temporal resolution needed for a thorough understanding of the phase change process. Additionally, these sensors can be fabricated in situ, flush with the test surface and require no bonding step thus by-passing some critical sources of error in measurements. K-type, chromel-alumel micro-thermocouples were deemed suitable for this study firstly due to their excellent linear temperature response characteristics and secondly due to the relative insen-

sitivity of the emf-temperature relationship to changes in composition. A detailed description of the manufacturing methodology will be given in chapter III. In this section, a brief review of thin film temperature sensors is presented in addition to a review of operating principles of thermocouples.

1. Thin film sensors & surface temperature measurements

Harris et al. in [91] reported the concept of thin film thermocouples in the 1930's. Marshall et al. [92] studied various combinations of thermocouple elements. Bullis et al. [93], Assanis et al. [94], Debey et al. [95], Tian et al. [96], and Laugier [97] used TFT for various surface temperature measurements. TFT possess excellent high frequency response [98] due to its low thermal inertia. They can be fabricated at locations where a beaded thermocouple would interfere in the normal functioning of the object. Furthermore, the minimal thermal inertia and small feature size leads to a reduced distortion of the temperature and velocity fields in its vicinity. Thin film sensor research at the NASA Glenn Research Center (GRC) [99] has led to the development of many novel thin film sensors. The TFT developed at GRC are primarily intended for gas turbine surface temperature measurements and space based applications. TFT developed at GRC are comprised of Platinum - 13 % Rhodium and Platinum on Nickel based alloys, Silicon, Silicon Carbide, Silicon Nitride, ceramic matrix composites and aluminum oxide ceramics for high temperature measurements. Novel carbide based TFT (WC, TaC, TiC, ZrC, HfC) possessing positive and negative thermoelectric emf (VC) have been developed at GRC. Oxidation temperatures for carbide thermoelements range from 800 - 1200 ℃. Silicide based thermoelements ($TiSi_2$, $CrSi_2$, $ReSi_2$, $MoSi_2$, WSi_2, $TaSi_2$) were also used in the TFT. The oxidation temperatures for these thermoelements range from 1200 - 1800 ℃. Oxidation of the thermoelements at elevated temperatures results in deviation from linearity.

Miller [100] micro-fabricated silicon RTD and silicon diodes on a silicon substrate and performed pool boiling experiments. The instrumented surface was placed in a vertical orientation with FC-72 as the test fluid. In that study, approximately 81 sensors were fabricated on a 1.27 cm $\times$ 1.27 cm chip and artificial sites in the form of inverted pyramids were created. Bubble departure frequencies in the range of 25-35 Hz was measured alongwith temperature fluctuations of the order of 0.5 ℃. Ahn et al. [101] used thin film thermocouples to measure the surface temperature fluctuations in film boiling in order to verify the presence of cold spots. Lüttich and others [6], [7], recently used micro-machined TFT to estimate the surface temperature and heat flux fluctuations in pool boiling. However, the TFT was covered with a sputtered layer of gold 0.001 mm in thickness leading once again to an indirect estimation of surface temperature and heat fluxes by solving the inverse heat conduction problem. Myers et al. [8] used a micro-heater and a high-speed camera to obtain spatio-temporally resolved temperature and heat flux measurements in pool boiling of FC-72.

2. Thermocouples and their operating priniciple

A flow of heat occurs in a metal bar subjected to a temperature differential at its ends due to transfer of energy by collisions between more energetic and less energetic electrons (thermal conduction). A second, less perceptible effect also occurs in the form of a drift of the electron cloud from the hotter end towards the cooler end [102]. This secondary effect although small is the source of thermocouple emf. The motion of the electron cloud causes the accumulation of positive and negative charges at the end of the bar resulting in an electric field that prevents further electron cloud drift. This is known as Seebeck effect. The electric field produced is proportional to the temperature gradient.

$$\Upsilon = \frac{dV}{dx} = \kappa \bigtriangledown T \tag{2.8}$$

The net thermoelectric emf between two ends of the metal bar are given by:

$$V = \int_{T_1}^{T_2} \kappa(x, T) dT \tag{2.9}$$

In a homogeneous material the Seebeck coefficient does not vary along the length of the material and the resulting potential is thus a function of end temperatures. The potential developed is also independent of the diameter and length of the material. Contrary to the popular belief, the thermocouple potential is not produced at the junction, rather, the emf is produced and distributed throughout the length of the material in response to the temperature distribution [102]. The maximum thermoelectric emf is produced at the location of the maximum temperature gradient. In order ensure that the measured thermocouple temperature corresponds to the temperature at the junction, the maximum temperature gradient needs to be confined to the vicinity of the sensing junction. Two different metals having positive and negative Seebeck coefficients are used to increase the strength of the signal.

Lead wire connections may cause spurious junctions which, if maintained at different temperatures cause the generation of spurious potential. Therefore, data acquisition systems have Cold Junction Compensation (CJC) to correct for the spurious emf. In the present study, the spurious junctions can be formed at the bond pads and within the data acquisition system. The latter is compensated by a built-in CJC circuit whereas the former results in little or no production of emf as, the bond pads are approximately at the same temperatures in the experiments.

F. Concluding Remarks

Previous studies pertaining to fundamentals of pool boiling, heat transfer enhancement in pool boiling, thin film sensors, boiling chaos and time series analysis have

been reviewed. Enhancement of pool boiling critical heat flux using micro-engineered surfaces and CNT coated surfaces have been discussed.

1. Clearly, porous media influence the Helmhotz-Taylor instability wavelengths thereby affecting CHF (Ref. [35]). This shows that pool boiling dynamics is strongly influenced by the surface condition. The influence of surface condition and subcooling on the surface temperature fluctuations has not yet been investigated by researchers.

2. A review of chaos in bubbling from submerged orifices shows the presence of chaotic dynamics. Nucleation in pool boiling is very similar and research data from studies with heat flux as a controlling parameter do show that a single nucleation site shows chaotic dynamics.

3. Studies of boiling on few artificial nucleation sites shows complex behavior due to thermal and hydrodynamic interactions caused by the bubble departure process. Positive Lyapunov exponents have been estimated in these experiments implying the presence of chaotic dynamics.

4. Currently, there have been only two studies of chaos in boiling on surfaces with many nucleation sites. One study employed a small wire with dimensions comparable to the capillary length scale whereas the second used liquid crystal thermography technique to measure surface temperature fluctuations. The liquid crystals had a slow response time and significant noise level thereby precluding a thorough analysis.

5. A computational study, showed transition from a periodic state to a chaotic state through period doubling bifurcations in a pool boiling system with multiple nucleation sites.

6. Currently, there is no experimental study in literature, that deals with the impact of subcooling and surface texturing on boiling dynamics on large surfaces with many nucleation sites. It is clear therefore, that there is a need to investigate the impact of multiple nucleation sites, subcooling and surface texturing on the dynamics of surface temperature fluctuations to enable application of phase change to electronics cooling.

7. The review shows that it is necessary to employ reliable, high frequency surface temperature measurement techniques in order to obtain suitable time-series data. A review of literature shows, thin film thermocouples can accomplish this with some surface modifications.

CHAPTER III

DESCRIPTION OF EXPERIMENTS

A. Introduction

Test facilities used in pool boiling experiments may be broadly classified as constant heat flux type and constant temperature type. As the name suggests, the heat flux supplied to the test surface is maintained at a constant value in the former whereas, the surface temperature is maintained at a constant value in the latter. Constant heat flux facilities cannot sustain transition boiling. Any increase in heat flux beyond the CHF causes the system to transition to the burnout point in the film-boiling regime. Constant temperature test facilities make use of a secondary vapor to heat the surface. The vapor flows through a closed loop and gives up its latent heat upon condensation to the test surface at a constant temperature. Recently, micro-heaters with individual power control [103] have been employed to maintain the test surface at a constant temperature.

Surfaces used in these experiments were characterized in a goniometer for estimation of contact angles with deionized water and the test fluid PF-5060. The TFT were micromachined insitu using photolithography to transfer the pattern to the substrate. This was followed by Physical Vapor Deposition (PVD) of the chromel or alumel targets and lift-off to create the TFT. The textured surface used in these tests were created by Chemical Vapor Deposition (CVD).

The details of the experimental setup, test section fabrication and experimental procedure are elaborated in the following sections.

B. Test Surface Preparation & Description of Test Liquid

The test surfaces used in the experiments were made of silicon. The silicon wafers were rectangular in shape. The exposed area of the test surfaces measured 2.35 × 1.25 inches^2 (59.69 mm × 31.75 mm). The baseline tests (for pool boiling heat fluxes) were conducted using silicon substrates with micro-machined TFT. A second set of tests was conducted over silicon substrates with TFT coated with MWCNT. The steps involved in micro-fabrication of TFT and CVD of MWCNT are described in the following sections.

1. Micro-fabrication of TFT

The micro-fabrication process for TFT comprised of a two-stage, eight-step process involving:

1. First layer photolithography to form pattern
2. Oxygen plasma descum
3. First layer metal deposition
4. Lift-off
5. Second layer photolithography
6. Oxygen-plasma descum
7. Second layer metal deposition
8. Lift-off

2. Lithography & oxygen plasma de-scum

Lithography is a standard step in most MEMS fabrication. Most lithographic techniques currently in use, employ a polymeric compound known as 'resist' which is exposed to energetic particles (electrons or ions) or photons (X-rays, Ultra-violet light). The exposed areas are chemically modified leading to differential solubility in a developing solution [104]. If the solubility is enhanced (due to scission of polymer chains Ref. [104]), the resist is known as a positive photoresist whereas if the solubility is decreased (due to cross-linking of polymer chains Ref. [104]), the resist is referred to as a negative photoresist. A mask is commonly employed to transfer the pattern on the substrate containing the resist in 'parallel mode' [104] by 'contact' or 'proximity' alignment.

In the present study, contact photolithography was employed using ultraviolet light for exposure. A standard camera film was used as a mask. The pattern was printed on a A4 paper and reduced by a factor of 10 upon transfer to the mask. The positive mask was pasted using a cellotape on to a 4 inch $\times$ 4 inch (101.6 mm $\times$ 101.6 mm) quartz plate. The quartz plate was then placed on the chuck of a Quintel 400A mask aligner. The quartz plate was secured in place by vacuum. Mechanical grade silicon wafers (Manufacturer: University wafers) measuring 75 mm in diameter were used as substrates. The wafers were cleaned using acetone and isopropyl alcohol to remove any organic residue. The wafers were then baked at 200 ℃ for 5 minutes to remove trapped moisture present in cavities. After this, the wafers were placed in a spin-coater (Model: Laurell WS-650S) and covered with Shipley-1827 positive photoresist using a dropper. The wafer was secured on the spin-coater chuck by vacuum and the lid was closed. The spin-coater was pre-programmed to rotate at 3000 r.p.m. for 1 minute with an acceleration of 1000 rpm/s. Thus, a 2.7 μm thick

layer of resist coated the surface of the wafer. A pre-exposure bake of the coated wafer was conducted at 115 ℃ for 1 minute. The wafer was then placed on the chuck of the mask-aligner and secured in place by vacuum. After this, any alignment operations (required for patterning the second layer) were performed. After the necessary alignment operations, the photoresist was exposed to ultra-violet light for 20 seconds. The wafer was then removed from the sample-holder and developed using MF-319 solution (Manufacturer: Shipley) for 1 minute and 18 seconds. The wafers were cleaned using de-ionized water to remove traces of the developer solution bearing photoresist. A plasma descum operation was performed using the (Manufacturer: March Plasma Systems, Model: CS-1701) reactive ion etcher. The descum operation was performed under partial vacuum in an oxygen environment. This step removed traces of photoresist and dirt present (after developing) within the patterned areas.

3. Metal deposition

Metallic thin films can be deposited using a evaporation/physical vapor deposition (PVD), sputtering, CVD or electroplating [105]. In this study, the chromel and alumel metals were deposited using PVD. The CHA ebeam evaporator depicted in fig. 5 was located at the National Nanotechnology Infrastructure Network (NNIN), Micro-Electronics Research Center (MERC), University of Texas at Austin. Chromel and alumel wires (Manufacturer: Omega) were stripped of their sheathing and cut to 1.5 cm pieces. The cut chromel or alumel wires were placed in a graphite crucible (separate crucible liners were used for each metal) liner. The crucible liners containing the metal targets and adhesion promoters were placed within the crucible of the CHA. The CHA had four crucibles on a rotating turntable. The silicon wafers with the patterns were placed on the underside of a rotating carriage above the crucibles. The wafers bearing the TFT patterns of a particular layer (either chromel or alumel) were

fixed on the carriage by means of spring loaded clips. The dome of the CHA was closed and system pumped down to a pressure of 5.0×10^{-6} Torr. The pump-down took 45 minutes to an hour. Once the deposition pressure was attained, the power supply unit was turned on. The e-beam was turned on and focused on the targets within the crucible liners. The power to the electron beam varied from one run to another ($\sim$ 37% for chromel and alumel) for a single metal and varied with the type of metal. A record of the power used was maintained in a log-book at MERC. The first layer consisted of 250 Å thick titanium which promoted adhesion between silicon and chromel or alumel. Chromium was another adhesion promoter that was used in making some of these samples. However, chromium itself could have a significant thermoelectric potential of its own which could affect the performance of the TFT. Once, the titanium was been deposited, the shutter was closed, the power to the electron gun was turned off and the crucible liner bearing the other target metal (chromel or alumel) was brought into position. The target metal was deposited after the parameters such as density were changed on the CHA controller. The thickness of the deposited chromel or alumel layer was $\sim$ 2500 Å.

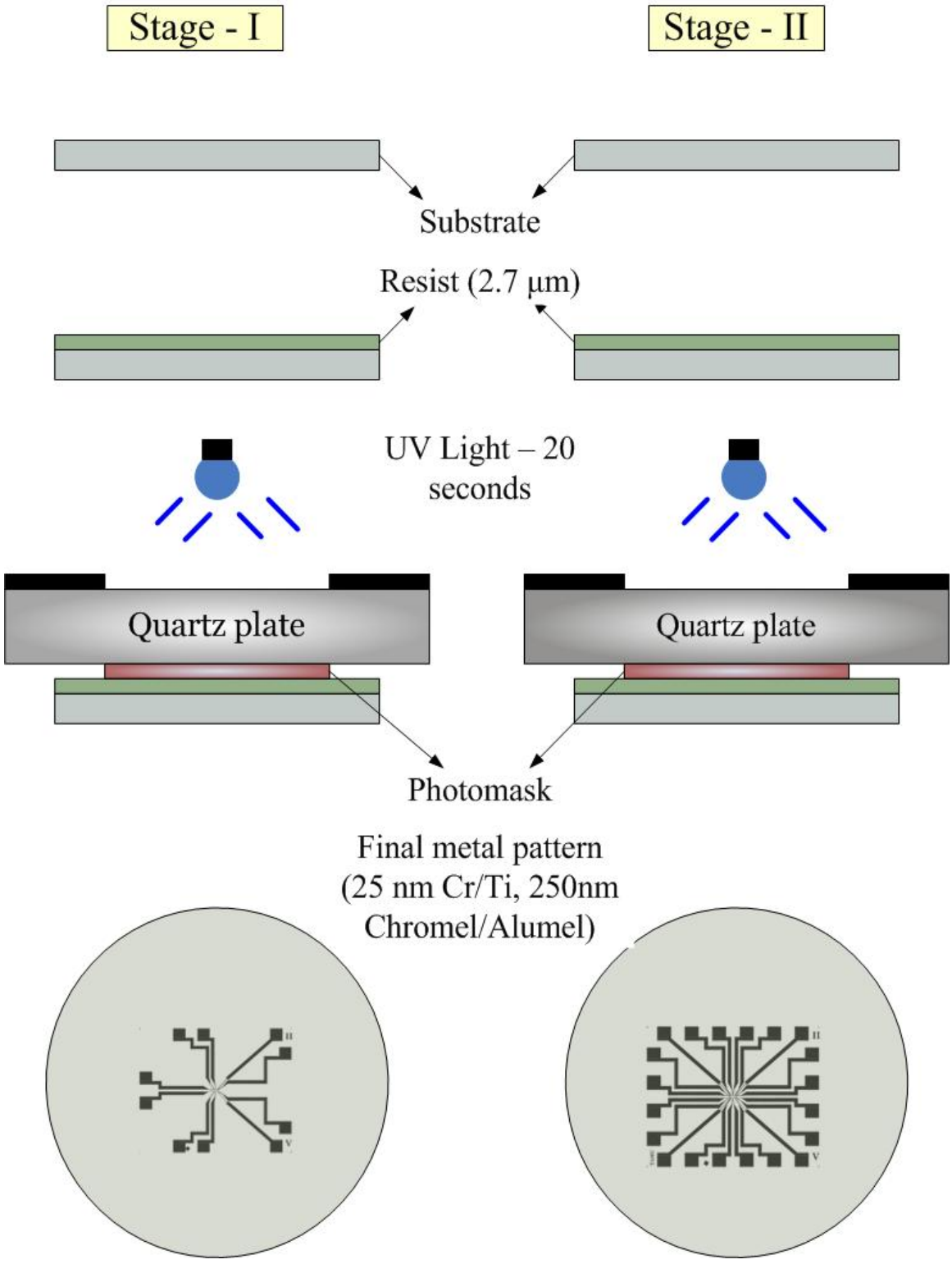

Fig. 4.: Overview of the micro-fabrication process

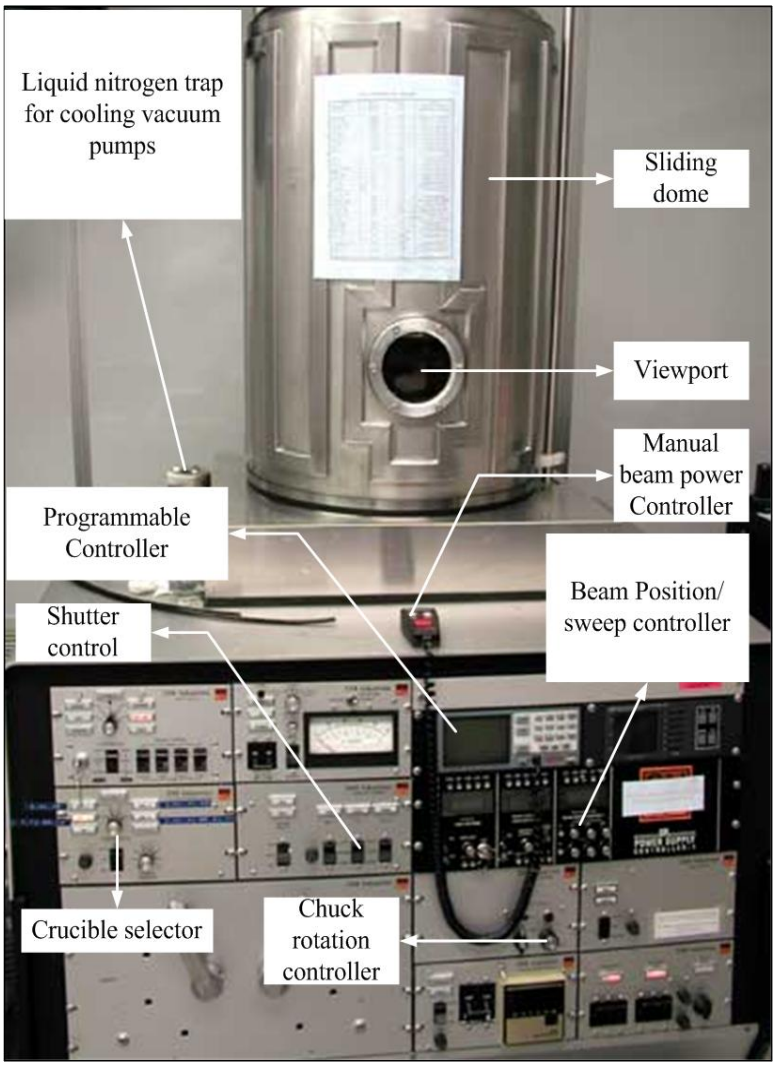

Fig. 5.: CHA Electron beam evaporator. The E-beam evaporator was employed for physical vapor deposition of metallic films as thin as 1 Å.

4. Lift-off

A lift-off step was performed to remove the photoresist bearing the deposited metal on the unpatterned areas. An ultra-sonicator filled with water was heated to 65 ℃. The ultrasonics were switched on once the water reached 60 ℃. The silicon wafers were placed in beakers with approximately 50 ml of Remover PG. The beakers were then placed in the hot water bath. The ultrasonic waves combined with the chemical action of Remover PG resulted in the removal of the excess metal and photoresist on the unpatterned areas. Thereby, the metal only remained on the patterned areas. The wafer was then cleaned with acetone and iso-propyl alcohol and dried with pressurized nitrogen. The wafer was then patterned again using the aforementioned steps for the second metal layer. Fig 6 depicts the silicon wafer with TFT after the second-stage lift off and CNT synthesis, with both metal layers. Some carbon fibers were clearly visible near the junctions (fig. 6(a)) under SEM. The junctions were ~ 50 μm in width (fig. 6(b)).

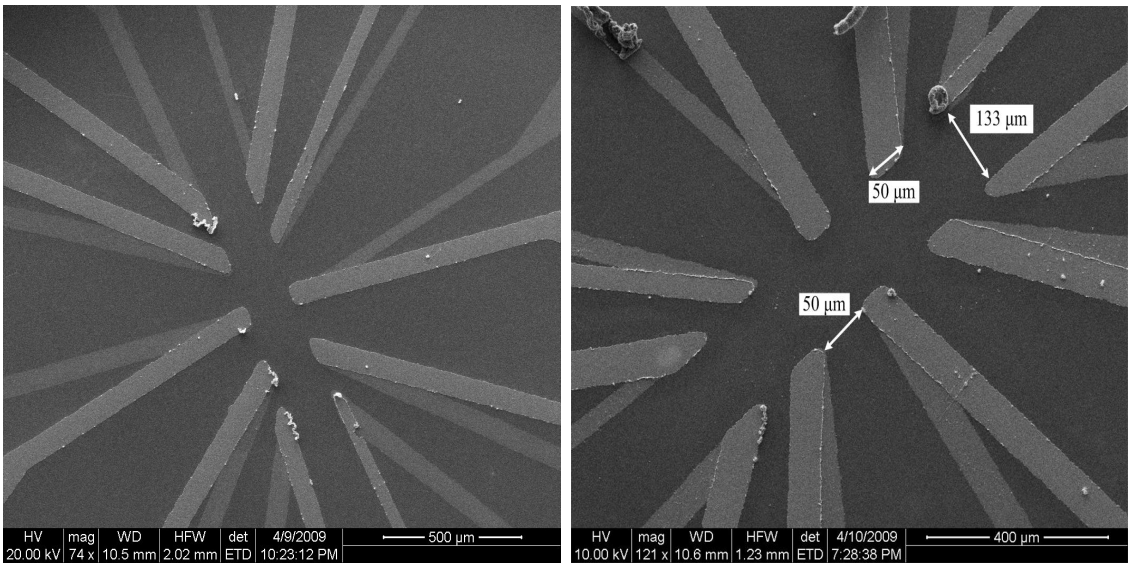

(a) TFT on silicon substrate (b) TFT junctions

Fig. 6.: SEM micrographs depicting silicon substrates with TFT. SEM images were acquired using FEI Quanta 600 FE-SEM. Figs 6(a) & 6(b) depict top view of TFT junctions after deposition of both metal layers and lift-off for two different wafers. The pitch of the TFT array varied between 50 & 133 μm. (Images courtesy: Mr. Navdeep Singh; The FE-SEM acquisition was supported by the NSF grant DBI-0116835, the VP for Research Office, and the TX Eng. Exp. Station.)

5. MWCNT synthesis

Arc-discharge and chemical vapor deposition (CVD) are commonly employed to synthesize MWCNT. In arc discharge, high currents are passed through opposing carbon anode and cathode. Arc-discharge method results in high-quality MWCNT and SWCNT. MWCNT's produced by this method are 5 - 30 nm in diameter, 10 microns

in length and very straight indicating high crystallinity. The high crystallinity is a result of the high temperatures ($\sim$ 3000 - 4000 ℃) involved in this process. In CVD [106], a catalyst is heated to high temperatures in a tube furnace usually made of quartz. Fig. 7(a) shows a typical furnace, employed for CVD, in the Multiphase flow and Heat Transfer Lab (MPFHL). A mixture of hydrocarbon gas (usually low molecular weight alkenes or alkynes) and an inert gas (for e.g. argon or hydrogen) is passed through a reactor maintained at 500 - 1000 ℃ . In addition, hydrogen gas is used to maintain a reducing atmosphere in some studies. At elevated temperatures, catalysts such as iron combine with the Transition metal nanoparticles present on the silicon substrate act as catalysts. The hydrocarbons are dissociated due to the presence of catalyst particles, followed by agglomeration of carbon atoms on the metal nanoparticles. The metal nanoparticle saturated with carbon, forms low energy tubular carbon solids possessing sp^2 structures. Ethylene and acetylene are commonly used as sources of carbon alongwith iron, cobalt or nickel as catalyst particles. Carbon has a finite solubility in these metals at elevated temperatures. Temperatures employed in CVD processes range from 550 ℃ - 800 ℃ (Ref. [106]). MWCNT produced by CVD processes possess a large amount of defects, however, it is possible to produce long, aligned nanotubes unlike arc-discharge and laser ablation methods. Depending upon the type of substrate used (porous silica, porous silicon, plain silicon), the growth rates can be varied. Plain silicon substrates show a lower growth rate compared to porous silicon. Alignment of MWCNT is due to the base-growth mode wherein the nanotubes are pinned to the catalyst particles located at the base of the substrate. The multi-walled structure of MWCNT can be verified by Transmission Electron Microscopy (TEM). Fig. 7(b) shows a TEM micrograph, depicting the multi-walled structure of a sample synthesized at MPFHL. Fig. 8 shows an SEM micrograph of a typical MWCNT 'forest' synthesized on a silicon substrate at MPFHL.

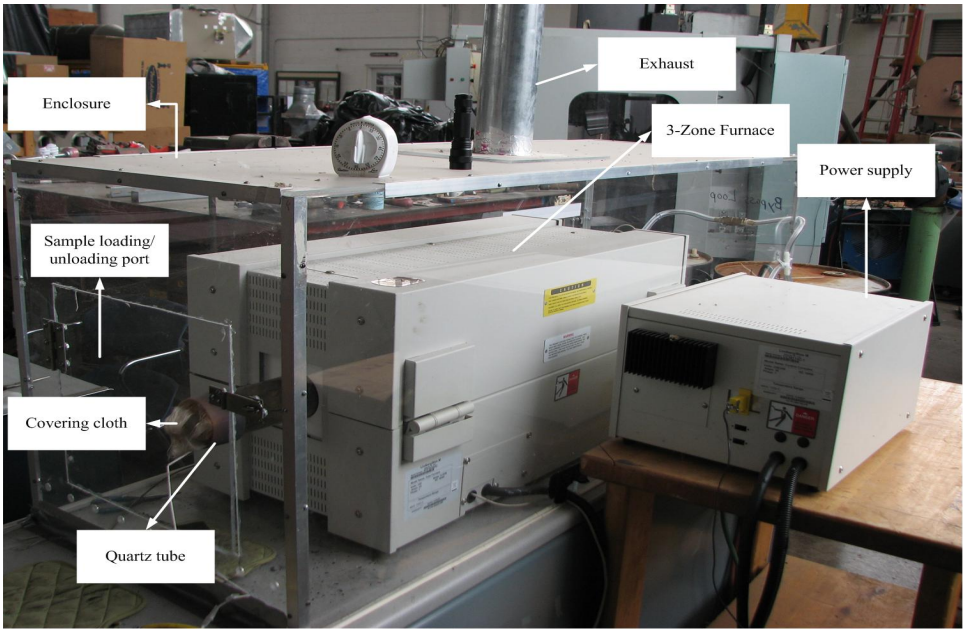

(a) Three zone CVD furnace for MWCNT synthesis

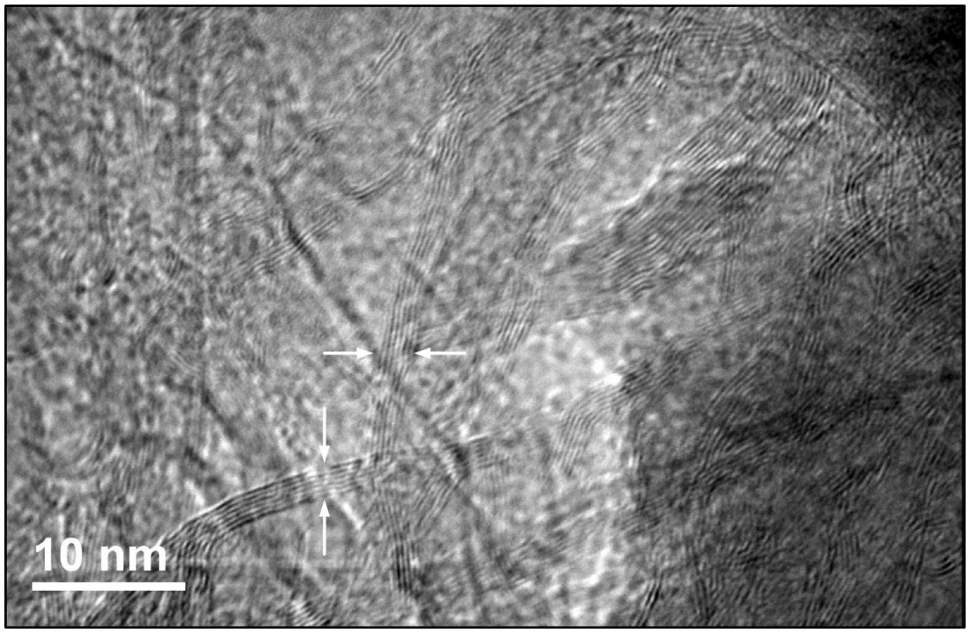

(b) Transmission Electron Micrograph showing multi-walled structure of CNT (Courtesy: Mr. Pratanu Roy, Mr. Donghyun Shin, Dr. Hansoo Kim. Acquired using JEOL JEM-2010)

Fig. 7.: CVD Apparatus used for synthesis of MWCNT & TEM image of MWCNT.

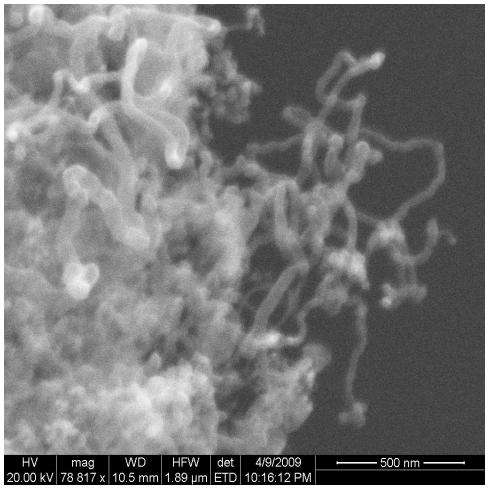

(a) MWCNT forest

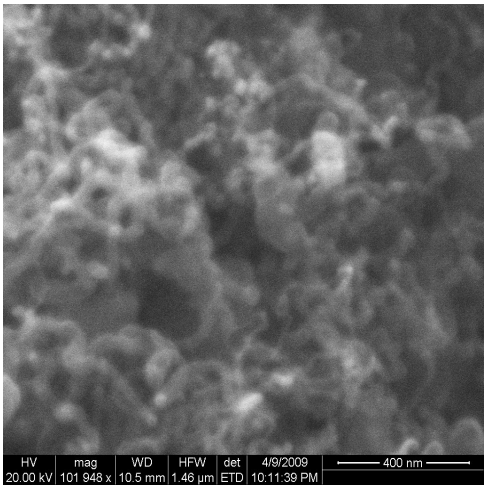

(b) MWCNT forest

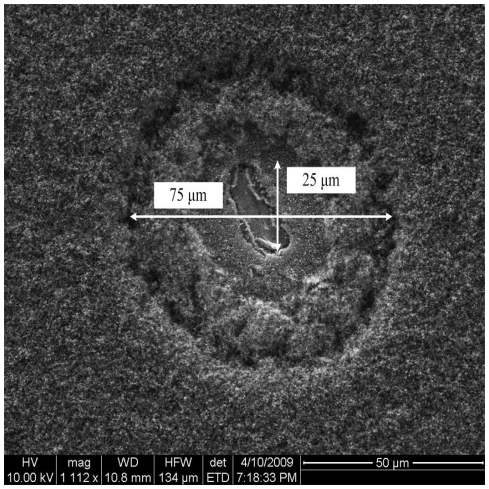

(c) A possible nucleation site

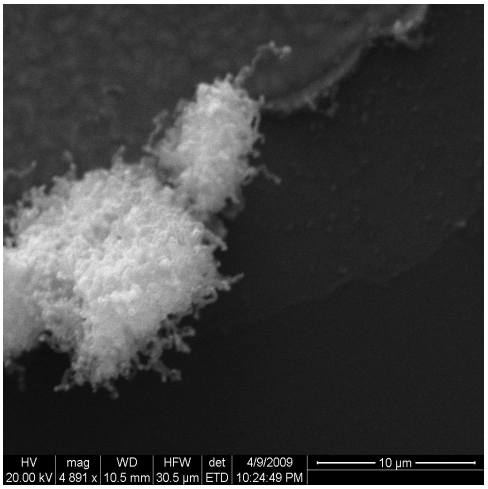

(d) MWCNT on TFT junction

Fig. 8.: FEI Quanta 600 FE-SEM micrographs depicting MWCNT on silicon substrates with TFT. Figs 8(a) & 8(b) depict top view of 30 nm diameter MWCNT forests. Figs. 8(c) & 8(d) depict a possible nucleation site and TFT junctions with a few CNT respectively. (Images courtesy: Mr. Navdeep Singh; The FE-SEM acquisition was supported by the NSF grant DBI-0116835, the VP for Research Office, and the TX Eng. Exp. Station.)

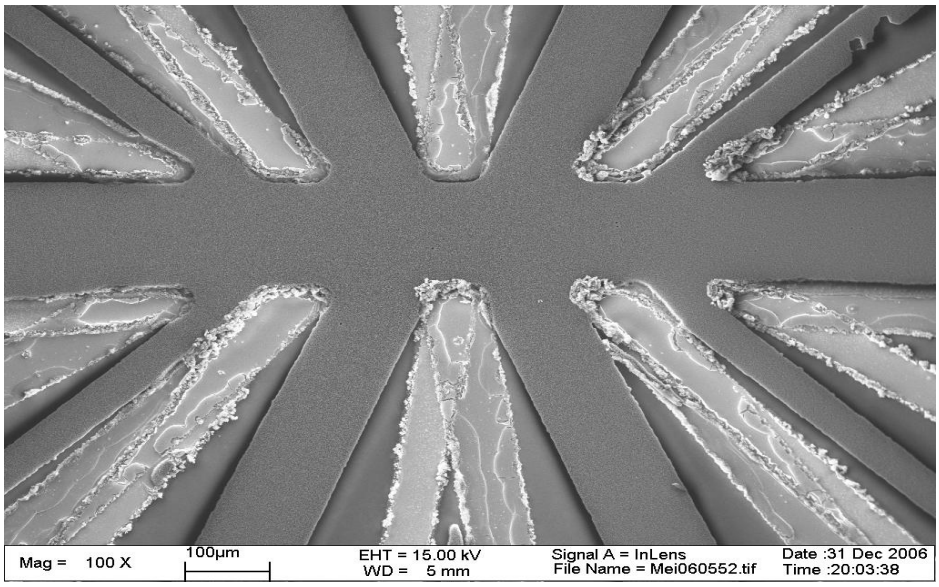

(a) Vertically aligned MWCNT surrounding TFT

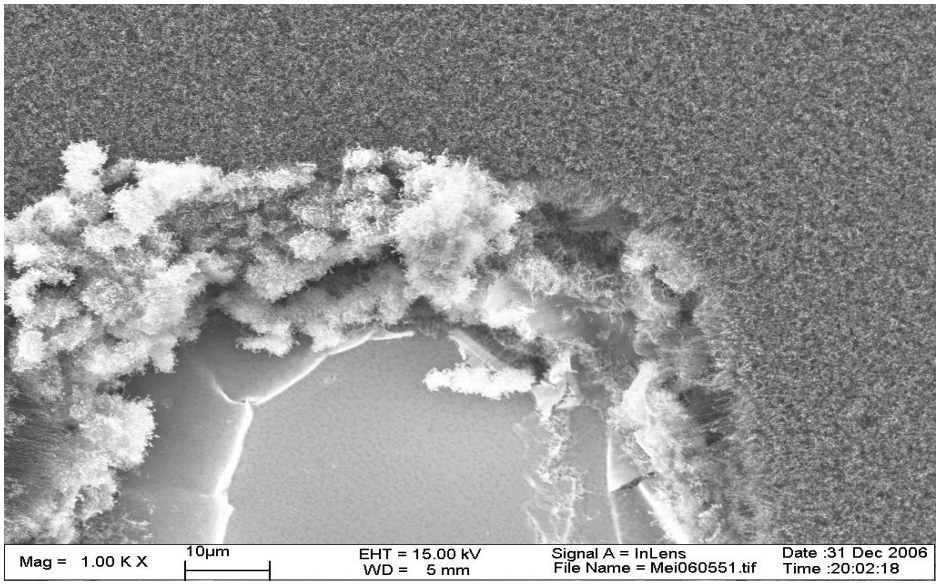

(b) Randomized growth of MWCNT near TFT junction

Fig. 9.: SEM micrographs depicting 8-15 nm diameter MWCNT forests on silicon substrates with TFT. Top view: figs 9(a) & 9(b).(Images courtesy: Dr. Mei Zhang, Nanotechnology Institute, University of Texas at Dallas.)

The present study employed CVD for growth of carbon nanotubes. The CNT test samples for the present study were prepared at University of Texas, Dallas, in a similar furnace. The furnace comprised of a quartz tube placed in a three-zone furnace located in an enclosure. The enclosure prevented the excess feedstock and other gases from leaking into the surroundings. Prior to synthesis of the MWCNT, the patterned TFT on the test surface was covered with a 2.7 μm thick layer of SC-1827 positive photoresist by employing a negative photomask. This was done to prevent the growth of CNT on the TFT due to catalytic action of nickel. Presence of comducting CNT on the TFT junction could result in shorting. Subsequently, a 5 nm thick layer of iron was deposited on the test surface using E-beam evaporation. The iron layer served as a catalyst for CNT synthesis. MWCNT forests were grown by CVD using acetylene as the carbon feedstock. Acetylene (5 mol %, 580 sccm) and helium was passed through a quartz tube maintained at atmospheric pressure. The quartz tube was maintained at 680 ℃. The growth rate of carbon-nanotubes was $\sim$ 1 - 2 μm/min. The total growth time varied depending upon the desired nanotube length. Previous SEM and thermal gravimetric studies (Ref. [53]) indicated that the purity of MWCNT produced by the process was high ($\sim$ 96 - 98 % carbon as MWCNT, 2 - 4 % amorphous carbon). The MWCNT produced by this method were vertically aligned and had diameters ranging from $\sim$ 8 nm - 15 nm (Ref. [53]).

Figures 9 through 11 depict SEM images of the actual test substrate after MWCNT synthesis. A few circular patches are visible on the surface that may serve as potential nucleation site. However, a typical sample possesses few such sites. In an earlier study (Ref. [40]), MWCNT coatings were found to enhance heat transfer rates at CHF by $\sim$ 60%. Increased nucleation was observed on MWCNT coated surfaces. It was theorized that pores and surface defects resulted in the enhanced nucleation activity. Based on the SEM micrographs, the actual test surfaces had a few ($\sim$ 400)

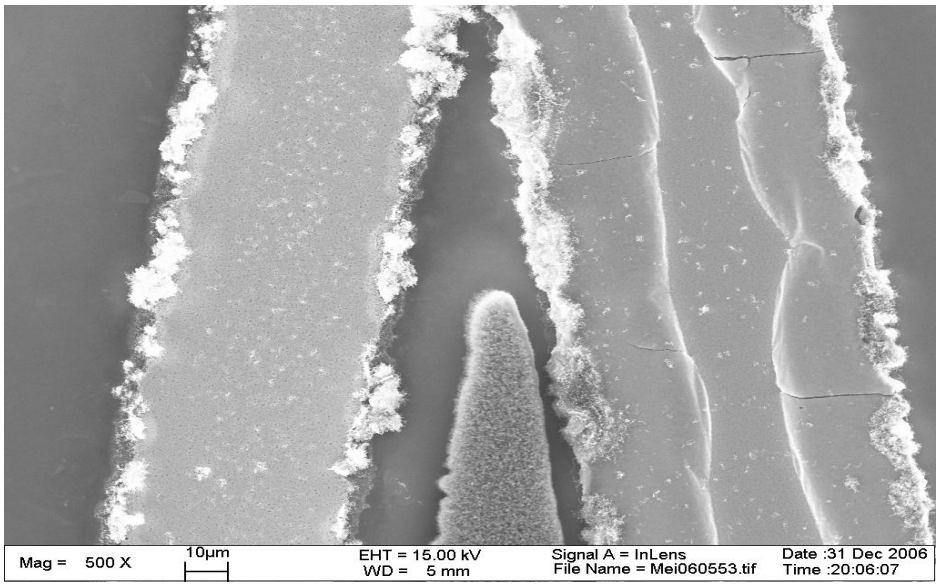

(a) Minor cracks in patterned TFT after MWCNT synthesis

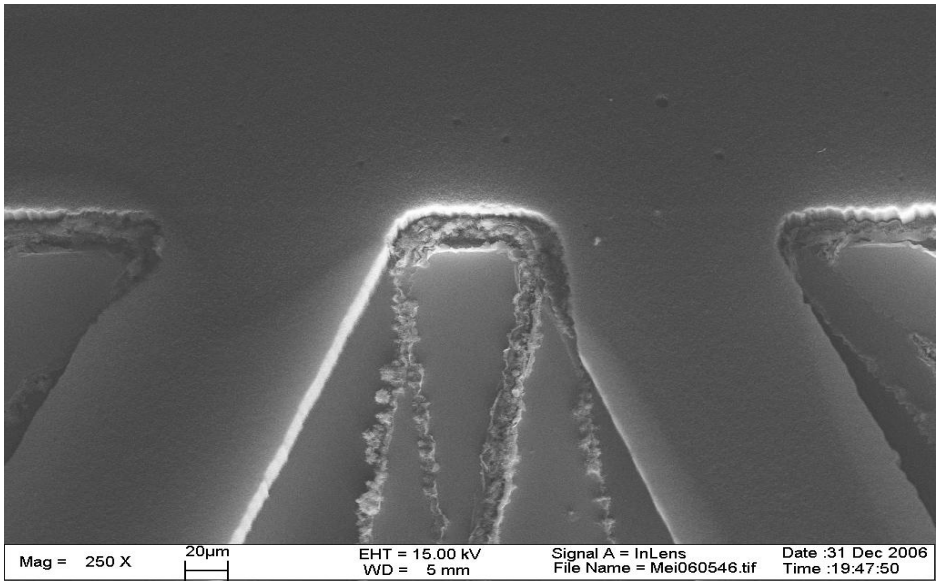

(b) MWCNT on TFT junction

Fig. 10.: SEM micrographs depicting MWCNT on silicon substrates with TFT. (Images courtesy: Dr. Mei Zhang, Nanotechnology Institute, University of Texas at Dallas.)

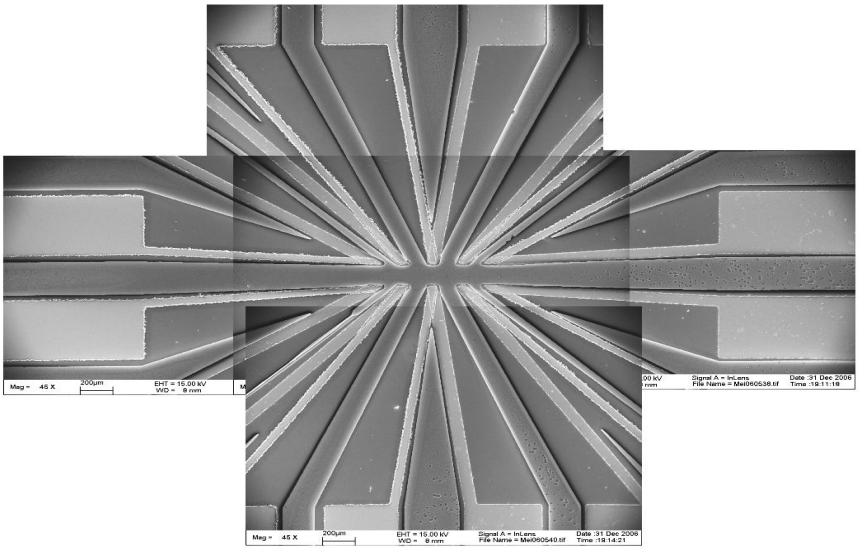

Fig. 11.: Composite SEM image of test substrate with TFT & MWCNT

surface defects ranging from 2 to 20 μm in diameter encompassing a total surface area of $\sim$ 3 mm^2. At present, it is not clear whether, the models of Macbeth (Ref. [34]) and Liter (Ref. [35]) are applicable. The former, due to the notable absence of 'large' pores surrounded by smaller 'feeder' pores on the substrate and the latter due to the length scale of the nanotubes (8 - 16 μm). However, it is clear that the presence of CNT coatings reduces the Taylor instability wavelengths resulting in the observed increase in heat transfer rates near CHF.

6. Measurement of contact angle and its influence on boiling heat transfer

One of the key requirements in pool boiling experiments is that the test liquid wet the surface very well to obtain repeatable measurements. PF-5060 (Manufacturer: 3M Co.), a dielectric liquid refrigerant with a boiling point of 56°C was used as the working fluid in all the tests. It is one of the liquids capable of meeting the requirements

of electronic chip cooling. This liquid had a very low contact angle ($\sim 13^{\circ}$) with silicon and most other substrates. Table III summarizes some of the key properties of this refrigerant. Contact angle measurements were conducted using a goniometer

Table III.: Properties of PF-5060

Property	Liquid	Vapor
Density (kg/m^3)	1610.68	12.52
Kinematic viscosity (m^2/s)	2.78×10^{-7}	1.15×10^{-6}
Prandtl number	9.8	0.81
Specific heat (J/kg-K)	1132.62	651
Thermal conductivity (W/m-K)	0.0539	0.0124
Surface tension (N/m)	8.448×10^{-3}	
Latent heat of vaporization (J/kg)	85034.34	

(fig. 12(a)). Measurements with **25** μm tall MWCNT (fig. 12(b))showed a contact angle of $\sim$ 150°with de-ionized water and angles of $\sim$ 9°(fig. 12(c)) with PF-5060. The volatility together with the highly weeting nature of PF-5060 made contact angle measurements difficult. The superhydrophobicity of the CNT coated surface with water can be explained by the Cassie-Baxter model. The Wenzel model is not applicable here as the initially hydrophilic substrate (silicon) turns hydrophobic upon CNT deposition. According to the Wenzel model, the wetting/non-wetting characteristic of the underlying substrate can only be enhanced. Thus, a hydrophilic surface becomes more hydrophilic due to roughness and a hydrophobic surface becomes more hydrophobic. According to the Wenzel model, a hydrophilic surface cannot turn hydrophobic. On the other hand, the Cassie Baxter model is based on the premise of existence of air pockets underneath the droplet on a rough surface. According to the

Cassie Baxter model, a hydrophilic surface can become hydrophobic.

From a previous study (Ref. [40]), contact angle of DI water over a CNT coated surface was determined to be 135° for 9 μm tall MWCNT and 153° for 25 μm tall CNT. Therfore, according to the Cassie-Baxter model (Ref. [107]),

$$\cos\phi_s = -1 + \beta_s(\cos\phi_{Si} + 1) \tag{3.1}$$

The contact angle on the smooth silicon surface is 14°. Substituting this in (3.1), together with contact angles of 135° and 153° for the 9 μm and 25 μm tall CNT, the air fraction underneath the water droplet is found to be 94.5% and 85.2% respectively. These correspond to surface enhancement factors (ratio of real to apparent surface areas) of 1.029 and 1.026. With PF-5060, the values of these enhancement factors are different as it completely wets the nanotubes. For this case, using a pitch of 30 nm between MWCNT in lateral and transverse directions and a diameter of 15 nm, with a height of 25 μm, the number of nanotubes on the surface is estimated to be 1.11×10^{15} with a total area of 2.481 m^2. The surface area enhancement factor is therefore, $\sim$ 1310. In an earlier study [40], the 'fin effect' of nanotubes was claimed to be one of the factors responsible for the observed enhancement in heat transfer. While a substantial area enhancement is observed for PF-5060. In contrast, for water, the surface area enhancement is minimal. If the 'fin effect' is indeed dominant then, tests with water should yield very little to no heat transfer enhancement compared to tests with PF-5060. Additionally, increase in the number density of fins beyond a certain optimal level results in poor convection currents leading to a decrease in heat transfer performance. Given the extremely small pitch of the MWCNT, it is logical to expect conduction to be the dominant heat transfer mechanism in the region between the substrate and top of the nanotubes. If this is the case, then thermal interfacial resistance is expected to be a dominant factor in a heat transfer model. Laminar,

single-phase, forced convection, heat transfer tests with PF-5060 and water as working fluids may help quantify the fin effect. In a two-phase scenario, surface parameters play a dominant role in heat transfer. Presence of pores and other defects affect bubble departure frequencies and diameters significantly. It is therefore, difficult to conclusively prove or repudiate the 'fin-effect' hypothesis from two-phase experiments.

C. Description of Test Facility

The experimental setup used in this study was of the constant heat flux type. A copper heating cylinder with five embedded cartridge heaters was used as a heat source. A DC power supply was used to provide constant power to the heaters. A cooling coil in a closed-loop connected to a constant temperature bath, served as a heat sink. Thermodynamically, the system comprising of the heating surface, the test liquid and the cooling coil placed within the viewing chamber can be approximated as a closed system. There was a minor loss of vapor (mass-exchange) through the vent hole and minimal energy exchange with the surroundings. This was insignificant for all practical purposes. Figure 13 shows the schematic of the test facility. The test facility comprised of:

1. a viewing chamber,
2. a constant temperature bath,
3. an image acquisition system and,
4. a data acquisition system.

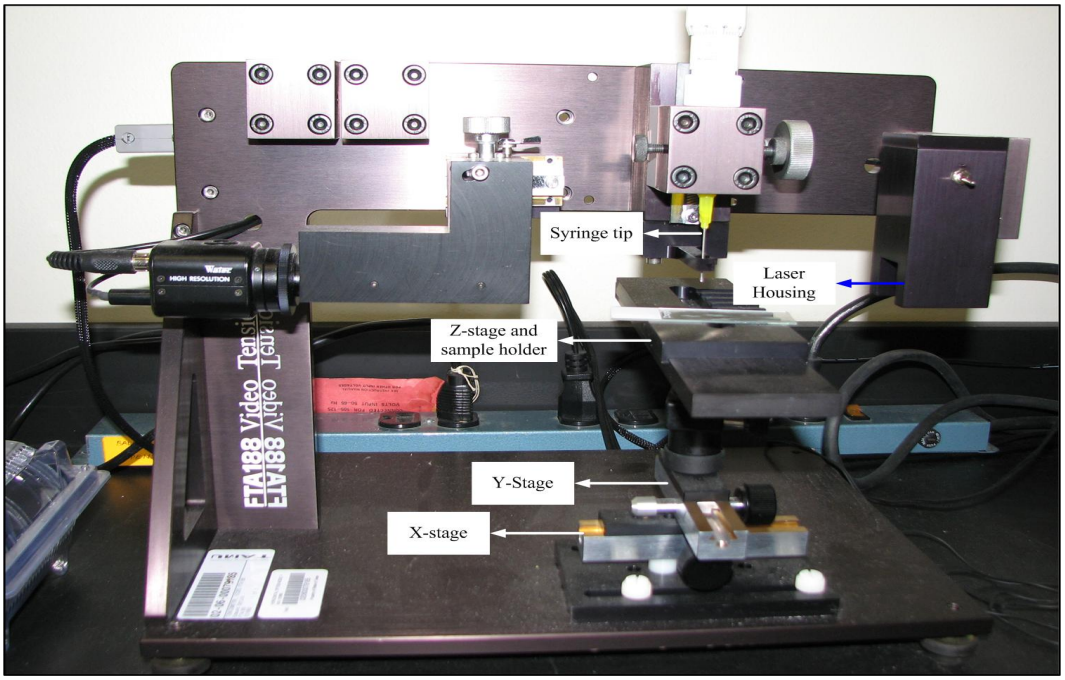

(a) Goniometer for contact angle measurement

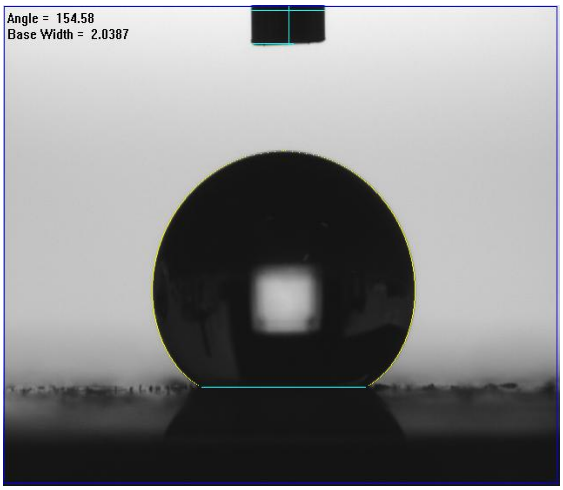

(b) Water

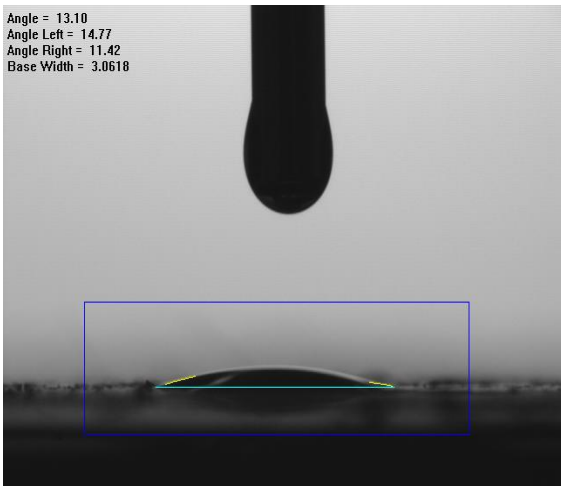

(c) PF-5060

Fig. 12.: Contact angle measurements. Figs. 12(b) & 12(c) showing contact angle measurements with water & PF-5060. Fig. 12(b) shows the superhydrophobic nature of surfaces coated with vertically aligned MWCNT. Fig. 12(c) shows the wetting characteristic of PF-5060.

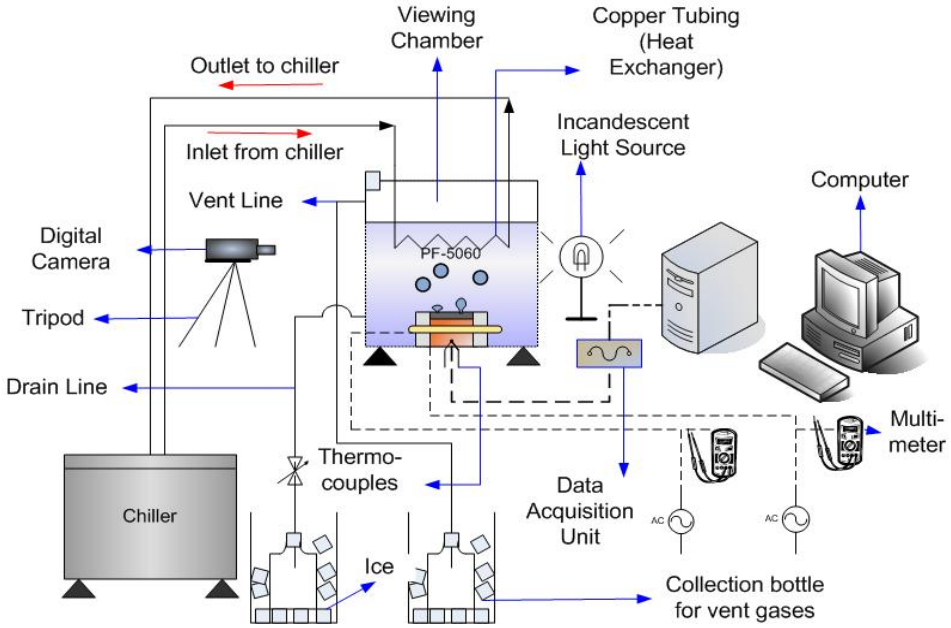

Fig. 13.: Schematic layout of the test facility

1. Viewing chamber

Figure 14 depicts a schematic of the viewing chamber and the heater. The viewing chamber consisted of a cylindrical copper heater 2 inches (50.8 mm) tall and 3.5 inches (88.90 mm) in diameter placed at the bottom of the chamber at the center. The heater was surrounded by an annular stainless steel jacket 3.9 inches (99.06 mm) in inner diameter and 4.5 inches (114.30 mm) in outer diameter. The air-gap between the heater and the stainless steel jacket acted as a thermal insulator, minimizing heat loss in the radial direction. At the elevated temperatures encountered in the film-boiling regime, this arrangement also functioned as a radiation shield minimizing radial heat losses. The high thermal conductivity of copper ($\sim$ 398 W/mK) and the insulating effect of the surrounding air ensured one-dimensional heat conduction within the cylinder. The frame was constructed by welding 12 beams with an 'L' cross-section.

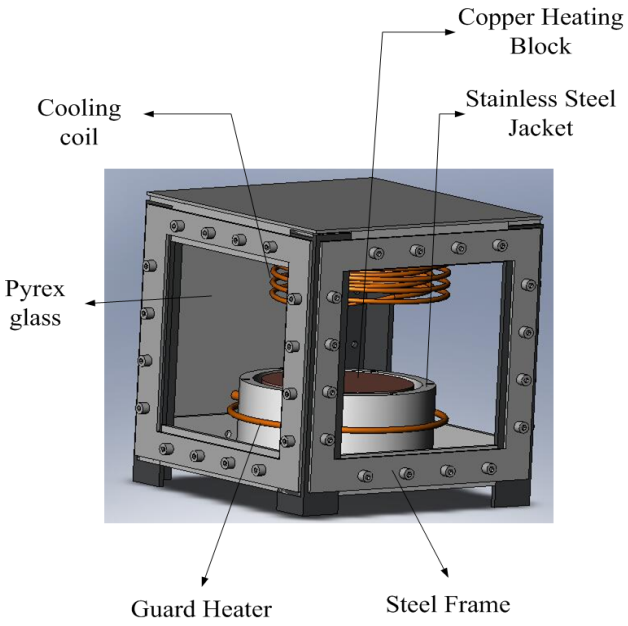

Fig. 14.: Solid model of the viewing chamber

The steel frames were then welded to four steel pillars (not shown) which formed the legs of the setup. The length of the legs were adjustible using screws provided at the base. Therefore, the system could be levelled. The base and one side of this frame were welded to steel sheets. The side sheet had two $1/4^{th}$ inch (6.35 mm) dia. holes on its sides located $\sim$ 0.5 inch (12.7 mm) and 5.5 inches (139.7 mm) from the base. The hole near the base on the side wall was used to drain the test fluid at the end of the test. The hole near the top was used to vent the non-condensables and vapors formed during degassing and the experiment. The steel sheet forming the base of the viewing chamber had an access hole at its base. The thermocouple lead wires and power lines passed through the access hole into the viewing chamber. The remaining three sides were enclosed by a four-layered arrangement consisting of:

i) a $1/8^{th}$ inch (3.175 mm) thick silicone rubber sheet 6.25 inches $\times$ 6.25 inches (158.75 mm $\times$ 158.75 mm) with a central square opening 4.5 inches $\times$ 4.5 inches (114.3 mm

× 114.3 mm) ii) a square pyrex sheet, 6 inches × 6 inches × $1/4^{th}$ inch (152.4 mm

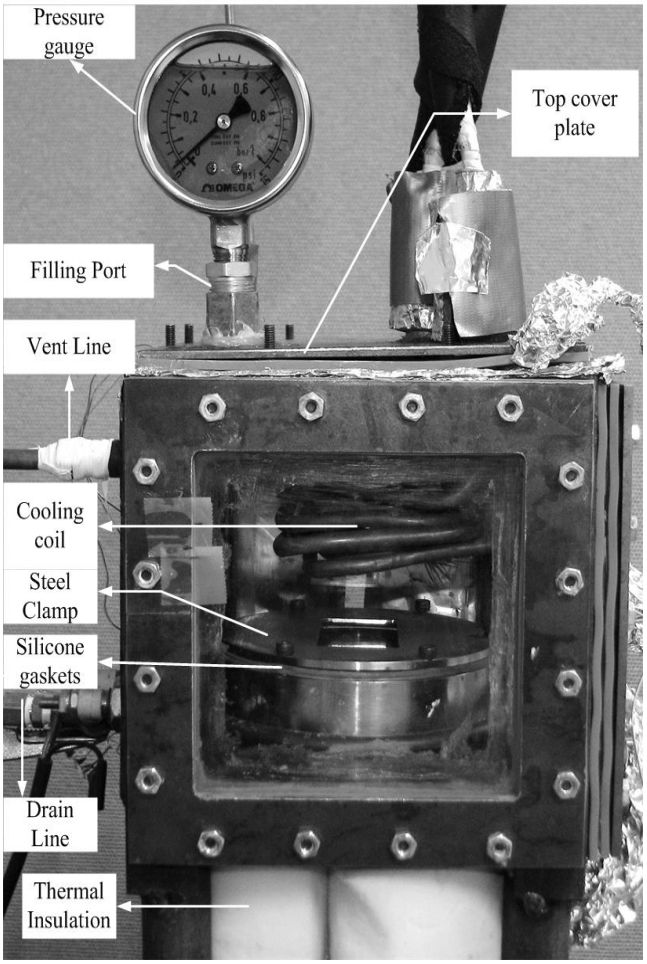

Fig. 15.: Digital image of viewing chamber

× 152.4 mm × 6.35 mm) iii) a silicone rubber sheet of same dimensions as above iv) a square steel frame with dimensions same as the silicone rubber sheets. This four layered arrangement was bolted to the steel frame using sixteen M-4 screws. The copper heating cylinder (heater) and the stainless steel jacket was bolted to the base of the viewing chamber with six M-4 screws each. The transparent sides facilitated acquisition of high-speed movies and photographs during the experiments. The top of the viewing chamber was covered by a stainless steel cover. Four ports

were provided on the top cover plate to facilitate the filling of the test chamber, to monitor the temperature of the test liquid using the chiller probe and two ports for the inlet and exit of the heat exchanger coils. The port for filling the test chamber also functioned as a port for monitoring the system pressure using a liquid-filled pressure gauge (Manufacturer: Omega, Model: PGM-63L-15PSI/1BAR) once sealed. Figure 15 depicts a digital image of the viewing chamber with the pressure gauge, heat exchanger coils, stainless steel jacket surrounding the heating block, the guard heater surrounding the jacket and the insulated bottom.

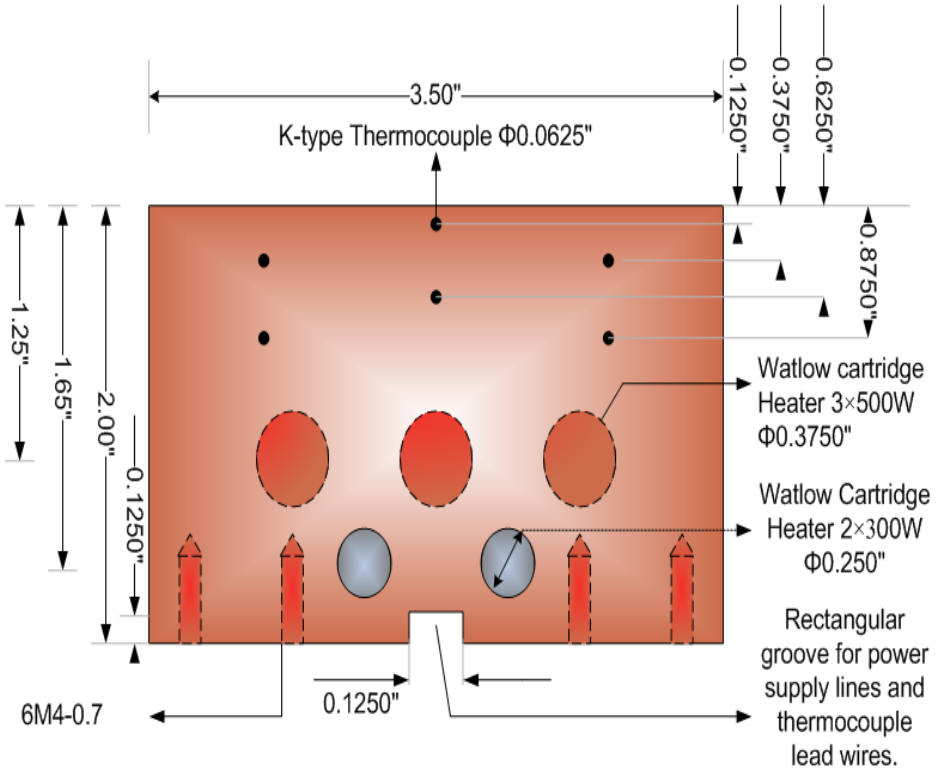

Fig. 16.: Schematic of the copper heater

Figure 16 shows the schematic of the copper cylinder. The temperature distribution within the copper cylinder was measured with twelve sheathed K-type thermocouples (Manufacturer: Omega, Model: GKMQSS-040U-12, special limit of error).

The sheath was made of stainless steel and was 12 inches (202.8 mm) long. The sheath diameter was 0.04 inches (1.016 mm) and the junction was not grounded. The thermocouple tip was isolated from the sheath thus providing better electrical insulation and avoiding the formation of a mixed alloy at the tip [102]. The sheath served as a shield against electrical interference. These thermocouples were calibrated and inserted at various radial and axial locations within the copper cylinder. Holes measuring 0.0625 inches (1.5875 mm) in diameter were drilled in the heater at desired locations for this purpose. The thermocouples were inserted at the desired locations within the copper heater and held in place by means of silicone glue applied at the openings after insertion of the thermocouples. The thermocouple leads were bent around the cylinder and passed through the rectangular slot machined underneath the copper cylinder for this purpose. The leads passed through a hole provided at the base of the viewing chamber to the data acquisition system. The lead wires are bundled together and sheathed in a aluminum foil to reduce the susceptibility of the thermocouple to radio frequency noise. Additionally, the terminal block and the lead wire bundles are grounded to reduce noise levels. All thermocouple wires (including the lead wires) used in this study were of 'class 2' or 'special limits of error' (SLE). These tolerances pertained to the as received condition of the thermocouples and was not an indicator of thermocouple performance.

2. Constant temperature bath

Figure 17 shows a digital image of the constant temperature bath (Manufacturer: Polyscience, Type: Circulator model 9612) used in this study. The programmable constant temperature bath maintained the coolant (50 % ethylene glycol and 50 % water) at a constant temperature. The constant temperature bath could maintain the coolant temperature within $\pm 0.01^{\circ}$C of the set-point temperature. The readout

on the programmable contoller was accurate upto ±0.25°C. The temperature readout was not used in calibration of the thermocouples to minimize bias. A separate NIST calibrated mercury in glass, partial immersion thermometer with a resolution of 0.1 ℃ was employed for this purpose. The bath functioned as a heat sink in the pool boiling experiments with the coolant being circulated through thermally insulated copper tubes to the heat exchanger coil placed within the viewing chamber. The constant temperature bath was used to maintain the coolant at a constant temperature during calibration of exposed wire thermocouples used in the experiments.

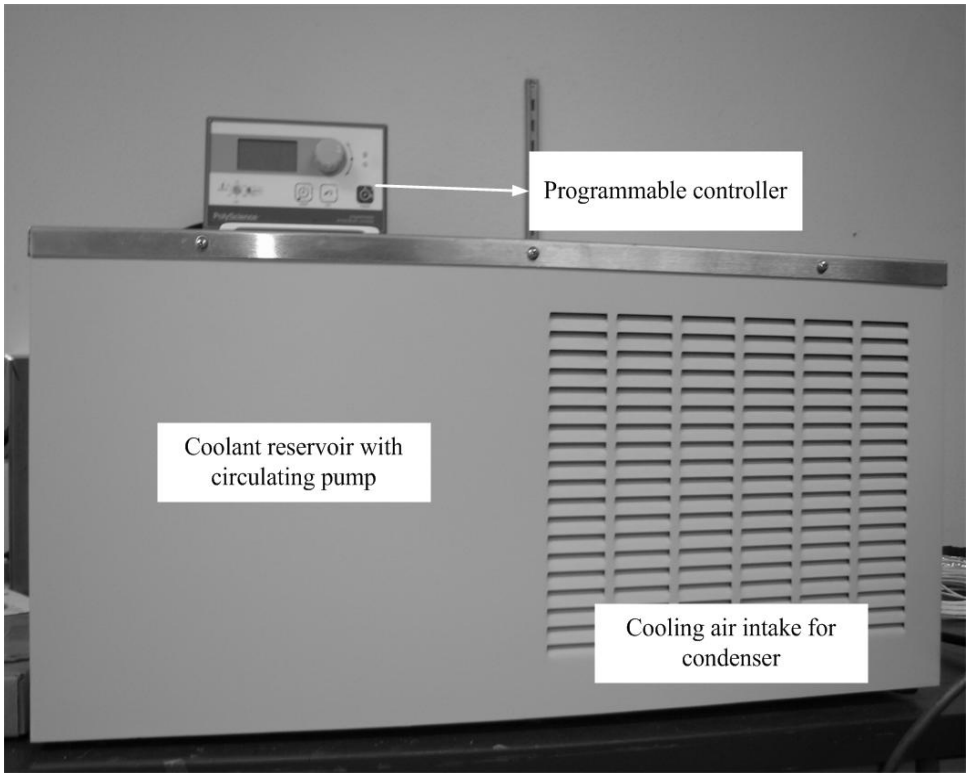

Fig. 17.: Digital image of the constant temperature bath

3. High speed imaging system

An image acquisition system consisting of a digital camera (Manufacturer: Canon, Model: S3 IS) and a high-speed camera (Manufacturer: Fastec Imaging, Model: Troubleshooter HR) was employed in these experiments. The high-speed camera was capable of acquiring monochrome images at 16,000 frames/s at a reduced resolution of 1280 $\times$ 32 pixels. The camera was equipped with a CMOS array and had 8-bit resolution in monochrome. In this study, high speed images were acquired at frame rates of 500 frames/s at a resolution of 1280 $\times$ 1024 pixels and at 1000 frames/s at a resolution of 1280 $\times$ 512 pixels. A microscope lens (Manufacturer: Infinity Photo-Optical Company, Model: KC with IF 3.5, IF 4.0 objectives) was fitted to the high speed camera to enable suitable magnification of the images. The magnification (MAG.) provided by the IF-3.5 objective ranged from 1.71 to 2.13 for working distance (WD) ranging from 86 to 100 mm. The corresponding field of view (FOV) for the lens ranged from 3 - 3.75mm. Corresponding parameters for the IF-4.0 objective were, 2.33 to 2.91 (MAG.), 64 to 71 mm (WD) and 2.2 to 2.75 mm (FOV). Halogen lamps were used to provide adequate lighting to the system during high-speed image acquisition.

4. Data acquisition system

A data acquisition system was used to record the steady state temperature data furnished by the TFT and exposed thermocouples placed within the copper block at high frequencies. Additionally, the system was used to monitor the transient temperature data between steady state data points. The thermocouple was a non-referenced/ floating/ ungrounded signal source as its signal was not referenced to the ground. A differential, or non-referenced, measurement system was used to measure

the floating analog thermocouple signals in these experiments. A differential system has the advantage of eliminating common mode noise.

The data acquisition system (Manufacturer: National Instruments) consisted of three parts:

i) a SCXI terminal block

ii) a SCXI module

iii) a chassis

The front mounting SCXI-1303 terminal block had a shielded enclosure with screw terminals providing connections to transducers. The thermocouple wires were safely held in place using strain relief clamps. The SCXI analog input modules amplified, isolated, filtered and multiplexed signals from the thermocouples. The SCXI-1000 chassis had a rugged, rack-mountable enclosure that provided power to the SCXI system and interfaced with the PCI data acquisition (DAQ) board within the computer. The SCXI-1102 system was designed for high-accuracy thermocouple measurements. Each input channel included an instrumentation amplifier and a 2 Hz lowpass filter. The SCXI-1102 analog input channels along with the input channels of other modules could be scanned at rates of up to 333 kS/s (3 μs per channel). The SCXI-1102 can acquire millivolt, volt, 0 to 20 mA, and 4 to 20 mA current input signals. Each module could multiplex its channels into a single DAQ device channel.

D. Experimental Procedure

The TFT were packaged before the test with $\sim$ 1.0 - 1.5 cm long, thick gage, chromel and alumel wires. Fine Gage chromel and alumel wires were welded to the other end of these thick wires and passed to the data acquisition system. In order to ensure adequate electrical contact between the lead wires and the bond pads, silver print

was applied to the base of the lead wires before application of glue. A glue held the leads (Manufacturer: Aremco, Product: 526- A, B) in place on the bond pads of the TFT. The glue was cured at 175 ℃ for 24 hours. Once the first layer of glue cured, two or three more layers of glue was applied to ensure reliable bonding. This was followed by the application of J-B Weld. Calibrated K-type wire-bead thermocouples were bonded to the packaged TFT wafer to facilitate calibration of the TFT. All wire-bead thermocouples used in this test were calibrated in a constant temperature bath. A partial-immersion, mercury in glass, NIST thermometer was used as a reference standard in all calibrations.

1. Calibration of thermocouples

The wire-bead thermcouples were calibrated in a constant temperature bath with a calibrated NIST thermometer used as a reference standard. The NIST thermometer possessed a temperature resolution of ±0.1 ℃. The constant temperature bath possessed a temperature stability of ±0.01 ℃. The wire bead thermocouples were immersed in the constant temperature bath set at a specific temperature. The signals were monitored in real-times through the data acquisition system. Once steady-state conditions were attained, the temperature recorded by the wire-bead thermocouples and the thermometer were saved. The temperature of the constant temperature bath was then increased to the next setting. In this way, a six-point calibration was obtained spanning 0 - 50 ℃. The calibrated wire-bead thermocouple was then fixed on the test substrate bearing TFT as mentioned above.

2. Wafer installation and leak testing

The top surface of the copper heating block was cleaned and heat sink compound (Manufacturer: Dow Corning) was applied. A 75 mm Pyrex wafer was placed on

the copper cylinder after application of heat sink compound on one of its sides. The underside of the Pyrex wafer without heat sink compound was placed in contact with the copper cylinder with the heat sink compound applied. The wafer was clamped by means of a steel clamp as shown in fig. 18. The steel clamp was covered with a Teflon gasket ($\sim$ 1/8" thick) on its underside to prevent the test fluid from leaking. Furthermore, the gasket prevented the silicon wafer from cracking which would occur if the steel clamp were resting directly on the sides of the wafer or if the screws were tightened using too much torque.

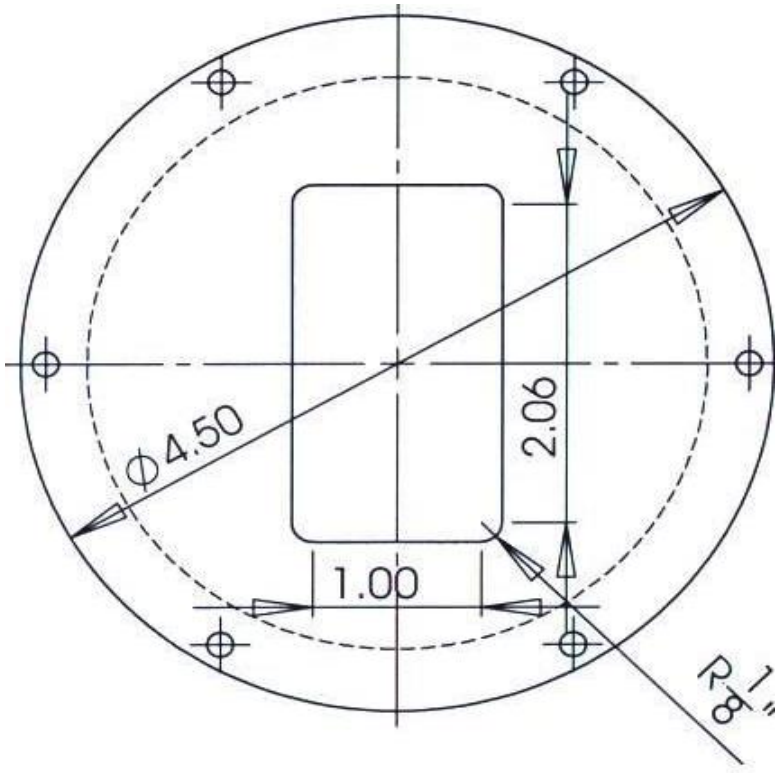

Fig. 18.: Schematic of stainless steel clamp used in pool boiling experiments

Fig. 19 depicts the schematic of the test section after tightening the clamps. A leak test was conducted using de-ionized water to check for the presence of leaks. Any leaks present due to improper clamping caused the water to drip through the air

gap present between the steel ring and heating block to the hole at the base of the chamber. If any water dripped through the base of the viewing chamber, the screws were tightened further and the system rechecked for leaks.

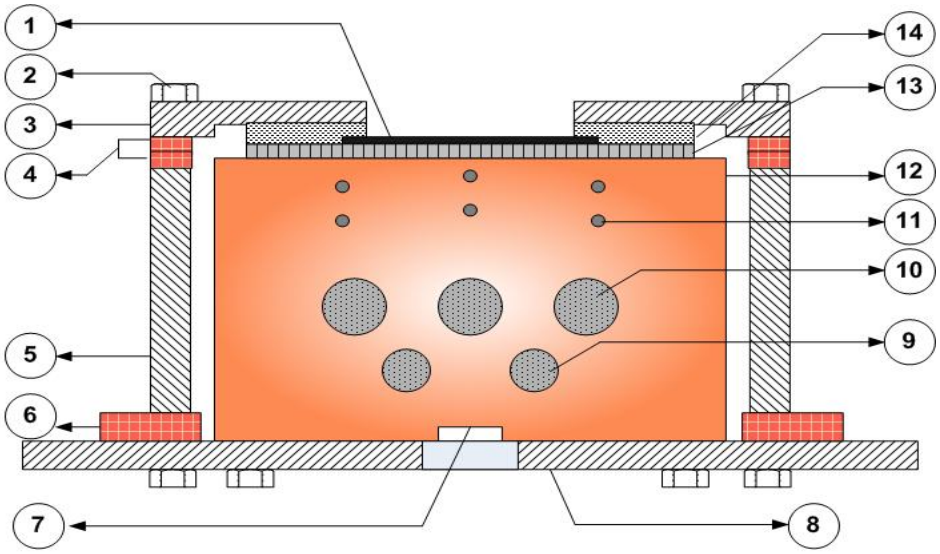

1. Test surface
2. M-4 nut
3. Steel clamp
4. Silicone rubber gaskets (1/16")
5. Steel jacket
6. Silicone rubber gasket (1/8")
7. Groove for lead wires
8. Bottom cover plate with hole for lead wires
9. 300W cartridge heater
10. 500W cartridge heater
11. K-type thermocouple
12. Copper cylinder
13. Pyrex glass wafer
14. Teflon gasket

Fig. 19.: Schematic of test section after installation of test wafer

3. Calibration of TFT

The TFT were calibrated insitu, in air, with the attached, calibrated wire-bead thermocouple as a reference standard. The viewing chamber was sealed and padded with insulation at the bottom on outside. The copper heating block temperature was

raised. In order to prevent formation of convective rolls within the chamber, the constant temperature bath was set to match the temperature of the test surface. Upon reaching steady state, the thermocouple and TFT data were recorded. Following this, the temperature of the heating cylinder was changed once more.

4. Degassing step

After performing a leak test the apparatus was allowed to dry for a day. The cooling coil was lowered into the viewing chamber and top steel plate was clamped using screws, on the viewing chamber framework. Prior to start of the actual experiment a degassing step was performed. This was done to partially remove the trapped gases within the test fluid and to prevent premature nucleation. The bulk test fluid was heated to its boiling point ($\sim$ 56 ℃) and maintained at that temperature for 10 minutes for partial degassing.

5. Data acquisition

The temperature of the chilling unit iwas fixed to achieve a desired temperature level of the test fluid. The tubular heater power supply was disconnected (for subcooling cases). Power supply to the cartridge heaters was modulated by the variac. The system was allowed to reach steady state for each power setting. The temperature of the test fluid was carefully monitored in LABVIEW and adjustments to the chiller temperature level were made accordingly during the time taken to reach steady state. The temperatures within the copper block were also monitored continuously in LABVIEW. Once steady state was achieved, the DAQ system was used to record the thermocouple readings for a period of two minutes at a rate of 200 Hz. The temperature readings were used to evaluate the heat fluxes and wall superheats. These were then used to construct the boiling curve for PF-5060. The current and volt-

age supplied to the cartridge heaters were recorded manually using the clamp type ammeter and multimeter respectively. In addition the chiller temperature and time was recorded. A high-speed camera system was employed to record images of pool boiling.

CHAPTER IV

ANALYSIS OF EXPERIMENTAL DATA

A. Introduction

Heat flux passing through the copper heating cylinder is evaluated using Fourier's law of one-dimensional conduction. Thermocouples placed at various radial and axial locations under saturated pool boiling conditions show a difference of ~ 0.2℃ in temperature at the first steady state data point. Near CHF, the maximum temperature differential recorded within the heating cylinder is ~ 1.86℃ and in the film boiling regime the corresponding differential is ~ 0.82℃. The high thermal resistance on the sides of the heating cylinder due to air coupled with the low thermal resistance on the test surface resulting from phase change heat transfer further ensures that Fourier's law of one-dimensional conduction is valid. The plot of average temperatures recorded by vertically aligned thermocouples as a function of axial distance shows a linear trend validating the assumption of one dimensional heat conduction. The average surface heat flux is plotted as a function of the wall superheat. The thin-film thermocouples furnish the averaged local surface temperatures required for evaluation of the wall-superheat. The pool boiling curves are thus based on spatio-temporally averaged heat fluxes and temporally averaged, local surface temperatures. Thus, the pool boiling curves are 'quasi-local' in nature.

The surface temperature fluctuations are ~ 1 - 2℃ in magnitude in most cases. The high frequency, surface temperature variation data is used for nonlinear time series analysis using the TISEAN© package. The data is used to investigate the presence of local temporal chaotic dynamics. Pool boiling in general and saturated pool boiling in particular is highly turbulent at CHF. Turbulence is characterized

by the presence of vortices across different length scales, mixing and fluctuations in the velocity field of the fluid. Recently, it has been suggested that turbulence is spatio-temporally chaotic. In pool boiling systems, the departure of bubbles (in both saturated and subcooled cases, and at low and high heat fluxes) causes a wake which is usually turbulent in nature. The turbulent wake of the bubbles leads to vigorous mixing. This vigorous mixing coupled with phase change leads to high rates of heat transfer. While phase change heat transfer is a dominant component in the total heat transfer rate, turbulent convective heat transfer is also a key contributor to heat transfer. The variation in bubble departure frequencies gives rise to transient conduction which also plays a dominant role. This has led to the development of convective models for predicting pool boiling heat transfer rates (Ref. [4]).

Spatio-temporally chaotic systems are difficult to analyze in entirety due the large number of 'degrees of freedom' in space and time. From an experimentalist's point of view it is often intractable if not impossible to instrument the test section in all spatial dimensions with instruments having infinitesimal temporal resolution without affecting the observed parameter or parameters significantly. Additionally, all experiments involve an environmental noise component which for all practical purposes is random. The influence of this (noise) random, undesired input on deterministic chaotic dynamics may or may not be significant. As discussed earlier the signal to noise ratio must be high. If this is not the case, the dynamics may no longer be deterministic and the stochastic nature of noise will swamp the chaotic dynamics. Whilst chaotic systems possess many of the features of random systems such as unpredictability, it results from completely deterministic governing equations and known boundary conditions. In the present chapter, local temporal data is used to determine the presence of local temporal chaotic dynamics. Local phase portraits are generated and topological variations in these are observed with variations in heat fluxes indicating the varia-

tions in the number and nature of fixed points and limit cycles. Currently only two comprehensive sources of reference exist in literature devoted to non-linear analysis of time series data(Refs. [85], [108]). All non-linear time-series analysis carried out in this study is based primarily on [85]. The data analysis procedure is discussed in detail in the following sections.

B. Calculation of Heat Fluxes

The mean heat flux in the vertical direction within the copper heating cylinder was determined using the temperatures recorded by the thermocouples placed at various axial locations along the centerline:

$$\overline{q''_{Cu}} = \frac{\sum_{i=1}^{n} k_{Cu} \frac{\delta T_i}{\delta x_i}}{n} \tag{4.1}$$

The principle of conservation of energy results in the following relation for the mean heat flux on the boiling surface:

$$\overline{q''_w} = \frac{q''_{Cu}}{A_w} A_{Cu} \tag{4.2}$$

Heat losses occur within the test section due to imperfect insulation, heat loss through the insulated base of the viewing chamber, and lastly, through conduction of heat in the radial direction within the copper cylinder and subsequent loss through convection on the periphery of the cylinder. Major sources of heat loss in the test section include convective losses from the sides of the block, conductive losses through the insulated base of the test section and the losses occurring within the gap between the top of the copper heating surface and the base of the test surface. Heat losses were estimated by comparing the total power input to the cartridge heaters with the axial heat transfer

rate evaluated by taking the product of equation (5.1) with the cross-sectional area of the copper heating cylinder. The difference between the power supplied and the axial heat transfer rates yields the heat losses. Heat losses in nucleate boiling ranged from a maximum of 29% at the lowest heat flux setting to ∼7% near CHF. Heat losses were higher in the film boiling regime (∼39%) due to significant convective and radiative losses from sides of the heating cylinder resulting from the increase in thermal resistance along the axial direction due to the insulating effect of the vapor blanket covering the test surface.

1. Estimation of experimental uncertainties

The experimental uncertainty for the thermocouples located within the copper cylinder involves two components. A statistical uncertainty component for the temperature fluctuations shown by the thermocouples and a Kline and McClintock analysis for evaluating the uncertainty in heat fluxes. For thermocouples located within the copper block the following sources of bias existent in the calibration procedure are neglected:

1. The limited temperature stability of the constant temperature bath ∼ 0.01℃.
2. The bias due to limited resolution (∼ ±0.05℃) of the NIST calibrated, partial immersion, mercury-in-glass thermometer.

The relative uncertainty in the heat flux estimated for two vertically aligned thermocouples (j, k) is:

$$\omega_{q''_{Cu}} = \sqrt{\left(\frac{\omega_{k_{Cu}}}{k_{Cu}}\right)^2 + \left(\frac{\omega_{T_j}}{T_j - T_k}\right)^2 + \left(\frac{\omega_{T_k}}{T_j - T_k}\right)^2 + \left(\frac{\omega_{\delta x}}{\delta x}\right)^2} \tag{4.3}$$

The uncertainty in the averaged surface heat flux was obtained by taking the root mean squared sum of the uncertainties in heat flux estimates obtained for each pair

of vertically aligned thermocouples neglecting the uncertainties in the cross-sectional areas of the wafer and the copper heating cylinder. The resulting expression for total uncertainty is:

$$\omega_{q''_w} = \frac{1}{n}\sqrt{\sum_{i=1}^{n}\left(\omega_{q''_{Cu,i}}\frac{q''_{Cu,i}}{\overline{q''_{Cu,i}}}\right)^2} \tag{4.4}$$

The uncertainty in surface temperature estimates on the test wafer could stem from many sources:

1. The resolution of the data acquisition system was set by the data acquisition hardware to a 16-bit accuracy, which was equivalent to an absolute error of 0.0046℃ $\sim$ 0.005℃ for the rated temperature range of 300℃.

2. The standard deviation of temperature fluctuations at steady state conditions was measured to be $\sim$ 0.05℃. Hence a total uncertainty of the temperature measurement was estimated to be $\sim$ 0.055℃.

3. Using uncertainty values of $\sim$ 1.0% for thermal conductivity of copper and of $\sim$3.0% (machining accuracy) for the distance between two thermocouples embedded in the copper cylinder, the estimated maximum uncertainty of the surface heat flux near the Leidenfrost (MHF) point was $\sim$14%. The uncertainty was estimated to be $\sim$6% near the CHF.

A statistical uncertainty analysis is conducted for the TFT. The sources of bias/fixed calibration errors and precision/random errors are summarized in table IV. TFT are calibrated in situ in air, before the experiments as described in Chapter III. A calibrated wire-bead K-type thermocouple is used as a reference standard. A relatively large uncertainty of $\sim \pm$0.45℃ at 108.9℃ surface temperature results due to large uncertainties in the wire-bead thermocouple. However, for surface temperatures ranging from $\sim$ 58℃ to $\sim$ 90℃ , the total uncertainty varies between $\sim \pm$0.18-0.35℃.

Table IV.: Sources of errors in TFT measurements

Source	Type	Magnitude
Constant temperature bath	Bias	±0.01℃
NIST thermometer	Bias	±0.05℃
DAQ	Bias	±0.005℃
Wire bead thermocouple	Bias	±0.43℃
Random	Precision	∼ ±0.12℃

This is unavoidable if the TFT are calibrated in air using the wire bead thermocouple as a reference standard. In order to assess the reliability of calibration (of TFT) in air, another calibration is conducted in a constant temperature bath with an NIST thermometer as the reference standard. The calibration correlations obtained by both methods show a difference of ∼ 5℃ in calibrated temperature at an assumed uncalibrated surface temperature of 126℃. The calibration in air almost encompasses the entire range of surface temperatures encountered during the tests whereas the calibration in the constant temperature bath does not encompass the entire temperature range. Calibration in the constant temperature bath is limited to a maximum temperature of 50℃ due to the limited operating range of the NIST thermometer. Thus, the calibration coefficients obtained for calibration in air is used for temperature measurements.

C. Reconstruction and Characterization of Attractors in Phase Space

The subject of "Dynamics" involves the description of evolution of systems with time. Thus, 'dynamical systems' is a term applied to an equation or a system of equations describing the temporal evolution of a system. Time evolution can be described un-

ambiguously only if the system is deterministic. Predictability of stochastic signals is limited to measured moments, linear autocorrelation, and other statistical quantities. Stochastic tools however, can be applied successfully to deterministic systems with large degrees of freedom.

Dynamical systems can consist of differential equations or iterated maps/difference equations. Thermo-fluid systems are modeled by partial differential equations expressing the fundamental laws of mass, momentum and energy conservation. Due to the dependence of parameters on spatial location and time, the dynamics is spatio-temporal in nature. Due to the inherent non-linearity present in these systems, an analytical treatment is possible only for a few cases with simple boundary conditions. In such cases, it is desirable to obtain a qualitative, geometric picture of the solutions and their behavior in an abstract parameter space known as the '*phase space*'. The various '*states*' through which the system passes for a given initial condition forms a '*trajectory*' in phase space. The geometric picture therefore, consists of groups of trajectories which present a portrait of evolution of the system corresponding to different initial conditions. The concept of a phase space in dynamical systems theory differs from the notion of phase-space in statistical physics, wherein the phase space dimension is twice the number of degrees of freedom. Additionally, in statistical physics, the phase space has the positions and momenta of particles for its coordinates which is not strictly true in case of phase spaces in dynamical systems theory. The phase space is spanned by the ensemble of variables present and is theoretically infinite in case of a continuous medium possessing properties with spatial dependence. However, even in such systems the number of variables or the '*active degrees of freedom*' spanning the phase space can be reduced to a few variables because of some collective behavior. Asymptotic stability, implies the presence of attracting chaos in case of dissipative systems. Thus, all trajectories originating from parts of

the phase space representing various initial conditions, would tend to converge onto an invariant, minimal set known as the 'attractor' [109]. In case of chaotic dynamics, the attractor shows a sensitive dependence on the initial conditions and is therefore called a 'strange attractor' [110].

The aim of time-series analysis is to reconstruct the dynamics of the system using the time-series record of a single or a few variables. The principal objectives are [109]:

1. Identifying and reconstructing the structure of the attractor

2. Quantification of attractor and phase-space dimensionality and interpreting it. For instance, a dimensionality of one indicates the presence of self-sustained periodic oscillations, while a dimensionality of two indicates the presence of quasi-periodic oscillations. A non-integral dimensionality greater than two indicates the presence of chaotic dynamics.

3. Constructing simple map-like models using Poincaré sections, local or global models based on attractor geometry.

Topological and differential embeddings are two types of embedding techniques used for attractor reconstruction [111]. In topological embedding a one-to-one correspondence exists between attractors in the original phase space and the attractors in the reconstructed phase space. Differential embeddings aim to preserve the differential structure of the attractor and quantities such as Lyapunov exponents. However, differential embeddings are not commonly used as they are difficult to implement in case of strange attractors with fractal geometry [111]. From the definition of 'state', points on the attractor of a dynamical system in the original system phase space have a one-to-one correspondence with measurements of a limited number of system variables. A measurement carries some information about the current state of the

system. Therefore by extension, some information about all the variables governing the system is contained in each measurand. This forms the basis of embedding theory. Thus, the following equation would hold true for a dynamical system [111]:

$$\mathbf{y} = (y_1(t), ..., y_n(t)) = \mathbf{G(x)} = (g_1(\mathbf{x}), ..., g_n(\mathbf{x})) \tag{4.5}$$

Here, $\mathbf{y}$ is a vector-valued function of the system state $\mathbf{x(t)}$ in the original full phase space. $\mathbf{G}$ is a measurement function and the n-dimensional vector space comprised of the vectors $\mathbf{y}$ is called the 'reconstruction space'. As long as n is greater than twice the box-counting dimension (D_0), almost every C^1 measurement function $\mathbf{G}$ defines a one-to-one correspondence between the state in the full phase space and n-dimensional vectors $\mathbf{y}$ [111]. Thus, the measurement function is a topological embedding of the attractor 'A' into the reconstructed phase space. In most cases, the smallest embedding dimension greater than the fractal or correlation dimension is sufficient. The condition $n \geq 2D_0$ just guarantees an embedding.

Very often, it is not possible to simultaneously monitor/measure all variables of interest in an experiment. Generally, one or a few variables are measured in any experiment. In such a case, delay co-ordinate vectors are used [111]. Thus,

$$\mathbf{F}(\mathbf{x}(t)) = (y(t-\tau), ...y(t-n\tau)) = (g(\mathbf{x}(t-\tau)), ..., g(\mathbf{x}(t-n\tau))) \tag{4.6}$$

In a dynamical system, $\mathbf{x}$(t) uniquely determines $\mathbf{x}$(t-τ) thus in the delay coordinates, the measurement function 'g' is the same unlike the general case considered in (4.5) above where 'n' different measurements yielded 'n' different measurement functions. Thus, a bad choice of delay 'τ' in (4.6) above will lead to a breakdown of the one-to-one mapping criterion of the attractor 'A'. For instance, if the attractor 'A' is a single periodic orbit (i.e. a circle in phase space) with a period τ, then the delay vectors lie on a straight line in $\Re$, the real line. However, the mapping of a circle onto a line isn't

one-to-one. A similar argument holds true for an orbit with period 2τ. However, for systems with a finite number of fixed points with periods 'pτ', where $3 \leq p \leq n$, the function 'g' in (4.6) above, leads to a one-to-one mapping of the attractor 'A' for any choice of 'g'. The estimation of optimal delay was the focus of intense research. This is discussed in the following section.

The time-series data obtained in this study is analyzed using TISEAN© software package. The routines in this package have been pre-validated on a number of test cases such as the Henon attractor, Lorenz attractor etc. for which theoretical estimates are present.

1. Estimation of optimal time delay

Packard and co-workers [112] suggested the use of a time-series and its successive derivatives as coordinates for attractor reconstruction. However, the procedure is highly sensitive to noise and is demanding computationally [113]. As discussed above, Takens introduced the method of delay reconstruction which is in common use and provides a one-to-one mapping of the attractor from the original to the reconstructed phase space. Although simple in theory, the success of delay reconstruction hinges on finding an '*optimal*' delay time and a suitable (unknown) embedding dimension for noisy, finite experimental data. A very small delay time ($\tau \ll$ recurrence time (τ_r)) results in linearly dependent coordinates causing the reconstructed attractor to lie along the hyperdiagonal in the reconstructed phase space. A very large value of τ on the other hand results in the coordinates being independent by stretching and folding. As a consequence, the attractor is highly folded. Some of the methods for delay estimation are summarized below based on Refs. [114], [115].

1. ***Autocorrelation:*** In this approach, (an autocorrelation function measures the

similarity/redundance of a time-series with a delayed version of itself. Similarity is maximum when the delay is zero. A plot of the value of the autocorrelation function with delay is generated. The delay corresponding to the first zero of the autocorrelation function is generally chosen as the optimal value although alternative criteria do exist. At this value of delay, the two coordinates become linearly independent. This method however, cannot be successfully extended to higher dimensions and may yield incorrect results because of correlation between other coordinates.

2. ***Mutual Information:*** Mutual information is used to measure the general dependence of two quantities in information theory and in probability theory. Mutual information measures the amount of information shared by two quantities. In the present case, if x(t) is known, the amount of information known about x(t+τ) is quantified by the mutual information. Successive delay coordinates are thus relatively independent for low values of the mutual information function. This method has been widely used for embedding but suffers from the drawback in that it becomes impractical for dimensions greater than four.

3. ***High-order correlations:*** Albano and co-workers suggested the use of higher order moments to estimate the "coincident time" i.e. the time at which the correlation functions exhibited the first coincident extrema.

4. ***Extrema of Correlation integral*** Liebert and Schuster observed that the first minimum of the logarithm of the generalized correlation integral coincided with the first minimum of the mutual information function. Hence, the value of delay corresponding to the first minimum of the correlation integral is suitable for delay reconstruction. Although computation of the correlation integral is relatively easier than the computation of the mutual information function, the

procedure is still computationally costly. Additionally, this method offers no significant benefit over the mutual information function.

5. ***Wavering Product:*** Liebert et al. [114] proposed the use of a 'wavering product' to estimate the delay τ and the embedding dimension d_E. False recurrences are present when the attractors are embedded in a dimension less than its box-counting dimension. Hence, the wavering product measures the distribution of the sets of nearest neighbors for different dimensions. The wavering product is also a function of the delay τ. The first minimum of the wavering product results in a optimal value of delay. The computational cost of this method is high apart from its high sensitivity to noise.

6. ***Fill-factor:*** Buzug et al. [115] proposed the use of a '*fill factor*' as a measure incorporating the utilization of the phase space by the attractor as a function of the delay time. The delay at which the maximum fill-factor occurs is chosen as the optimal delay. This technique cannot account for overfolding and in some cases, no significant extrema exist.

7. ***Singular Value Decomposition:*** This technique was suggested by Broomhead et al. In this approach, delay coordinates are replaced with dominant modes from a singular value decomposition.

Table III summarizes the various methods used to determine optimal delay time. In the present study, the first minimum of the mutual information function is used to estimate an optimal delay time. Although the optimal delay time varies with embedding dimension, it is impractical to determine a optimal delay for each embedding dimension especially for dimensions exceeding four. Evaluation of delays for using mutual information in higher dimensions becomes increasingly demanding in terms

Table V.: Methods to determine the optimal time delay

Method	Formulae	Advantages	Disadvantages
Autocorrelation	$\bar{y} = \frac{1}{N}\sum_{n=1}^{N} y(n)$ $\sum_{n} [y(n) - \bar{y}]\,[y(n+T) - \bar{y}]$	Low computational cost, easy to implement	No well-defined relation to dynamics, fails often.
Mutual information	$I_\tau = \sum_{y(n),y(n+\tau)} P(y(n), y(n+\tau)) \times$ $log_2\left[\frac{P(y(n),y(n+\tau))}{P(y(n))P(y(n+\tau))}\right]$	Connected to the information generating properties of chaotic dynamics, reliable	difficult to extend to higher dimensions
High-order Correlations	$\mathrm{C}(\vec{x}_1,\ldots,\vec{x}_n)=$ $\sum (-1)^{q-1}(q-1)\left\langle \prod_{j\in\nu_1} \vec{x}_j \right\rangle \ldots$ $\left\langle \prod_{j\in\nu_q} \vec{x}_j \right\rangle$ $(\vec{x}_1,\ldots,\vec{x}_n) = (\vec{y}_1,\ldots,\vec{y}_n)^T$	Easy implementation	No clear relation to dynamics

of size of the data set and the computational requirements. Although, the delay estimated for two dimensions may be sub-optimal, nevertheless, it has been known to yield satisfactory results in literature [108]. Eq (4.7) gives the mutual information between two quantities/measurements.

$$I_{x_i y_j} = log_2 \left[\frac{P_{XY}\left(x_i, y_j\right)}{P_X\left(x_i\right) P_Y\left(y_j\right)} \right] \tag{4.7}$$

The probabilities are determined by constructing a histogram of the fluctuations in x_i, y_j. The individual probabilities P_X, P_Y are determined by partitioning the measured data into intervals of a given (arbitrary) size. The probability is then given by the ratio of number of points within the interval to the total number of points multiplied by the interval size. The joint probabilities are obtained by partitioning the n-dimensional space into n-dimensional boxes and using the procedure above. The optimal partioning size is unknown and is determined by systematically refining the grid size. Usually this procedure is limited to a dimension of four or lower due to algorithmic limitations. The average mutual information over all measurements is therefore,

$$I_{XY} = \sum_{x_i, y_j} P_{XY}\left(x_i, y_j\right) log_2 \left[\frac{P_{XY}\left(x_i, y_j\right)}{P_X\left(x_i\right) P_Y\left(y_j\right)} \right] \tag{4.8}$$

The seminal work of Fraser and Swinney extended this concept to time-series measurements. The average mutual information between two measurements y(t) at time instant 't' and y(t+τ) at time instant 't+τ' is given by the expression

$$I_{y_t y_{t+\tau}} = log_2 \left[\frac{P_{XY}\left(y_t, y_{t+\tau}\right)}{P_X\left(y_t\right) P_Y\left(y_{t+\tau}\right)} \right] \tag{4.9}$$

If the set 'X' is the collection of measurements y(n) and the set 'Y' the collection of measurements y(n+τ), then the average mutual information between the two sets of

measurements is:

$$I_\tau = \sum_{y(n),y(n+\tau)} P(y(n), y(n+\tau)) log_2 \left[\frac{P(y(n), y(n+\tau))}{P(y(n))P(y(n+\tau))} \right] \tag{4.10}$$

For $\tau = 0$, the above expression is similar to the Kolmogorov-Sinai entropy. Due to divergence of nearby trajectories in case of a chaotic signal, the average mutual information function goes to zero for large delays. In other words, the measurements become independent and no information is gained about the other by measuring one. Fraser et al. [116] suggested the use of the first minimum of the mutual information function as the optimal value for delay. At this value of delay, the coordinates are relatively independent but not to the extent that they cease to have any connection at all [108]. The aforementioned expression can be generalized to higher dimensions as well. However, the computational cost increases rapidly with increase in dimension. Additionally, as mentioned above, higher dimensions require larger datasets leading to inaccuracies in estimation in case of truncated datasets. Generally, a time delay estimate obtained from a two dimensional delay reconstruction suffices. In the present study, the source code (obtained from Dr.Fraser) for determining mutual information employs a binning procedure and an automated bin refinement step based on a χ^2 test, thus leading to fine binning where needed. The mutual information code in the TISEAN© software package does not have a refinement step leading to uncharacteristically large values of the delay time. The optimal delay times determined in this study are obtained in two dimensions. The other parameter of interest in the embedding step is the (unknown) embedding dimension. This is discussed next.

2. Embedding dimensions: false-nearest neighbors and recurrence plots

The determination of correlation dimensions using a time-delay reconstruction of data is inherently difficult as neither the optimal delay time τ nor the embedding dimension 'n' known. Using the techniques described above, one can arrive at an estimate for τ. However, the embedding dimension, is still unknown. The method of false-nearest neighbors uses a simple geometric reasoning to determine suitable embedding dimensions. In chaotic dynamics, two neighboring vector fields undergo almost the same evolution for a small interval of time, despite the exponential divergence of nearby trajectories. The fundamental principle of the false-nearest neighbors algorithm is to look for neighbors in an assumed embedding dimension which are not real neighbors in the true phase space. If the trajectories belonging to a true embedding dimension of n_0 is embedded in a dimension n such that $n < n_0$ then, due to the reduction in the number of axes, some points will be projected falsely into the neighborhood of each point. The following procedure is followed to determine the false nearest neighbors:

1. An embedding dimension, 'n' is assumed
2. For each point in the vector field, closest neighbors are determined in dimension 'n' and 'n+1'
3. The ratio of the distances between the nearest neighbors in dimensions 'n', 'n+1' is computed
4. If the ratio is larger than a threshold 'f', the neighbor is false

The threshold has to be large enough to allow for an exponential divergence due to chaos. If the standard deviation of the data is σ_1, the fraction of false nearest neighbors is given by

$$\chi_{fnn}(f) = \frac{\sum_{i=1}^{N-n-1} \varphi\left(\frac{|\mathbf{y}_m^{(n+1)} - \mathbf{y}_{k(m)}^{(n+1)}|}{|\mathbf{y}_m^{(n)} - \mathbf{y}_{k(m)}^{(n)}|} - f\right) \varphi\left(\frac{\sigma_1}{f} - |\mathbf{y}_m^{(n)} - \mathbf{y}_{k(m)}^{(n)}|\right)}{\sum_{i=1}^{N-n-1} \varphi\left(\frac{\sigma_1}{f} - |\mathbf{y}_m^{(n)} - \mathbf{y}_{k(m)}^{(n)}|\right)} \tag{4.11}$$

where, $\mathbf{y}_{k(m)}^{(n)}$ is the nearest neighbor to the vector $\mathbf{y}_m$ in n dimensions and k(m) is the time series index of the element differing from k [85]. The two step functions in the above expression test for the 'trueness' of the neighbors and suppress all pairs with distance larger than the threshold $\frac{\sigma}{f}$. The false nearest neighbors are determined for different values of the ratio factor 'f' False neighbors also occur in the true embedding dimension n_0 as result of noise in experimental data. The false nearest neighbor test provides a rapid and convenient method for estimating a suitable embedding dimension.

The concept of recurrence was introduced in 1890 by Henri Poincaré [117]. Introduced by Eckmann in 1987 [118], recurrence plots provide a convenient way to visualize recurrences in a system. A system possessing a chaotic attractor returns to an arbitrarily small neighborhood of its points/states. This is the underlying principle of recurrence plots. These near repetitions of the state of the system is known as a '*recurrence*'. The matrix

$$A_{ij} = \varphi\left(\epsilon - |\mathbf{y}_i - \mathbf{y}_j|\right) \tag{4.12}$$

where, φ is the step function and ϵ is the tolerance parameter. If a recurrence occurs in the reconstructed space in the ϵ-neighborhood of its location at time j then, the matrix $A_{ij} = 1$ otherwise $A_{ij} = 0$. Therefore, the matrix represents the times at which the states of the system are similar. Two neighboring points in a deterministic system evolve in a similar manner despite the exponential divergence of nearby trajectories.

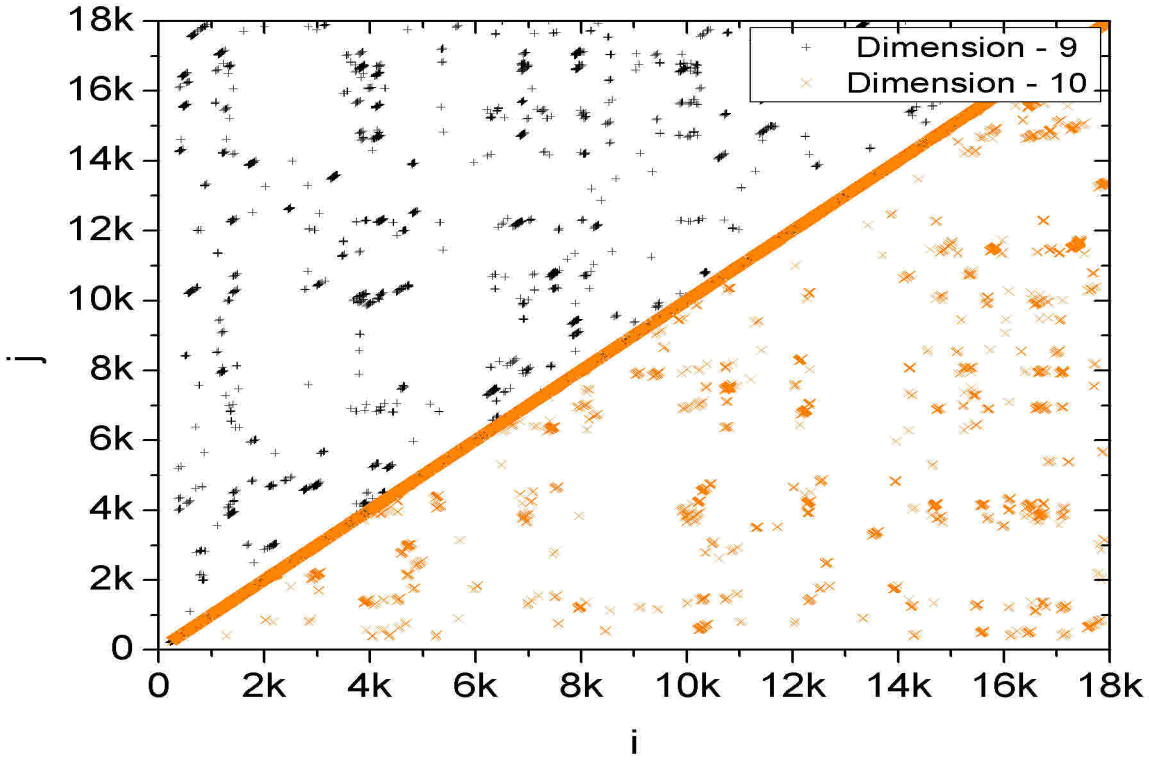

Fig. 20.: Recurrence plot at CHF for data provided by TFT-1 at 10 ℃ subcooling after noise reduction.

Hence, if black dots are used to represent the values at (i,j) where A_{ij}=1. Therefore in a graph of i versus j many black dots appear parallel to the main diagonal forming short lines parallel to the main diagonal. The presence of many isolated black dots indicates insufficient embedding dimensions, or a strong noise component. The presence of many isolated dots indicates a weak or absent deterministic component. If the neighborhood size ϵ in the neighbor search criterion is too small, no recurrences will occur [117] and no structures are observed in the recurrence plots. If ϵ is too large, consecutive points are included as neighbors and thicker and larger diagonals will be observed [117]. The neighborhood size is chosen by hit and trial in this study although more sophisticated methods exist [117]. Thus, the recurrence plot provides a quick test for the determination of a suitable embedding dimension. Figure 20 shows

a recurrence plot for the 10 ℃ subcooled case. Recurrence plots were generated for data before noise reduction for the bare surfaces only. This resulted in an estimate of the required embedding dimensions for all test cases.

3. Noise-reduction

The goal of noise reduction is to separate a noisy signal into two components. One component is the noise in the system while the second is the actual signal. This act of separating the signal into two components requires a criterion or a set of criteria in order to decide what constitutes the desired signal and what constitutes noise. In case of periodic and quasiperiodic signals, the criterion is that sharp peaks within narrow frequency bands constitute the signal whereas the broad-band low power spectrum constitutes noise. Separation of signals into multiple components based on time scales is not possible with chaotic signals by virtue of its being broad-banded. However, determinism plays a key role in separation of chaotic signals from noise. The measured signal is assumed to be deterministic with an unknown map g. The measured signal can be decomposed as:

$$x_n = y_n + \kappa_n, y_n = f(y_{n-m}, ..., y_{n-1}) \tag{4.13}$$

The noise, κ_n, is assumed to be random, have rapidly decaying auto-correlations and no correlations with the signal. In order to clean the signal, an implicit equation of the form:

$$y_n - g(y_{n-m}, ..., y_{n-1}) = 0 \tag{4.14}$$

is solved for one of the coordinates in the middle. The unknown function 'g' is replaced by locally constant function.Thus, in order to estimate $\hat{y}_{mid}$, for a given vector with mid-coordinate as $\hat{y}_{mid-known}$, delay vectors $x_n = (x_{n-m+1}, ..., x_n)$ are

formed and nearest neighbors to $\mathbf{x}_{n0}$ are determined and averaged over all neighbors. The averaged value is then used as a cleaned value. This approach is implemented in the TISEAN© code as 'lazy'. An alternative version corrects more than just the central component and is implemented in TISEAN© as 'nrlazy'. The nrlazy algorithm is found to perform better in the present study and is employed for noise-reduction.

Figure 21 compares the cleaned signal with the noisy signal and the removed noise for a particular case. Apparently, the removed noise is uncorrelated with the original signal whereas the clean signal is strongly correlated with the original (noisy) signal. This shows that the noise removal algorithm successfully cleans the signal to a significant extent.

Figure 22 compares the Fourier spectra of the noisy signal with the clean signal. The Fourier spectra at the $\sim$ 0 - 20 Hz frequency range remains virtually intact whereas the high frequency peak at 60 Hz due to A.C. noise is removed almost completely. Therefore, the noise removed signal preserves the signals of interest in the low frequency range.

4. Estimation of correlation dimensions, Theiler window and space-time separation plots

Dissipative chaotic systems possess attractors with fractal geometry. Hence these attractors are known as 'strange attractors'. In practice, the data set is finite and the instruments have a finite resolution leading to a smearing of measurements at small scales. The correlation dimension is an invariant but the correlation sum is not. In the absence of knowledge of the characteristics of attractors such as its self-similarity, the concept of correlation dimension has to be carefully used [85].

The correlation integral or sum is well-defined for a given space scale ϵ for a

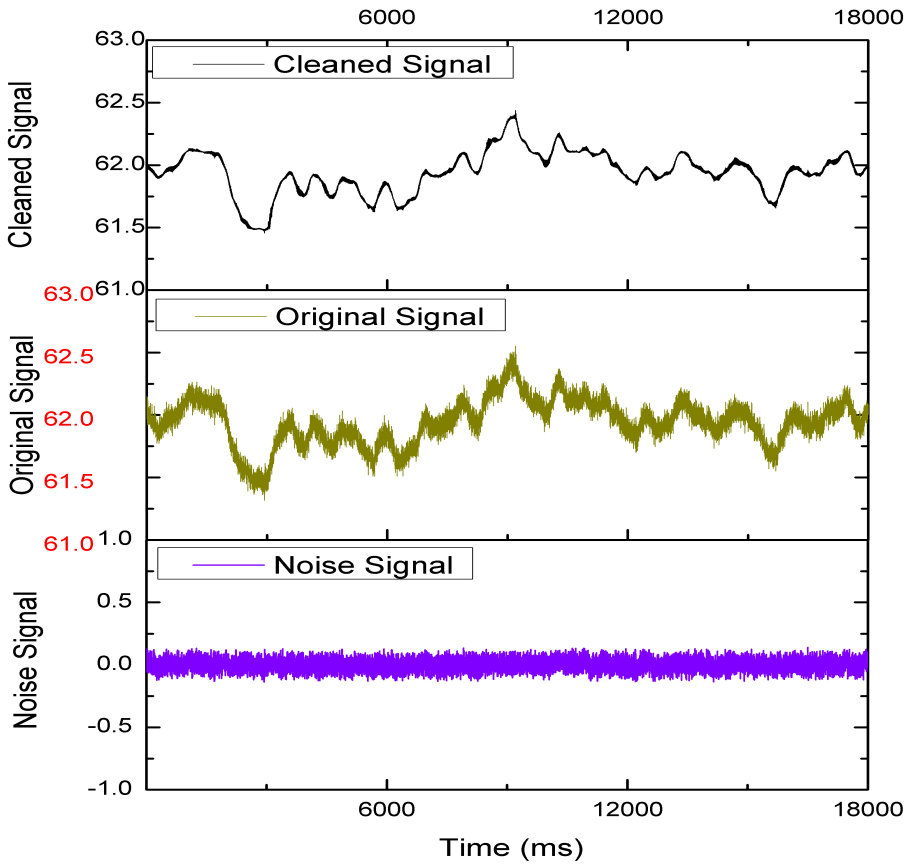

Fig. 21.: Comparison of original, noise cleaned & noise signals.

finite set of points. However, in order to assign a number called 'correlation dimension' requires unbiased interpretation. A typical plot of local slopes of D(n,ϵ) versus the space scale ϵ shows a macroscopic regime where any scaling or self-similarity is destroyed as the size of macroscopic structures on the attractor determines its value. At smaller length scales a true scaling regime exists carried by a plateau in the local slopes vs. space scale plot. Further down, at smaller scales noise and statistical effects dominate. The noise scale affects the correlation sum up to length scales three times the noise level. Hence, even a noise level of 2-3% does not show a significant scaling

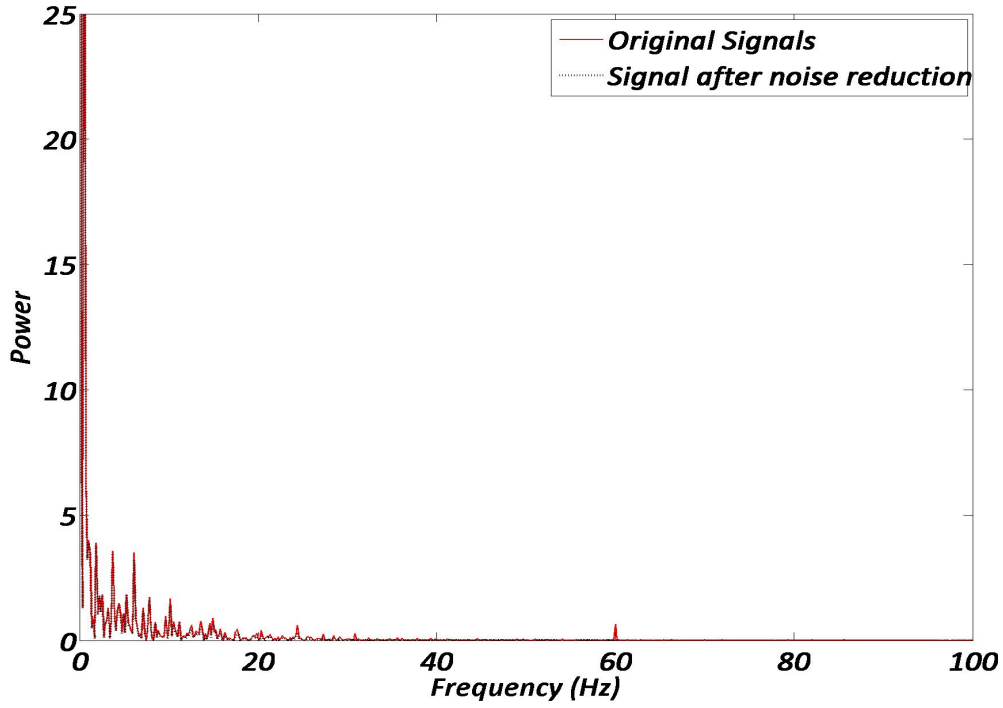

Fig. 22.: Comparison of Fourier spectra of original & noise cleaned signals.

region [85]. In the present study, the presence of low dimensional (temporal) chaos is being verified and the presence of a low-dimensional attractor is assumed. Various quantifiers of chaos are then evaluated with the hope that the hallmarks of chaos are found and as a consequence justify the assumption of chaotic dynamics a posteriori. In boiling-chaos literature, log-log plots of the correlation integral vs. space-scale are used to determine a scaling region by fitting a straight line through multiple points and claiming these to be the 'scaling region'. If the slopes of the lines are found to be relatively constant, a correlation dimension is said to exist. However, this practice is deprecated in current chaos literature [85]. A straight line can always be fit through multiple points. A true scaling region can be found only by looking at the plot of local slopes as a function of the log of the space-scale.

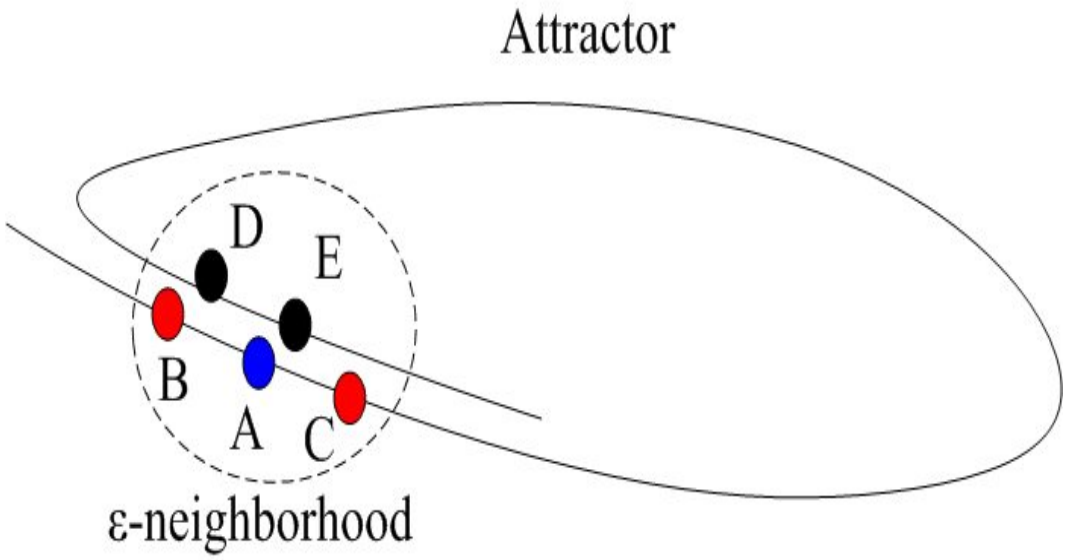

(a) Concept of Theiler window

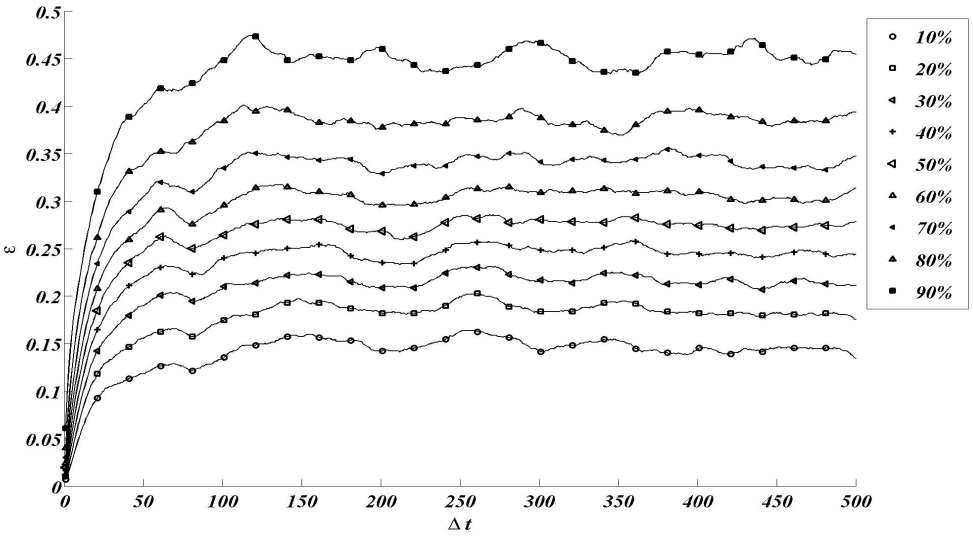

(b) Space-time separation plot showing clear a plateau for 10 ℃ subcooled pool boiling after noise reduction.

Fig. 23.: The concept of Theiler window 23(a) and a sample space-time separation plot 23(b). In 23(a), points B and C are close in time to point A and should be neglected in the correlation sum. Points D and E are true, long-time recurrences and should be included in the correlation sum.

In most chaos quantifiers, one is interested in determining long-time recurrences in the vicinity of a given point. Such recurrences are independent of the time elapsed between the two readings in a time-series record. A problem commonly existing in time series data is the existence of temporal correlations which leads to a reduction in the dimensional estimate. High-frequency experimental recordings often show this tendency. Two readings, separated by a small time-interval are often strongly correlated. On the attractor geometry, this refers to points immediately succeeding or preceeding a given point. In the presence of such temporal correlations, infinite dimensional stochastic signals lead to finite, low-dimensional signals as shown by Theiler [119], [120]. This problem is addressed by rejecting temporally correlated points from the computation of the correlation integral. This 'time window' is known as the 'Theiler Window'. Space-time separation plots introduced by Provenzale [121] can be used to identify the presence of temporal correlations. In the presence of temporal correlations, the probability that a given pair of points is separated by a distance less than ϵ depends on both ϵ and the time elapsed between the two. Therefore, the temporal dependence can be detected by plotting the number of pairs as a function of the space scale and temporal separation τ on a contour plot. The saturation of the contours indicates the absence of temporal correlations. The time interval beyond which, the space time contour saturates is the Theiler window. Figure 23(b) shows a representative space-time separation plot. Although finite correlation dimensions are indicative of chaotic dynamics, there are situations wherein 'false positives' may result from limited datasets. These include stochastic processes, possessing power-law spectrum with random, independent, uniformly distributed Fourier phases (colored noise) and certain stochastic linear auto-regressive and non-linear processes with a power-law Fourier spectrum. Estimates of correlation dimensions for such systems diverge upon increase in the length of the dataset. However, this is not practically

possible in case of experimental time-series records. The space-time separation plot is a convenient tool, capable of distinguishing stochastically dominated signals from deterministic ones. Stochastic signals fail to show a saturation in the contours of the space-time separation plot in contrast to deterministic signals.

5. Lyapunov exponents and spectrum

This discussion follows Ref. [122]. Lyapunov exponent is an invariant measuring the divergence of nearby trajectories. It is important to estimate Lyapunov exponents as it is directly related to the K-entropy. The K-entropy quantifies the loss of information within a chaotic system. Therefore, it is directly related to the prediction horizon of a chaotic system. Consider a flow, described by the following autonomous differential equation (Ref. [122]):

$$\dot{\mathbf{x}} = \mathbf{f}(\mathbf{x}) \tag{4.15}$$

The distance between two infinitesimally close trajectories (fig. 24)develops in time according to:

$$\dot{\boldsymbol{\varepsilon}} = g(t)\boldsymbol{\varepsilon} \tag{4.16}$$

Here, g_{ij} is the Jacobian matrix at $\mathbf{x(t)}$ given by:

$$g_{ij}(t) = \frac{\partial f_i}{\partial x_j}\mathbf{x}[t, \mathbf{x}(\mathbf{0})] \tag{4.17}$$

Integrating (4.17)

$$\boldsymbol{\varepsilon(t)} = \{\hat{A}e^{\left[\int_0^t dt' g(t')\right]}\}\boldsymbol{\varepsilon}(0) \equiv h(t)\boldsymbol{\varepsilon}(0) \tag{4.18}$$

Here, $\hat{A}$ is the time-ordering operator, introduced because matrices g(t) and g(t') at two different instants of time do not commute. The Lyapunov exponents are therefore:

$$(e^{\lambda_1}, \ldots, e^{\lambda_n}) = \lim_{t\to\infty}(\text{magnitude of eigen values of } h(t))^{1/t} \tag{4.19}$$

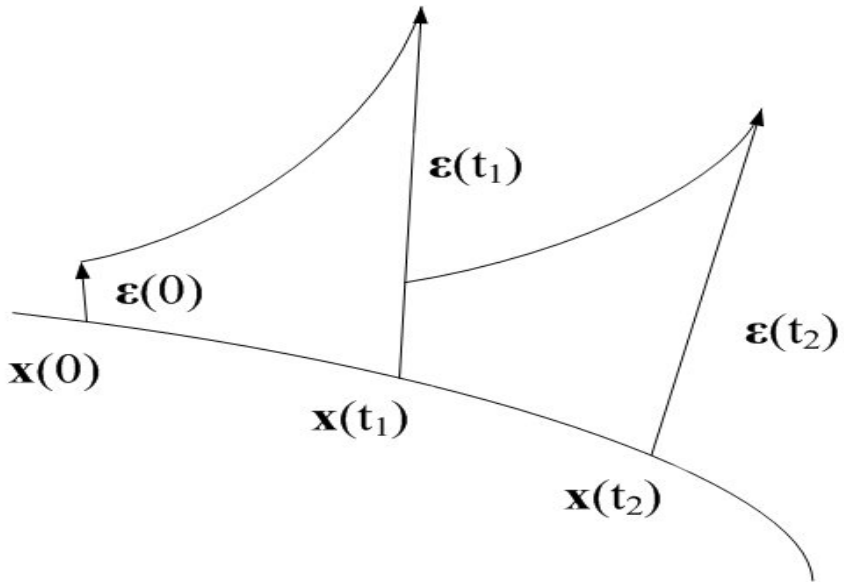

Fig. 24.: Evaluation of Lyapunov exponents [122]. The divergence of nearby trajectories is computed for a few timesteps and renormalized after each timestep and averaged.

The interpretation of Lyapunov exponents in terms of attractor geometry is given in table VI. The Lyapunov exponents vary with the choice of initial condition. The method of Sano and Sawada is employed with locally linear fits to approximate the dynamics to calculate the Lyapunov spectrum in the present study. The locally linear fit is valid when neighborhood size is small. However, the neighborhood size should be larger than the noise level in the data. The competing effects of noise, ill-conditioned Jacobian matrices, requirement of small neighborhood size and lack of adequate neighbors in regions of low attractor density, lead to poor estimates of Lyapunov exponents. Furthermore, the effect of temporal correlations in time-series data on the Lyapunov spectrum is unknown. The Theiler windows could not be employed to embed the attractors as the algorithm employed for embedding does not support this currently. Additionally, the embedding dimension is apriori unknown.

Therefore, in addition to true exponents, spurious or false exponents appear as well. Currently, there is no surefire test to separate spurious exponents from true exponents. In the absence of confirmatory tests, 'robustness' of exponents (Ref. [85]) to change in embedding dimensions and number of nearest neighbors is used to identify spurious exponents.

Table VI.: Interpretation of Lyapunov exponents [123]

λ_1	λ_2	λ_3	λ_4	*Attractor*	*Dimension*
-	-	-	-	Fixed point	0
0	-	-	-	Periodic/Multiply periodic	1
0	0	-	-	2-Torus/quasi-periodic	2
0	0	0	-	3-Torus/3-quasi-periodic	3
+	0	-	-	Chaos/strange attractor	> 2
+	+	0	-	Hyperchaos	> 3

6. Hypothesis testing: surrogate data tests

One of the main goals of non-linear time series analysis is to detect the presence or absence of underlying non-linear dynamics in a time-series. It is necessary to determine whether non-linear dynamics is indeed present in the resulting time-series. This is accomplished by subjecting the original time series and many artificially generated time series to a test with a prescribed null hypothesis and a specific level of significance. The artificial time series or surrogate data sets are similar to the original time series in certain respects (e.g. similar Fourier spectrum) while satisfying the null hypoth-

esis. These data sets are then subjected to a discriminating test. The test involves determination of a suitable parameter (e.g. time-reversal asymmetry, correlation dimensions etc.) for all data sets. A large difference in value of the parameter between the original and surrogate data sets indicates that the null hypothesis concerning the data set is false.

In the present study, surrogate data is generated using a constrained phase randomization. The data is assumed to result from a stationary linear stochastic process with Gaussian inputs. Surrogate data sets are generated to satisfy this hypothesis while having a spectrum similar to the original time-series. The original and surrogate data sets are subjected to a two-sided hypothesis testing involving time-reversal asymmetry, a strong indicator of chaotic dynamics [85]. The significance level of these tests are highly conservative (99%). Usually a significance level of 95% suffices. In order to generate the surrogate data sets the FFT of the data is taken aand multiplied by random phases [85]:

$$\tilde{f}_k = \frac{1}{\sqrt{N}} \sum_{n=1}^{N} \breve{f}_n e^{\frac{i2\pi nk}{N}} e^{i\psi_k} \tag{4.20}$$

The inverse FFT is taken resulting in:

$$\breve{f}_n = \frac{1}{\sqrt{N}} \sum_{k=1}^{N} f_n e^{\frac{i2\pi nk}{N}} \tag{4.21}$$

Thus, the resulting series contains random numbers with a prescribed spectrum with different ψ_k yielding different surrogate datasets. Here, ψ_k represents the phase randomization. The time reversal asymmetry statistic, given below is computed for all the datasets [85]:

$$\chi = \frac{\langle (x_n - x_{n-d})^3 \rangle}{\langle (x_n - x_{n-d})^2 \rangle} \tag{4.22}$$

If the value of this statistic corresponding to the original dataset is lower or higher than that for all surrogates, then the null hypothesis of linear stochastic process with

Gaussian inputs is invalid. It must be noted that each test statistic has a finite power to distinguish chaotic data from the assumed null hypothesis. Therefore, false positives and false negatives can be obtained [85].

CHAPTER V

BARE SILICON SURFACE: RESULTS AND DISCUSSION

A. Introduction

In the present chapter, we present the results of saturated and subcooled pool boiling experiments on silicon substrates. The TFT shows a linear response with respect to the calibrated wire-bead temperature with slopes varying between 0.95 and 1. Boiling curves are plotted for the saturated and subcooled experiments based on the surface temperatures recorded by TFT and heat fluxes based on radially averaged, axially extrapolated temperature at the top of the copper heating cylinder. A plot of temperature at the top center of the copper heating cylinder vs. the axially averaged surface heat flux is used to assess the impact of subcooling on heat transfer rates.

The surface temperature fluctuation data and results of spectral analysis is discussed in the following section. This is followed by results and discussion of non-linear time series analysis. Time-series analysis is conducted on high-frequency time-series data obtained from TFT measurements of surface temperature fluctuations. The following sequence of steps is employed in analysis of the time-series.

1. The mutual information function is used to estimate the optimal delay as discussed in the previous chapter. Additionally, the impact of the boiling regime and subcooling on the mutual information function is assessed.

2. A suitable embedding dimension is determined from recurrence plots and the false nearest neighbor test. Recurrence plots also serve as visual aids for determining the presence of deterministic chaos.

3. Space-time plots are constructed to estimate the Theiler windows.

4. This is followed by estimates of correlation dimensions for the noisy data. The correlation dimension estimate for the noisy data is compared for both saturated and subcooled pool boiling. The impact of subcooling on attractor dimension is evaluated. This is followed by an estimate of all the above quantifiers after noise reduction.

Optimal delay, space-time separation plots, phase plots, phase plots from principal component analysis, correlation dimensions, Lyapunov exponents are evaluated and surrogate data tests are conducted on the noise reduced data. The Lyapunov spectrum is evaluated for embedding dimensions ranging from three to eight. Positive exponents are obtained in FDNB, at CHF and in film-boiling, indicating the possible presence of chaotic dynamics. The Kaplan-Yorke dimensions estimated from Pesin's conjecture (Ref. [85]) shows dimensions varying from $\sim$ 0 - 5. In continuous systems, chaotic dynamics is obtained for embedding dimensions greater than two.

B. Saturated & Subcooled Pool Boiling Heat Transfer: Results & Discussion

1. TFT calibration results

Thin-film thermocouples on the bare silicon surface are calibrated both in situ and separately in a constant temperature bath. Two calibrated, beaded K-type thermocouples are glued on the surface of the wafer using JB weld. Figure 25 depicts results of in situ calibration of TFT. An NIST thermometer with a temperature resolution of 0.1 ℃ . The TFT response is observed to be linear in both cases. Due to a maximum temperature limitation of 50 ℃ on the NIST thermometer, the TFT cannot be calibrated over its entire operating range within the constant temperature bath. The overall uncertainty in the temperature reading of the TFT ranges from $\sim$ 0.11 - 0.46 ℃. Calibration of the TFT in the constant temperature bath results in a slight

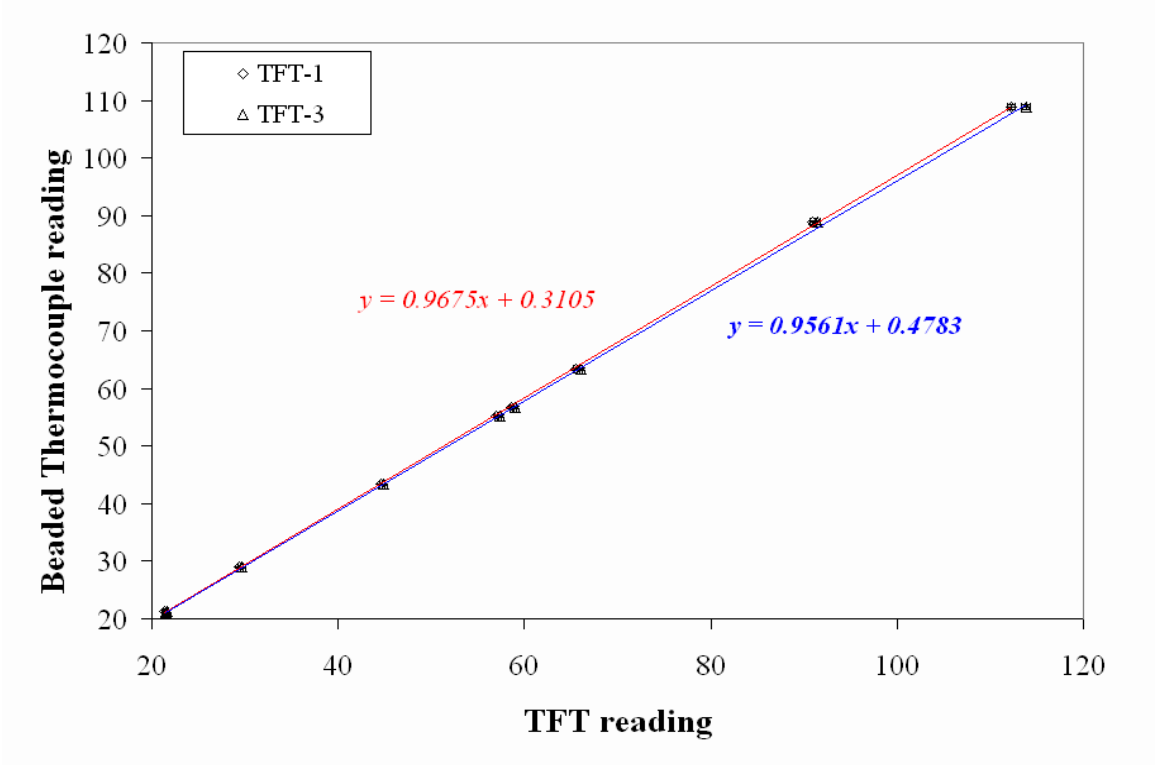

Fig. 25.: Calibration curves showing the linear response of TFT.

variation in the least squares fit. The deviation between the two fits results in a calibrated temperature differential of 1.2 - 2.5 ℃ for assumed, uncalibrated, TFT temperatures varying between 56 - 75 ℃. This corresponds to the surface temperatures encountered in nucleate boiling. The temperature differential between the two calibrations within the film boiling regimes is of the order of 4 - 5 ℃ corresponding to an assumed uncalibrated TFT reading of $\sim$ 100 ℃. The distance between the actual TFT junctions and the reference wire-bead junction leads to some deviation of the insitu calibration curve compared to the calibration conducted by placing the wafer within a water bath.

2. Pool boiling curves

Pool boiling curves for saturated cases are shown in the figure 26(a). The peak heat fluxes are 11.04 and 11.51 W/cm^2 respectively for the first and second runs. Sudden onset of nucleate boiling occurs at wall temperatures of $\sim$ 63.87 ℃ (TFT-1) and $\sim$ 62.66 ℃ (TFT-3) at a heat flux of 1.97 W/cm^2. TFT-3 showed three 'outliers' in the first experiment. Sudden excursions of $\sim$6 ℃ occurs at heat fluxes of $\sim$ 5.11 W/cm^2, $\sim$ 8.35 W/cm^2, $\sim$ 9.9 W/cm^2.

Film boiling occurs at wall temperature levels exceeding 106 ℃. Due to significant disruption of the vapor film by the bond pads, film boiling could not be sustained below this level. From Berenson's correlation [124], the minimum wall temperature required for sustained film boiling is $\sim$ 91.2 ℃ i.e. a wall superheat of 35.3 ℃ however, this is much lower ($\sim$ 15 ℃) than the experimentally observed values. It is therefore, concluded that the presence of bond pads, causes a significant disruption of the vapor film necessitating the increase in wall superheat. The minimum heat fluxes in the first and second runs are $\sim$ 5.7 W/cm^2 and $\sim$ 5.8 W/cm^2 respectively. A difference of $\sim$ 7 - 10 ℃ exists in the wall superheat values shown by TFT-1 and TFT-3 in the film boiling regime in each run.

Figure 26(b) shows the pool boiling curve for liquid subcooling of 10 ℃ . TFT-1 shows a significant deviation of $\sim$ 6 ℃ beyond ONB between runs as well as in comparison to TFT-3. The figure shows peak heat fluxes of the order of 11.28 W/cm^2 at a wall temperature level of $\sim$ 75 ℃. Film boiling occurs at wall temperatures in excess of 109 ℃. Minimum heat fluxes in both runs are 6.29 W/cm^2.

Figure 27 shows the saturated and subcooled pool boiling curves for different runs with wall temperature based on averaged temperature at top of the copper heating cylinder. The thermocouples located within the copper heating cylinder are less prone

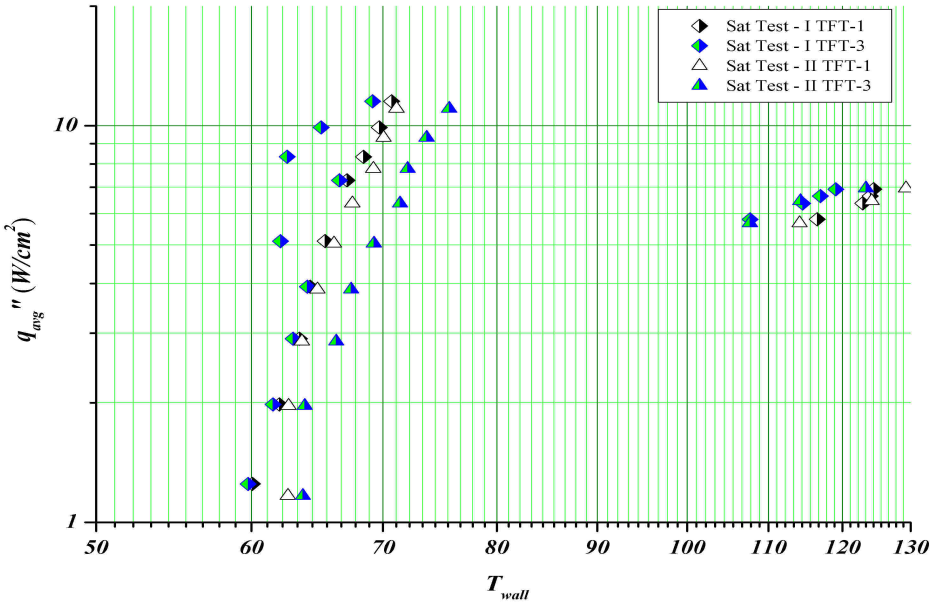

(a) Saturated pool boiling curve based on TFT surface temperatures

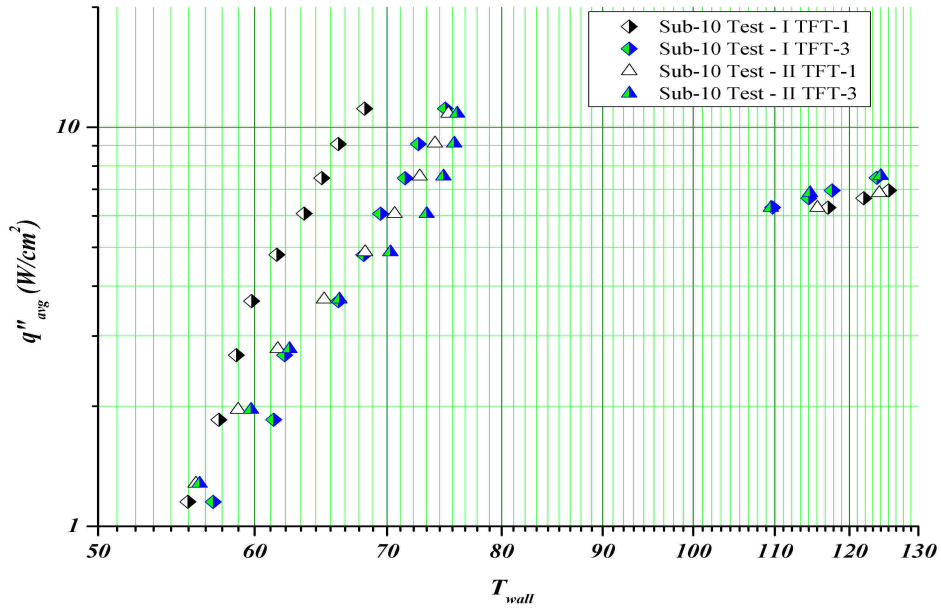

(b) 10 ℃ subcooled pool boiling curve based on TFT surface temperatures

Fig. 26.: Pool boiling curves for saturated and subcooled pool boiling.

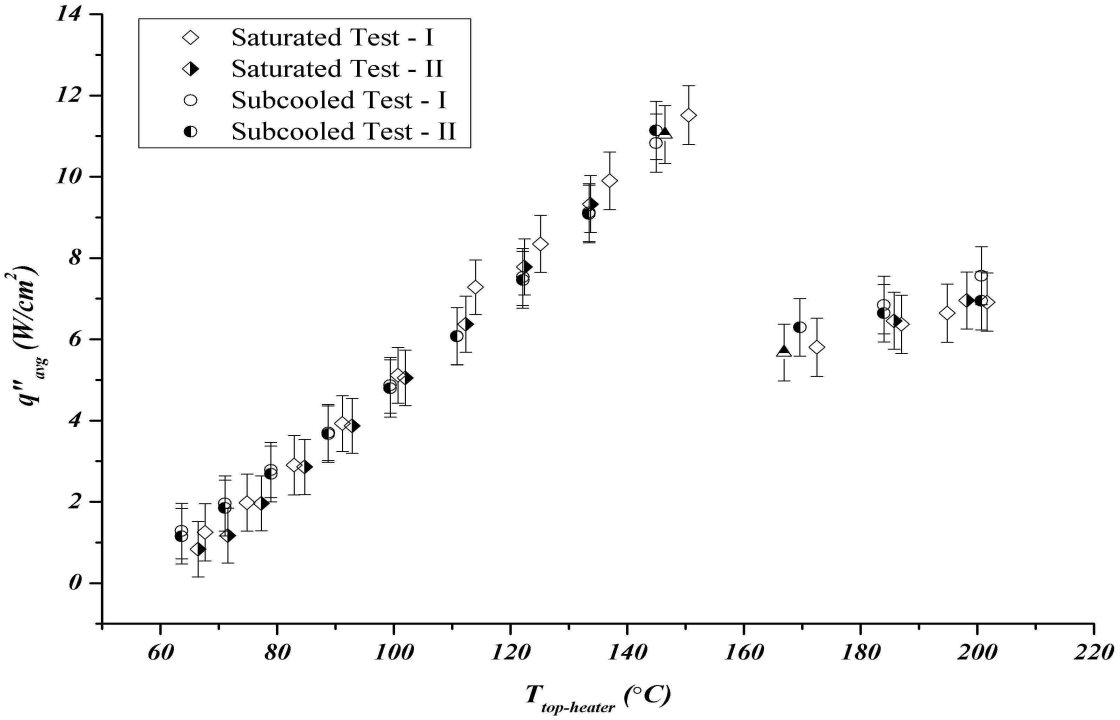

Fig. 27.: Saturated and 10 ℃ subcooled pool boiling on a silicon surface. The temperature at the top of the copper heating cylinder is estimated from the axial temperature profile within the copper cylinder.

to drift and bias, apart from the effects of nucleation which causes local temperature fluctuations on the surface of the test surface. The pool boiling curves show good repeatability between runs. Heat transfer rates are similar between runs and no significant improvement in heat transfer rates is observed between the saturated and the subcooled experiments.

3. Discussion of pool boiling heat transfer results

The relaxation microlayer thickness is estimated by the following expression (Ref. [125]):

$$\delta_{mlay} = \sqrt{\left(\frac{12}{\pi}\right) \alpha_l t_g} \tag{5.1}$$

In the above expression, t_g is the microlayer relaxation time. The thickness of the TFT is 250 nm which is less than the thickness of the microlayer ($\sim$ 21.56 μm) and hence provides high-fidelity measurements of surface temperatures. Calibration of thin film thermocouples is the object of research at NIST [126]. Differences in TFT configurations coupled with the fragile silicon substrates make calibration, standardization and packaging of TFT a difficult task. Calibration of TFT involves, maintaining the junctions at specific temperatures. Given the small form factor, it is difficult to maintain the junction alone at specific temperatures. As described in chapter III, the TFT are calibrated in situ in air using a calibrated, wire-bead thermocouple as a reference. The wire-bead thermocouple is located at a distance of $\sim$ 1.5 cm from the junctions of the TFT on the test surface. In the present tests, the TFT show a linear response for the temperature range of interest.

Deviations exist in averaged surface temperature for a given TFT between runs as well between different TFT for the same run in nucleate boiling. Irreproducibility of active nucleation sites between runs seems to be the primary cause for this deviation whereas the presence or absence of active nucleation sites in vicinity of the TFT seems to be the cause for the latter. Another possible source of this deviation is the cross-talk of thermocouple sensor arrays through the semi-conducting silicon substrate. Alternatively, slight differences in composition of the evaporated metallic film forming the TFT and the connecting wires could result in spurious e.m.f. A combination of these effects could explain the deviation in temperatures shown by TFT. Similar behavior was encountered in the saturated pool boiling tests for TFT-3 at high heat fluxes.

As mentioned earlier, inception of nucleate boiling is vital to succesful thermal management of electronics. Inception of nucleate boiling was observed to occur at a wall superheat level of $\sim$ 6 ℃. The critical cavity size for nucleation for a cavity

surrounded by uniformly superheated liquid is given by the following expression:

$$r_{crit} = \frac{2\sigma T_{sat}(P_l)}{h_{fg}\rho_v[T_l - T_{sat}(P_l)]} \tag{5.2}$$

The critical cavity size for nucleation (uniformly superheated liquid) at wall superheat levels of 4 ℃ , 6 ℃ , 7 ℃ and 8 ℃ are determined to be 1.31 μm, 0.87 μm, 0.75 μm and 0.65 μm respectively. The minimum, active, cavity size for a non-uniformly superheated liquid is given by Hsu's criterion [4]. This is given by the following equation:

$$r_{crit} = \frac{\delta_{bl}}{4}\left[1 - \frac{T_{sat} - T_\infty}{T_w - T_\infty} \pm \sqrt{\left(1 - \frac{T_{sat} - T_\infty}{T_w - T_\infty}\right)^2 - \frac{12.8\sigma T_{sat}(P_l)}{\rho_v h_{lv}\delta_{bl}(T_w - T_\infty)}}\right] \tag{5.3}$$

By setting the term within the square root to zero, the theoretical wall superheat required to initiate nucleation is found to be 3.79 ℃ for saturated pool boiling. In the saturation experiments, nucleation was observed at wall superheat levels of 4 ℃ in the first run and 7 ℃ with fluxes of the order of 1 W/cm^2. Therefore, the theoretical limit given by Hsu's criterion is in agreement with observations in the first run. The smallest, active, cavity size at wall superheat levels of 4 ℃ 6 ℃ , 7 ℃ and 8 ℃ are 0.18 μm, 0.12 μm, 0.1 μm and 0.09 μm respectively according to Hsu's criterion. Corresponding values for subcooled pool boiling are 0.35 μm, 0.25 μm, 0.23 μm and 0.21 μm. According to Hsu's criterion, the sizes of largest active nucleation sites at the above superheat levels are 5.20 μm, 7.96 μm, 9.30 μm and 10.69 μm in saturated pool boiling. Corresponding values for 10 ℃ subcooled boiling are 2.72 μm, 3.79 μm, 4.21 μm, 4.58 μm. According to the correlation of Wang and Dhir (2.2) the corresponding diameter of active nucleation cavities is 0.29 μm which is significantly lower than the critical cavity size for nucleation in a uniformly superheated liquid. The boiling heat transfer coefficient is observed to vary from 3333 W/m^{2}K at ONB to

~ 8000 W/m^{2}K at CHF for saturated pool boiling. At CHF, temperature fluctuations of the order of $\pm$ 2 ℃ is observed. This corresponds to a fluctuation of $\sim \pm$ 1000 W/m^{2}K in the heat transfer coefficient assuming the local heat flux is constant.

Arik and Cohen [127] developed a correlation for predicting CHF for thermal management of electronics. The correlation accounts for the the thermal properties of the heater, subcooling and liquid. The expression is:

$$q''_{max} = \frac{\pi}{24}\rho_v h_{lv}\sqrt[4]{\frac{\sigma g(\rho_l - \rho_v)}{\rho_v^2}} \times \left(\frac{S}{S+0.1}\right) \times \left[1 + \left\langle 0.3014 - 0.01507 \times \left(\frac{W_h}{L_{cap}}\right)\right\rangle\right] \times \left(1 + 0.03\left(\frac{\rho_l}{\rho_v}\right)^{0.75}\left(\frac{C_{pl}}{h_{lv}}\Delta T_{sub}\right)\right) \quad (5.4)$$

Here, $S = \delta_h\sqrt{\rho_h C_{ph} k_{ph}}$, accounts for the heater thermal properties. The CHF predicted by this correlation is 13.16 W/cm^2 and 15.17 W/cm^2 for saturated and 10 ℃ subcooled pool boiling respectively. Thus, the correlation overpredicts peak heat flux in saturated pool boiling by 12.5% and subcooled pool boiling by 29.6%.

Figure 28 depicts the variation of heat transfer coefficients with wall superheat for all test runs and both cases. The results clearly show the variation of heat transfer coefficients with wall superheat in saturated pool boiling. The heat transfer coefficients range from 2000 - 8000 W/m^2 except for three data points based on temperature data of TFT-1. The three points in FDNB show coefficients ranging from 8000 - 13000 W/m^2. Heat transfer coefficients in the film boiling regime range from 950 - 1150 W/m^2 and is constant for the most part. The heat transfer coefficients in subcooled, nucleate boiling show significant differences amongst TFT and amongst runs. TFT-1 shows heat transfer coefficients ranging from $\sim$ 8000 - 12000 W/m^2 in the nucleate boiling regime whereas TFT-3 shows heat transfer coefficients ranging from 3500 - 10000 W/m^2. TFT-3 on the other hand, shows heat transfer coefficients ranging from 3500 - 6000 W/m^2 for most of the nucleate boiling regime. The relative uncertainty in

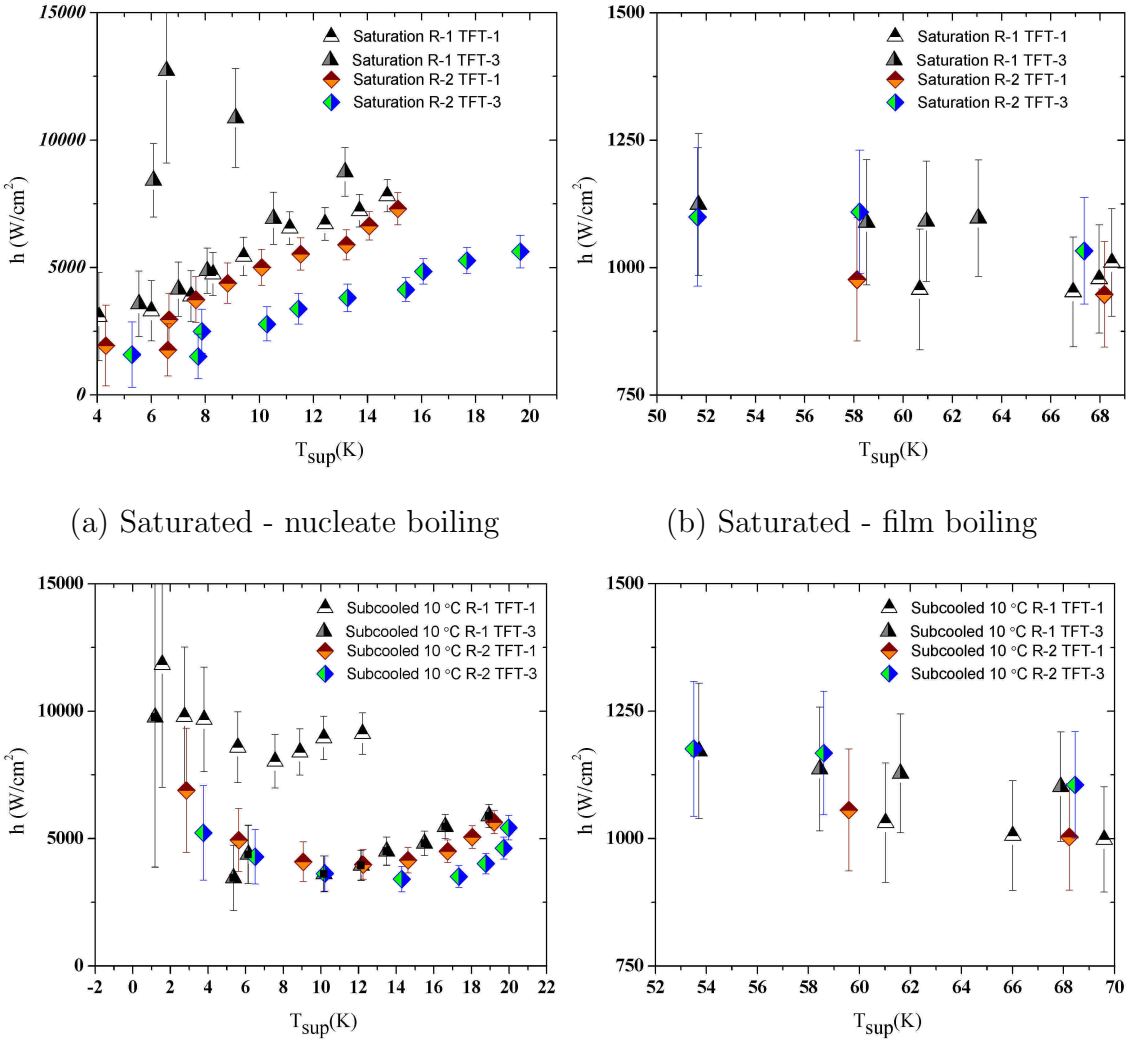

(a) Saturated - nucleate boiling

(b) Saturated - film boiling

(c) Subcooled - nucleate boiling

(d) Subcooled - film boiling

Fig. 28.: Heat transfer coefficients based on time-averaged surface temperature measurments for saturated and subcooled pool boiling experiments.

the estimates of the heat transfer coefficients for the first two data points is high. In the film boiling regime, the heat transfer coefficient ranges from 1000 - 1200 W/m^2K and a slight gradual decrease is observed with increase in wall superheat.

To summarize, ONB occurs at a superheat close to that predicted by Hsu's criterion in saturated pool boiling. The rates of heat transfer at CHF are significantly lower than that predicted by the correlation of Arik and Cohen for saturated and subcooled pool boiling. This clearly indicates the need for better predictive tools for CHF.

C. Pool boiling temperature-time series & its analysis

The results of non-linear time-series analysis are discussed in this section. High-frequency surface temperature fluctuation data acquired at quasi-steady condition, for a duration of 18 seconds at a frequency of 1kHz is analyzed. Techniques of non-linear time-series analysis are applied as the Fourier spectrum is broad-banded suggesting the presence of multiple periodicities, randomness or chaos. The variation of temperature with time for different regimes of pool boiling is discussed first. Optimal embedding dimension determined from the first minimum of the mutual information function is used as the optimal value of delay for delay embedding. The possibility of presence of deterministic dynamics is assessed using the variation of the value of mutual information with delay. Suitable embedding dimensions are determined using the false nearest neighbors test and recurrence plots. The use of recurrence plots in determining the noise level in experiments is discussed. Once suitable embedding dimensions and delay times are determined, correlation dimension estimates are obtained for saturated and subcooled pool boiling. The impact of subcooling on the correlation dimensions is assessed. This followed by analysis of noise reduced data

for a saturated pool boiling run alongwith phase plots for saturated and subcooled pool boiling. Lastly, the Lyapunov spectrum is determined for different embedding dimensions.

1. Temperature-time series

The fluctuations in surface temperature depends on the local nucleation characteristics, latent heat of the fluid and the thermal conductivity of the heater surface. The thermal conductivity of silicon is approximately 119 W/mK at a temperature of 350K and 99 W/mK at a temperature of 400K. Figures 29 and 30 show the variation of surface temperatures for a time-period of 18 seconds in different regimes of saturated pool boiling. The high frequency surface temperature data is acquired at 1kHz for 30 seconds. At low wall superheat near ONB, surface temperature fluctuations are less than $\pm$ 0.3 ℃. The noise in the data is significant ($\pm$ 0.05 ℃) compared to the range of the temperature fluctuations. A closer analysis of the time series within a timespan of 0.5 seconds (fig. 29(b)) shows the presence of temperature fluctuations occurring over time-intervals of $\sim$ 20ms. Since no nucleation was observed at this wall superheat, it is concluded, that the source of the temperature fluctuations is the 60Hz AC noise. High speed images of the boiling process revealed, bubble cycle times (includes waiting time, growth and departure times) of the order of 50ms which correponds to a frequency of 20Hz, confirming this hypothesis. In PNB, temperature fluctuations of the order of 0.5 $\pm$ 0.3 ℃ are observed over time spans of 100 ms - 1 second. The longer timespan probably corresponds to nucleation in vicnity of the TFT junctions. As the wall superheat increases, the frequency of temperature fluctuations increase while the overall range is $\sim$ 0.75 ℃. The appearance of new timescales corresponds to the activation/deactivation of nucleation sites in vicinity of the TFT and the increased bubble departure frequencies at existing sites.

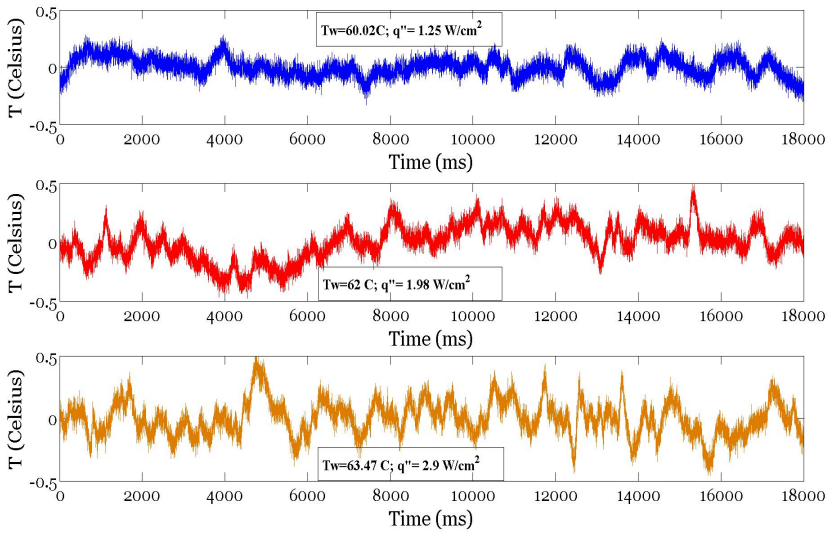

(a) Temperature fluctuation for a total time of 18 seconds

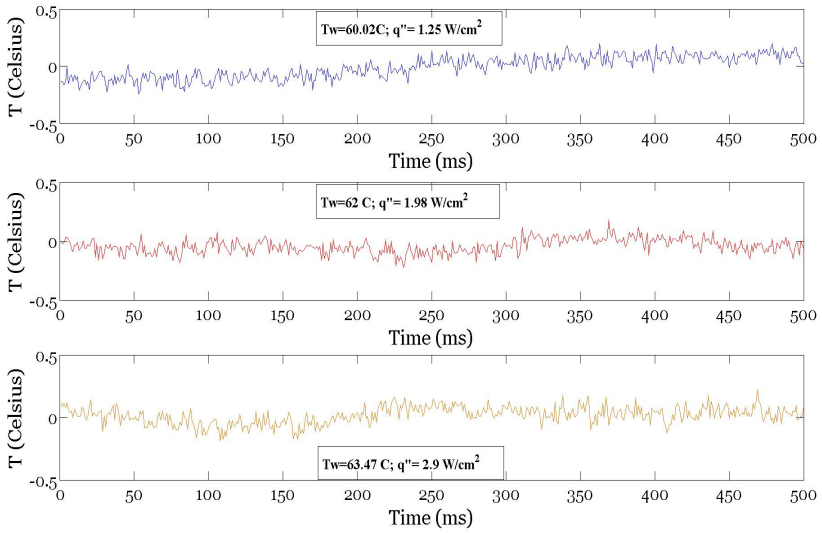

(b) Temperature fluctuation for a total time of 0.5 seconds

Fig. 29.: Surface temperature fluctuations recorded by TFT-1 (1000Hz), in saturated pool boiling (Run-I) before ONB, at ONB, and in PNB before noise-reduction.

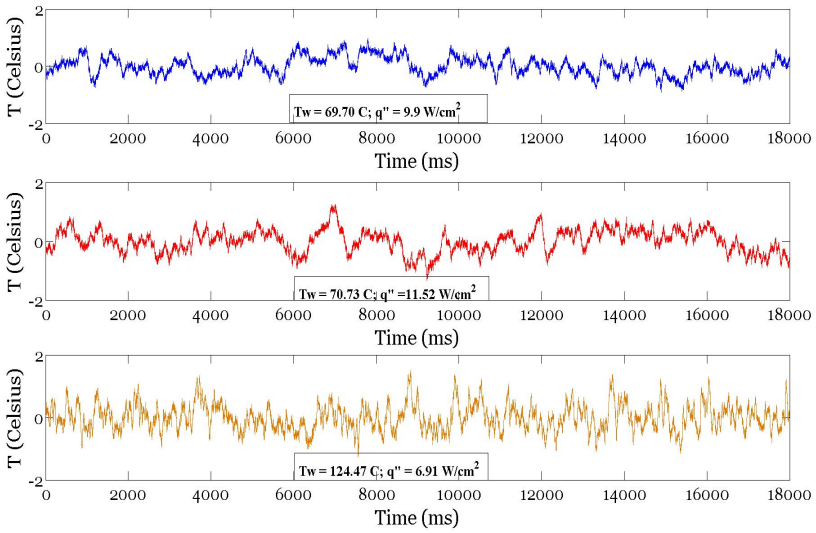

(a) Temperature fluctuation for a total time of 18 seconds

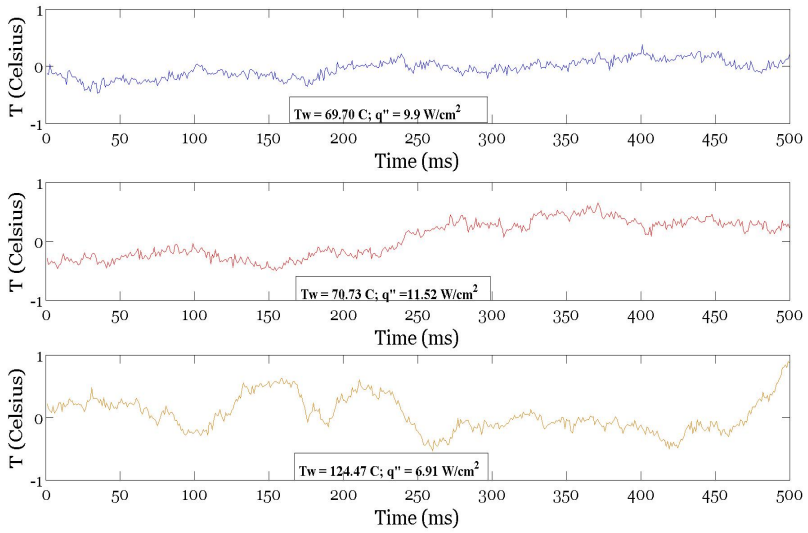

(b) Temperature fluctuation for a total time of 0.5 seconds

Fig. 30.: Surface temperature fluctuations recorded by TFT-1 (1000Hz), in saturated pool boiling (Run-I) at FDNB, CHF, film boiling before noise reduction.

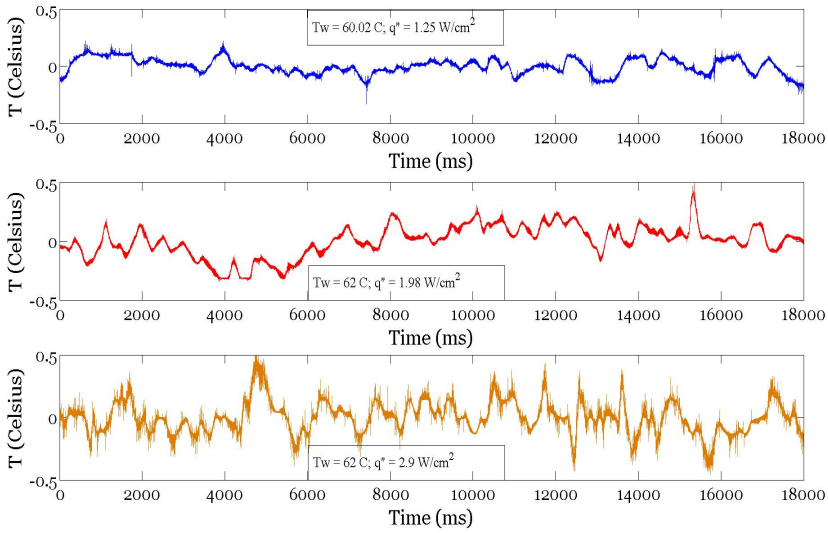

(a) Temperature fluctuation for a total time of 18 seconds

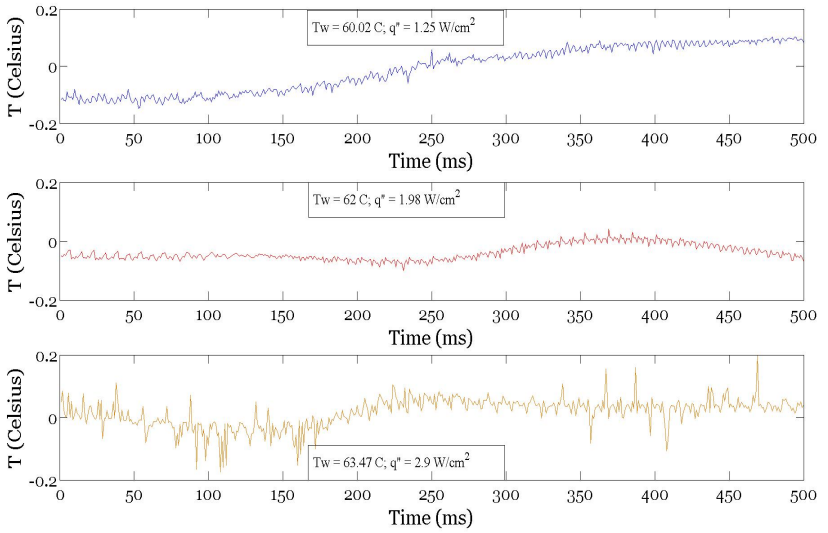

(b) Temperature fluctuation for a total time of 0.5 seconds

Fig. 31.: Surface temperature fluctuations recorded by TFT-1 (1000Hz), in saturated pool boiling (Run-I) before ONB, and in PNB after noise reduction.

Figure 30 depicts the temperature variation in FDNB, at CHF and in film boiling. The range of temperature fluctuations is of the order of ~ 2℃ in contrast to fluctuations of ~ 0.75℃ in PNB. Depending on the type of liquid in use the magnitude of these fluctuations vary and may be as high as 10℃ as reported in literature [10]. Compared to PNB, both FDNB and CHF show more frequent temperature excursions with higher magnitudes. This occurs as a result of the dominance of microlayer evaporation towards the total heat transfer rate. Film boiling on the other hand shows temperature fluctuations on time-scales spanning 100 - 300 ms superimposed on low frequency (~ 0.5 Hz) fluctuations. Theoretical studies in film boiling regimes show the existence of periodic bubble departure with temporally alternating departure sites (Ref. [9]). The temperature fluctuations visible on these time scales (~ 100 ms) is probably caused by this periodic departure of bubbles. However, it is also clear from the images that the surface temperature fluctuations are not dominated by a few frequencies. The existence of these peaks point to the occurence of liquid-solid contacts due to the vapor recoil caused by the bubble departure process.

Figures 31 and 32 depict the temperature fluctuations for the same cases considered above after noise reduction. Clearly, the noise removal process removes the high frequency noise present in the thermocouple signals. As in the case of noisy signals no single dominant periodicity is visible in any of the regimes on time-scales of the order of ~ 50 ms which corresponds to the bubble cycle time. However, the possibility of co-existence of multiple periodicities cannot be excluded. The cleaned signals in FDNB, CHF and in film boiling show temperature fluctuations of the order of ± 1 ℃ .

The magnitude of temperature fluctuations in 10 ℃ subcooled pool boiling is similar in magnitude to temperature fluctuations in the saturation case in FDNB, near CHF and in film-boiling. In FDNB and at CHF, temperature fluctuations of

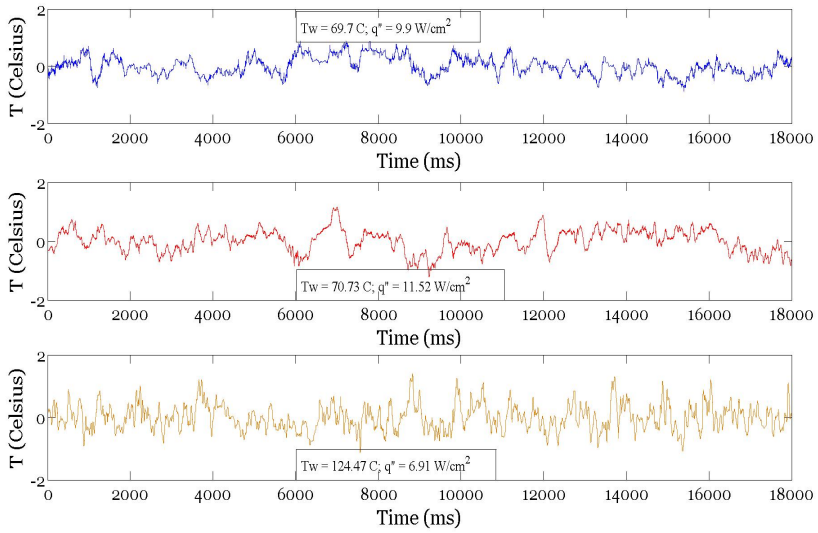

(a) Temperature fluctuation for a total time of 18 seconds

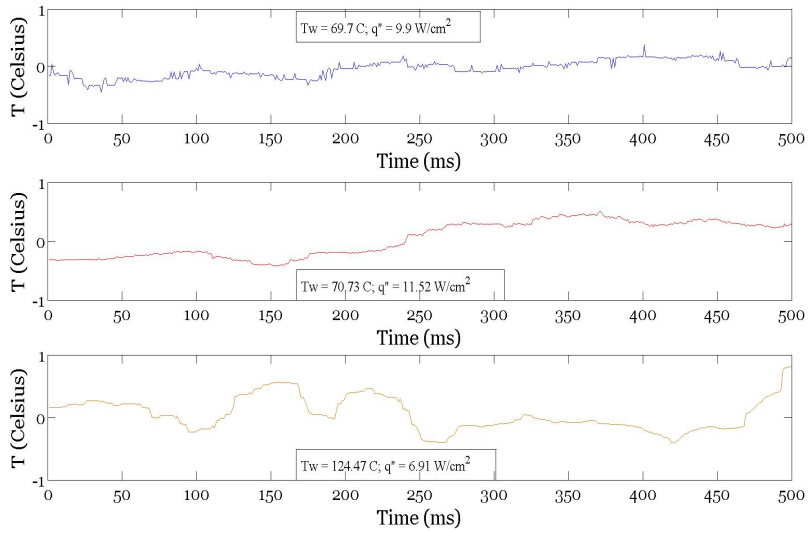

(b) Temperature fluctuation for a total time of 0.5 seconds

Fig. 32.: Surface temperature fluctuations recorded by TFT-1 (1000Hz), in saturated pool boiling FDNB, CHF, film boiling (Run-I), after noise reduction.

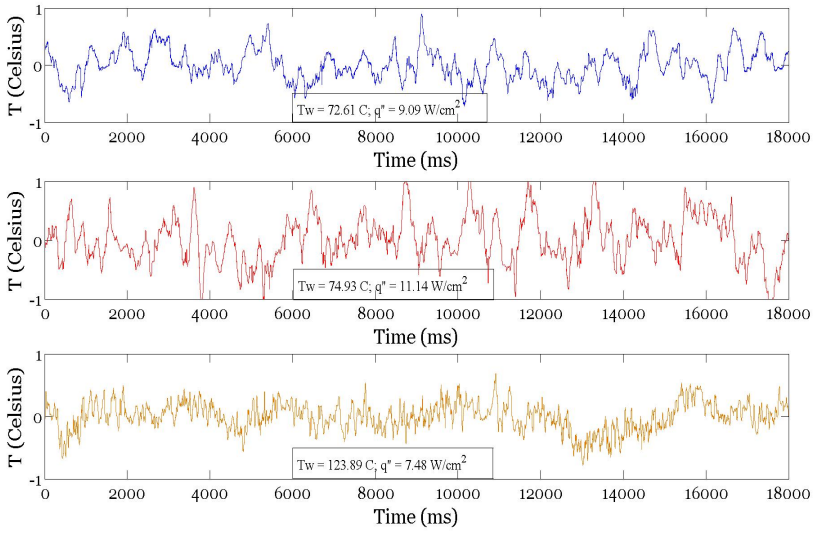

(a) Temperature fluctuation for a total time of 18 seconds

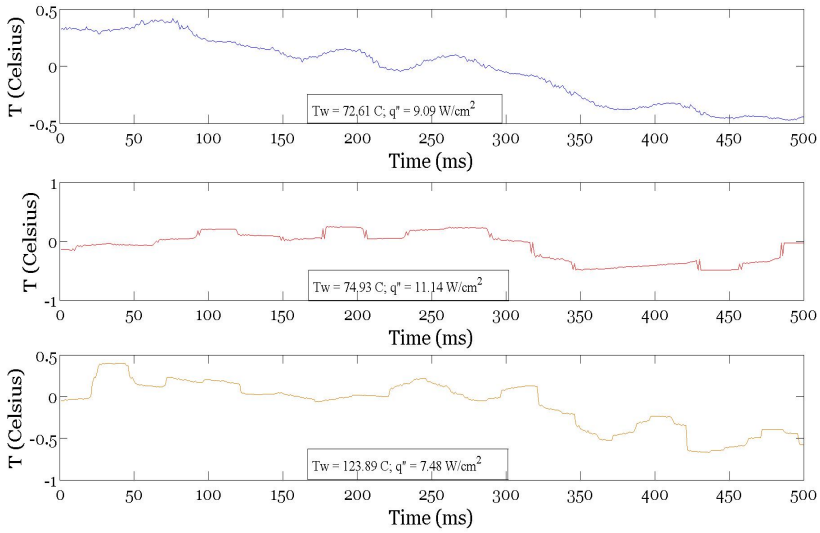

(b) Temperature fluctuation for a total time of 0.5 seconds

Fig. 33.: Surface temperature fluctuations recorded by TFT-3 (1000Hz), in 10 ℃ - subcooled pool boiling FDNB, CHF, film boiling (Run-I), after noise reduction.

the order of 2 ℃ is observed. The surface temperature fluctuation in subcooled film boiling is more pronounced compared to saturated film boiling. This could be indicative of more frequent liquid solid contacts due to a decrease in the thickness of the vapor film blanketing the surface.

2. Fourier Spectra

Fourier spectra analysis is useful in distinguishing periodic, multiply-periodic and quasi-periodic signals. Spectral analysis aids in identification of routes to chaos through mechanisms such as period-doubling bifurcations, quasi-periodic bifurcation etc. Bifurcations in chaotic systems follow certain universal patterns which vary depending upon the class of bifurcations enroute to chaos. The universal characteristics can be employed to predict the occurrence of subsequent bifurcations and the associated parameter values.

Figures 34 & 35 show the Fourier spectra of temperature signals in saturated pool boiling. The data is acquired for 18 seconds at a frequency of 1 kHz. The Nyquist frequency is therefore 500 Hz and the corresponding frequency resolution is 0.055 Hz. Significant power is present in the 0 - 30 Hz range. Sharp peaks are observed alongwith a broadband structure (0 - 20 Hz) and noise. The number of dominant frequencies is seen to increase with increase in heat flux. In the convective regime, a few dominant peaks and broadbanded structure is visbile in the 0 - 5 Hz range. The broadband structure ranges from 0 - 10 Hz in PNB, FDNB, CHF and from 0 - 20 Hz in the film boiling regime. Some differences in the dominant frequencies in PNB and FDNB is clearly observed among the two functioning TFT indicative of spatial temperature differences. The presence of a broadbanded structure is possibly indicative of chaotic dynamics. No simple periodic temperature fluctuations were observed in the film boiling regime. In the film boiling regime, an increase in heat

flux, results in an increase in the number of dominant frequencies.

Figures 36 & 37 depict frequency spectra for subcooled pool boiling at a subcooling level of 10 ℃ . Compared to saturated pool boiling, subcooled pool boiling shows a smaller active bandwidth in the convective regime, ONB and PNB. FDNB, CHF and film-boiling have similar spectra in both saturation and subcooled pool boiling. The magnitude of the power spectrum of these signals is lower in the subcooled case compared to the saturated pool boiling. The magnitude of the power spectrum shows that the frequency distribution is different for both TFT once again showing the spatial variation of temperature fluctuations.

To summarize, increase in heat-flux results in an increase in the number of active frequencies in nucleate boiling. This is due to the increase in the number of active nucleation sites. Additionally, a broad band spectrum is clearly observed in the range of 0 - 20 Hz. The gradual appearance of broadband structure is indicative of a bifurcation. Additional experiments with small increments in the power supplied to the heater are needed to confirm the presence of bifurcations. The frequency spectra were observed to comprise of two fundamental, disparate frequencies with the remaining peaks observed at frequencies of $mf_1 \pm nf_2$. The magnitudes of the fundamental frequencies varied with wall superheat.

In the saturated and subcooled experiments only 11-13 quasi-steady state data points were obtained. The current duration of these tests is $\sim$ 30 hours. Therefore, it is very difficult to conduct experiments with small increments to the power supply.

3. Mutual information

The mutual information indicates a general dependence/correlation between two quantities. Figure 38(a) shows the variation of optimal delay time determined from the first minimum of the mutual information function as a function of wall superheat

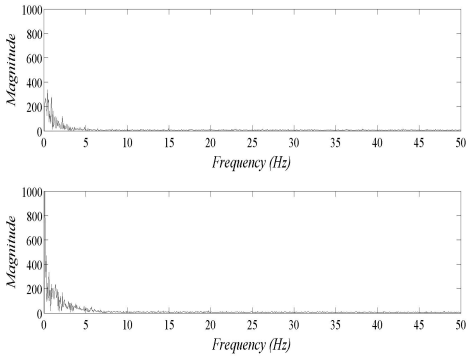

(a) Convective regime

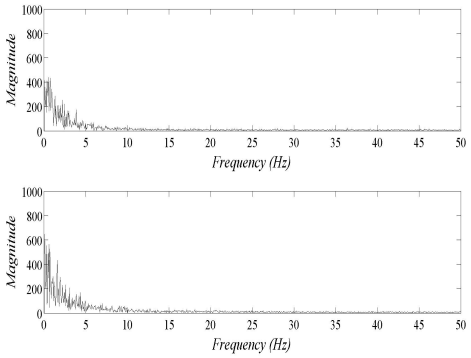

(b) ONB

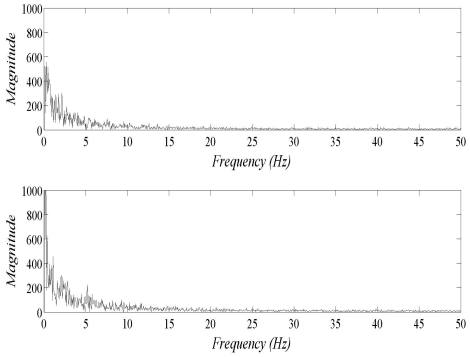

(c) PNB

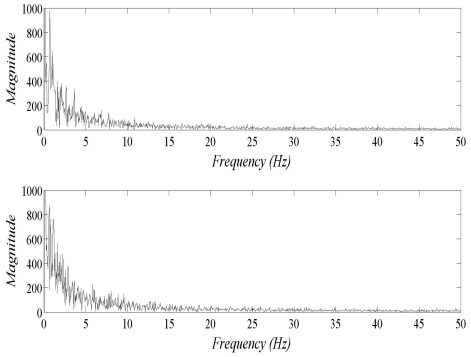

(d) FDNB

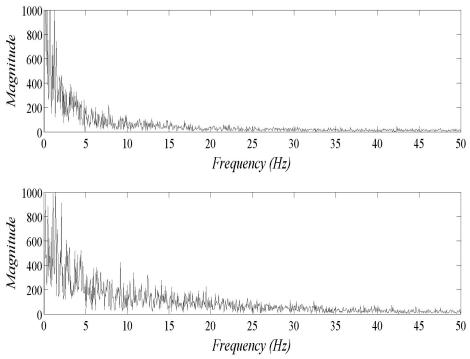

(e) CHF & Leidenfrost Point

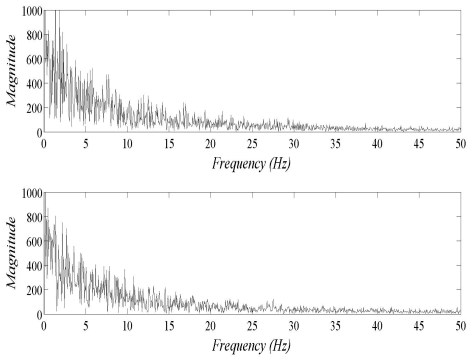

(f) Film Boiling

Fig. 34.: Fourier spectra for saturated pool boiling test-I corresponding to high frequency temperature measurements of TFT-1 after noise reduction.

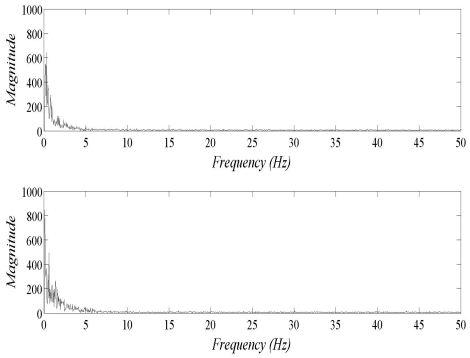

(a) Convective regime

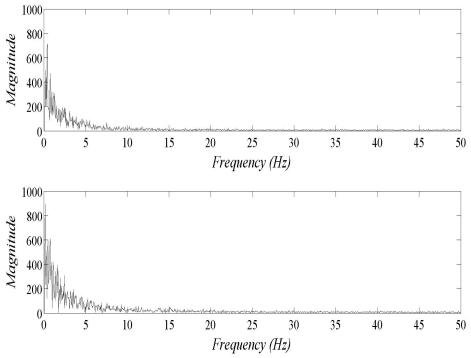

(b) ONB

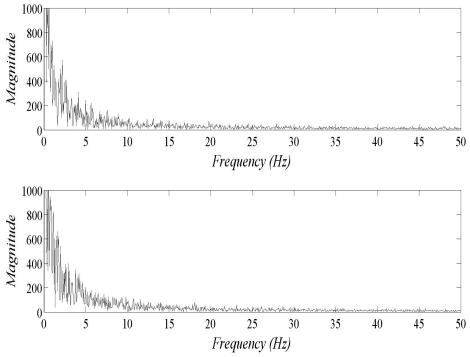

(c) PNB

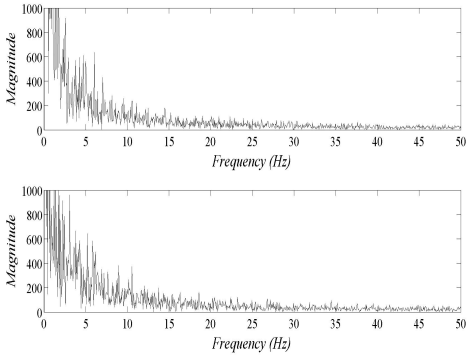

(d) FDNB

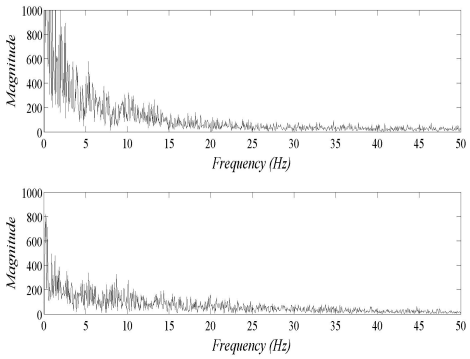

(e) CHF & Leidenfrost Point

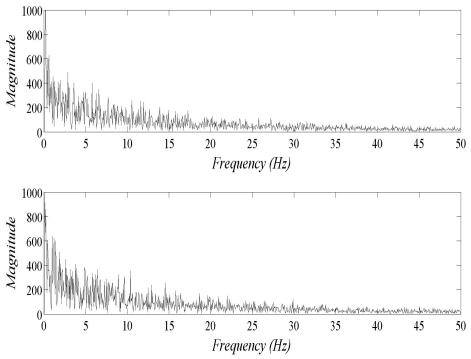

(f) Film Boiling

Fig. 35.: Fourier spectra for saturated pool boiling test-I corresponding to high frequency temperature measurements of TFT-3 after noise reduction.

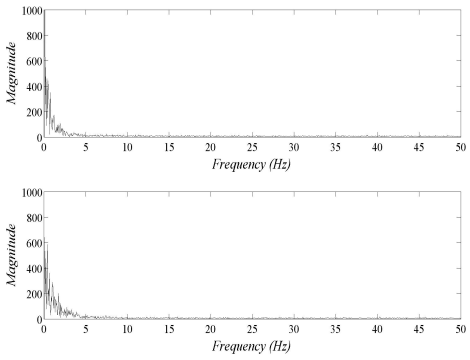

(a) Convective regime

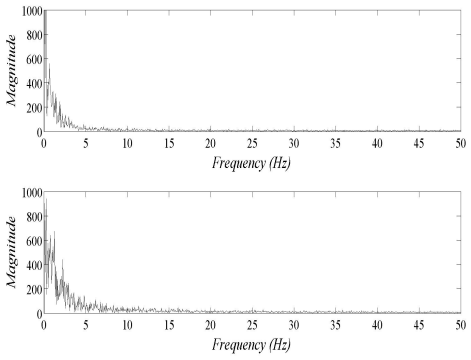

(b) ONB

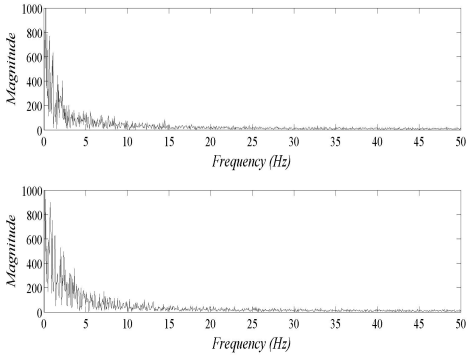

(c) PNB

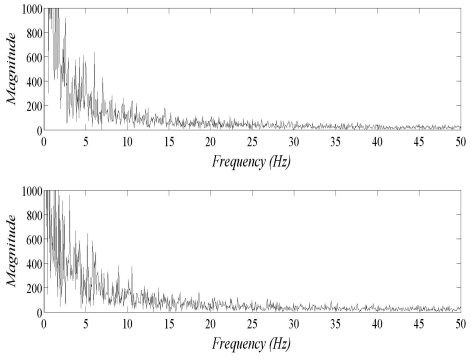

(d) FDNB

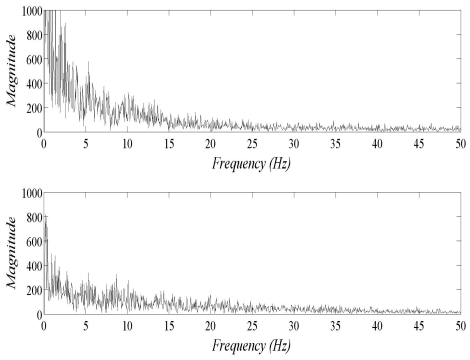

(e) CHF & Leidenfrost Point

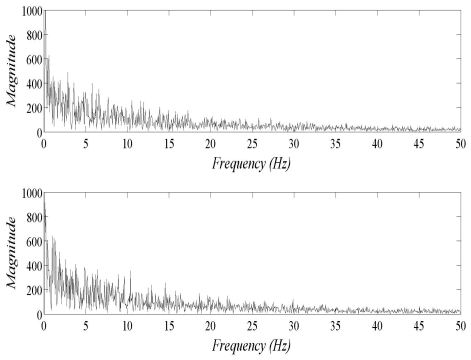

(f) Film Boiling

Fig. 36.: Fourier spectra for 10 ℃ subcooled pool boiling test-I corresponding to high frequency temperature measurements of TFT-1 after noise reduction.

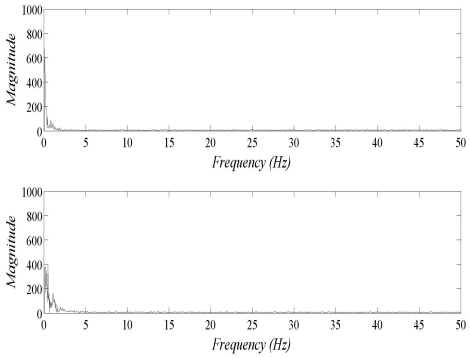

(a) Convective regime

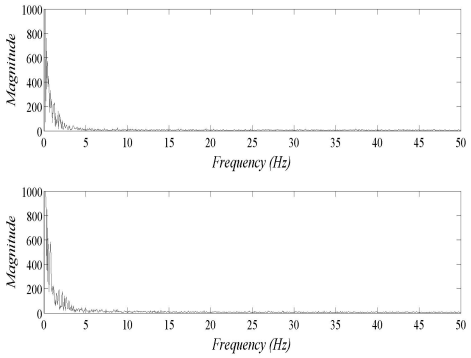

(b) ONB

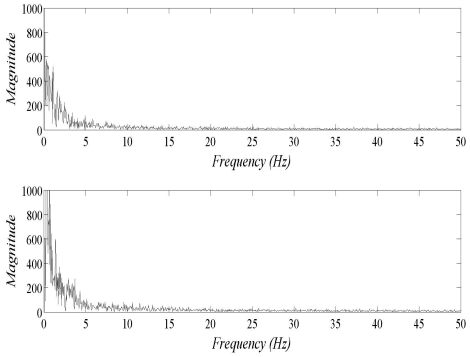

(c) PNB

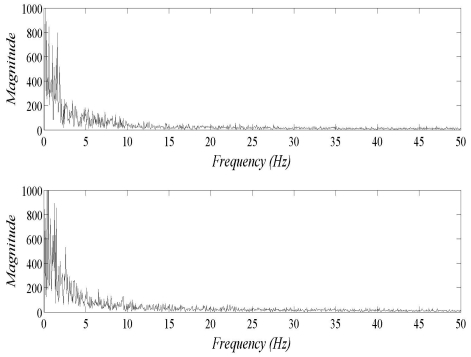

(d) FDNB

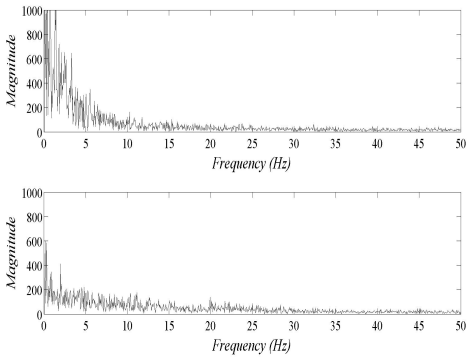

(e) CHF & Leidenfrost Point

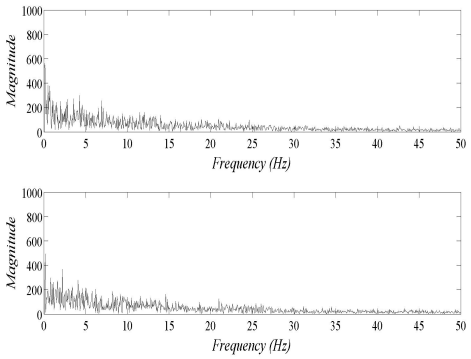

(f) Film Boiling

Fig. 37.: Fourier spectra for 10 ℃ subcooled pool boiling test-I corresponding to high frequency temperature measurements of TFT-3 after noise reduction.

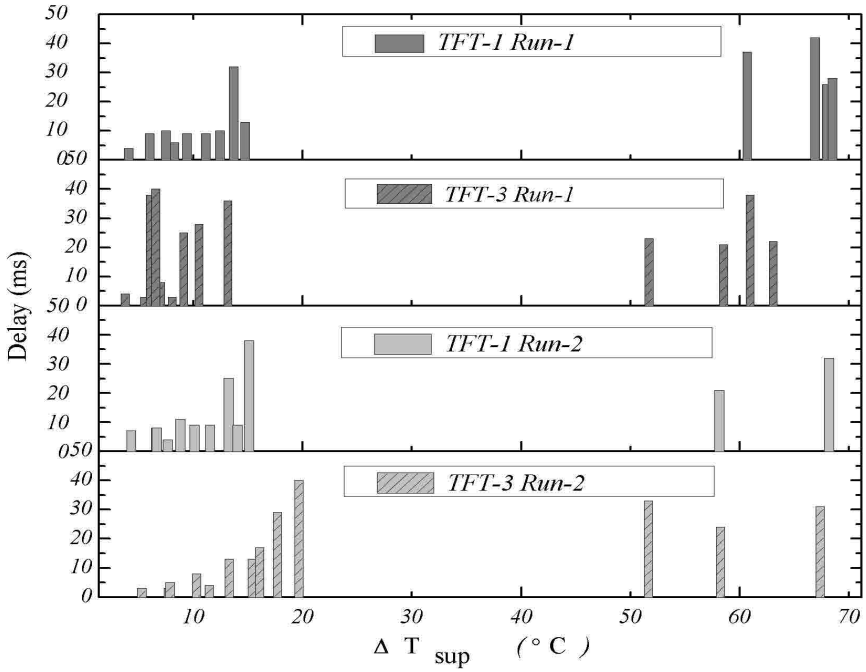

(a) Saturated pool boiling

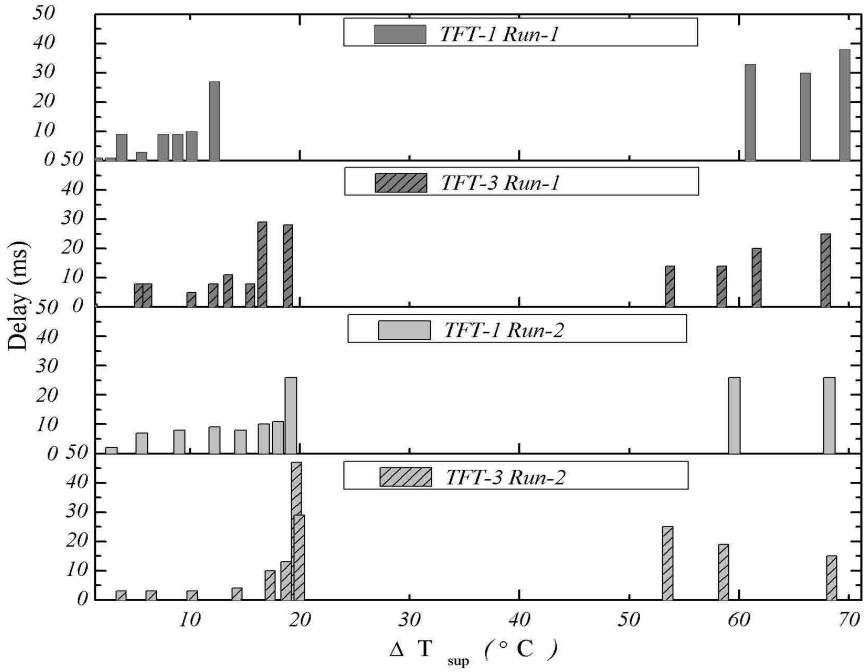

(b) 10 ℃ Subcooled

Fig. 38.: Optimal delay vs. wall superheat for all TFT and all runs before noise reduction.

for saturated pool boiling. In general, the optimal delay in FDNB, at CHF and in film boiling is greater than that near ONB and in PNB. Surface temperature recorded by TFT-3 deviated from that recorded by TFT-1 at three wall superheat conditions in FDNB. Part of this temperature difference is possibly due to differences in local nucleation characteristics. Heavy nucleation at the periphery of the wafer, resulted in occlusion of the bubble departure processes in vicinity of the TFT junctions. Therefore, the high speed camera could not be used to record the bubble departure sequence at the junctions of the TFT in FDNB. The optimal delay time for TFT-1 is similar in both runs ($\sim$ 10ms) in PNB. In FDNB, TFT-1 has an optimal delay time of $\sim$ 30ms in both runs. At CHF, the first test shows an optimal delay of $\sim$ 10ms for TFT-1 whereas in the second run it shows a delay of $\sim$ 40ms. These values correspond to the bubble cycle times in an averaged sense [128].

Figure 38(b) shows the variation of the mutual information function with wall superheat for two runs conducted at 10 ℃ subcooling. The optimal delay time increased near CHF and in film boiling. This is similar to observations in saturated pool boiling. The mutual information function increased in magnitude beyond ONB compared to its value in the convective regime for corresponding assumed delays. The mutual information function was similar in magnitude at corresponding delay times for saturated and subcooled pool boiling at different stages of the boiling curve. This is clear from figures 39(a) & 39(b). Minor differences could be due to differences in wall superheat between the two experiments.

Figure 39(a) shows the variation of the mutual information as a function of the delay for a maximum delay of 10 ms at different wall superheat levels. At low wall superheat levels (before ONB), the mutual information function had relatively low values compared to values in FDNB, near CHF and in film boiling for a given delay. Additionally, the mutual information rapidly decayed from the infinitely high

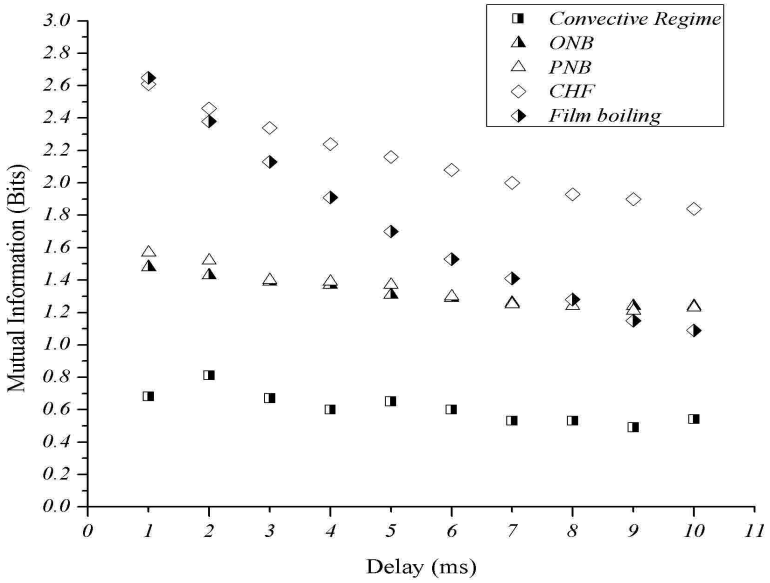

(a) Saturated pool boiling

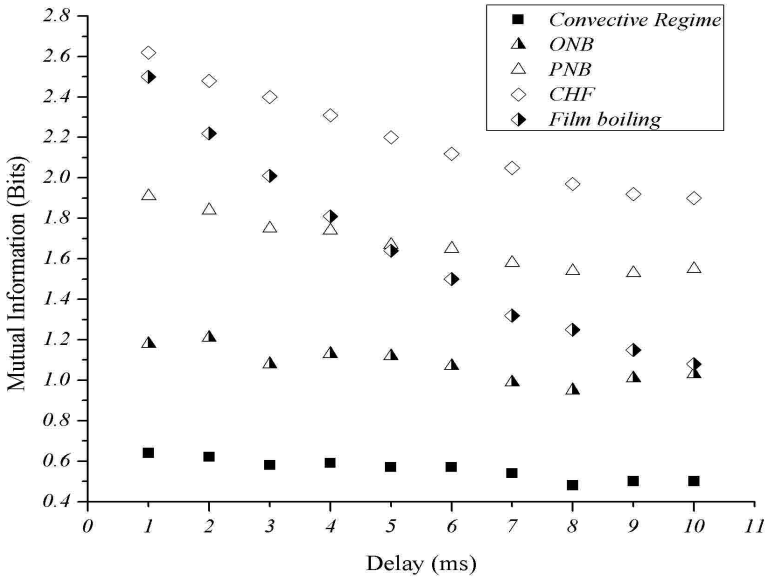

(b) 10 ℃ Subcooled

Fig. 39.: Mutual Information as a function of delay at different stages of saturated (TFT-1, Run - I) & subcooled (TFT-III, Run - I) pool boiling before noise reduction.

value corresponding to a delay of zero. This indicates, that a weak correlation exists amongst successive measurements before ONB, implying a system with a large degree of freedom i.e. a random process or alternatively, the existence of noise. The work of Banerjee and Dhir [9] indicated the presence of convective rolls within a viewing chamber of similar construction. Stable, convective, Rayleigh Benard rolls have low dimensionality ($\sim$ 3-4). However, the temperature fluctuations caused by these rolls on the test surface could not be resolved by the TFT on account of background noise [85]. Additionally, a broad band spectrum, characteristic of chaos is not observed near ONB in the real-time Fourier spectra. Thus, noise gives rise to the apparent high dimensional behavior in these regions of the pool boiling curve. However, beyond ONB, the real-time Fourier spectra show a broad banded structure with frequency span and power level at each frequency increasing with increase in wall superheat. Furthermore, beyond ONB, the mutual information is observed to increase significantly ($\sim$ 2 times) indicating a greater correlation amongst successive values i.e. the successive measurement retains some information about the previous measurement. Additionally, the decay of mutual information from zero lag to a lag of one millisecond is less steep indicating the persistence or memory of its previous state. This is indicative of predominantly deterministic processes.

4. Phase plots

Phase plots are useful in understanding system dynamics. Presence of periodic, multiply periodic and quasi-periodic dynamics can be determined from phase-plots. Additionally, in some cases, Poincaré maps can be constructed to obtain map-like models of system dynamics.

Figure 40 shows the phase plots using time-delayed variables or in the terminology of Moon [129], the pseudo-phase-space variables. The plots are generated for

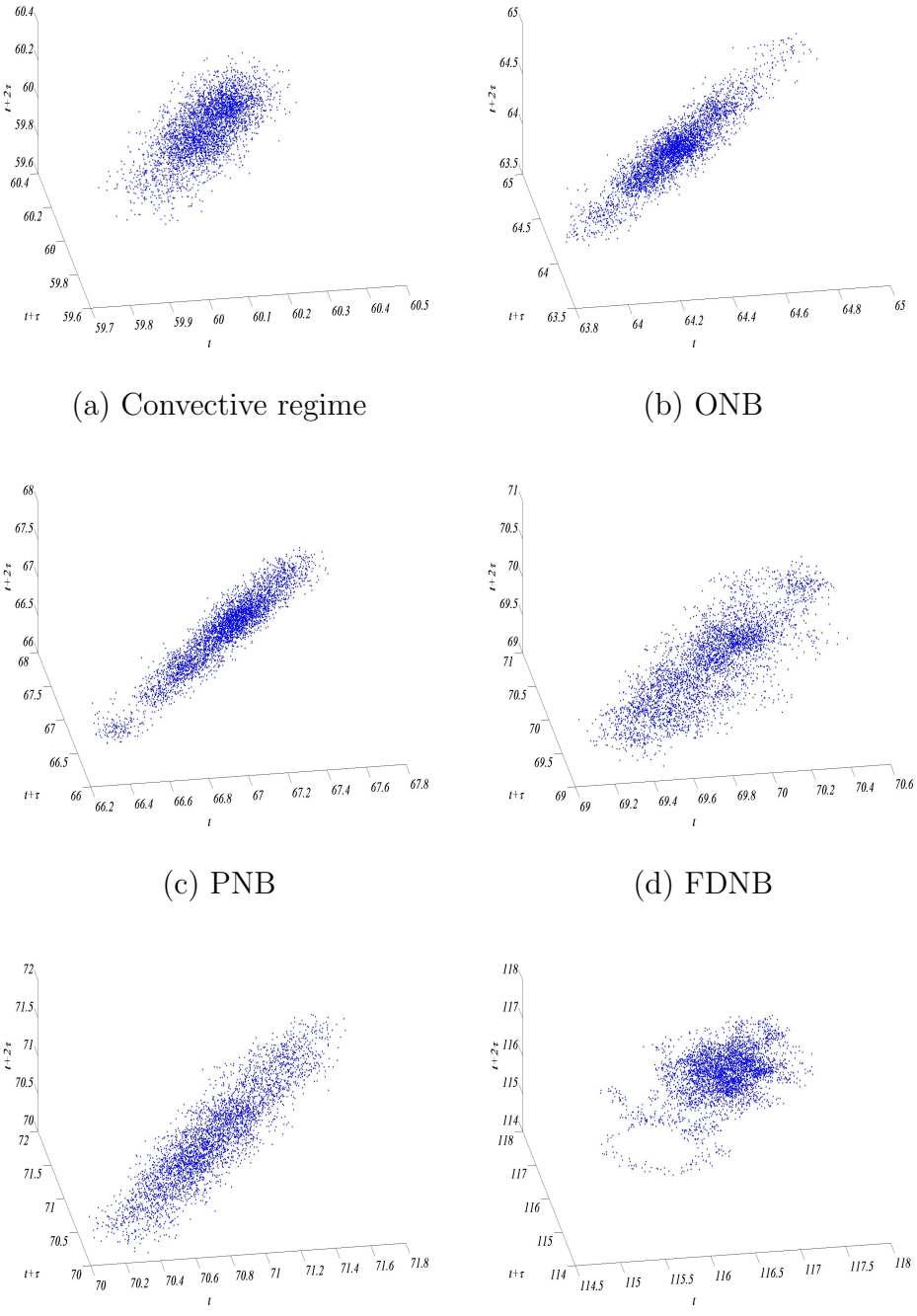

(a) Convective regime

(b) ONB

(c) PNB

(d) FDNB

(e) CHF

(f) Film Boiling

Fig. 40.: Phase plots for saturated pool boiling test-I corresponding to high frequency temperature measurements of TFT-1 before noise reduction.

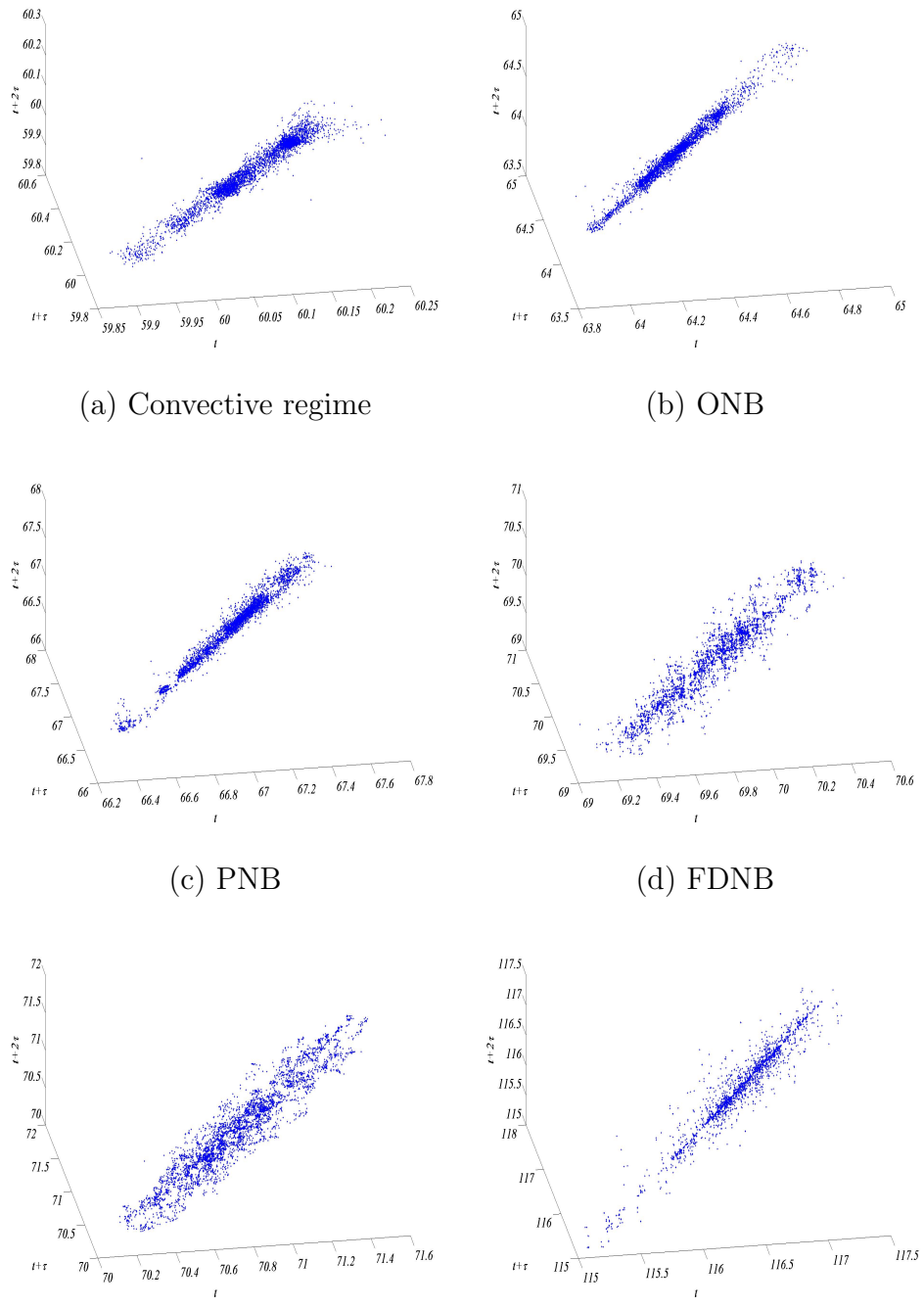

(a) Convective regime

(b) ONB

(c) PNB

(d) FDNB

(e) CHF

(f) Film Boiling

Fig. 41.: Phase plots for saturated pool boiling test-I corresponding to high frequency temperature measurements of TFT-1 after noise reduction.

saturated pool boiling based on data furnished by TFT-1 in test-I. Phase plots are shown for the convective regime, the PNB regime, the FDNB regime, at CHF and in film boiling. It is evident from figure 40(a), that the dimensionality is either too high or alternatively, significant amount of noise exists in the convective regime. As mentioned previously, stable convective rolls are present in the test fluid especially in subcooled pool boiling wherein temperature gradients of the order of $\sim$ 10 ℃ exist between the cooling coil and the test surface before inception. In saturated pool boiling, this temperature differential is of the order of $\sim$ 3 - 4 ℃ in the convective regime. Thus, convective rolls are not expected to be present. No geometric structure implying the presence of deterministic processes can be distinguished from figure 40(a). This could result from projection of a higher dimensional attractor to lower dimensions, due to the dominance of stochastic processes or due to random noise. The maximum radius of the 'attractor' is $\sim$ 0.4 along each of the three axes. In figures 40(b) and 40(c) elongated, obloid structures are observed with a rather dense 'packing' in the middle. The attractor radii are 1.2 and 1.6 respectively. The density of points is an indicator of the number of 'visits' to a particular state with the caveat that projections affect the number of 'visits'. In contrast, the structures in figures 40(d), 40(e) & 40(f) corresponding to FDNB, CHF and film-boiling show an even distribution of points with all states being visited more or less equally. The radii of these structures in these regimes are $\sim$ 1.2, $\sim$ 1.6 & $\sim$ 3 respectively. The comparatively larger size of the structure in film-boiling is due to the large fluctuations in temperature present in this regime in the window of observation. Additionally, the phase-plot in film-boiling (ref. fig. 40(f)) seems to possess a fractal geometry.

Figure 41 depicts phase plots for saturated pool boiling after noise reduction (discussed in the following section). An elongated structure is observed in the convective regime (Ref. fig. 41(a)) with a dense structure at a few locations. Similar

structures are observed in ONB and PNB (Ref. figs. 41(b) & 41(c)). At FDNB and CHF, a fractal structure is seen (Ref. fig. 41(d), 41(e)) with an even distribution of points. This indicates the possibility of deterministic chaotic dynamics. The phase plot for film boiling shown in fig. 41(f) shows a dense distribution of points about a line. However, other attractors in the film boiling regime in the same test and for the same TFT show a clear fractal structure.

Figure 42 depicts the phase plots for 10 ℃ subcooling test-I for different pool boiling regimes. The structure of the 'attractor' is not completely unfolded in three-dimensions and as a result a many self-intersections are observed. In most cases the 'attractor' if one exists, shows a wool-ball shape as observed in saturated pool boiling. However, some differences are clearly seen between the phase plots in the convective ONB regime figure 42(b) in comparison to the ones at PNB [fig. 42(c)], FDNB [fig. 42(d)], CHF [fig. 42(e)] and film-boiling [fig. 42(f)]. The structure is an ellipsoid in the convective regime, densely packed and cigar-shaped in ONB and PNB and finally spread out and more unfolded in FDNB, at CHF and film-boiling. Furthermore, the fractal structure in FDNB, at CHF and in the film-boiling regimes implies the presence of deterministic dynamics. This implies that, deterministic dynamics may be present in these regimes. Since the structure is not unfolded fully in three-dimensions at all these points, higher dimensional dynamics (≥ 4) could be present.

Figure 43 shows the phase portraits after noise reduction on the original data set. No significant change in structure is visible in the convective regime (Ref. fig. 42(a)). Points are densely distributed in a 'ball' and no other geometrical structure is discernible. A fractal geometrical structure is clearly visible in FDNB. Some fractal structures are also visible at CHF and in film boiling. Compared to the phase plots in saturated pool boiling depicted in figs. 41(d), 41(e) and 41(f), the phase plots in

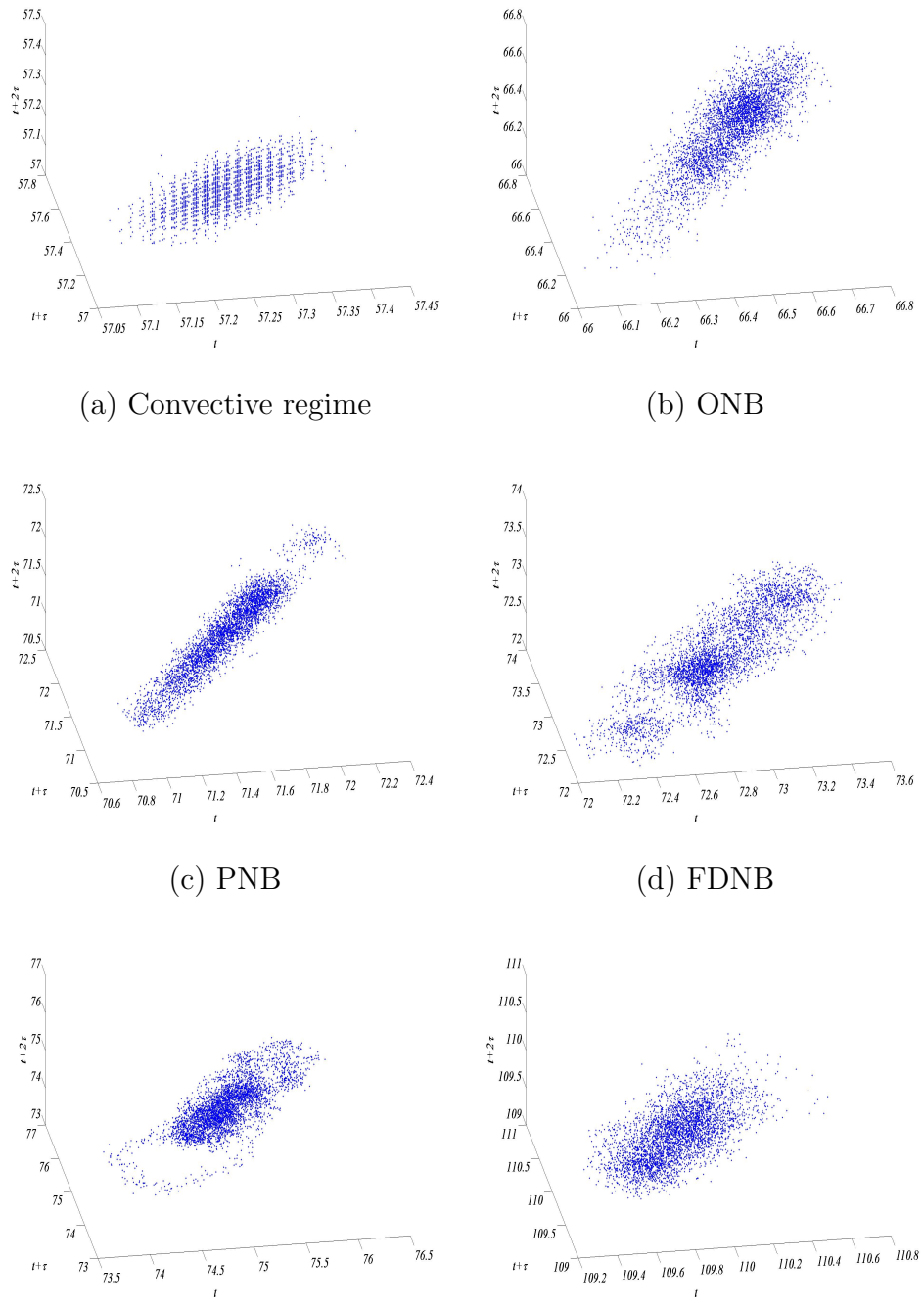

(a) Convective regime

(b) ONB

(c) PNB

(d) FDNB

(e) CHF

(f) Film Boiling

Fig. 42.: Phase plots for 10 ℃ subcooled pool boiling test-I corresponding to high frequency temperature measurements of TFT-3 before noise reduction.

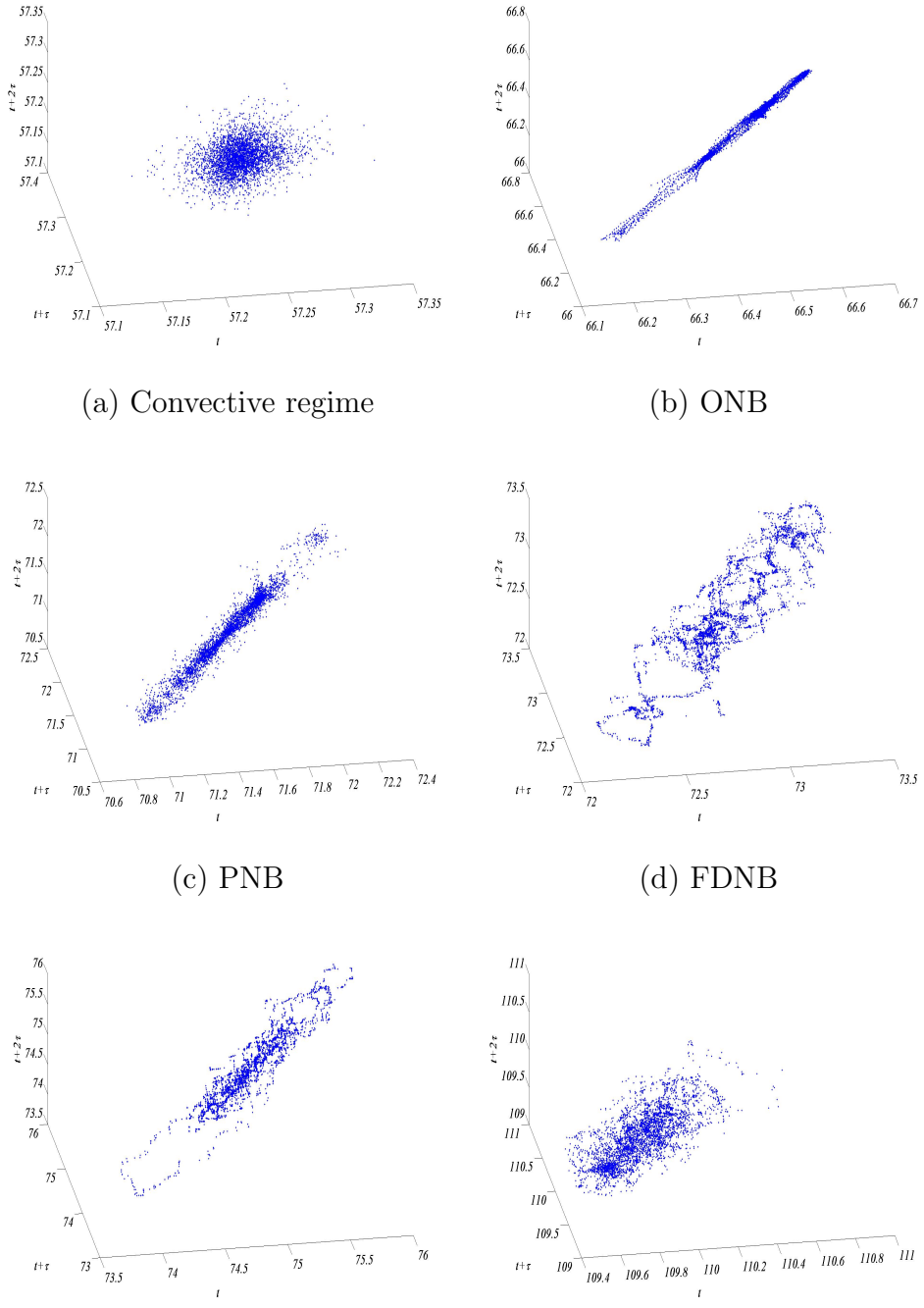

(a) Convective regime

(b) ONB

(c) PNB

(d) FDNB

(e) CHF

(f) Film Boiling

Fig. 43.: Phase plots for 10 ℃ subcooled pool boiling test-I corresponding to high frequency temperature measurements of TFT-3 after noise reduction.

subcooled pool boiling in the corresponding regimes (Ref. figs. 43(d), 43(e), 43(f)) show a more fractal structure.

5. Phase plots using singular value decomposition (SVD)

A few fractal structures could be distinguished in the phase plots depicted in the previous section. However, in most cases, structure in different directions were not clearly visible. Singular Value Decomposition (SVD), is a useful tool to determine the dominant directions of signal variation. SVD characterizes the time series in its most relevant directions in the embedding space $\Re^m$ Ref. [85]. As seen in the previous section, the phase plots do not extend significantly in certain directions. SVD computes a series of one-dimensional subspaces ordered according to their relevance. This ordering of subspaces is accomplished by computation of eigen values of the covariance matrix given below:

$$C_{ij} = \langle \mathbf{y}_i \mathbf{y}_j \rangle = \frac{1}{N-m+1} \sum_{n=1}^{N-m+1} y_{n-m+i} y_{n-m+j} \tag{5.4}$$

The covariance matrix is a real symmetric matrix possessing real eigenvalues and orthogonal eigenvectors. The eigenvalues are the squred lengths of the semi-axes of the hyper-ellipsoid fitting the cloud of data points. The corresponding eigenvectors are the direction cosines of the axes. The time-series data is projected on the first three significant eigenvectors and plotted to obtain the phase plots. The remaining eigen values are orders of magnitude smaller and therefore not considered.

Figure 44 depicts phase plots generated by SVD from temperature fluctuation data in saturated pool boiling. Clearly, no significant structure is observed in the convective regime (fig. 44(a)). At ONB and in PNB, the ellipsoidal structure (convective regime) gives way to a less 'dense' fractal structure. An increase in wall superheat results in a decrease in the 'density' of the structure. Furthermore, the form of the

attractor is seen to vary with heat flux. It is clear that the dynamics of surface temperature fluctuations vary with wall superheat in saturated pool boiling.

Figure 45 depicts phase plots generated by SVD from temperature fluctuation data in subcooled pool boiling. Again, no significant structure is observed in the convective regime (fig. 44(a)). At ONB and in PNB, the ellipsoidal structure (convective regime) gives way to a less 'dense' fractal structure. Increase in wall superheat once again results in a decrease in the 'density' of the structure. The form of the attractor is seen to vary with heat flux. It is clear that the dynamics of surface temperature fluctuations vary with wall superheat in subcooled pool boiling as well.

To summarize saturated and subcooled pool boiling have different attractor geometries. A comparison of the attractors in different regimes of pool boiling in saturated and subcooled pool boiling reveals significant differences. The attractors in subcooled pool boiling possess less dense structures compared to the structure of attractors in saturated pool boiling. Similarly, attractor geometry varies with heat flux in both saturated and subcooled pool boiling. This is indicative of a change in the dynamics of the system.

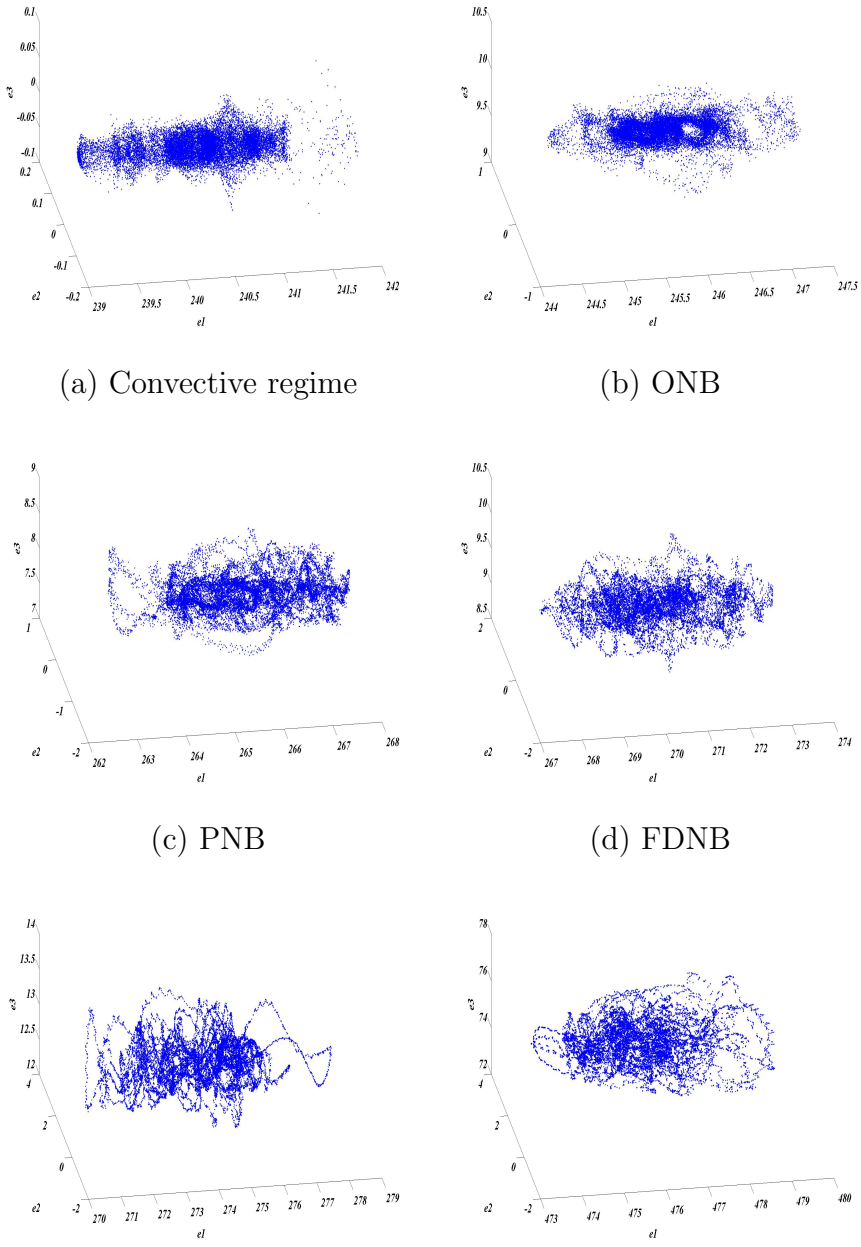

(a) Convective regime

(b) ONB

(c) PNB

(d) FDNB

(e) CHF

(f) Film Boiling

Fig. 44.: Phase plots for saturated pool boiling test-I corresponding to high frequency temperature measurements of TFT-1 after noise reduction.

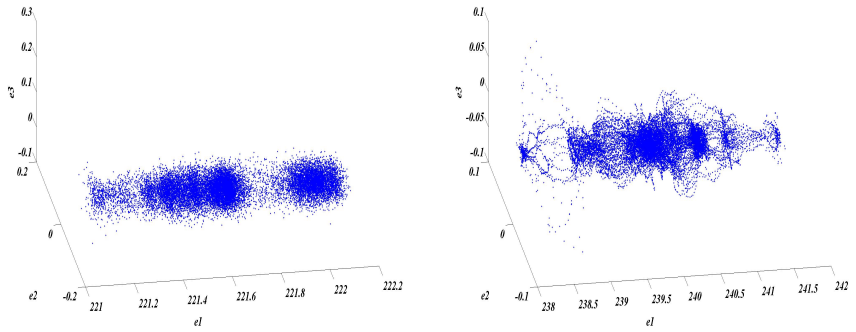

(a) Convective regime

(b) ONB

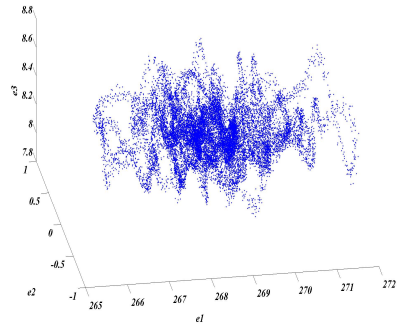

(c) PNB

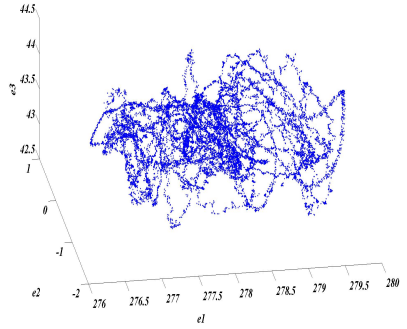

(d) FDNB

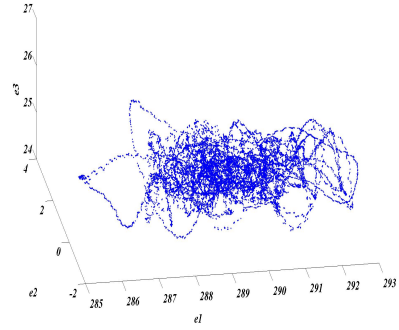

(e) CHF

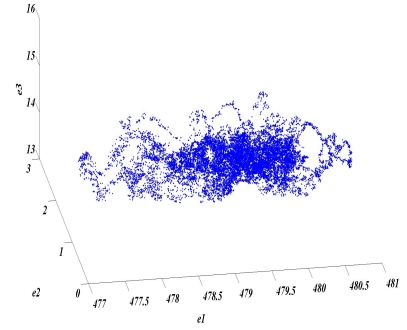

(f) Film Boiling

Fig. 45.: Phase plots for 10 ℃ subcooled pool boiling test-I corresponding to high frequency temperature measurements of TFT-3 after noise reduction.

6. Recurrence plots

Recurrence plots allow the visualization of trajectories in higher dimensional phase spaces. According to Eckmann et al. [118], recurrence plots show macro-scale/large-scale and small scale patterns which he classified as typology and texture respectively. A comprehensive account of the meaning of patterns observed in recurrence plots is given in Ref. [117]. In short, appearance of many isolated dots/homogeneity indicates the presence of random process, oscillating processes have recurrence plots with recurring diagonal lines or periodic structures oriented along the diagonal, abrupt changes cause white spaces in the recurrence plots whereas white space in the upper left and lower right corners indicates the presence of drift. Texture can be classified as single isolated-points which indicates that the state exists for a very short time either due to noise or insufficient embedding, diagonal lines which occur when parts of the trajectories are parallel with the length of the diagonals denoting the duration, vertical or horizontal lines are indicative of states that change very slowly or are stationary. The nearest neighbor criterion $\sim \epsilon$ is presently chosen by hit and trial to obtain enough neighbors. The choice of the nearest neighbor criterion is critical and is currently subject to a lot of debate. A very small value for $\sim \epsilon$ results in too few neighbors being found whereas a very large value leads to thicker, longer diagonal structures as consecutive points on the trajectory are counted as recurrences. The default scheme in the TISEAN© package uses $\epsilon \sim 0.001 \times$data interval. This value is found to be too small in this study especially in higher dimensions. Values of $\sim \epsilon$ in this study ranged from ~ 0.005 for an embedding dimension of three for the convective regime to ~ 0.1 for an embedding dimension of 10 in the film boiling regime. The artifacts associated with inappropriate neighbor search criteria (mentioned in chapter 5) are absent.

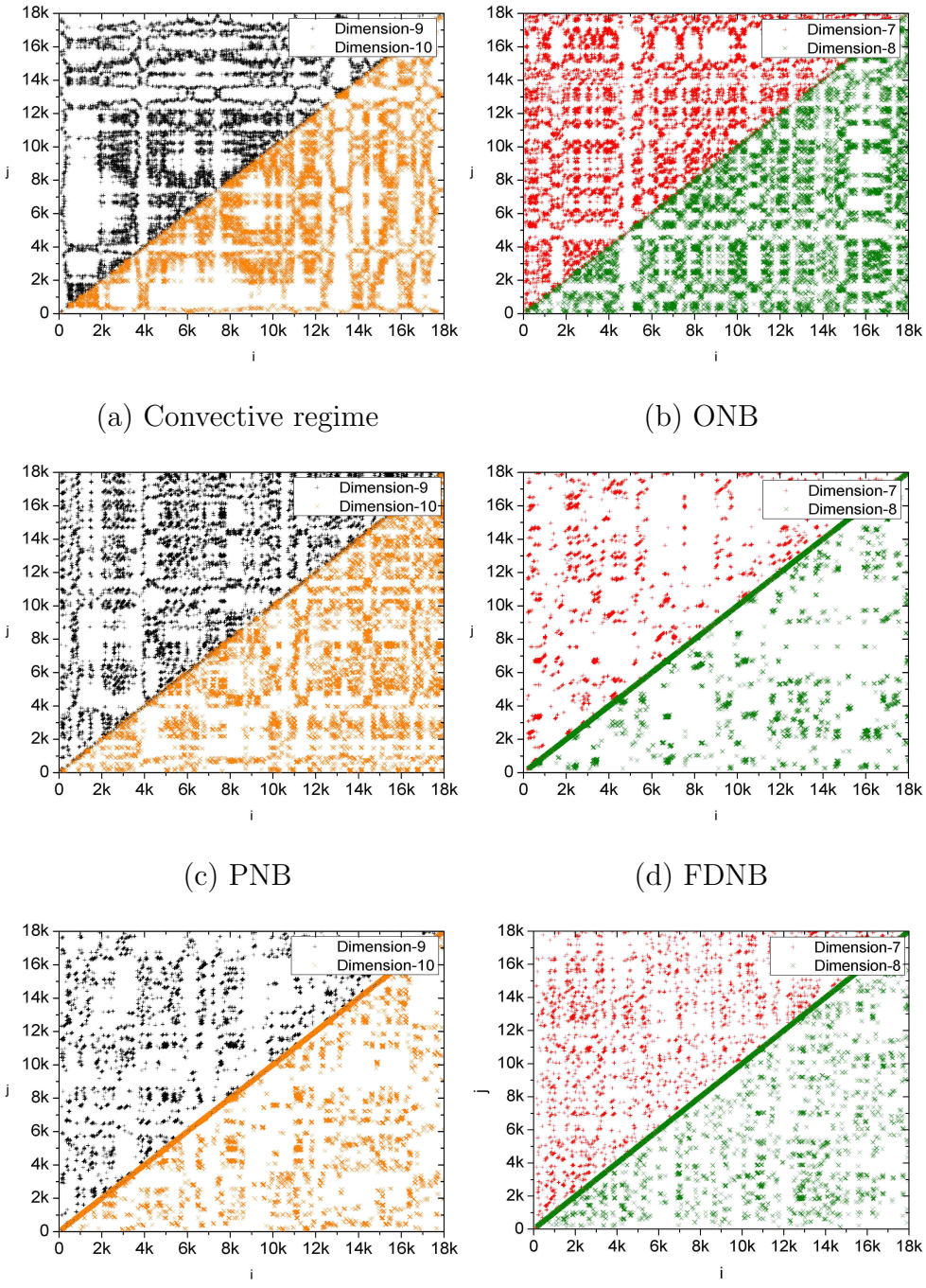

(a) Convective regime

(b) ONB

(c) PNB

(d) FDNB

(e) CHF

(f) Film Boiling

Fig. 46.: Recurrence plots at various stages of saturated pool boiling (TFT-I, Run-I) using data before noise reduction.

Figure 46 summarizes recurrence plots for saturated pool boiling before ONB, at ONB, in PNB, FDNB, CHF and film boiling regimes for the first test based on TFT-1 data. As a suitable embedding dimension is not known beforehand, the recurrence plots are generated for embedding dimensions greater than or equal to three. Usually, embedding dimensions of 3, 6, 7, 8, 9 & 10 are employed. However, in some cases within the film boiling regime, recurrence plots are generated for embedding dimensions of 3, 4, 5, 6, 7 and 8. The reason for this is the sparsity of patterns at higher dimensions. Figure 46(a), shows the recurrence plots for the first steady-state data-point ($T_{wall} \sim 60$ ℃) on the saturated pool boiling curve for embedding dimensions of 9 and 10. Short lines parallel to the main diagonal are not observed for long durations despite the high embedding dimension. Many isolated points are seen indicating that the process involves a significant noise component/false neighbors due to insufficient embedding. Since, Banerjee and Dhir [9] showed the presence of stable convective rolls, phase turbulence is ruled out. Hence the system cannot be high dimensional in the convective regime. Therefore, it is inferred that the isolated points occur due to a large noise component. Furthermore, a significant amount of white spaces are seen indicating the presence of abrupt changes in dynamics. Many horizontal and vertical lines exist in the recurrence plot shown in figure 46(a), indicating states that remain stationary or change very slowly. Any determinism is masked by high frequency noise. Thus, in the convective regime, noise masks the presence of any deterministic dynamics. States change very slowly with time in the convective regime and there are some states that are not visited i.e. abrupt jumps occur in the dynamics.

Figure 46(b) depicts the recurrence plot for embedding dimensions of 7 and 8 corresponding to ONB ($T_{wall} \sim 63$ ℃). Several short parallel lines exist alongwith many isolated points. The distance between the diagonal lines isn't fixed thus in-

dicating the process may be quasi-periodic or chaotic. The process is most likely chaotic as the lines are short and are located in the vicinity of isolated points. Thus, weak determinism could exist alongwith a noise-component near ONB. Figure 46(c) shows the recurrence plot in PNB. Few isolated points exist and most points form short parallel lines parallel to the diagonal indicating the presence of deterministic dynamics.

Figure 46(c) depicts the recurrence plot for embedding dimensions of 9 and 10 corresponding to PNB. Short lines parallel to the main diagonal are observed alongwith a few isolated points. The dynamics, thus seems to be deterministic and possibly chaotic. Figure 46(d) depicts the recurrence plot for saturated pool boiling in the FDNB regime for embedding dimensions of 7 and 8. Many short lines parallel to the main diagonal with non-constant spacing (in the vertical direction) are observed in addition to isolated data points hinting at the presence of chaotic dynamics. Similar trends are seen in figures 46(e) & figures 46(f) which show the recurrence plots at CHF and in the film boiling regimes.

Figure 47 summarizes recurrence plots for TFT-1 for the second 10 ℃ subcooled run. Isolated dots are present in the convective regime indicating the presence of noise. White patches in the figure indicate states that are not visited. In addition, the presence of horizontal and vertical lines indicates the presence of stationary/slowly varying states. Many isolated points are present indicating the dominance of noise. A similar scenario exists in the recurrence plot near ONB shown in Figure 47(b). A checkerboard pattern is observed with many horizontally and vertically aligned points in 9 and 10 embedding dimensions. This indicates a strong correlation between points or a very slowly varying process. Figure 47(c) shows a band merging type-scenario with many small diagonal lines alongwith a few checkerboard patterns although these are not very clear. In addition, presence of isolated points and horizontally and

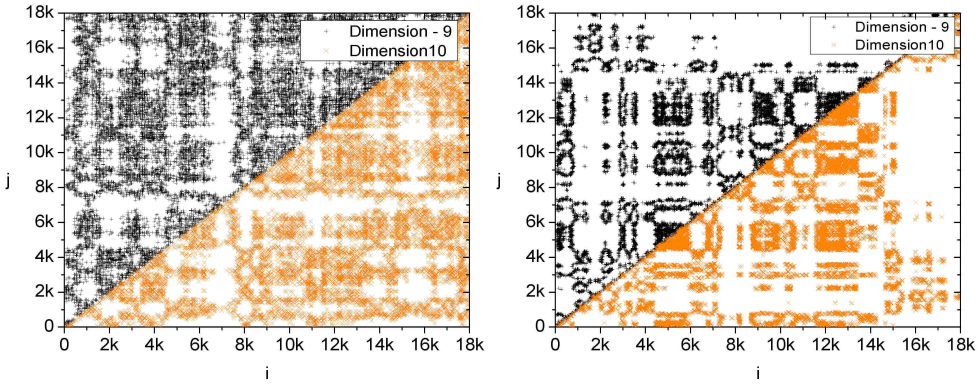

(a) Convective regime

(b) ONB

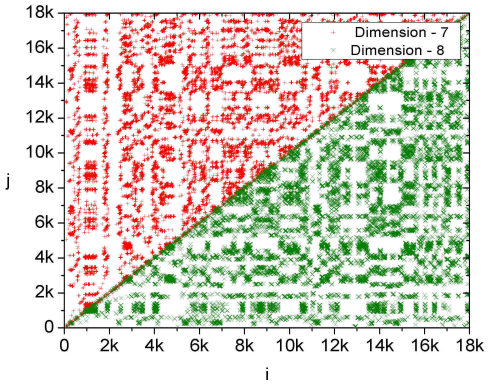

(c) PNB

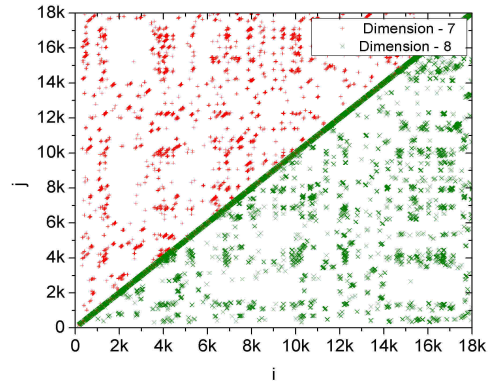

(d) FDNB

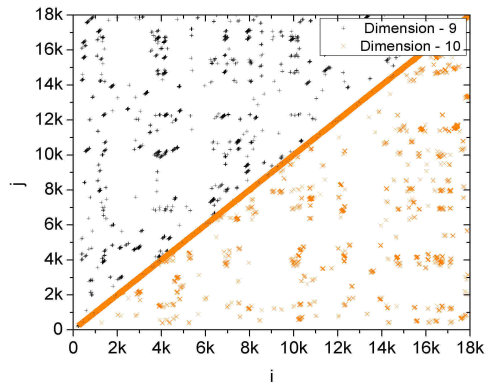

(e) CHF

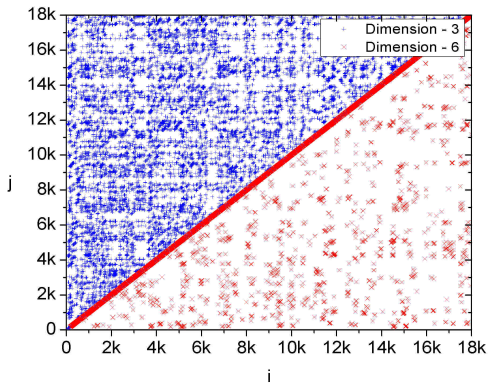

(f) Film Boiling

Fig. 47.: Recurrence plots at various stages of 10 ℃ subcooled pool boiling using data before noise reduction

vertically aligned points are seen indicating the presence of noise and a few slowly varying states. In figures 47(d) & 47(e), many short lines parallel to the main diagonal is seen. This indicated the presence of deterministic dynamics, possibly chaotic. Similar trends, in the form of short parallel lines are seen for embedding dimensions of 3 and 6 in the film boiling regime.

7. False nearest neighbors

False nearest neighbors test is conducted to determine suitable embedding dimensions for attractor reconstruction. As discussed in the previous chapter, the projection of an attractor onto a lower dimension results in the appearance of many false neighbors. As the embedding dimension is increased, the number of false neighbors decreases until it reaches a value close to zero for $D_E \geq 2D_A+1$, where, D_E is the embedding phase space dimension and D_A is the (unknown) attractor dimension. Therefore, the false nearest neighbor test gives an estimate of the attractor dimension.

Figure 48 depicts the fraction of false nearest neighbors at various points on the saturated pool boiling curve. The false nearest neighbors test also serves as a measure of the strength of noise. In the presence of a small amount of noise, a few false neighbors are always present irrespective of the embedding dimension chosen. However, in this case a rapid drop in the fraction of false nearest neighbors is observed from a fraction of ~ 1 corresponding to an embedding dimension of 1 to a value $\ll 0.1$ for embedding dimensions exceeding the actual dimension of the attractor.

In the presence of large amount of noise, however, the fraction of false neighbors initially decreases with increase in embedding dimension and then begins to increase. This is clearly seen in figure 48(a) where effects of noise and lack of sufficient neighbors cause severe fluctuations in the percentage of false nearest neighbors. Additionally, it is observed that the noise level for a threshold f ~ 2 is about 30% for an embedding

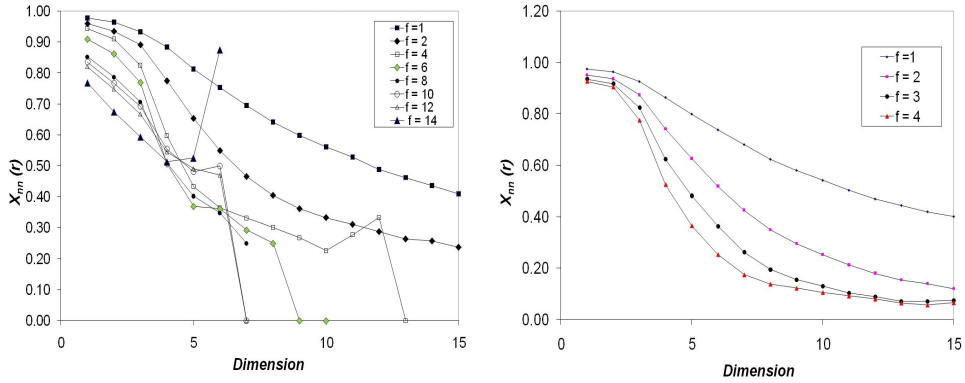

(a) Convective regime

(b) ONB

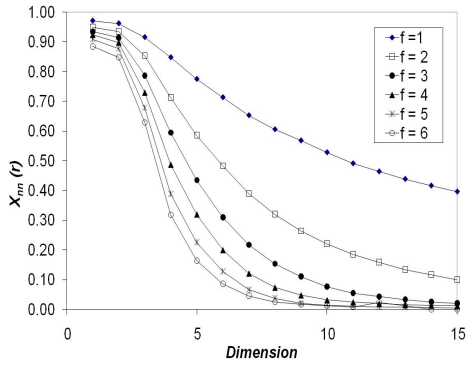

(c) PNB

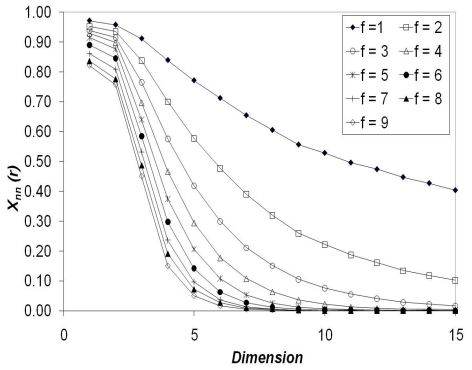

(d) FDNB

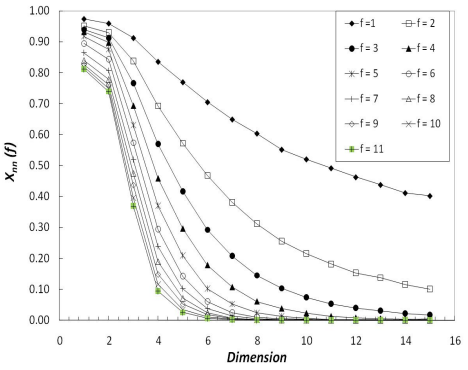

(e) CHF

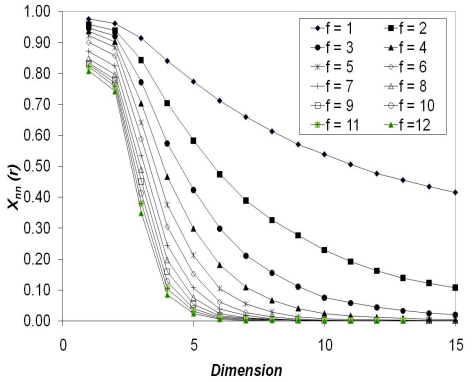

(f) Film Boiling

Fig. 48.: False nearest neighbors in saturated pool boiling test - I, TFT - I, before noise reduction.

dimension as high as 15. This points to the dominance of noise in the signals in the convective regime. An increase in the factor 'f' causes a decrease in the threshold. As the dimension increases and the 'f' value decreases, a point is reached where neighbors are absent or too few leading to the fluctuations seen in figure 48(a). The few neighbors present in this scenario is an artifact of noise rather than dynamics.

Near ONB, the fraction of false neighbors is $\sim$ 10 % for ratio factors 'f' of 3 and 4. At higher wall superheats, corresponding to PNB, FDNB, CHF and film-boiling, the fraction of false neighbors is of the order of 0.01 or lower for a ratio factor of 12. Thus, the dominance of noise in the signals decrease with an increase in the wall superheat. In FDNB, CHF and film boiling, the fraction of nearest neighbors drops to nearly zero for embedding dimensions of 7 - 9. This indicates, that the attractor has a dimension of $\sim$ 3 - 4 in FDNB, at CHF and in film-boiling. Similar trends are observed for 10 ℃ subcooling.

8. Theiler windows & correlation dimensions

Figure 49 depicts space-time separation plots for the second 10 ℃ subcooled run corresponding to TFT-I for an embedding dimension of five. The calculations are performed in TISEAN© using the 'stp' command with suitable choices for delay and embedding dimension for a total time of 500 steps. The space-time separation plots were also determined for embedding dimensions of three, ten and fifteen. The trends in the plots did not vary with the choice of embedding dimensions. The space-time separation plot is useful in determining the presence of temporal correlations in the time-series data and in ascertaining the presence of stochastic signals. Temporal correlations in data can lead to low dimension estimates using the correlation sum. The problem of temporal correlations can be addressed using a suitable 'Theiler' window. The Theiler window estimates the time period or time-window within which

the time-series data is correlated. Pairs with temporal distances less than this time is excluded from the correlation sum. Presence of temporal correlations in the data leads to a temporal dependence of the probability that the distance between a pair of points is less than a threshold ϵ apart from the threshold itself.

Figure 49 shows contour plots at various wall superheats . Each contour depicts the distance ϵ within which a certain fraction (denoted by the contour level) of pairs are found for a fixed temporal separation. Saturation of the contours (i.e. 'levelling-off' of the contours) indicates the absence of temporal correlations. In case of 1/f noise or short data sets, the space-time separation plots do not saturate. Absence of saturation indicates the dominance of noise and any determinism is therefore weak. This effect is clearly present in the convective regime and near ONB. Additionally, in the convective regime, persistent periodicities ($\sim$ 15 ms period) are present. These periodicities correspond to a frequency of 67 Hz which is very close to the 60 Hz A.C. noise. The periodicities present in this regime are attributed to the dominant A.C. noise which arises due to low SNR (Signal to Noise Ratio). However, with increase in the wall temperature, the curves saturate indicating little or no temporal correlations above the Theiler window. Additionally, the periodicities present in the convective regime are not observed due to the higher SNR. The Theiler window varies with the wall temperature in the nucleate boiling regime but is approximately constant in the film-boiling regime. These trends are consistent in all experimental runs. The space-time separation plots clearly show the dominance of stochastic processes in the convective and ONB regimes. In partial nucleate boiling, saturation is observed especially at high wall superheat levels. FDNB, CHF and film boiling clearly, show a saturation in the contours, indicating the dominance of deterministic processes. Additionally, both ONB and the convective regimes show the presence of periodicities which persists for a long time. The source of these periodicities is unclear. They may

be a result of the noise present in the system or due to formation and departure of bubbles at ONB.

Figure 50 depicts the variation of the correlation sum C(ϵ, m) with the space-scale ϵ for different embedding dimensions 'm', plotted on a log-log scale. Each figure corresponds to a different steady state point on the pool boiling curve. The figure depicts the variation of correlation dimension only for some key points on the boiling curve for the first saturation run. Figure 50(a) shows the variation of the correlation sum with space-scale for the convective regime on the saturated pool boiling curve. The curves for various embedding dimensions show oscillations. Oscillations in the correlation sum plots are often the result of 'lacunarity' [120]. Lacunarity has been suggested as a means of estimating the 'fractality' of fractal sets [120]. Lacunarity was first introduced in [130] as an attempt to quantify the texture of a fractal alongwith other terms such as succolarity. Lacunarity is an indicator of the presence of large gaps in a fractal. Thus, two fractals with same fractal dimensions and topology can have different lacunarity. Few methods have been suggested to measure 'lacunarity' in literature however, discrepancies exist regarding their validity. The presence of oscillations makes the accurate determination of slopes on the log-log plot difficult. A line may be fit encompassing many points to minimize the effect of the oscillations. However, in such a case, any attempt to compute dimensions based on the local slopes as advocated in [85] is nullified as a suitable convergence will not be obtained. Therefore, in all cases, dimensions have been estimated using a best-fit line. In some cases, especially near CHF and in film-boiling, these oscillations are not very prominent. However, in these regimes, large fluctuations are observed in the plot of local slopes making accurate estimation of a dimension very difficult. Additionally, all experimental plots of the correlation sum vs. space scale are limited by the effects of noise at very small space scales and by the lack of neighbors further down the

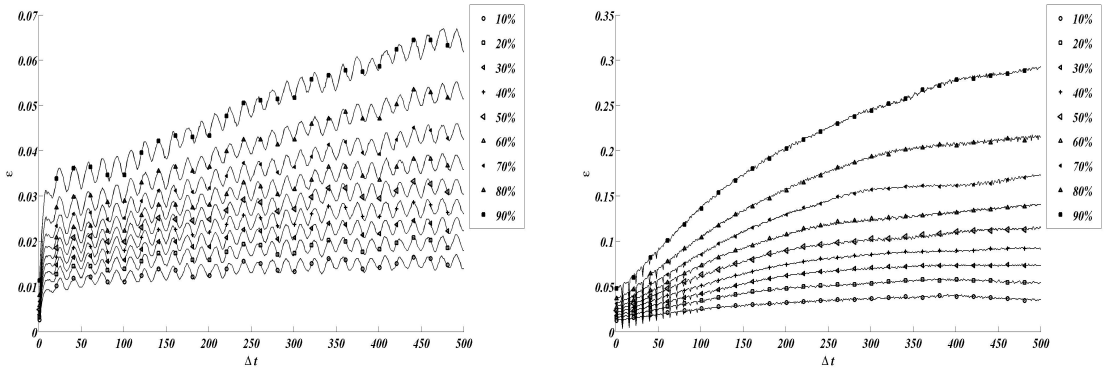

(a) Convective regime

(b) ONB

(c) PNB

(d) FDNB

(e) CHF

(f) Film Boiling

Fig. 49.: Space-time separation plot for an embedding dimension of 5, in 10 ℃ sub-cooled pool boiling test-II, TFT-1, at various wall superheat levels after noise reduction.

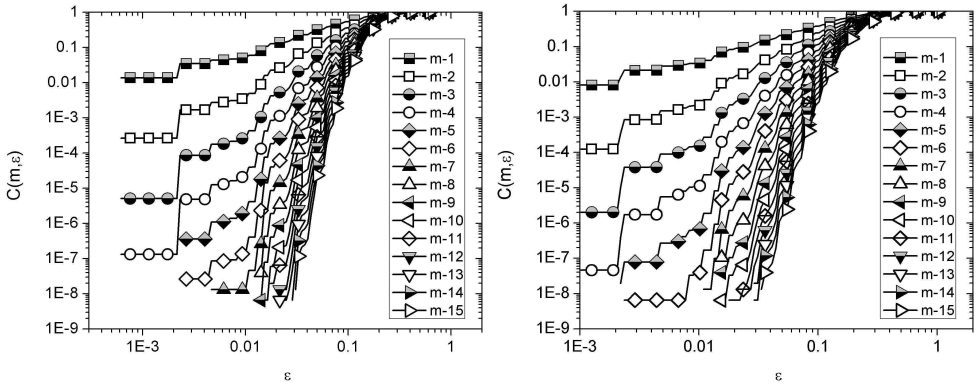

(a) Convective regime

(b) ONB

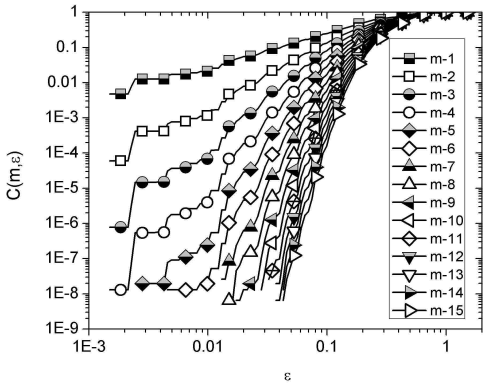

(c) PNB

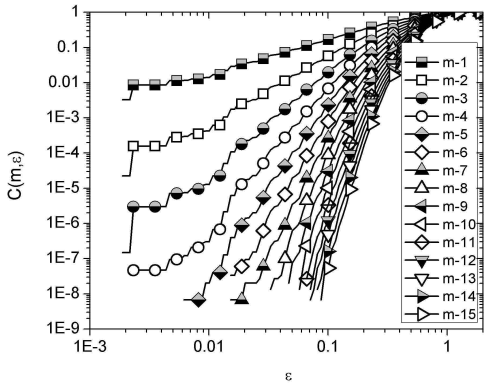

(d) FDNB

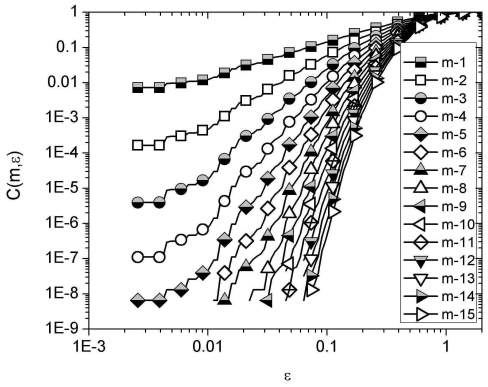

(e) CHF

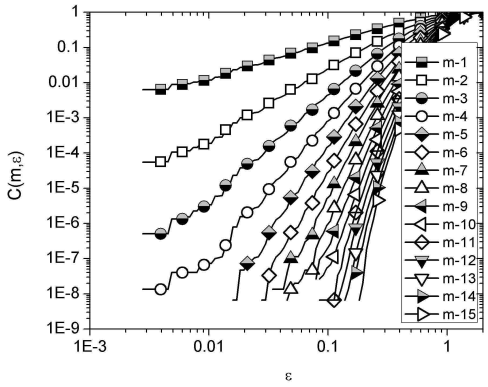

(f) Film Boiling

Fig. 50.: Correlation sum vs. space scale for various embedding dimensions in saturated pool boiling test - I, TFT-1 before noise reduction.

scale. Higher up in the space-scale, the finite radius of the attractor destroys the scaling behavior. A scaling range may be found between these two extremes if the slopes of the log-log plot plateau. Figures 50(a) & 50(b) shows the effects of noise for scales below ~ 0.002 for embedding dimensions less than six. For dimensions greater than or equal to six, the effects of noise is confined to scales below ~ 0.02. Any scaling behavior is therefore confined between 0.02 and 0.1. Figure 50(c) & 50(d) show the variation of the correlation sum with space scale for PNB and FDNB. The effects of lacunarity are not seen in FDNB for higher embedding dimensions ($m \geq 12$). Some oscillations however, seen in figure 50(c). Some effects of lacunarity are seen in figures 50(e) & 50(f) for embedding dimensions less than 10. Some saturation in slopes is also seen for the FDNB, CHF and film boiling regimes. At higher embedding dimensions, there is a lack of neighbors at smaller space scales leading to oscillations. Figure 51 depicts the plot of local slopes for saturated pool boiling test-I for various embedding dimensions. As seen in figure 51(a), strong oscillations exist below a space-scale of 0.2 making it difficult to estimate a dimension. Some saturation is seen above an embedding dimension of 5. However, the presence of oscillations makes the estimation of dimension difficult. The effects of noise and lack of neighbors seems to appear for space scales below ~ 0.07. These effects are also observed in figure 51(b). In PNB and FDNB, the oscillations are less severe and saturation of the curves are observed above embedding dimensions of 5 although no plateau is seen. In figures 51(e) and 51(f), minor oscillations are seen to exist in the local slopes. The plot of correlation dimensions vs. space scale is shown in figure 52. Oscillations occur in the correlation sum in figure 52(a) possibly due to lacunarity. Effects of noise and limited resolution are seen at space-scales below 0.03. Similar oscillations are also seen in other regimes possibly indicating the fractal nature of the attractors. The amplitude of oscillations is seen to decrease with increase in

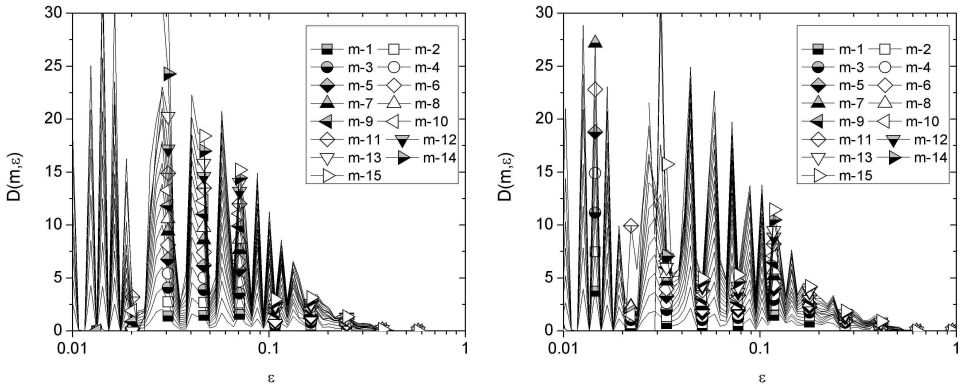

(a) Convective regime (b) ONB

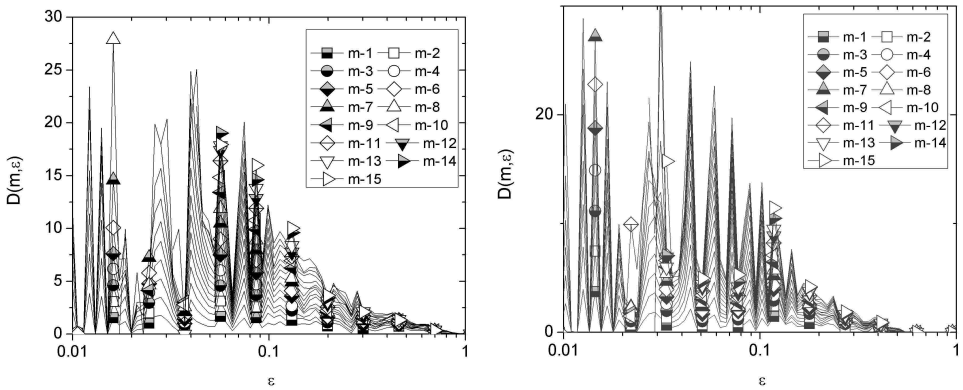

(c) PNB (d) FDNB

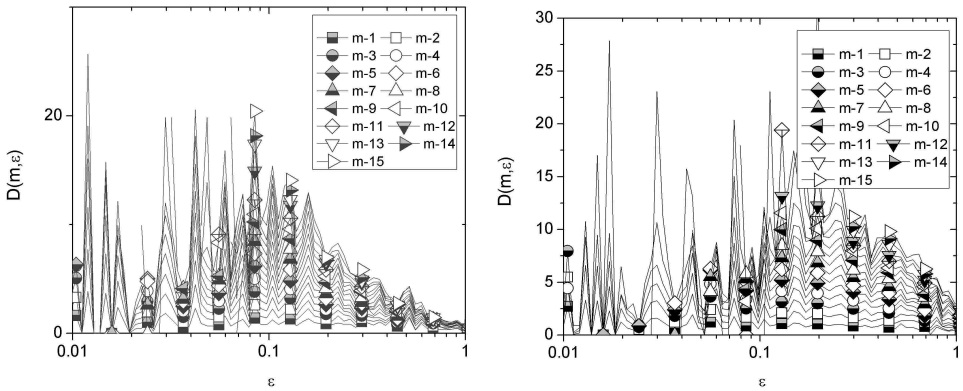

(e) CHF (f) Film Boiling

Fig. 51.: Local slopes of correlation sum vs. space scale for various embedding dimensions in saturated pool boiling test - I, TFT-1, before noise reduction.

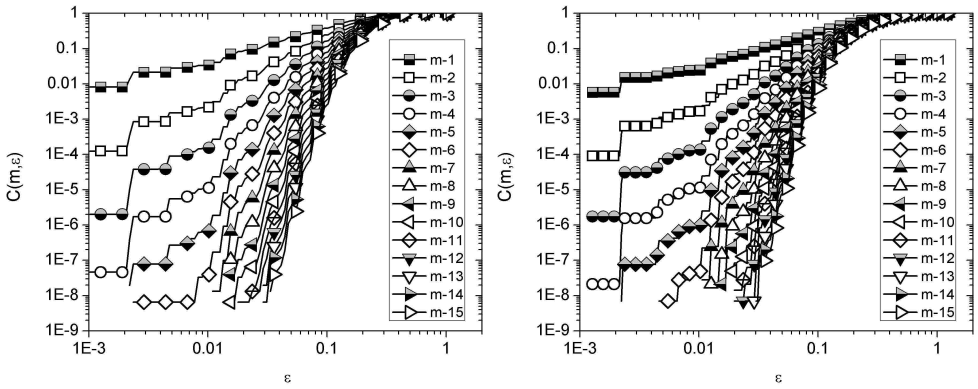

(a) Convective regime

(b) ONB

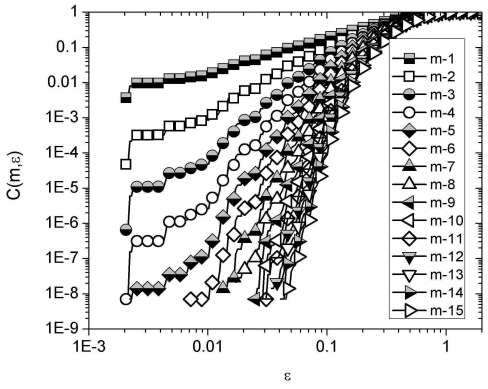

(c) PNB

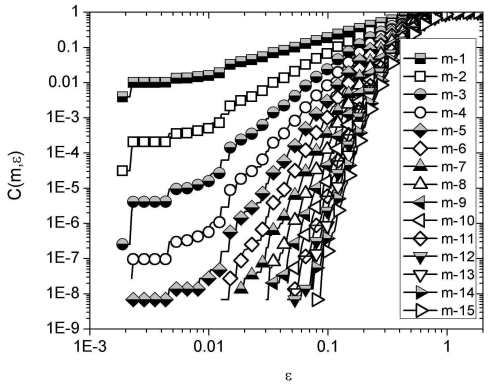

(d) FDNB

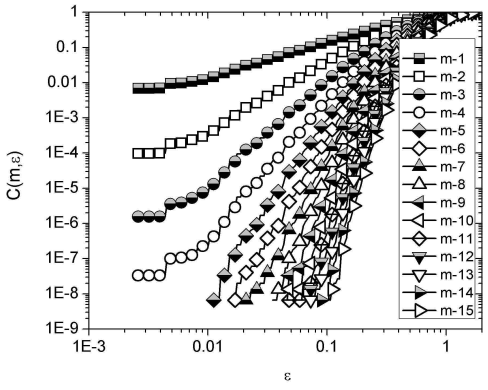

(e) CHF

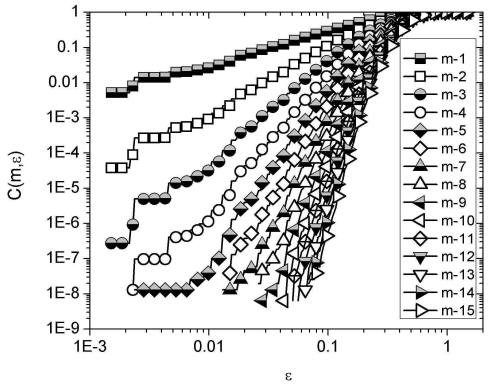

(f) Film Boiling

Fig. 52.: Correlation sum vs. space scale (TFT-3) for various embedding dimensions in 10 ℃ subcooled pool boiling test - I, TFT-3 before noise reduction.

wall superheat. Additionally, saturation of slopes of the correlation sum is observed especially at CHF and in the film boiling regime. Figure 53 shows the variation of correlation 'dimension' along the entire saturated pool boiling curve. It must be noted that the slope of the correlation sum vs. space-scale graph did not saturate/plateau often due to the effect of lacunarity and noise. Presence of noise results in a bias of the correlation dimension estimates to higher values. The values of 'dimensions' presented in the graph above may thus be taken as a representative upper-bound of the correlation dimension. Lack of adequate saturation in the slopes of the correlation sum vs. space-scale plots precludes the assignment of a dimension. However, at some points along the boiling curve especially in FDNB, at the CHF and in the film-boiling regime, saturation of slopes are observed. The assignment of a correlation dimension to these points is appropriate. Differences are seen in the dimensions shown by TFT-1 and 3 within a single test. This could stem from many factors, for e.g.:

1. differences in the geometry of local attractors due to spatio-temporal chaos
2. differences in the noise levels,
3. differences in resolution of the two TFT

Similarly, differences are seen in the correlation dimension values between two runs for TFT-1 and TFT-3 respectively. This could be because of the variation of the structure of the attractor between runs, due to differences in noise levels and due to minor differences in the initial and boundary conditions present in any experiment. Figure 54 depicts the variation of correlation dimensions along the entire 10 ℃ pool boiling curve. There are differences in the dimensionality shown by the TFT within a given run and for a given TFT between runs. The variations in the attractors between runs are due to the differences in the location and number of active nucleation sites

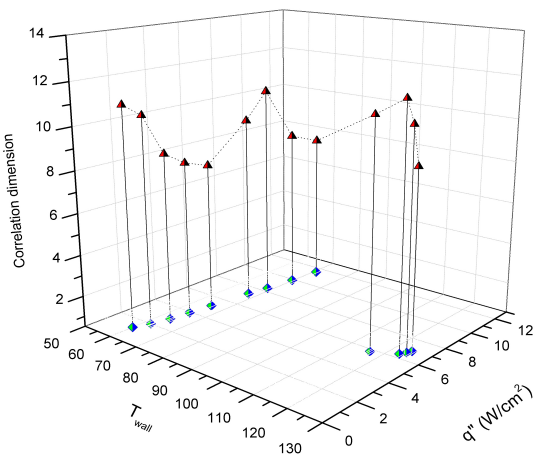

(a) TFT-1 Test-I

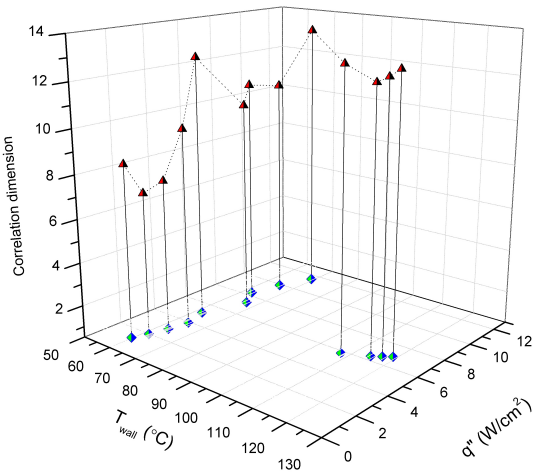

(b) TFT-3 Test-I

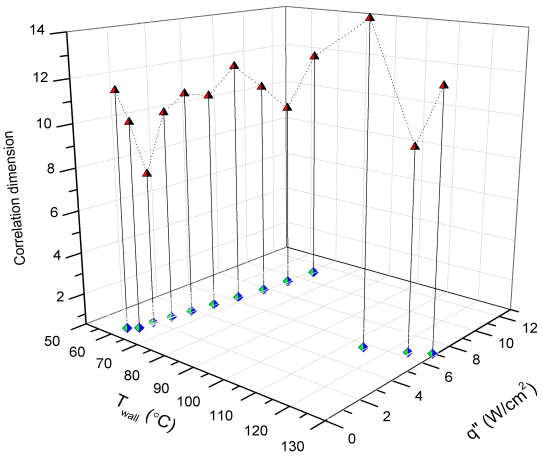

(c) TFT-1 Test-II

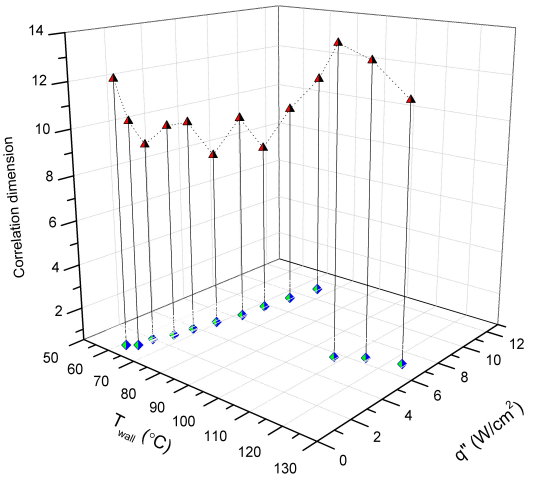

(d) TFT-3 Test-II

Fig. 53.: Variation of correlation dimensions along the saturated pool boiling curve in Tests I & II for TFT-1, 3, before noise reduction.

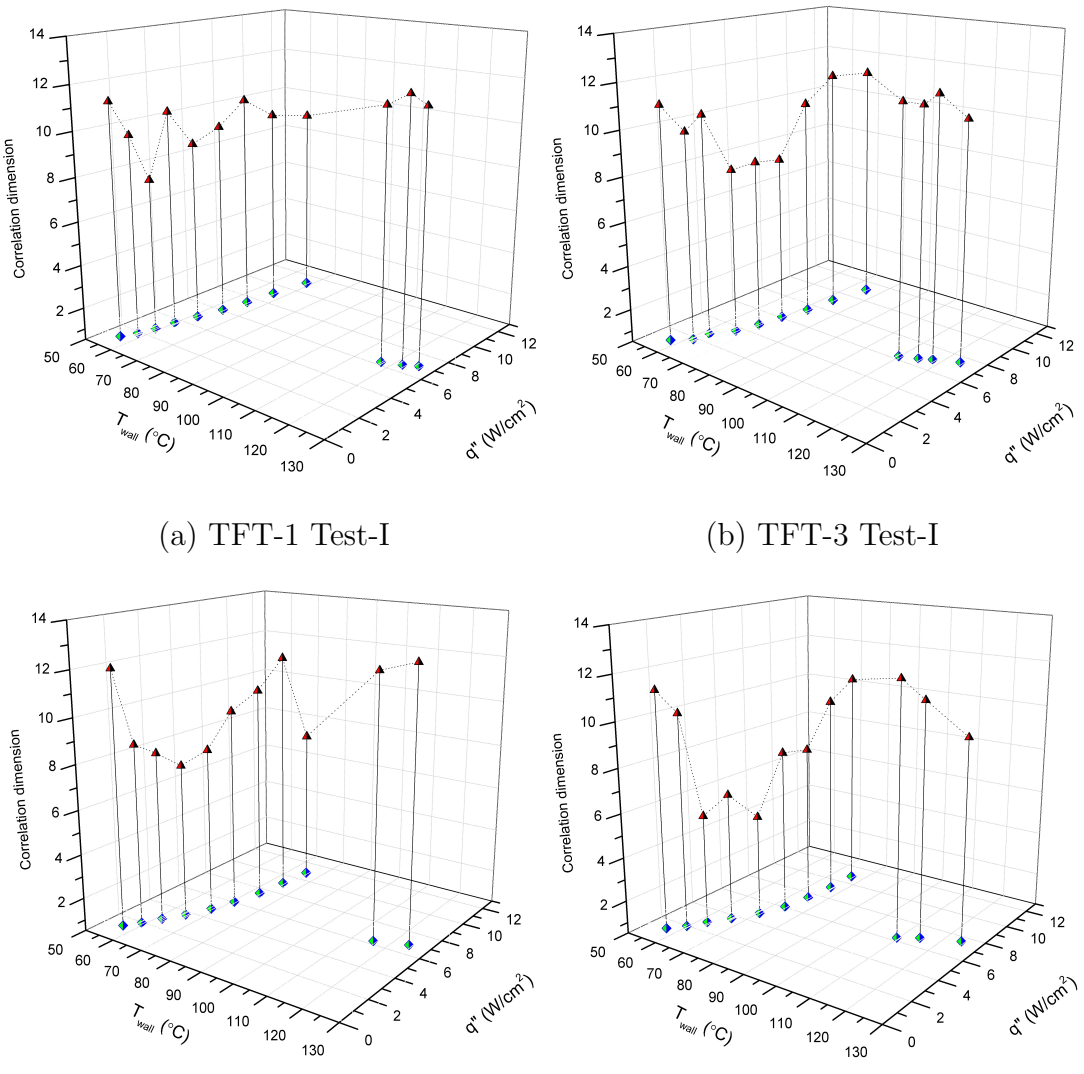

(a) TFT-1 Test-I

(b) TFT-3 Test-I

(c) TFT-1 Test-II

(d) TFT-3 Test-II

Fig. 54.: Variation of correlation dimensions along the 10 ℃ subcooled pool boiling curve in Tests I & II for TFT-1, 3 before noise reduction.

on the test surface. The variation in nucleation site activity results in differences in temperature and velocity in the vicinity of the TFT sensing junction. Bubble departure from a single cavity is known to proceed to chaos through bifurcations [56]. In the presence of multiple cavities, the on-off behavior coupled with the bifurcation of the bubble departure process plays a crucial role. Different sites could be activated or deactivated in each run causing a variation in the local dynamics leading to variations in the structure of the attractor. Additionally, noise could be playing a major role especially at smaller scales.

Figures 55, 56 depicts the variation of the correlation dimension along the pool boiling curve in saturated and subcooled pool boiling cases. In both cases, the slopes of the log of the correlation sum vs. space-scale are not linear for any range of space-scales in the convective regime, near ONB and in PNB. However, in FDNB, at CHF and in film-boiling linear variation is observed over a range of space-scales in the log-log plot of correlation sum vs. space scale alongwith a clear saturation in the slopes. Therefore, a correlation dimension can be assigned to points in FDNB, at CHF and in some of the film boiling points. In 10 ℃ subcooled pool boiling, the correlation dimension in FDNB is 6.59 and at the CHF it is 5.3. In film boiling the correlation dimension ranges from 6.48 at the Leidenfrost point to 7.67 at a wall temperature of 123.9 ℃. However, a clear scaling region is not present in the correlation sum vs. space scale plots for all film boiling points for all test runs. This may be a result of the limited dataset size and noise within the system. Furthermore, the embedding delay may not be optimal. The use of a constant delay time for all higher dimensional lagged vectors may result in sub-optimal embedding. This can also be inferred from the phase plots. In some cases, the delay vectors are observed to be very close to the principal diagonal (Ref. Fig. 41) of the pseudo-phase space. In saturated pool boiling, the correlation dimension in FDNB is 3.38 and is 4.8 at CHF. In film boiling, the

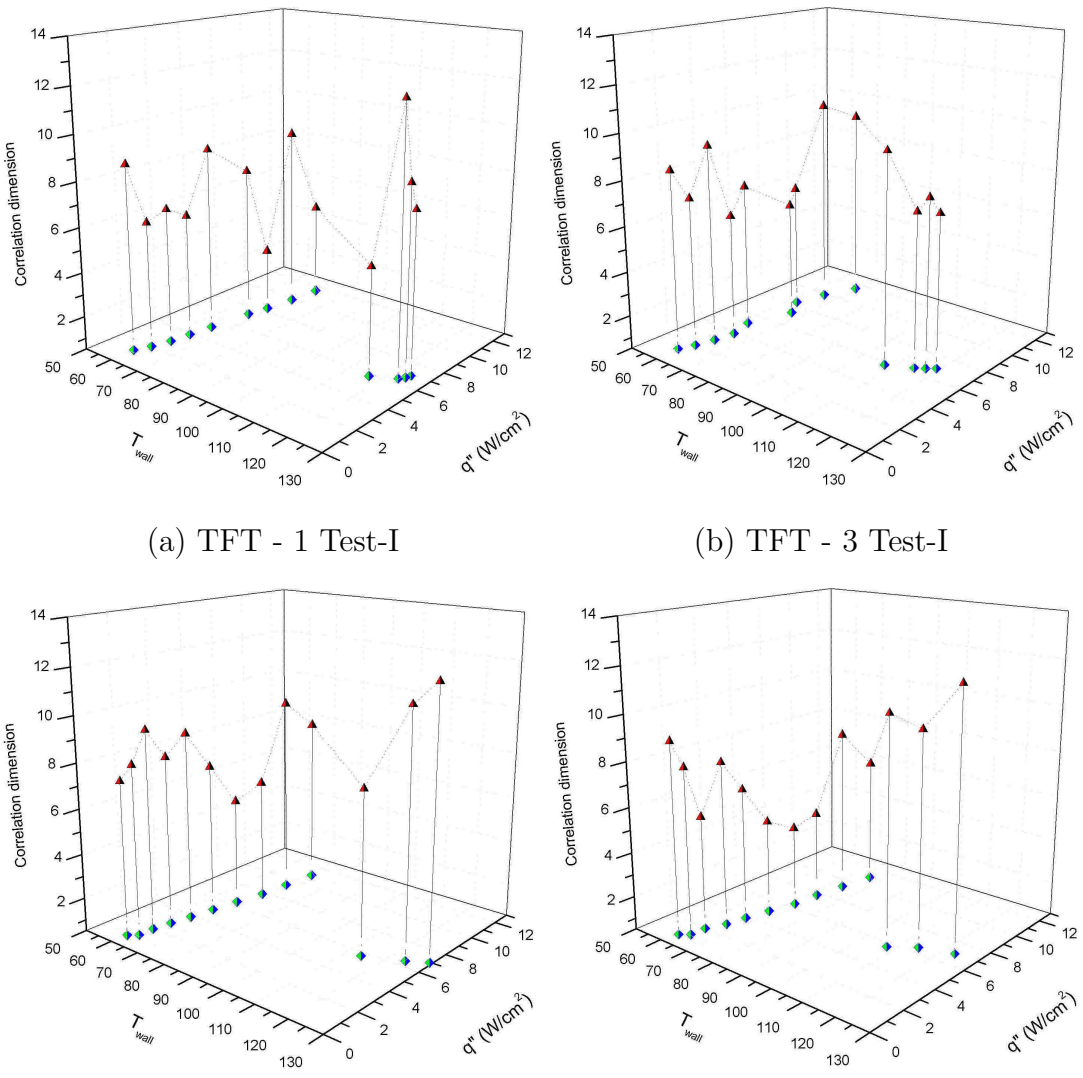

(a) TFT - 1 Test-I

(b) TFT - 3 Test-I

(c) TFT - 1 Test-II

(d) TFT - 3 Test-II

Fig. 55.: Variation of correlation 'dimensions' along entire boiling curve for saturated pool boiling after noise reduction.

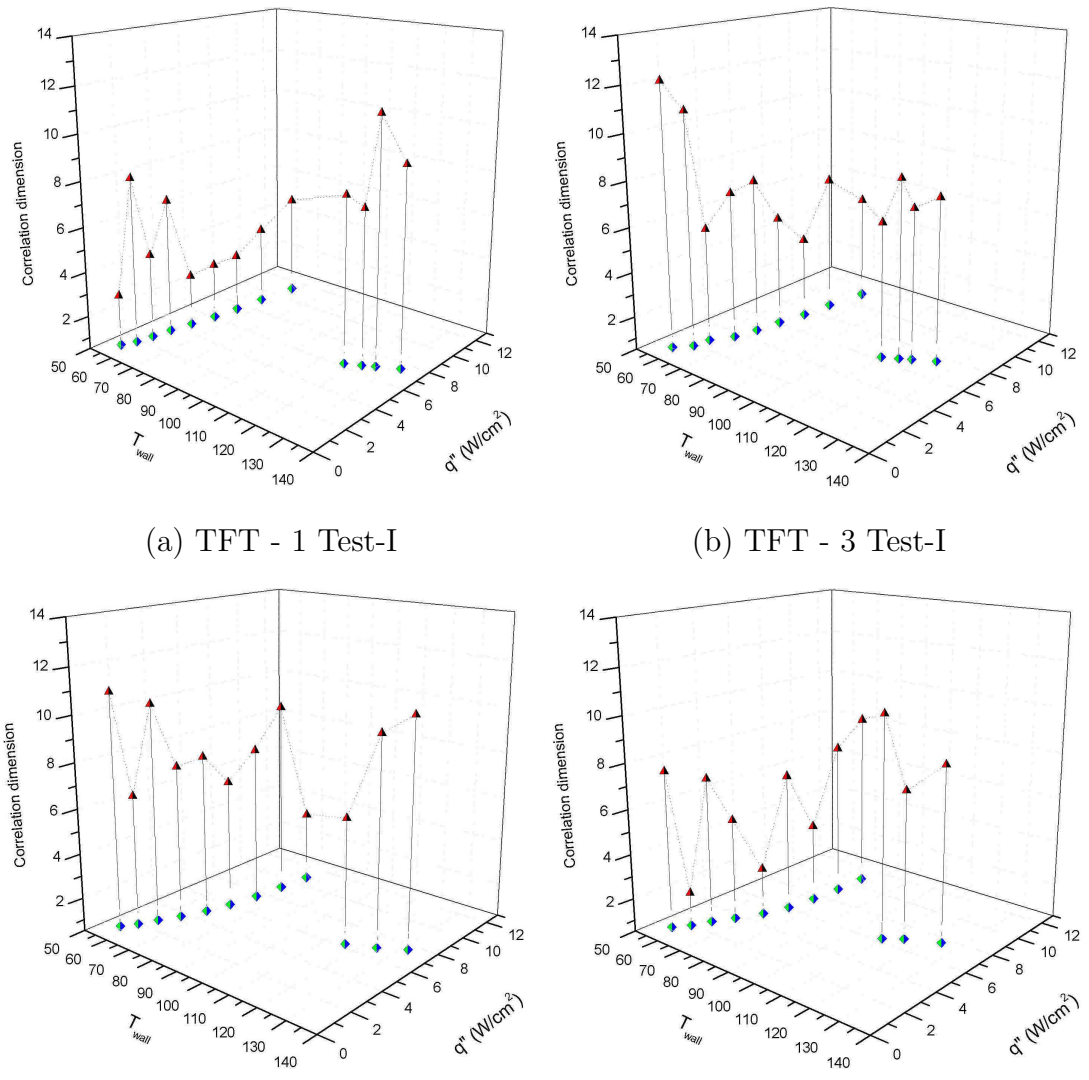

(a) TFT - 1 Test-I

(b) TFT - 3 Test-I

(c) TFT - 1 Test-II

(d) TFT - 3 Test-II

Fig. 56.: Variation of correlation 'dimensions' along entire boiling curve for 10 ℃ subcooled pool boiling after noise reduction.

dimensionality near the Leidenfrost point at a wall superheat of ~ 116.5 ℃ is 5.25 and at a wall temperature of ~ 124.5 ℃ it is 7.61. The higher dimensionality in subcooled pool boiling in FDNB and near CHF shows, that the number of parameters relevant to subcooled pool boiling is higher than that required in saturated pool boiling. The higher dimensionality of subcooled pool boiling at the Leidenfrost point implies that the number of parameters required to described the dynamics is higher than that required in saturated pool boiling. The correlation dimension estimates exceed the attractor dimension predicted by the false-nearest neighbor tests on the noisy data. This could stem from a number of sources such as inappropriate choice of delays, use of constant delay times in forming higher dimensional vectors and effects of noise. Thes results are summarized in table VII

9. Lyapunov exponents, Kaplan-Yorke dimension & validation

Positive Lyapunov exponents indicate divergence of nearby trajectories in phase space. The divergence of trajectories is a strong indicator of chaos. We determined the Lyapunov spectrum for dimensions ranging from 3 to 8 with a minimal neighborhood size of 0.003 and the number of neighbors set to 30, 50, 100 and 150. Neighborhood sizes of 100 and 150 led to unrealistic Kaplan-Yorke dimension estimates in few cases in the nucleate boiling regime. A few spurious positive exponents were observed in the convective regime. In many cases, these positive exponents were not robust and changed with the neighborhood size and embedding dimension.

Robust positive exponents were obtained in FDNB, near CHF and in film-boiling for saturated test cases. In saturated pool boiling, PNB showed negative Lyapunov exponents in most cases Table VII and Tables XI, XII, XIII (in appendix). All negative Lyapunov exponents indicate the presence of a stable fixed point. From Table VII, between wall superheat levels of 65.41 ℃ (Heat flux - 5.11 W/cm^2) and 68.43 ℃

(Heat flux - 8.35 W/cm^2) λ_1 changes from -0.03 to 0.03 (~ 0). This is indicative of a bifurcation between PNB and FDNB. Further increase in wall-superheat in the film boiling regime results in appearance of a positive Lyapunov exponent ($T_w \sim 116.7$ ℃, $\lambda_1 \sim 0.36$) indicating chaotic dynamics. In contrast, for the same run and heat flux levels, TFT-3 shows wall temperatures of 62.1 ℃ (5.11 W/cm^2), 66.5 ℃ (7.28 W/cm^2) and 62.6 ℃ (8.35 W/cm^2) with maximal exponents of 0.03, 0.02 and 0.01 bits/s respectively. The presence of positive exponents indicates possible presence of chaotic dynamics in vicinity of TFT-3. The difference in dynamics between TFT's 1 and 3 indicates that the dyanmics is not spatially coherent. Positive Lyapunov exponents are observed near CHF in both saturation runs for both TFT-1 and TFT-3 indicating the presence of chaos. Similar trends were observed for subcooled pool boiling Table VIII and Tables XIV, XV, XVI (in appendix).

Strange attractors are clearly present in saturated film boiling. Two positive exponents were obtained in some film boiling points (corresponding to number of neighbors 50) indicating the possible presence of hyper-chaotic dynamics. However, the second exponent is very close to zero and may be caused by numerical artefacts and noise. Discrepancy between the correlation dimension and the K-Y dimension results from presence of noise which affects both the Lyapunov exponent estimates and the correlation sum. Additionally, the choice of delay time may be sub-optimal thus influencing the correlation dimension estimate. Furthermore, the choice of points lying within the (assumed) scaling region results in some inaccuracies. The choice of neighborhood size and correlations within the time-series data affects the Lyapunov exponents (hence K-Y dimension) estimates. The Kaplan-Yorke conjecture is strictly valid for attractors possessing uniform density. It is evident from the phase-plots that the density is not strictly uniform. This is another cause for discrepancy between the correlation dimension estimates and the K-Y dimensions.

Table VII.: Saturated pool boiling run-1 TFT-1- Lyapunov exponents & dimension estimates

$\Delta\ T_w(℃)$	$q"(W/cm^2)$	λ_{robust}	$K\text{-}Y$	$D_C{}^a$	*Dynamics*	*T.R.A*
60.06	1.25	-0.03 ± 0.02, -0.16 ± 0.02, -0.25 ± 0.03,-0.4 ± 0.04, -0.56 ± 0.04, -1.29 ± 0.37	0	8.78	Fixed point	×
62.00	1.98	-0.03 ± 0.01, -0.34 ± 0.03, -0.75 ± 0.14	0	6.15	Fixed point	×
63.47	2.90	0.01 ± 0.04, -0.56 ± 0.15, -0.78 ± 0.05, -1.01 ± 0.14, -1.53 ± 0.24	∼ 1 or 0	6.57	Periodic/ fixed point	×
64.28	3.93	0 ± 0.02, -0.25 ± 0.03, -0.37 ± 0.04, -0.52 ± 0.04, 1.18 ± 0.32	0	6.04	Periodic/ Fixed point	×
65.41	5.11	-0.03 ± 0.02, -0.75 ± 0.03, -0.59 ± 0.05, -1.52 ± 0.18	0	8.80	Fixed point	×
67.12	7.28	-0.04 ± 0.03, -0.48 ± 0.05, -0.66 ± 0.05, -1.28 ± 0.09	0	7.43	Fixed point	P
68.43	8.35	0.02 ± 0.03, -0.05 ± 0.02, -1.46 ± 0.14	1, >2	3.38^a	Periodic/chaotic	×

Table VII. Continued.

$\Delta\ T_w(℃)$	$q"(W/cm^2)$	λ_{robust}	*K-Y*	$D_C{}^a$	*Dynamics*	*T.R.A*
69.70	9.90	0.01 ± 0.01, -0.03 ± 0.02, -0.14 ± 0.04, -1.17 ± 0.26	>2	8.73	Chaotic	×
70.73	11.52	0.03 ± 0.03, -0.03 ± 0.01, -0.3 ± 0.04, -1.33 ± 0.25	1, >2	4.80[a]	Chaotic	P
116.67	5.81	0.36 ± 0.09, 0.08 ± 0.04, -0.04 ± 0.03, -0.48 ± 0.07, -1.16 ± 0.2	>2	5.25[a]	Chaotic	P
122.90	6.37	0.04 ± 0.03, 0 ± 0.01, -0.03 ± 0.01, -0.07 ± 0.01, -0.04 ± 0.03	>2	12.09	Chaotic	P
123.96	6.65	0.03 ± 0.02, 0 ± 0.01, -0.02 ± 0.01, -0.05 ± 0.02, -0.14 ± 0.03	>2	8.76	Chaotic	×
124.47	6.91	0.04 ± 0.03, 0.01 ± 0.01, -0.02 ± 0.01, -0.05 ± 0.03, -0.06 ± 0.02	>2	7.61[a]	Chaotic	×

a Estimate Converged

The Kaplan-Yorke (K-Y) dimension ranged between 3 and 4 for saturated film boiling and between 2 and 4 for FDNB and most CHF data points (Table. VII) in saturated boiling. Some positive exponents were also estimated in PNB, with a K-Y dimension between 1 and 3 indicating the presence of periodic windows (possibly multiple periodicities) and chaotic behavior.

Table VIII depicts the Lyapunov exponents for 10 ℃ subcooled pool boiling. Most of PNB has a negative Lyapunov spectrum indicating the absence of chaotic dynamics. Chaotic dynamics occurs in FDNB, CHF and film boiling. The onset of chaotic dynamics is delayed to higher wall superheat levels compared to saturated pool boiling. In addition, the saturated case shows possible periodic dynamics in PNB at four wall superheat levels compared to two in the subcooled case. The uncertainty in accurately estimating the Lyapunov exponents makes it difficult to assess the exact nature of dynamics in the PNB regime.

The original and 199 other surrogate data sets were subjected to time-reversal tests at a level of significane of 99%. Results for one of the saturated pool boiling cases is summarized in table VII. The data sets failed to satisfy the null hypothesis near CHF, and in film boiling. In some of the other cases, the tests barely agreed with the null hypothesis, possibly due to the high signifcance level and the limited power of the test. In these cases, deterministic dynamics is evident from the positive Lyapunov exponents and fractal dimensionality. The surrogate data tests in subcooled film boiling shows two false positives in the PNB regime and negative results for all other cases. The negative results could be due to the high level of significance (99%) employed in these tests. Additionally, every test statistic has a finite distinguishing power and may yield negative results although the underlying dynamics is chaotic.

Table VIII.: Subcooled pool boiling Run-1 TFT-3 - Lyapunov exponents & dimension estimates.

$\Delta\ T_w(℃)$	$q"(W/cm^2)$	λ_{robust}	*K-Y*	D_C[†]	*Dynamics*	*T.R.A*
57.18	1.15	-0.08 ± 0.04, -0.62 ± 0.05, -0.78 ± 0.05, -1.41 ± 0.21	0	12.15	Fixed point	×
61.36	1.85	-0.11 ± 0.04, -1.09 ± 0.19, -1.42 ± 0.23	0	10.90	Fixed point	×
62.14	2.68	-0.02 ± 0.03, -0.29 ± 0.04, -0.74 ± 0.06	0 or 1	5.63[c]	Fixed point or Periodic	×
66.16	3.67	0.01 ± 0.01, -0.02 ± 0.02, -1.07 ± 0.14	≥1	7.11	Quasi-periodic or chaotic	×
68.13	4.79	-0.03 ± 0.02, -1.07 ± 0.12, -1.46 ± 0.21, 2.06 ± 0.3	0	7.45	Fixed Point	×
69.49	6.08	-0.03 ± 0.02, -1.09 ± 0.13, -1.69 ± 0.2	0	5.03[c]	Possibly Chaotic	P
71.51	7.46	-0.04 ± 0.03, -0.76 ± 0.09, -1.04 ± 0.09, -1.53 ± 0.15	0	4.16[c]	Possibly Chaotic	P
72.61	9.09	0.02 ± 0.01, -0.04 ± 0.02, -0.15 ± 0.04	> 2	6.66[c]	Chaotic	×

Table VIII. Continued.

$\Delta\ T_w(℃)$	$q"(W/cm^2)$	λ_{robust}	K-Y	D_C[†]	*Dynamics*	*T.R.A*
74.93	11.14	0.03 ± 0.02, -0.02 ± 0.01, -0.05 ± 0.02, -0.13 ± 0.02	> 2	5.30[c]	Chaotic	×
109.71	6.29	0.02 ± 0.02, -0.05 ± 0.02, -0.13 ± 0.02	> 2	6.48[c]	Chaotic	×
114.44	6.64	0.01 ± 0.02, -0.03 ± 0.01, -0.06 ± 0.02, -0.14 ± 0.03, -0.26 ± 0.04	> 2	8.42	Chaotic	×
117.61	6.95	0.03 ± 0.03, -0.01 ± 0.02, -0.04 ± 0.02, -0.1 ± 0.04	> 2	7.17[c]	Chaotic	×
123.89	7.48	0.02 ± 0.01, -0.01 ± 0.01, -0.03 ± 0.01, -0.06 ± 0.02, -0.12 ± 0.03	> 2	7.98	Chaotic	×

[b]Estimate Converged

D. Time-series Analysis: Physical Interpretation & Discussion of Results

1. Surface temperature fluctuations

Kenning and Yan (Ref. [90]) employed thermochromic liquid crystals to measure surface temperature fluctuations in pool boiling of water over thin stainless steel surfaces measuring 28.1 mm × 40.1 mm and 0.13 mm in thickness. Two surfaces with different wetting characteristics were employed. Temperature variations during the growth and departure of the bubbles were of the order of 10 ℃. The cold spot size during the bubble departure process was confined to the maximum projected area under the bubble (fig. 57). This observation contradicted earlier modeling assumptions. Figure 58 depicts surface temperature variations at various interacting sites at three different heat flux levels. Significant spatio-temporal temperature fluctuations were observed. The spatial variation in temperature decreased with increase in heat flux. Interaction of sites led to interesting behavior such as delayed growth, increased recovery time, site deactivation etc. The data clearly shows intermittent periodicities at the different nucleating sites at heat fluxes of 50.8 and 102 kW/m^2. Strong site interactions such as that between A and D leads to intermittency in buble departure and a loss of periodicity. At the highest heat flux, no dominant periodicities can be observed

Simultaneous visualization of the bubble departure process and temperature record was not possible in these studies. This was due to the heating of the bulk fluid and substrate caused by the halogen lights used in high speed image acquisition leading to departure from the quasi-steady-state condition. The temperature fluctuations encountered in this study was of the order of 0.5 - 3 ℃ depending on the boiling regime. The significant reduction in surface temperature fluctuations is attributed to the low latent heat of FC-72 (compared to water). No single dominant

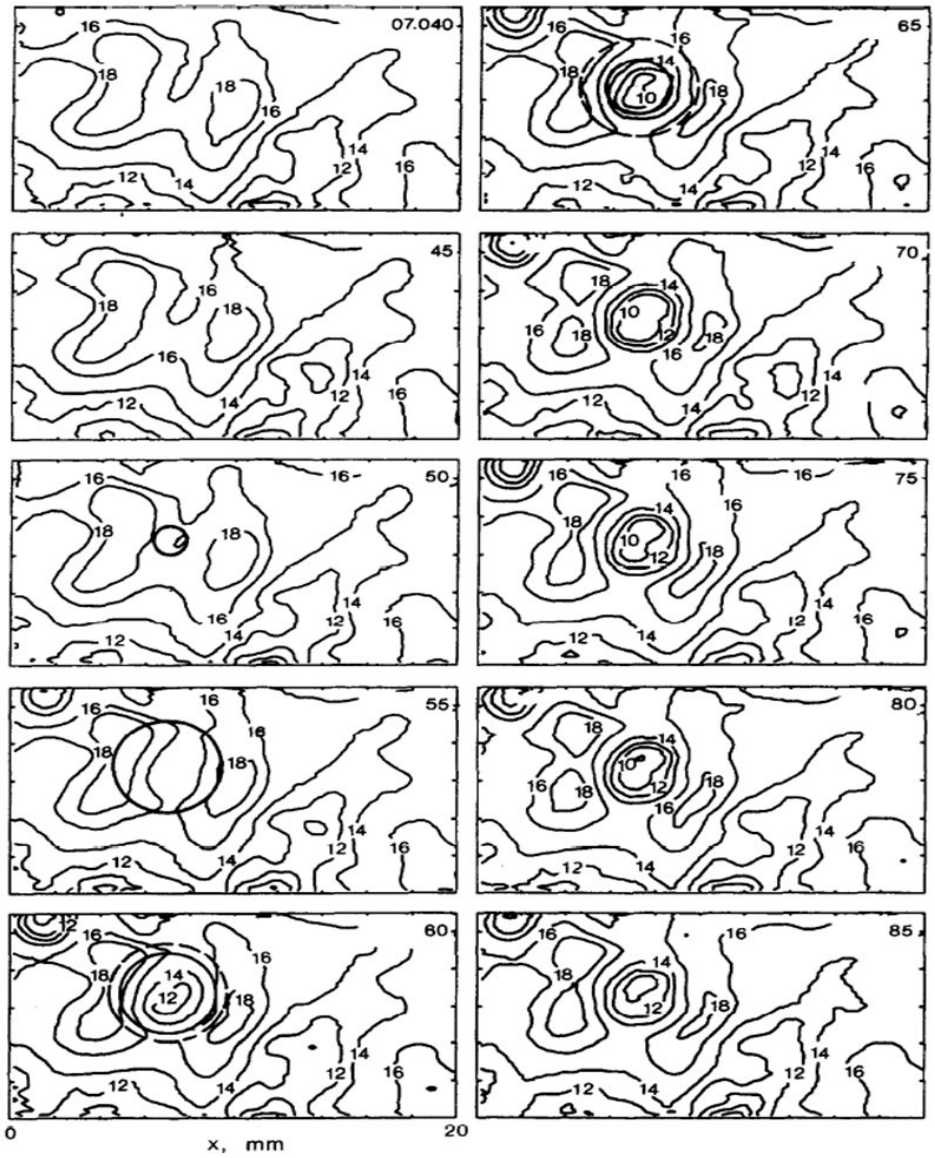

Fig. 57.: Temporal surface temperature fluctuation during ebullition cycle recorded in boiling of water over a 0.13mm thick stainless steel plate using thermochromic liquid crystal (0.01 mm thick, with 0.025mm thick polyester film) coated on the underside of the test surface.

Reprinted from International Journal of Heat and Mass Transfer, Vol. 39 (15), D.B.R. Kenning, Youyou Yan, Pool boiling heat transfer on a thin plate: features revealed by liquid crystal thermography, (1996), with permission from Elsevier.

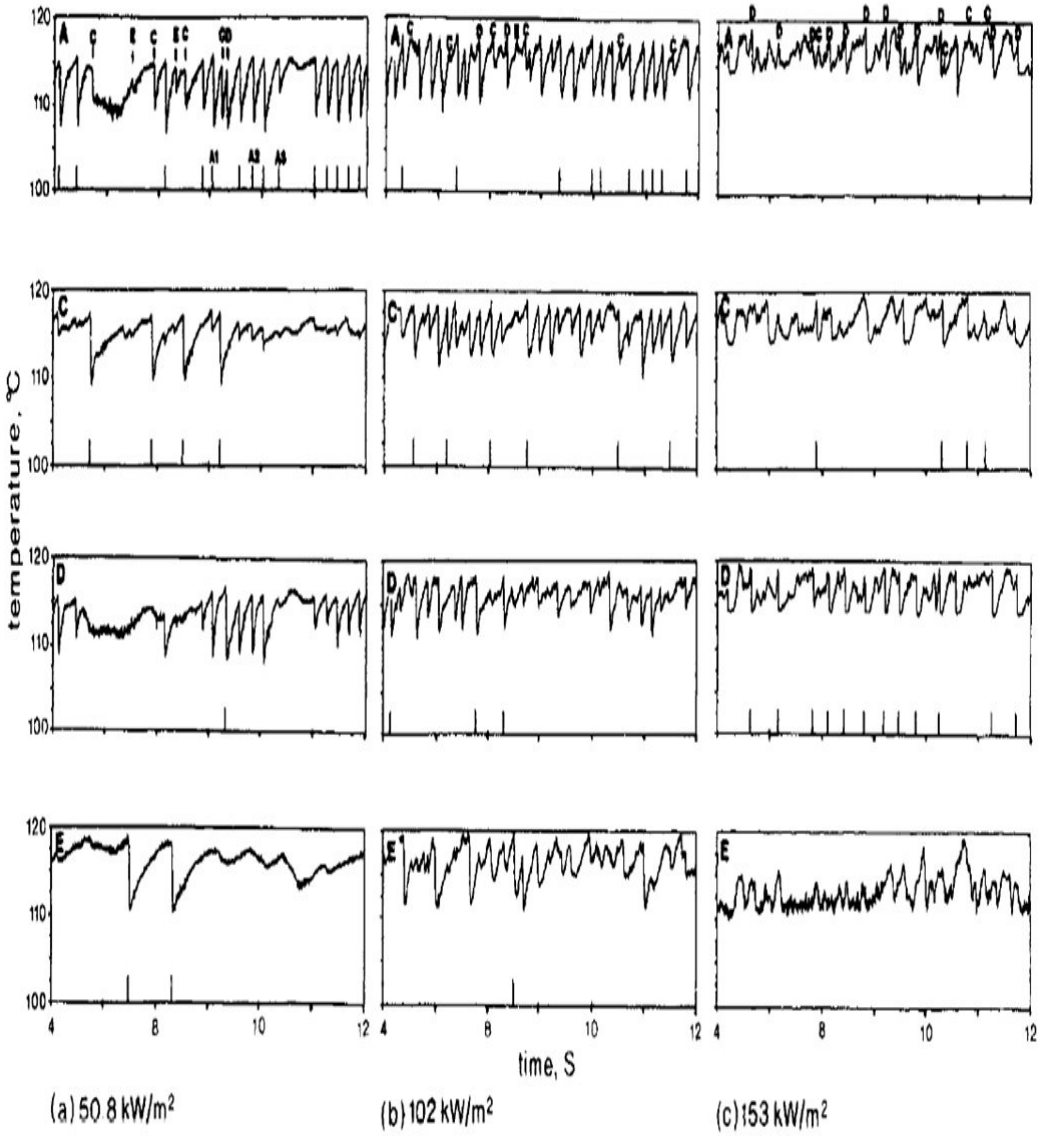

Fig. 58.: Surface temperature fluctuations at interacting sites A, C, D & E recorded in boiling of water over a 0.13mm thick stainless steel plate using thermochromic liquid crystal (0.01 mm thick, with 0.025mm thick polyester film) coated on the underside of the test surface.

Reprinted from International Journal of Heat and Mass Transfer, Vol. 39 (15), D.B.R. Kenning, Youyou Yan, Pool boiling heat transfer on a thin plate: features revealed by liquid crystal thermography, (1996), with permission from Elsevier.

periodicity is visible at ONB and PNB in any test case. This is due to the presence of multiple nucleation sites in vicinity of the TFT junctions with each site associated with a range of departure frequencies. Additionally, the higher thermal diffusivity ($\sim$ 7-8 times that of carbon steel) of the silicon wafer results in lower surface temperature fluctuations. This observation is in agreement with the numerical results of Banerjee and Dhir [9] wherein higher higher thermal conductivity of the substrate resulted in lower temperature variability. At higher heat fluxes, significant surface temperature fluctuations are visible in saturated and subcooled pool boiling due to dominance of microlayer evaporation effects. Sadasivan and Unal [5], observed the existence of multiply periodic, averaged surface temperature fluctuations at low heat flux levels in a computational study involving multiple nucleation sites on a 25 mm^2 test surface. Such periodicities are not visible in the current experimental data. In fact, the temperature fluctuations of the two TFT's in a given test for a specific heat flux level is different although they are only 50 μm apart. This is indicative of strong site interactions.

2. Fourier spectra & non-linear statistical quantifiers

No dominant periodicities are present at high heat flux levels (FDNB and CHF). In FDNB and CHF, bubble coalescences occur apart from strong site interactions. The bubble departure process transitions from a periodic to a chaotic state as shown in studies by Zhang et al. [57], Acharya et al. [56] and others. The Fourier spectra indicate broad band spectra with the number of dominant frequencies that increase with the wall superheat. The active frequencies are of the form of $mf_1 \pm nf_2$ which is an indicator of quasi-periodic bifurcations. Clearly, in FDNB, CHF and film boiling regimes, low-dimensional chaotic dynamics is present. Homoclinic and heteroclinic bifurcations are less well-known bifurcations that occur in disspative systems governed

by partial differential equations. These belong to a class known as global bifurcations. Global bifurcations result in a change in attractor structure and occur in higher dimensions. The phase plots show a clear change in attractor geometry with an increase in heat flux especially near CHF, in FDNB and film boiling indicating the presence of global bifurcations.

In a study on a small size wire with water as the test liquid, Shoji et al. [70], showed that film boiling was low dimensional chaotic ($D_C \sim 3.2$). Convergence (in dimension estimates) was not obtained in FDNB and at CHF in contrast to the present study. Furthermore, convergence was obtained at points in the nucleate boiling regime and dimensions (fractals) were estimated between 6.0 - 8.0. The convergence of dimensional estimates in nucleate boiling in that study is due to the difference in dynamics caused by the small (compared to bubble departure diameters) wire diameter (80μm, 100μm). A small wire diameter leads to bubble coalescence on the surface. Additionally, the size of the bubbles were of the same magnitude as the size of the wire. In the study by Shoji and co-workers, data was sampled at 10 kHz frequency. Fluctuations in the electrical resistance of the wires were used to determine the temperature fluctuations. The number of datapoints used to estimate the correlation dimensions was not reported. In light of more recent literature [85], the high frequency of data acquisition used could have resulted in a significant temporal correlation between the datapoints. A high degree of correlation between the data points results in low dimensional estimates (opposite to that of noise). The presence of correlation wasn't checked using space-time separation plots [85]. Therefore, the dimensional estimates could have been spurious. As a result of the small wire-size, large excursions in temperature were observed. This is due to the effect of cold-spots [9]. In contrast, the test surface employed in this study is much larger than the bubble departure diameter. Thus, the effect of the cold-spots is confined to small regions

on the wafer in vicinity of the bubble. Globally, the structure of the attractor is influenced by interactions between cold-spots due to the presence of multiple, active nucleation sites. Locally, the variations in the bubble departure process results in variations in the geometry of the attractor resulting in variation of the dimensions existing between the TFT in a single run. In the present study, the fractal values of correlation dimension and positive Lyapunov exponents in FDNB, near CHF and in film boiling indicate the presence of chaotic dynamics. The change in Lyapunov exponents from negative through zero to positive is indicative of bifurcations from stable fixed points to strange attractors. The presence of limit cycles with a single or few fundamental periods could not be confirmed. However, this does not rule out the possibility of multiple periodicity based on the K-Y dimension estimates. A numerical study by Sadasivan and Unal [5], showed the existence of multiply periodic surface temperature fluctuations at low heat flux levels. The simulations showed an increase in the number of periods with an increase in heat flux. At a sufficiently high heat flux, aperiodic behavior was observed. Similar behavior is observed in the present study. However, contrary to Ref. [5], occurrence of period doubling bifurcation could not be observed.

E. Concluding Remarks

Surface temperature fluctuations were recorded in saturated and 10 ℃ subcooled pool boiling. The key conclusions of the heat transfer and non-linear time series analysis are:

1. The microlayer thickness is estimated to be 21.6 μm. The peak heat flux is significantly lower than that predicted by hydrodynamic models.

2. The magnitude of surface temperature fluctuations is observed to increase with

increase in wall superheat and wall heat flux, in saturated and subcooled pool boiling.

3. A broad banded frequency spectrum appears with the bandwidth increasing with rising superheat and wall heat flux.

4. The dominant frequencies present in the spectrum are of the form $mf_1 \pm nf_2$. This is indicative of quasi-periodic bifurcation route. Additional experiments are required to confirm this.

5. Low-order deterministic chaos is present in FDNB, at CHF and in film-boiling for saturated and subcooled pool boiling. This is confirmed by the fractal dimensions and positive Lyapunov exponents.

6. The positive Lyapunov exponents range between 0.06 and 0.22.

7. The dimensionality in FDNB, at CHF and in film-boiling is lower in saturated pool boiling as compared to values in corresponding regimes in subcooled pool boiling. This is indicative of a difference in dynamics of saturated and subcooled pool boiling.

8. Computational studies in the film boiling regime suggest existence of periodic surface temperature fluctuations in this regime. However, no single, definite periodicity is visible in the temperature fluctuations in film-boiling regime in this study.

CHAPTER VI

NANO-TEXTURED SURFACE: RESULTS AND DISCUSSION

A. Introduction

Experiments on MWCNT coated surfaces were performed in saturation and 10 ℃ subcooled conditions. Tests were confined to the convective, ONB and PNB regimes. There were many problems associated with the fabrication and testing of these substrates. The primary difficulty encountered was the removal of the deposited TFT layer during CNT synthesis in the furnace. The high temperatures encountered within the furnace resulted in a warping of the metallic TFT layers on the silicon substrate due to differential expansion of the bimetallic thin-film layers. In many cases, the entire vacuum deposited metal layers were removed. The e.m.f of the TFT no longer corresponded with K-type thermocouples due to irreversible hysteresis effects associated with the cyclic heating and quenching in the CNT furnace and the deposition of iron catalyst on the surface. The processes involved in CNT synthesis led to irreversible changes in the Seebeck coefficient. The thermocouples also showed some drift between one run and the next, which necessitated recalibration. Despite repeated calibrations and good linear fits, a significant bias of 4 - 10 ℃ resulted in the pool boiling experiments. However, this bias does not affect the magnitude of temperature fluctuations and by extension the results of non-linear time-series analyses. Quantities such as correlation dimension involve calculation of differences/distances which depend on magnitude of the fluctuations. Due to the presence of bias, the boiling curve based on TFT temperature data cannot be employed for direct comparison with saturation data.

The boiling curve based on thermocouples placed within the copper block is

plotted. Results of non-linear time-series analysis is presented. Lyapunov exponents, correlation dimensions are calculated in the convective, ONB and PNB regimes after noise reduction. The analysis shows no perceptible difference in dynamics due to bubble departure processes in convective regime, at ONB and in PNB.

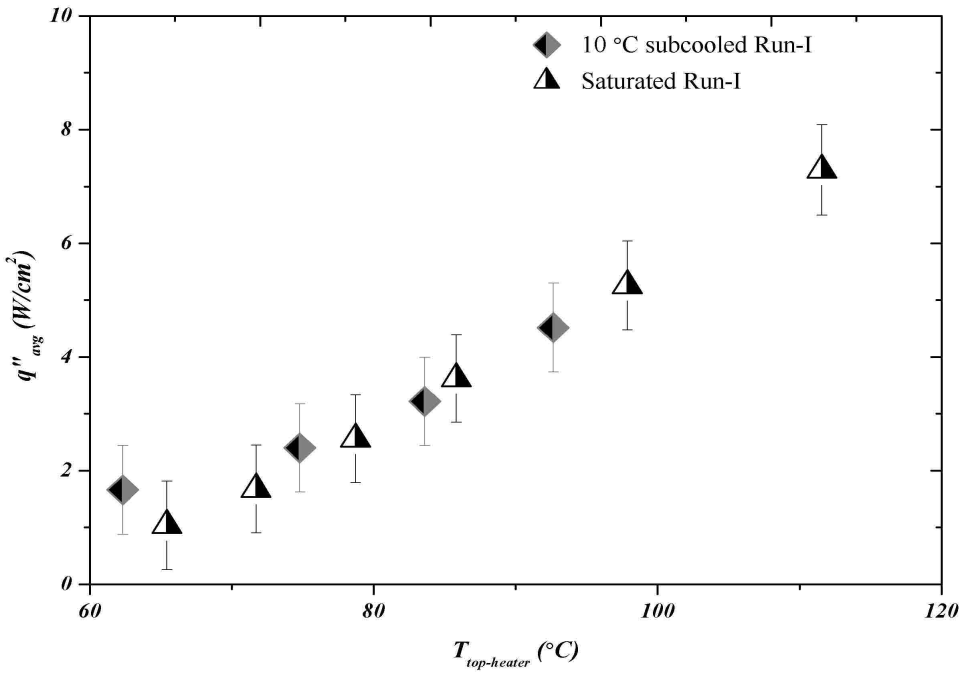

Fig. 59.: Low heat flux boiling curve for MWCNT coated surface under saturated and 10 ℃ subcooled conditions.

B. Heat transfer: Results & Discussion

Figure 59 depicts the boiling curves for saturated and subcooled pool boiling of PF-5060 over a MWCNT coated surface. Heat flux levels spanning convective, ONB and PNB regimes were sustained in the experiments. Heat flux levels span 1.8 - 4.5 W/cm^2 in subcooled pool boiling and from $\sim$ 1 - 7 W/cm^2 in saturated boiling. Onset of nucleation is observed at heat flux levels of $\sim$ 1.8 W/cm^2 and 2.2 W/cm^2 in

saturated and subcooled boiling. This corresponds to copper block temperatures of 72 ℃ and 74 ℃. Similarly, onset of boiling is observed at $\sim$ 2 W/cm^2 in saturated pool boiling at wall superheat levels of 72 ℃ - 74 ℃. Nucleation is concentrated on the patterned TFT. Little or no nucleation is observed on the CNT coated areas. No heat transfer enhancement is observed in the low-heat flux regime when compared to the bare silicon surface (fig. 27). No enhancement in heat transfer is observed between saturated pool-boiling for MWNCT coated surfaces. The results are in keeping with observations of [40] et al. wherein no signifcant enhance ment in heat transfer was observed in ONB and PNB. A comparison of the boiling curve with that in Ref. [40] shows that heat flux levels are much lower than the CHF ($\sim$ 18 W/cm^2) observed for MWCNT coated surfaces.

C. Temperature Time-series & its Analysis

1. Temperature-time series

Figure 60 depicts surface temperature fluctuations measured in saturated pool boiling on the CNT coated surface after noise reduction. In the convective regime, temperature fluctuations are less than 0.5 ℃. In PNB, temperature fluctuations range from 0.5 - 1 ℃. The maximum temperature variation in the convective regime is of the order of $\pm$ 0.25 ℃. With an increase in heat flux, the magnitude and instances of temperature excursions about the mean are observed to increase. No dominant periodicities are visible in the temperature fluctuations. The magnitude of temperature fluctuations at ONB and in the convective boiling regime are similar to those observed in saturated pool boiling over the bare silicon surface. However, temperature excursions are more frequent in boiling over the bare surface compared to the CNT coated surface.

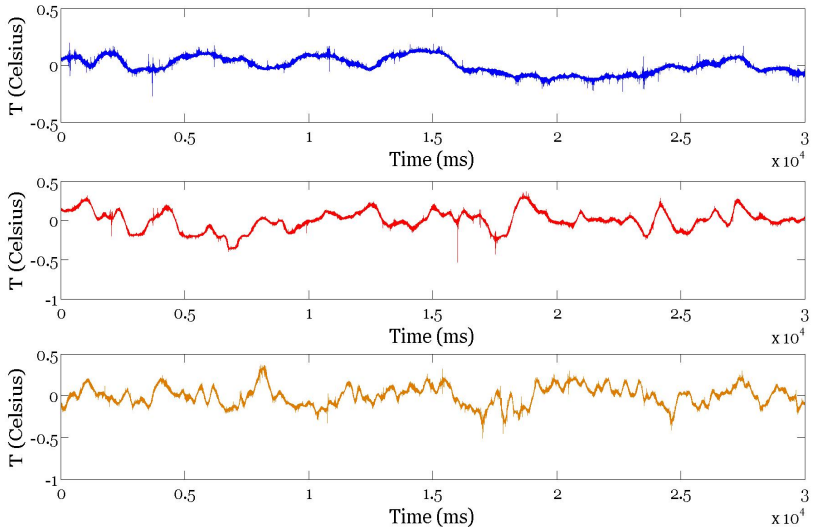

(a) Surface temperature fluctuations in convective, ONB regimes

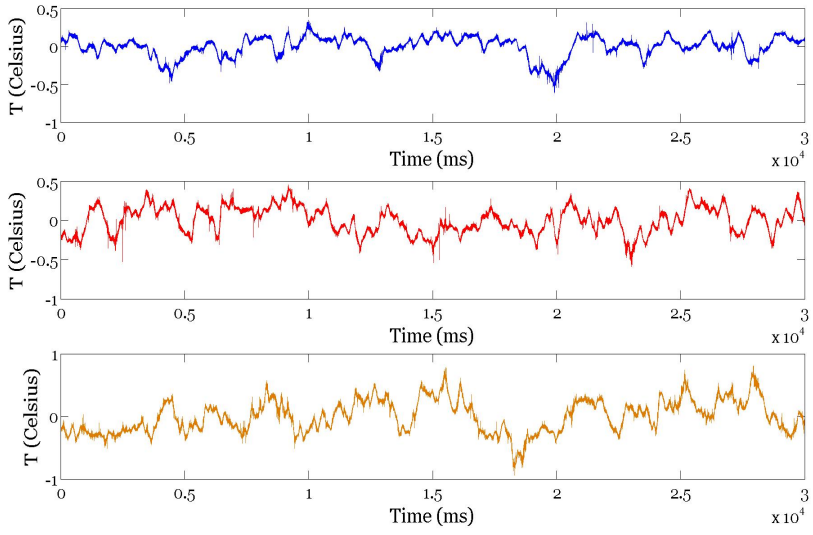

(b) Surface temperature fluctuations in PNB

Fig. 60.: Surface temperature fluctuations in saturated pool boiling on CNT coated substrate after noise reduction.

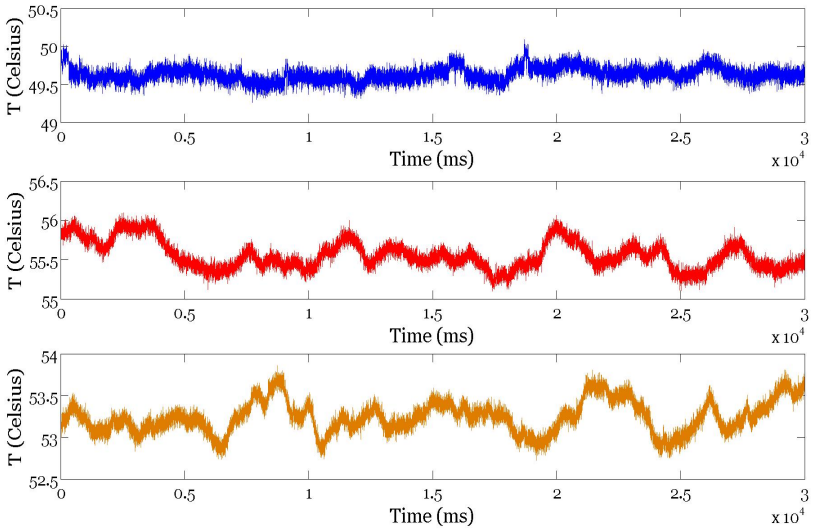

(a) Surface temperature fluctuations before noise reduction

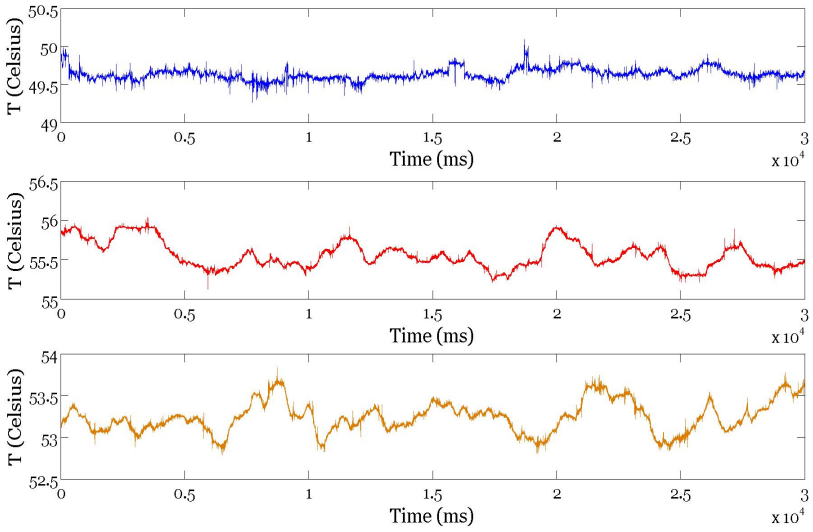

(b) Surface temperature fluctuations after noise reduction

Fig. 61.: Surface temperature fluctuations in subcooled pool boiling on CNT coated substrate before and after noise reduction.

Figure 61 depicts surface temperature fluctuations on the CNT coated substrate before and after noise reduction for the convective, ONB and PNB in subcooled boiling. In the convective regime, no significant temperature excursion is observed. The maximum temperature variation in the convective regime is less than ± 0.25 ℃. With an increase in heat flux, the magnitude and instances of temperature fluctuations are observed to increase. For instance, the fluctuations are of the order of ± 0.5 ℃ in PNB. No significant periodicities are visible in the temperature fluctuations. This is similar to the saturated pool boiling case where temperature fluctuations of the order of ± 0.3 ℃ are observed. However, the duration and frequency of fluctuations in subcooled pool boiling on the CNT coated surface are significantly lower than that for saturated pool boiling on the bare surface. The temperature excursions are similar to those observed in 10 ℃ subcooled pool boiling.

2. Fourier spectra

Figure 62 shows the Fourier spectra saturated pool boiling over CNT coated substrates. Similar to spectra observed in saturated boiling over the bare surface, a broad banded spectrum is observed here. Frequency peaks exist in the 0 to 2 Hz range. The number of frequency peaks increase with an increase in the heat flux level. These observations are consistent with observations made for boiling on bare substrates.

Figure 63 depicts the Fourier spectra in the convective, ONB and PNB regimes. Again, multiple periodicities are visible in PNB with an underlying broadband spectrum in the 0-2 Hz frequency range. This is lower than the bandwidth of active frequencies observed in subcooled pool boiling over a bare silicon substrate (0-5 Hz). This indicates the reduction in departure frequencies.

The bandwidth of active frequencies is observed to increase with an increase in

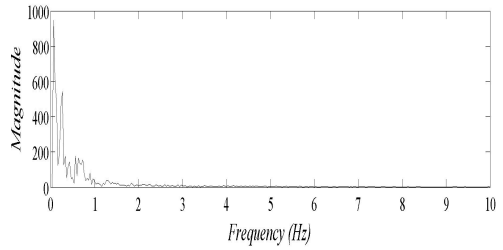

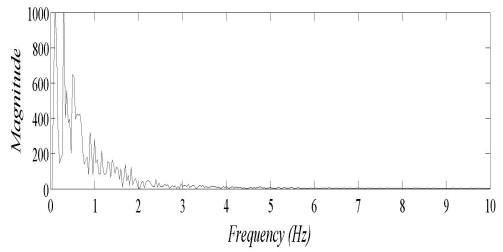

(a) Convective regime

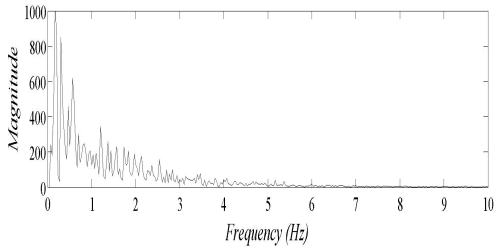

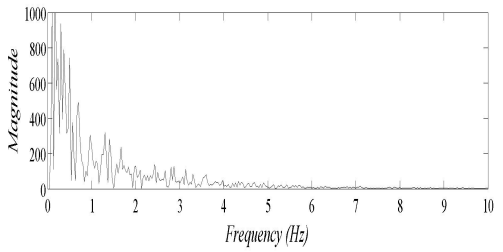

(b) ONB

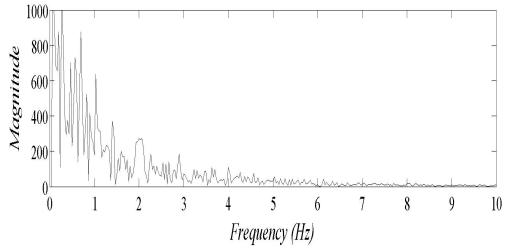

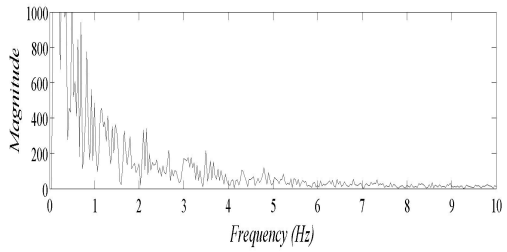

(c) PNB

Fig. 62.: Fourier spectra for saturated pool boiling over CNT coated substrate corresponding to high frequency temperature measurements.

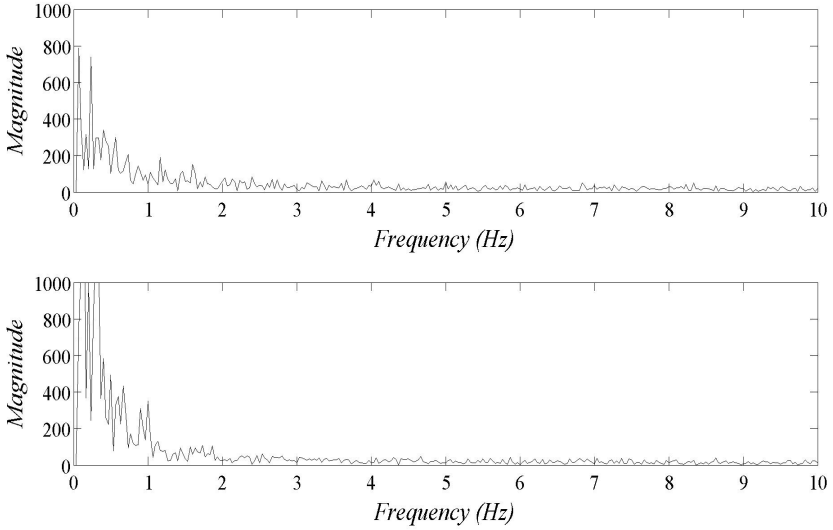

(a) Convection and ONB

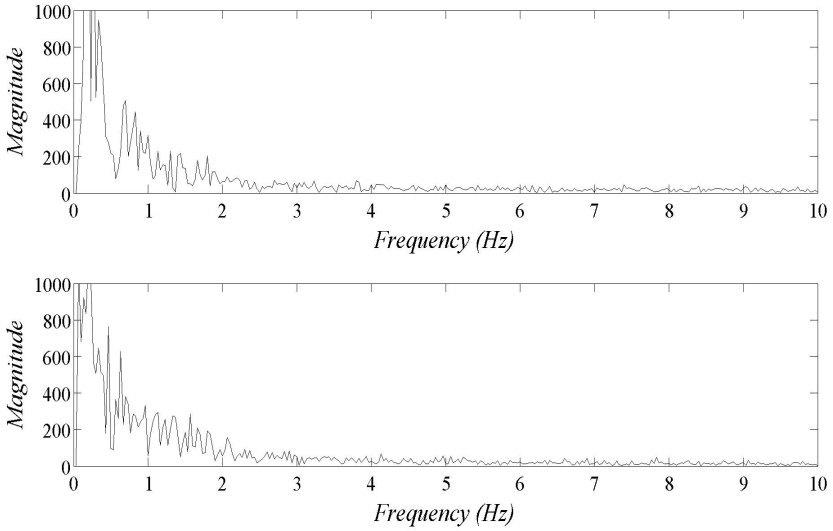

(b) PNB

Fig. 63.: Fourier transform of the surface temperature fluctuations recorded by TFT

wall-superheat/heat flux. In the convective regime, there are two dominant frequencies at $\sim$ 0.1 and 0.3 Hz with a minor broadband component in the 0-1 Hz range. The broadband component is due to noise in the system. At ONB, new dominant frequencies emerge in the 0-1 Hz range, with an underlying broadband spectrum in the 0-1 Hz range. In PNB, additional dominant frequencies appear in the 0-2 Hz range with an underlying broadband spectrum. The appearance of additional frequencies indicates the activation of other nucleation sites on the surface of the test chip. The broadband spectrum is a possible indicator of chaotic dynamics.

3. Phase plots using singular value decomposition(SVD)

Phase plots generated after projection of time-series data onto the three prinicpal eigen basis are shown in figure 64 for saturated pool boiling over MWCNT coated surfaces. In the convective regime no geometrical pattern is observed. At ONB, emergence of a geometrical pattern is observed. The patterns change continually with heat flux level. These observations are consistent with observations in boiling over the bare surface. The structures are (figure 65) close looped thereby indicating the presence of multiple periodicities. This explanation is consistent with observations of the Fourier spectra which shows multiple peaks at different frequencies.

Figure 66 depicts phase plots of surface temperature fluctuations using SVD. No clear structure is visible in the convective, ONB and PNB regimes. This could indicate dominance of noise or high-dimensional dynamics. However, the geometry of the structure varies from the convective regime to ONB. The attractor spreads more in the directions perpendicular to the semi-major axis at ONB as compared to the convective regime. Additionally, the attractor geometry in PNB is significantly different from those observed in the corresponding subcooled case on the bare silicon surface. This is a qualitative indicator of the change in dynamics due to surface

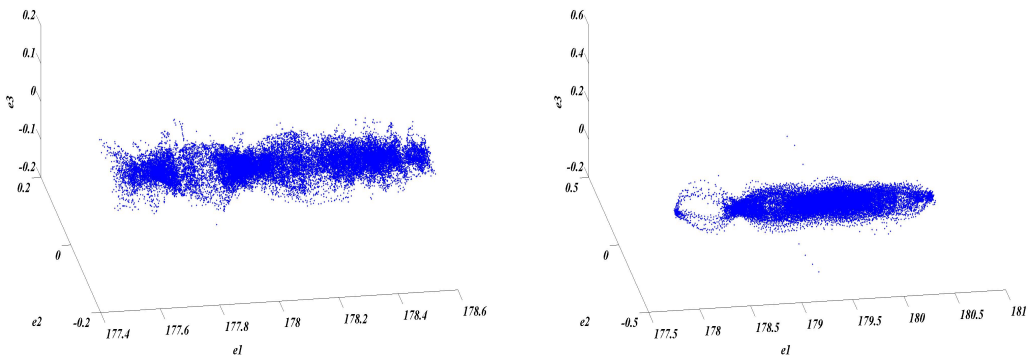

(a) Convective regime

(b) ONB

(c) PNB

(d) PNB

(e) PNB

(f) PNB

Fig. 64.: Phase plots for saturated pool boiling on CNT coated surface after noise reduction obtained from principal component analysis.

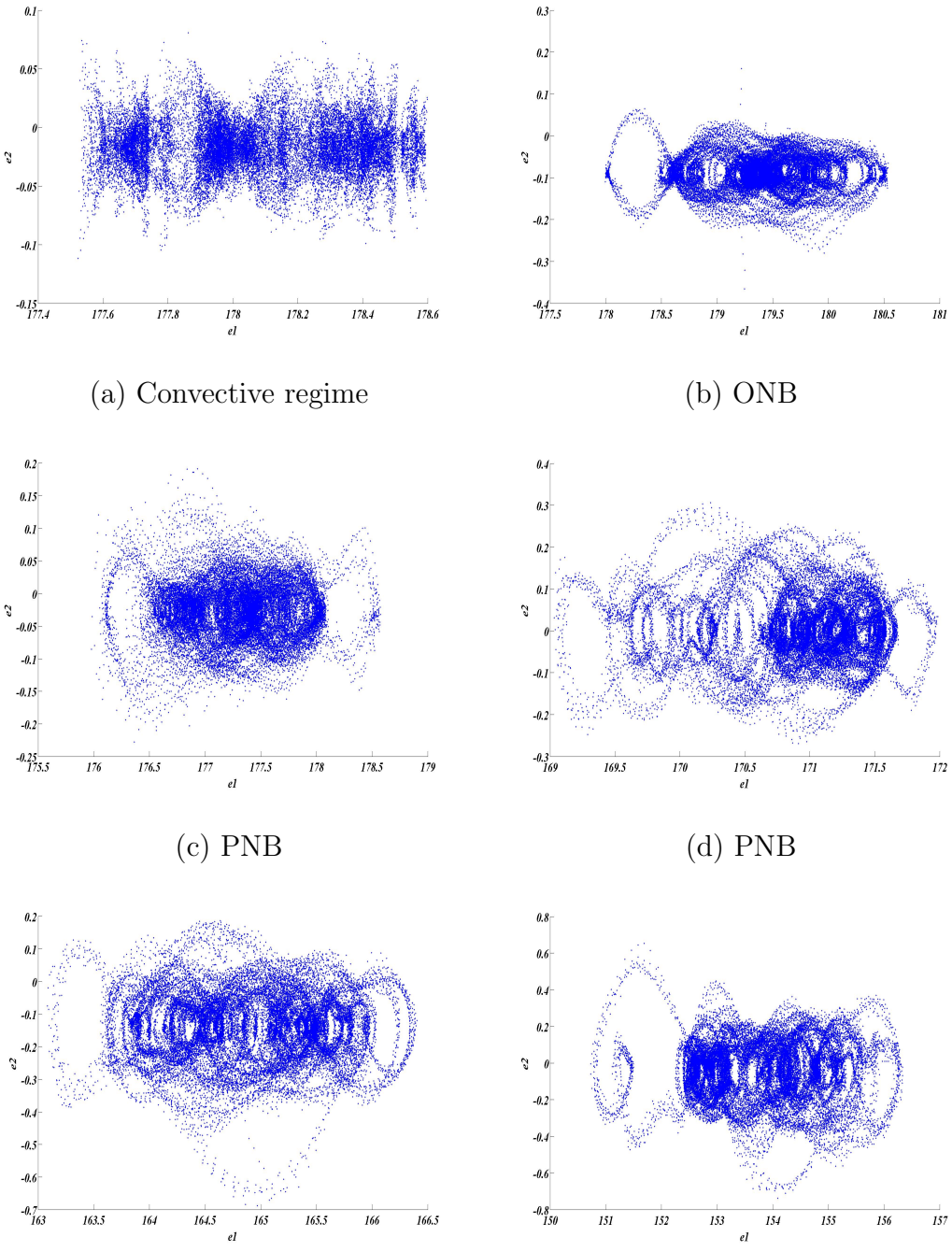

(a) Convective regime

(b) ONB

(c) PNB

(d) PNB

(e) PNB

(f) PNB

Fig. 65.: Phase plots for saturated pool boiling on CNT coated surface after noise reduction obtained from principal component analysis.

texturing. The geometry of the attractor is observed to vary with the wall-superheat level akin to the bare test chip.

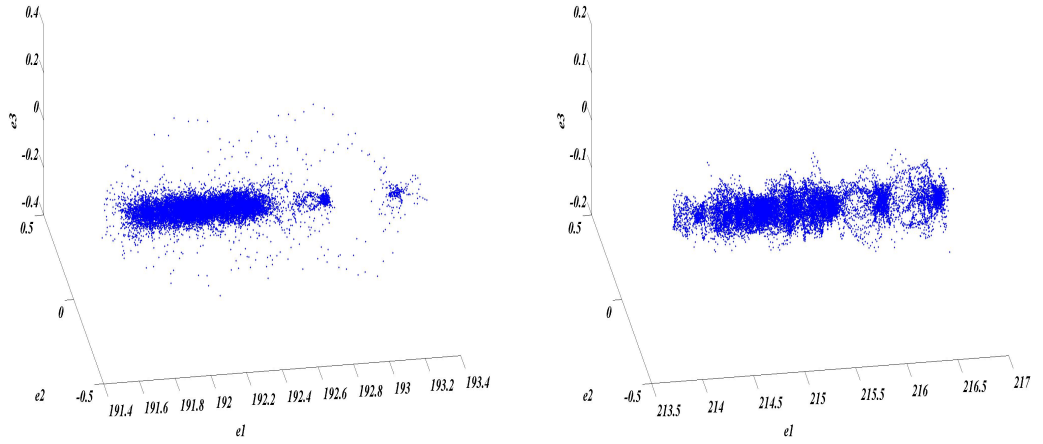

(a) Convection

(b) ONB

(c) PNB

(d) PNB

Fig. 66.: Phase plots of surface temperature fluctuations recorded by TFT

Compared to the phase plots in saturated pool boiling, the phase plots in subcooled pool boiling shows no clear structure. These observations for CNT coated surfaces are consistent with observations made for the bare surface. Subcooled pool

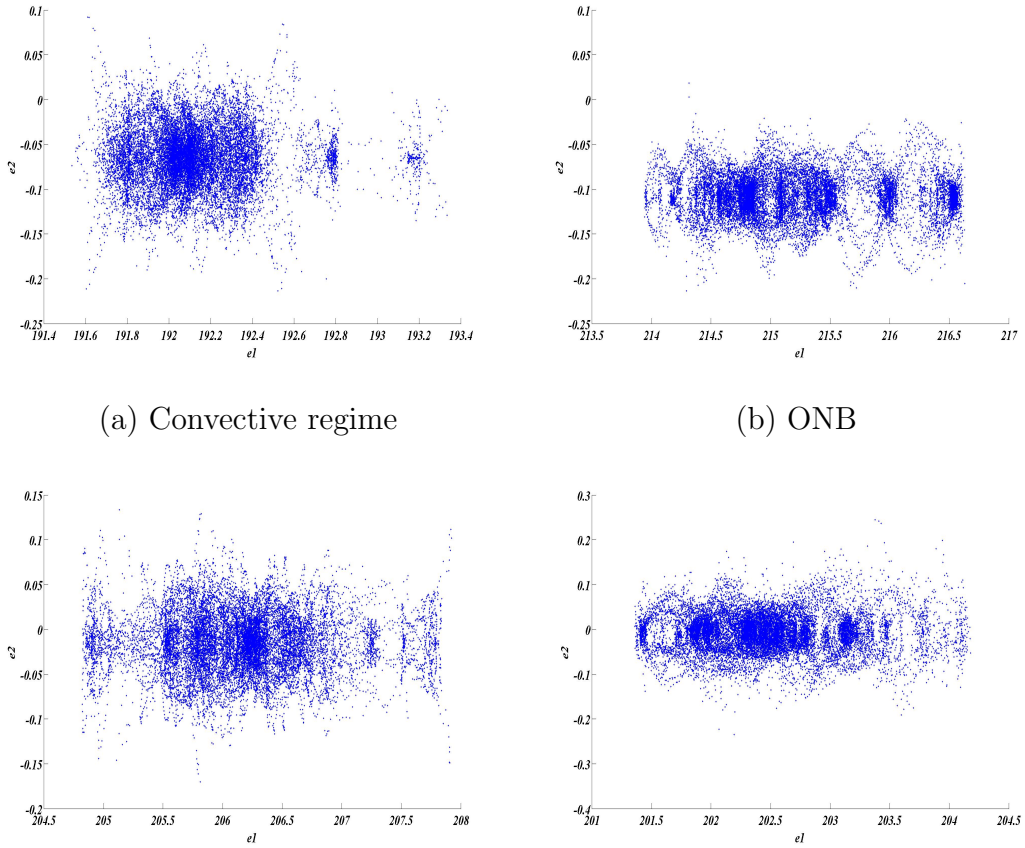

(a) Convective regime

(b) ONB

(c) PNB

(d) PNB

Fig. 67.: Phase plots for saturated pool boiling on CNT coated surface after noise reduction obtained from principal component analysis.

boiling over the bare surface shows no clear geometrical structure in most PNB points. This is a result of reduced number of nucleation sites at low heat flux levels in sub-cooled boiling compared to saturated boiling. Overall, it is inferred that increase in heat flux results in appearance of deterministic dynamics.

4. Correlation dimensions

The plot of correlation sum vs. space scale for the noisy data showed oscillations due to the presence of lacunarity. The variation of correlation sum with space scale is shown in figure 68. No saturation in slopes is visible in convective, ONB and PNB regimes. The slope of the correlation sum does not saturate in the convective regime and shows a slope of 7.7 at an embedding dimension of 15. At ONB, the slope is 7.73 corresponding to an embedding dimension of 15. The slope of correlation sum versus space scale does not saturate and rane from 6.79 - 9.7 corresponding to an embedding dimension of 15. Fig. 69 depicts the plot of correlation sum vs. space scale after noise reduction. A clear saturation in slopes is not present in any of the test cases. Some saturation in the slopes is observed at ONB and in PNB. However, a detailed analysis of slopes did not reveal signs of saturation. The estimated values of correlation 'dimensions' for an embedding dimension of 15, ranged from 7.37 - 8.58.

Based on the correlation sum, no change in dynamics is evident in PNB on the MWCNT coated substrate compared to the bare surface. Although no evidence of saturation is observed in pool boiling over either of the surfaces, the space time separation plots and phase plots show the emergence of clear geometric structures within PNB at higher wall superheat levels. This is indicative of deterministic dynamics within the system. However, the presence of noise in the system results in reduction of the saturation region. A clear interpretation of dynamics is however, not possible due to the contradiction between correlation dimensions and the phase plots. CHF

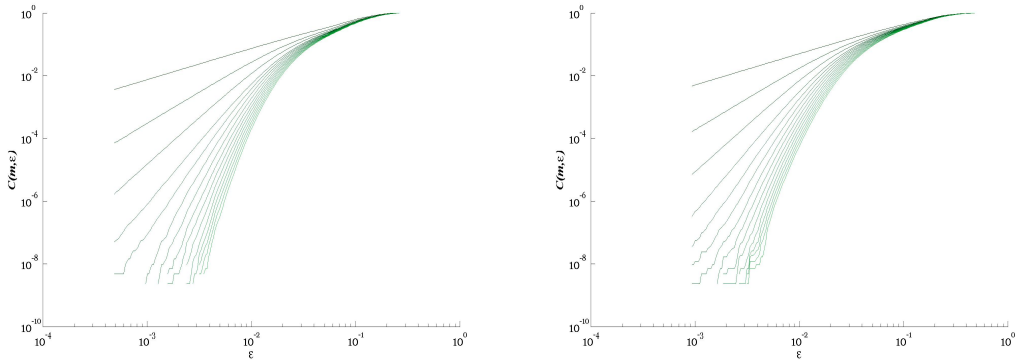

(a) Convective regime

(b) ONB

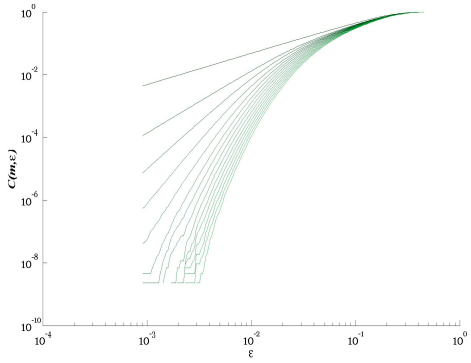

(c) PNB

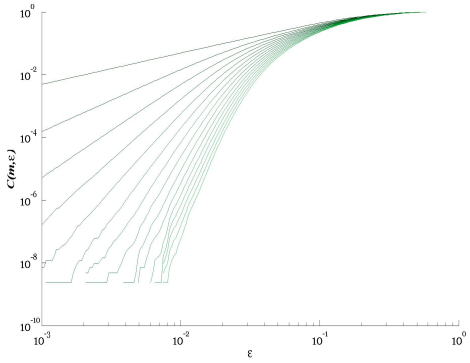

(d) PNB

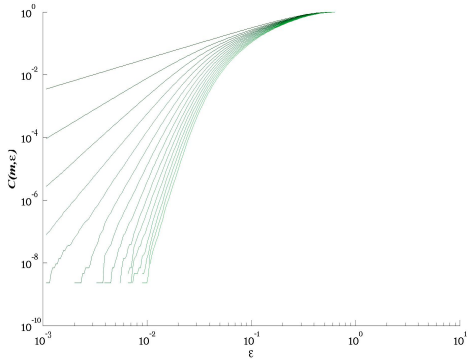

(e) PNB

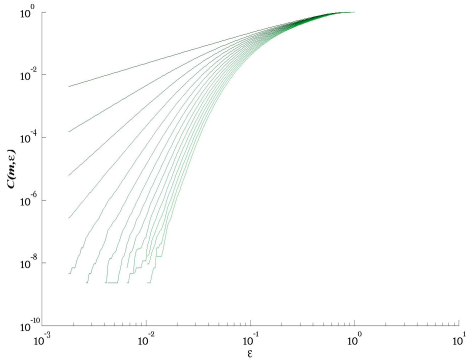

(f) PNB

Fig. 68.: Variation of correlation sum with space scale for saturated pool boiling on CNT coated surface after noise reduction.

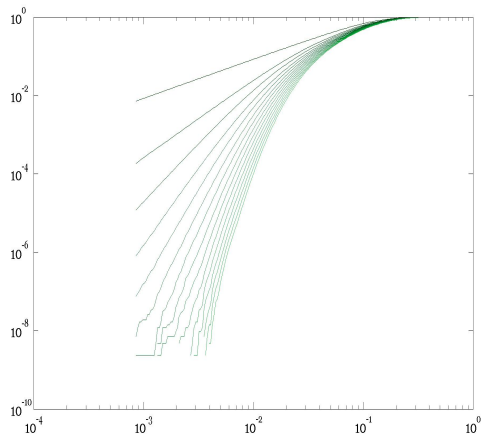

(a) Convective Regime

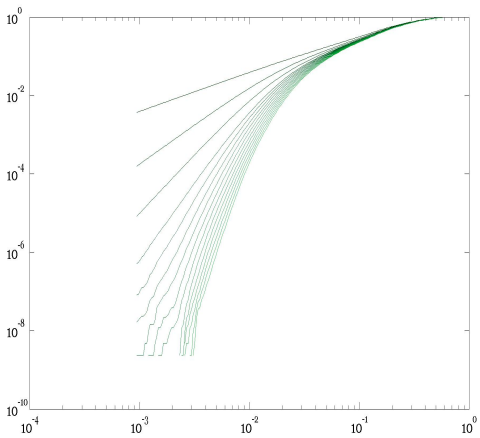

(b) ONB

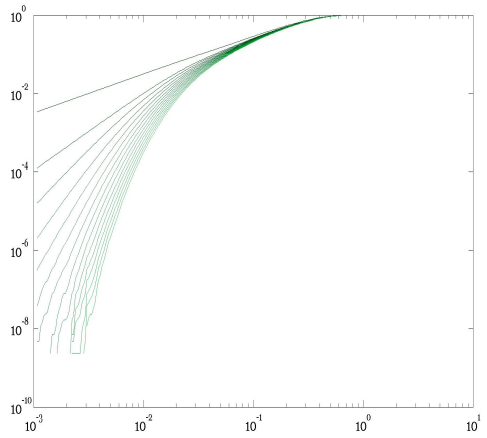

(c) PNB

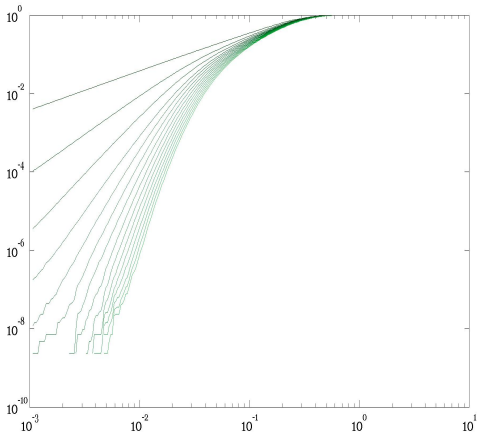

(d) PNB

Fig. 69.: Correlation sums of subcooled pool boiling on CNT coated substrate after noise reduction.

and film boiling regimes were not sustained in the tests for CNT coated substrates therefore, the impact of surface texturing on dynamics in these regimes could not be ascertained.

5. Lyapunov exponents & surrogate data analysis

Table IX and X summarize the Lyapunov spectrum and correlation dimension estimates. No convergence in correlation dimenson estimates is observed. Surrogate data tests failed in all cases and no robust, positive Lyapunov exponents were estimated. Similar behavior was observed in saturated pool boiling over a bare silicon wafer in convective, ONB and PNB regimes. No clear change in dynamics occurrs due to presence of carbon nanotubes on the test surface based on the slopes of the correlation sums and Lyapunov spectrum. Significant changes in dynamics could be present in FDNB, near CHF and film boiling but these reimes could not be sustained in the present tests. However, based on phase-plots the presence of multiply-periodic dynamics can be inferred.

Positive Lyapunov exponents are observed in all but one of the test conditions (Table X). The positive exponents in the convective regime ($T_{top-heater} \sim 62.26$ ℃) is close to zero and may very well be negative (in reality). The surface temperature fluctuations show only high frequency periodic fluctuations (noise) which is partially responsible for the false Lyapunov exponent. The positive exponent at ONB and the corresponding K-Y dimension of 1.159 seem to be false as no saturation in the correlation dimension plots are visible and the Fourier spectrum indicates multiple periodicities. At a higher heat flux level of 1.57 W/cm^2, a positive Lyapunov exponent of 0.1708 is calculated. A K-Y dimension of 2.038 suggests either chaotic or quasi-periodic dynamics. However, the correlation dimension plots fail to show any saturation in slopes. Therefore, it is not clear whether chaotic or quasi-periodic dynamics exists under these conditions.

D. Discussion & Summary of Results

Shoji and Takagi [19] investigated bubbling from isolated artificial cavities of conical, cylindrical and reentrant types, with diameters of 50 and 100 μm and depths of 30 and 50 μm. Phase portraits for the conical cavities showed the change of temperature fluctuations from a bi-periodic state to a chaotic state as heat flux was increased. Correlation dimensions ranged from 0.49 - 2.31. Maximum Lyapunov exponents ranging from -0.31 to 38.5 were estimated. Phase portraits and correlation dimensions could not be plotted for cylindrical and reentrant cavities due to small temperature fluctuations. From the aforementioned observations, it is concluded that nucleation from a single nucleation site is sensitive to the geometry of cavities and the heat flux level. Depending on heat flux, the dynamics of temperature fluctuations can change from simple periodic states to chaotic states.

Table IX.: Saturated pool boiling: Exponents & dimensions

$T_s(℃)$	$\Delta\ T_{Cu}(℃)$	$q"(W/cm^2)$	λ_{robust}	K-Y	D_C[†]	*Dynamics*	*T.R.A*
45.7	65.4	1.04	-1.03 ± 0.06, -1.34 ± 0.1, -1.82 ± 0.19	0	7.7	Fixed point	×
46.3	71.7	1.68	-0.05 ± 0.02, -0.72 ± 0.05, -1.07 ± 0.09, -1.99 ± 0.15	0	7.73	Fixed point	×
45.7	78.7	2.56	-0.06 ± 0.03, -1.17 ± 0.11, -1.62 ± 0.14	0	6.79	Fixed point	×
44.1	85.8	3.62	-0.03 ± 0.02, -0.14 ± 0.03, -0.59 ± 0.04, -1.06 ± 0.08	0	9.13	Periodic	×
42.7	97.9	5.26	-0.03 ± 0.01, -0.24 ± 0.03, -0.63 ± 0.05, -1.14 ± 0.09	0	9.7	Fixed point	×
39.6	111.6	7.29	-0.03 ± 0.02, -0.44 ± 0.03, -0.54 ± 0.03, -1.29 ± 0.1	0	7.46	Fixed point	×

[b]Estimate Converged

Table X.: 10 ℃ Subcooled pool boiling: Exponents & dimensions

$T_s(℃)$	$\Delta\ T_{Cu}(℃)$	$q"(W/cm^2)$	λ_{robust}	K-Y	$D_C{}^{\dagger}$	*Dynamics*	*T.R.A*
49.8	62.3	0.17	-0.02 ± 0.01, -0.07 ± 0.02, -0.26 ± 0.02,-0.37 ± 0.04	0	7.01	Fixed point	×
55.5	75.0	0.79	0.01 ± 0.01, -0.03 ± 0.01, -0.08 ± 0.01, -0.15 ± 0.03, -1.57 ± 0.25	0	6.69	Fixed point	×
53.3	83.6	1.57	-0.60 ± 0.06, -1.10 ± 0.10, -1.87 ± 0.25	0	5.45	Fixed point	×
52.3	92.7	2.69	-0.34 ± 0.04, -0.81 ± 0.11, -1.26 ± 0.18	0	7.09	Fixed point	×

[b]Estimate Converged

Pasamehmetoglu and Nelson [82] computationally investigated the effect of site location on bubble departure frequency and local heat flux. The thermal interaction between nucleating cavities through conduction within the heater were observed. The time and area averaged surface temperatures were found to depend on the site distribution. The maximum wall superheat and surface averaged wall superheat increased with increasing non-uniformity in site distribution. Mosdorf and Shoji [20] investigated chaos in nucleate boiling over a single nucleation site and showed the existence of low-dimensional deterministic chaos. In the same study, thermo-hydraulic interactions between artificial nucleating sites was investigated and a model was proposed to explain the onset of chaotic dynamics and site bubble emission synchronization. Furthermore, the distribution of active sites in the computational model was observed to vary in time in a chaotic manner. To summarize:

1. the size and shape of a nucleating cavity affects the bubble departure (and hence the surface temperature) dynamics

2. the surface temperature fluctuations are sensitive to the instantaneous, active site distribution

3. depending on the distance between nucleating sites, thermal and hydraulic interactions can influence bubble departure dynamics and the active site distribution

4. chaotic dynamics is present in pool boiling systems and is low-dimensional for single nucleation sites but rapidly increases in complexity for multiple nucleation sites

5. the dynamics has a spatial (site distribution) and temporal component (bubble emission frequencies)

The aforementioned studies and the studies mentioned in chapter II, literature review have been confined to few heat flux levels. Barring the study of [70] on a small size wire, no other study has been conducted on a large size heater encompassing nucleate boiling, CHF and film boiling regimes. The hydrodynamic features of each of these regimes is different as confirmed by visual observations of studies in open literature. Pool boiling tests on the plain surface clearly shows the difference in dynamics. In many test cases, in both saturated and subcooled pool boiling, correlation dimensions converged and positive Lyaunov exponents were estimated. Clear evidence of chaos was observed in FDNB, CHF and in some cases in the film boiling regime. The effects of noise and other artefacts made it difficult to estimate the actual dimensionality of the system. It is clear from the results though, that FDNB, CHF and film boiling differ significantly from nucleate boiling in terms of dynamics. Phase plots from singular value decomposition show variations in attractor geometry with heat flux levels indicating a change in the nature of surface temperature fluctuations and by extension a change in active site distributions. The attractor geometry differs from one run to another for the same test conditions. This is indicative of variations in active site distribution. The number of active frequencies increases with increasing heat flux as seen in the power spectrum thereby supporting this conclusion. Some convergence in dimension estimates was also observed in PNB especially at higher wall superheat levels where significant number of nucleation sites were active. The effect of surface texturing on dynamics of pool boiling appears minimal based on correlation dimension estimates. The phase space separation plots indicate the presence of multiply periodic behavior in PNB for both, the plain and the textured surface. In CHF, film boiling and FDNB the points appear to fill the pseudophase-space indicating the onset of chaotic temperature fluctuations. The correlation dimension estimates in film boiling did not converge in many cases possibly due to turbulence in the vapor

film. Chai et al. [131] proposed a new model for predicting heat fluxes considering site interactions and non-linear aspects of the bubble growth process. The predictions of the proposed model compared favorably with experimental nucleate boiling data for four different fluids quite well. The study showed the non-linear characteristics of bubble growth processes. At low wall superheat, bubble diameters damped with time whereas at higher wall superheats, bubble sizes were predicted to vary periodically with time and at still higher superheat levels, chaotic fluctuations in bubble size was predicted. The present study confirms this trend. At low wall superheat levels, the structure of the attractor is a fixed point with very low temperature fluctuations. At higher wall superheat levels, multiply periodic behavior is observed (due to multiple nucleation sites) followed by chaotic surface temperature fluctuations in FDNB, near CHF and in film-boiling.

E. Concluding Remarks

In the range of heat fluxes tested, no perceptible enhancement in heat transfer rates were observed due to presence of MWCNT on the surface. Compared to fluctuations on the silicon surface, temperature excursions on the textured surface are less frequent. However, the overall magnitude of temperature fluctuation appears to be constant. The Fourier spectra shows the existence of few dominant periodicities with an underlying broadband spectrum spanning 0 - 5 Hz. This broadband spectrum may be a result of noise.

The CNT coated surface did not show a clear evidence of chaotic dynamics in the regimes investigated. For the relatively low heat-flux levels tested in this study, no significant difference could be observed in the dynamics of pool boiling due to surface texturing. However, the dynamics may differ at high heat fluxes. The high heat flux

regimes could not be sustained in the present study due to failure of the TFT.

CHAPTER VII

SUMMARY OF ACCOMPLISHMENTS & RECOMMENDATIONS FOR FUTURE WORK

The following has been accomplished as a part of this study.

1. Pool boiling experiments have been conducted under saturated and sub-cooled conditions with surface micro-machined TFT on substrates with and without MWCNT. Surface temperature measurements were obtained during these tests.

2. Pool boiling curves were generated for the various tests and non-linear analysis, conducted on the surface temperature measurements acquired by the TFT spanning commonly encountered pool boiling regimes.

3. Attractor geometries have been successfully reconstructed in pseudo phase space using the measured temperature time-series and SVD.

4. Quantifiers such as, correlation dimensions and Lyapunov exponents varied with wall superheat and sub-cooling level in FDNB, at CHF and in film-boiling, indicating the change in underlying dynamics of boiling.

5. FDNB and CHF exhibit low-dimensional chaos. Most film-boiling points exhibit low-dimensional chaos.

6. Surrogate data tests using time-reversal asymmetry confirm the presence of chaotic dynamics in FDNB, near CHF and in film boiling in most test cases, confirming the presence of low-dimensional deterministic chaos.

7. FDNB, CHF and in some cases, film boiling, showed low correlation dimension estimates ($\sim$ 4 - 5) implying low-dimensional chaos.

8. The CNT coated surfaces did not show the presence of chaotic dynamics in the convective, ONB and low heat flux PNB regimes.

A. Potential Applications

Currently, electronic applications develop hotspots due to non-uniformity in power distribution. Prevention of these hotspots is crucial to reliable functioning of these devices. The TFT used in this study can be employed as an on-chip sensor to measure surface temperature fluctuations reliably. Subsequently, the TFT signals can be employed in a suitable feedback control loop to prevent the occurence of hotspots.

The presence of non-linear dynamics near CHF, in FDNB and in film-boiling shows a significant need for the development of new models geared towards electronics cooling applications where surface temperatures are of paramount importance. Global and local non-linear models can be employed for this purpose.

B. Scope for Future Work

There is a significant scope for further study in this area. Improvements are needed in the thin-film sensor design to reduce the effects of noise and poor contact at the bondpads. The former would require some kind of sheathing (possibly using photoresist) whereas the latter could be accomplished by wire-bonding. Additionally, the following areas could be part of separate studies:

1. Existing test instrumentation/micro-sensors need to be improved. For eg. new ceramic based TFT or diode-based sensors could be used to provide more reliable surface temperature measurement as opposed to K-type TFT. The K-type TFT is unable to withstand high temperatures within the CNT synthesis furnace and its characteristics change.

2. A new test section needs to be constructed to allow simultaneous high-speed visualization along the entire test surface for all heat flux regimes. Alternative techniques such as liquid crystal thermography can be explored for this purpose.

3. The dynamics in transition boiling regime has not been studied by any research group. A new test-facility needs to be designed for this purpose using micro-heaters or steam/vapor heating.

4. Currently, a lot of attention has been devoted to nano-fluids and spray cooling for electronic chip cooling applications. Tests should be conducted with different substrates (e.g. nanotextured, different heater material etc.) and nano-fluids under saturated and sub-cooled conditions to assess the dynamics and the dependence of quantifiers on the surface-fluid combination.

5. Non-linear prediction has not been explored as a part of this study. Time-series prediction and forecasting are the end-goals of time-series analysis. Various methods exist within the TISEAN package for purposes of prediction and forecasting. The results of the present study can be employed to develop map-like models on the attractor geometry.

6. Computational studies can be conducted to using the coupled map lattice approach to study the spatio-temporal characteristics of the boiling process.

REFERENCES

[1] J. Parry, R. Jukka, L. Clemens, Temperature and reliability in electronics systems – The missing link, Electronics Cooling Magazine 7 (4).

[2] J. Altet, S. Grauby, S. Volz, Advanced techniques for IC surface temperature measurement, Electronics Cooling Magazine 8 (1).

[3] ITRS, The next step in assembly and packaging: System level integration in the package (SiP), Tech. rep., International Technology Roadmap for Semiconductors (2007).

[4] V. Carey, Liquid-vapor Phase-change Phenomena: An Introduction to the Thermophysics of Vaporization and Condensation Processes in Heat Transfer Equipment, Taylor & Francis, Washington D.C., 2007, pp. 210–211, 222–245.

[5] P. Sadasivan, C. Unal, R. Nelson, Perspective: Issues in CHF modeling: The need for new experiments, Journal of Heat Transfer 117 (1995) 558.

[6] M. Buchholz, T. Lüttich, H. Auracher, W. Marquardt, Experimental investigation of local processes in pool boiling along the entire boiling curve, International Journal of Heat and Fluid Flow 25 (2) (2004) 243–261.

[7] T. Lüttich, W. Marquardt, M. Buchholz, H. Auracher, Identification of unifying heat transfer mechanisms along the entire boiling curve, International Journal of Thermal Sciences 45 (3) (2006) 284–298.

[8] J. Myers, V. Yerramilli, S. Hussey, G. Yee, J. Kim, Time and space resolved wall temperature and heat flux measurements during nucleate boiling with constant heat flux boundary conditions, International Journal of Heat and Mass Transfer 48 (12) (2005) 2429–2442.

[9] D. Banerjee, V. Dhir, Study of subcooled film boiling on a horizontal disc: Part 2 – Experiments, Journal of Heat Transfer 123 (2001) 285–293.

[10] D. Kenning, Wall temperature patterns in nucleate boiling, International Journal of Heat and Mass Transfer 35 (1) (1992) 73–86.

[11] C. Chang, R. Lahey, Analysis of chaotic instabilities in boiling systems, Nuclear Engineering and Design 167 (3) (1997) 307–334.

[12] V. Dhir, H. Abarajith, G. Warrier, From nano to micro to macro scales in boiling, Microscale Heat Transfer-Fundamentals and Applications: Proceedings of the NATO Advanced Study Institute on Microscale Heat Transfer-Fundamentals and Applications in Biological and Microelectromechanical Systems, Cesme-Izmir, Turkey, July 18-30 2004 (2005) 197.

[13] M. Cross, P. Hohenberg, Pattern formation outside of equilibrium, Reviews of Modern Physics 65 (3) (1993) 851–1112.

[14] A. Kitron, T. Elperin, A. Tamir, Stochastic modeling of boiling-site interaction, Physical Review A 44 (2) (1991) 1237–1246.

[15] R. Mallozzi, R. Judd, N. Balakrishnan, Investigation of randomness, overlap and the interaction of bubbles forming at adjacent nucleation sites in pool boiling, International Journal of Heat and Mass Transfer 43 (18) (2000) 3317–3330.

[16] R. Judd, On nucleation site interaction, Journal of Heat Transfer 110 (2) (1988) 475–478.

[17] R. Judd, A. Chopra, Interaction of the nucleation processes occurring at adjacent nucleation sites, Journal of Heat Transfer 115 (4) (1993) 955–962.

[18] D. Banerjee, G. Son, V. Dhir, Conjugate thermal and hydrodynamic analyses of saturated film boiling from a horizontal surface, ASME Heat Transfer Div Publ HTD 334 (3) (1996) 57–64.

[19] M. Shoji, Y. Takagi, Bubbling features from a single artificial cavity, International Journal of Heat and Mass Transfer 44 (14) (2001) 2763–2776.

[20] R. Mosdorf, M. Shoji, Chaos in nucleate boiling–nonlinear analysis and modelling, International Journal of Heat and Mass Transfer 47 (6-7) (2004) 1515–1524.

[21] M. Shoji, Studies of boiling chaos: A review, International Journal of Heat and Mass Transfer 47 (6-7) (2004) 1105–1128.

[22] K. Falconer, Fractal Geometry: Mathematical Foundations and Applications, Wiley, New York, 1990.

[23] H. Peitgen, H. Jurgens, D. Saupe, Chaos and Fractals, Springer Verlag, New York, 2004, pp. 605–713.

[24] P. Grassberger, I. Procaccia, Characterization of strange attractors, Physical Review Letters 50 (5) (1983) 346–349.

[25] A. Weigend, N. Gershenfeld, Time series prediction: Forecasting the future and understanding the past, in: Santa Fe Institute Studies in the Sciences of Complexity, Proceedings of the NATO Advanced Research Workshop on Comparative Time Series Analysis, held in Santa Fe, New Mexico, May 14–17, 1992, Reading, MA: Addison–Wesley,1994, edited by Weigend, Andreas S.; Gershenfeld, Neil A., 1994.

[26] T. Sauer, J. Yorke, M. Casdagli, Embedology, Journal of Statistical Physics 65 (3) (1991) 579–616.

[27] J. W. Palen, Shell and Tube Reboilers, in: G. F. Hewitt (Ed.), Handbook of Heat Exchanger Design, Hemisphere Pub. Corp., New York, 1990, pp. 200–400.

[28] M. Jakob, W. Linke, Effect of surfactant on boiling heat transfer, Phys. Z 36 (2).

[29] T. Drew, A. Mueller, Boiling, Transactions of AIChE 33 (1937) 449–471.

[30] S. Nukiyama, The maximum and minimum values of the heat Q transmitted from metal to boiling water under atmospheric pressure (English translation of the original paper published in Journal Japan Soc. Mech. Engrs vol. 37, 367-374 (1934)), Int. J. Heat and Mass Transfer 9 (1966) 1419–1433.

[31] E. Farber, R. Scorah, Heat transfer to water boiling under pressure, Trans. ASME 70 (4) (1948) 369–384.

[32] V. Dhir, Boiling heat transfer, Annual Review of Fluid Mechanics 30 (1) (1998) 365–401.

[33] V. Dhir, Boiling and two-phase flow in porous media, Ann. Rev. Heat Transfer 5 (1994) 303–350.

[34] R. Macbeth, Boiling on surfaces overlaid with a porous deposit: Heat transfer rates obtainable by capillary action, Tech. rep., AEEW-R–711, Atomic Energy Establishment, Winfrith (England) (1971).

[35] S. Liter, M. Kaviany, Pool-boiling CHF enhancement by modulated porous-layer coating: Theory and experiment, International Journal of Heat and Mass Transfer 44 (22) (2001) 4287–4311.

[36] T. Collier, J. Thome, J. Collier, Convective Boiling and Condensation, 3rd Edition, Oxford University Press, Oxford, Great Britain.

[37] C. Ramaswamy, Y. Joshi, W. Nakayama, W. Johnson, Effects of varying geometrical parameters on boiling from microfabricated enhanced structures, Journal of Heat Transfer 125 (2003) 103.

[38] J. Coursey, H. Roh, J. Kim, P. Boudreaux, Graphite foam thermosyphon evaporator performance parametric investigation of the effects of wWorking fluid, liquid level and chamber pressure, Proceedings of IMECE200 (2002) 1–6.

[39] C. Li, Z. Wang, P. Wang, Y. Peles, N. Koratkar, G. Peterson, Nanostructured copper interfaces for enhanced boiling, Small 4 (8) (2008) 1084–1088.

[40] V. Sathyamurthi, H. Ahn, D. Banerjee, S. Lau, Subcooled pool boiling experiments on horizontal heaters coated with carbon nanotubes, Journal of Heat Transfer 131 (2009) 071501.

[41] J. Chang, S. You, Enhanced boiling heat transfer from micro-porous surfaces: Effects of a coating composition and method, International Journal of Heat and Mass Transfer 40 (18) (1997) 4449–4460.

[42] H. Honda, H. Takamastu, J. Wei, Enhanced boiling of FC-72 on silicon chips with micro-pin-fins and submicron-scale roughness, Journal of Heat Transfer 124 (2002) 383–390.

[43] A. Oberline, M. Endo, T. Koyama, High resolution electron microscope observations of graphitized carbon fibers, Carbon 14 (1976) 133–135.

[44] A. Oberlin, M. Endo, T. Koyama, Filamentous growth of carbon through benzene decomposition, J. Cryst. Growth 32 (3) (1976) 335–349.

[45] M. Endo, A. Oberlin, T. Koyama, High resolution electron microscopy of graphitizable carbon fiber prepared by benzene decomposition, Japanese Journal of Applied Physics 16 (9) (1977) 1519–1523.

[46] S. Iijima, et al., Helical microtubules of graphitic carbon, Nature 354 (6348) (1991) 56–58.

[47] M. Dresselhaus, P. Eklund, Phonons in carbon nanotubes, Advances In Physics 49 (6) (2000) 705–814.

[48] J. Hone, M. Whitney, C. Piskoti, A. Zettl, Thermal conductivity of single-walled carbon nanotubes, Physical Review B 59 (4) (1999) 2514–2516.

[49] J. Che, T. Çagin, W. Goddard III, Thermal conductivity of carbon nanotubes, Nanotechnology 11 (2000) 65–69.

[50] S. Berber, Y. Kwon, D. Tománek, Unusually high thermal conductivity of carbon nanotubes, Physical Review Letters 84 (20) (2000) 4613–4616.

[51] P. Kim, L. Shi, A. Majumdar, P. McEuen, Thermal transport measurements of individual multiwalled nanotubes, Physical Review Letters 87 (21) (2001) 215–502.

[52] W. Yi, L. Lu, Z. Dian-lin, Z. Pan, S. Xie, Linear specific heat of carbon nanotubes, Physical Review B 59 (14) (1999) 9015–9018.

[53] H. Ahn, N. Sinha, M. Zhang, D. Banerjee, S. Fang, R. Baughman, Pool boiling experiments on Multiwalled Carbon Nanotube (MWCNT) forests, Journal of Heat Transfer 128 (2006) 1335.

[54] S. Ujereh, T. Fisher, I. Mudawar, Effects of carbon nanotube arrays on nucleate pool boiling, International Journal of Heat and Mass Transfer 50 (19-20) (2007) 4023–4038.

[55] J. Mitrovic, How to create an efficient surface for nucleate boiling?, International Journal of Thermal Sciences 45 (1) (2006) 1–15.

[56] N. Acharya, M. Sen, E. Ramos, Periodicity and bifurcations in capillary tube boiling with a concentric heating wire, International Journal of Heat and Mass Transfer 46 (8) (2003) 1425–1442.

[57] L. Zhang, M. Shoji, Nucleation site interaction in pool boiling on the artificial surface, International Journal of Heat and Mass Transfer 46 (3) (2003) 513–522.

[58] Z. Lei, M. Shoji, Aperiodic bubble formation from a submerged orifice, Chemical Engineering Science 56 (18) (2001) 5371–5381.

[59] A. Tufaile, J. Sartorelli, Chaotic behavior in bubble formation dynamics, Physica A: Statistical Mechanics and its Applications 275 (3-4) (2000) 336–346.

[60] A. Tufaile, J. Sartorelli, Henon-like attractor in air bubble formation, Physics Letters A 275 (3) (2000) 211–217.

[61] J. Cieslinski, R. Mosdorf, Gas bubble dynamics – Experiment and fractal analysis, International Journal of Heat and Mass Transfer 48 (9) (2005) 1808–1818.

[62] D. Kondepudi, I. Prigogine, Modern Thermodynamics: From Heat Engines to Dissipative Structures, John Wiley, New York, 1998.

[63] I. Mudawar, Assessment of high-heat-flux thermal management schemes, IEEE Transactions on Components and Packaging Technologies 24 (2) (2001) 122–141.

[64] T. Li, J. Yorke, Period three implies chaos, Amer. Math. Monthly 82 (10) (1975) 985–992.

[65] M. Shoji, R. Mosdorf, L. Zhang, Y. Takagi, K. Yasui, M. Yokota, Features of boiling on an artificial surface: Bubble formation, wall temperature fluctuation and nucleation site interaction, Journal of Thermal Science 11 (3) (2002) 226–234.

[66] M. Shoji, L. Zhang, Boiling on an artificial surface – Bubbling features and nucleation site interaction, in: Proceedings of the Twentieth UIT National Heat Transfer Conference, Maratea, Italy, 2002, pp. 37–42.

[67] L. Zhang, M. Shoji, Nucleation site interaction in pool boiling–Experimental study by employing artificial boiling surface, in: Proceedings of the Fifth ASME-JSME Thermal Engineering Joint Conference, Hawaii, March, 2003, pp. 16–20.

[68] M. Shoji, N. Negishi, H. Hatae, Y. Haramura, Nonlinear chaotic characteristics of saturated pool boiling of water on a horizontal copper surface, in: National Heat Transfer Symposium Of Japan, Vol. 33, 1996, pp. 253–254.

[69] J. Ellepola, D. Kenning, Nucleation site interactions in pool boiling, in: Proceedings of the 2nd European Thermal-Sciences and 14th UIT National Heat Transfer Conference, Vol. 3, 1996, pp. 1669–1675.

[70] M. Shoji, T. Kohno, N. Negishi, S. Toyoshima, A. Maeda, T. Bunkyo-ku, Chaos in boiling on a small-size heater, in: Proceedings, Japan Society of Mechanical Engineers, 1983.

[71] P. Hohenberg, B. Halperin, Theory of dynamic critical phenomena, Reviews of Modern Physics 49 (3) (1977) 435–479.

[72] H. Greenside, M. Cross, Stability analysis of two-dimensional models of three-dimensional convection, Physical Review A 31 (4) (1985) 2492–2501.

[73] H. Haken, Synergetics: Introduction and Advanced Topics, Springer Verlag, Berlin, 2004.

[74] T. Yanagita, Coupled map lattice model for boiling, Phys. Lett. A 165 (5/6) (1992) 405–408.

[75] T. Yanagita, Phenomenology of boiling: A coupled map lattice model, Chaos: An interdisciplinary journal of nonlinear science 2 (9) (1992) 343–350.

[76] M. Shoji, K. Tajima, Mathematical simulation model of boiling: Modes and chaos, in: Convective Flow and Pool Boiling Conference, Session X: Pool Boiling, Kloster Irsee, 1997.

[77] R. Mosdorf, Modeling of surface temperature fluctuation in nucleate boiling using two-dimensional model, Arch. Termodyn 21 (1999) 29–42.

[78] R. Mosdorf, Chaotic oscillations of the heating surface temperature, Arch. Thermodyn 22 (2001) 2–16.

[79] R. Mosdorf, Chaotic phenomena accompanying vapor bubbles generation in boiling, Sci. Mach 54 (2002) 158–161.

[80] R. Mosdorf, Modelling of heating surface temperature fluctuations in nucleate boiling using two-dimensional model, Archives of Thermodynamics 21 (1-2) (2000) 29–42.

[81] R. Mosdorf, Modeling of micro-convection around the vapor bubbles in a long period of time, in: CD Version of the International Conference on Multi-Phase Flow, Vol. 98.

[82] K. Pasamehmetoglu, R. Nelson, Cavity-to-cavity interaction in nucleate boiling: The effect of heat conduction within the heater, AIChE J. Symp. Ser. 283 (87) (1991) 342–351.

[83] R. Nelson, A. Bejan, Self-organization of the internal flow geometry in convective heat transfer, Tech. rep., LA-UR-2376, Los Alamos National Laboratory Report, Los Alamos (1997).

[84] L. Chai, M. Shoji, Thermodynamics bifurcations of boiling structure, International Journal of Heat and Mass Transfer 45 (23) (2002) 4675–4682.

[85] H. Kantz, T. Schreiber, Nonlinear Time Series Analysis, Cambridge University Press, England, 2004.

[86] J. Ellepola, P. McSharry, D. Kenning, Is nucleate boiling chaotic?(And who cares?), in: Proceedings Eurotherm Seminar, Vol. 48, Marvillet, EFS, Pisa, pp. 17–24.

[87] R. Mosdorf, P. Cheng, H. Wu, M. Shoji, Non-linear analyses of flow boiling in microchannels, International Journal of Heat and Mass Transfer 48 (21-22) (2005) 4667–4683.

[88] G. Lorenzini, C. Biserni, A vapotron effect application for electronic equipment cooling, Journal of Electronic Packaging 125 (2003) 475.

[89] C. Biserni, A. Fichera, I. Guglielmino, E. Lorenzini, A. Pagano, A non-linear approach for the analysis and modelling of the dynamics of systems exhibiting

Vapotron effect, International Journal of Heat and Mass Transfer 49 (7-8) (2006) 1264–1273.

[90] D. Kenning, Y. Yan, Pool boiling heat transfer on a thin plate: Features revealed by liquid crystal thermography, International Journal of Heat and Mass Transfer 39 (1996) 3117–3138.

[91] L. Harris, E. Johnson, The technique of sputtering sensitive thermocouples, Review of Scientific Instruments 5 (2004) 153.

[92] R. Marshall, L. Atlas, T. Putner, The preparation and performance of thin film thermocouples, Journal of Scientific Instruments 43 (3) (1966) 144–149.

[93] L. Bullis, Vacuum-deposited thin-film thermocouples for accurate measurement of substrate surface temperature, Journal of Scientific Instruments 40 (1963) 592–593.

[94] D. Assanis, F. Friedmann, A thin-film thermocouple for transient heat transfer measurements in ceramic-coated combustion chambers, International Communications in Heat and Mass Transfer 20 (4) (1993) 459–468.

[95] D. Debey, R. Bluhm, N. Habets, H. Kurz, Fabrication of planar thermocouples for real-time measurements of temperature profiles in polymer melts, Sensors & Actuators: A. Physical 58 (3) (1997) 179–184.

[96] X. Tian, F. Kennedy, J. Deacutis, A. Henning, The development and use of thin film thermocouples for contact temperature measurement, Tribology Transactions 35 (3) (1992) 491–499.

[97] M. Laugier, The construction and use of thin film thermocouples for the measurement of surface temperature: Applications to substrate temperature deter-

mination and thermal bending of a cantilevered plate during film deposition, Thin Solid Films 67 (1) (1980) 163–170.

[98] N. Sinha, Packaging and testing of thin film thermocouples for boiling studies, Master's thesis, Texas A&M University, College Station, TX, Dept. of Mechanical Engineering (2006).

[99] J. Wrbanek, G. Fralick, Thin film physical sensor istrumentation research and development at NASA Glenn research center, in: 52nd International Instrumentation Symposium, pp. 7–11.

[100] W. Miller Jr, Fabrication and calibration of micro temperature sensors on silicon for measurement of surface temperature during nucleate pool boiling in dielectric liquid., Ph.D. thesis, University Of Pennsylvania, Philadelphia, Pennsylvania, USA (1996).

[101] H. Ahn, V. Sathyamurthi, N. Sinha, S. Lau, D. Banerjee, Boiling experiments on vertically aligned carbon nanotubes and using surface micromachined Thin Film Thermocouple (TFT), in: AIAA/ASME Joint Thermophysics and Heat Transfer Conference Proceedings, 2006, pp. 84–93.

[102] R. Bentley, Handbook of Temperature Measurement: Theory and practice of thermoelectric thermometry, Springer Verlag, Singapore, 1998.

[103] V. Sathyamurthi, D. Banerjee, H. Sakamoto, J. Kim, Measurement of the fractal order of wall void fraction during nucleate boiling, International Journal of Heat and Fluid Flow 29 (1) (2008) 207–218.

[104] M. Di Ventra, S. Evoy, J. Heflin, Introduction to nanoscale science and technology, Springer Science and Business Media Inc., New York, 2004.

[105] M. Gad-el Hak, The MEMS Handbook: MEMS, design and fabrication, CRC press, Taylor & Francis, Florida, 2006.

[106] M. Dresselhaus, G. Dresselhaus, P. Avouris, Carbon nanotubes: synthesis, structure, properties, and applications, Springer Verlag, Berlin, 2001.

[107] P. De Gennes, F. Brochard-Wyart, D. Quéré, A. Reisinger, Capillarity and wetting phenomena: drops, bubbles, pearls, waves, Springer Science and Business Media Inc., New York, 2004.

[108] H. Abarbanel, Analysis of Observed Chaotic Data, Springer Verlag, New York, 1996.

[109] G. Nicolis, I. Prigogine, Exploring Complexity, Freeman, New York, 1989.

[110] S. Strogatz, Nonlinear Dynamics and Chaos, Addison-Wesley Reading, MA, 1994.

[111] E. Ott, T. Sauer, J. Yorke, Coping With Chaos, Wiley, New York, 1994.

[112] N. Packard, J. Crutchfield, J. Farmer, R. Shaw, Geometry from a time series, Physical Review Letters 45 (9) (1980) 712–716.

[113] T. Buzug, G. Pfister, Comparison of algorithms calculating optimal embedding parameters for delay time coordinates, Physica. D 58 (1-4) (1992) 127–137.

[114] M. Rosenstein, J. Collins, C. De Luca, Reconstruction expansion as a geometry-based framework for choosing proper delay times, Physica D 73 (1) (1994) 82–98.

[115] T. Buzug, G. Pfister, Optimal delay time and embedding dimension for delay-time coordinates by analysis of the global static and local dynamical behavior of strange attractors, Physical Review A 45 (10) (1992) 7073–7084.

[116] A. Fraser, H. Swinney, Independent coordinates for strange attractors from mutual information, Physical Review A 33 (2) (1986) 1134–1140.

[117] N. Marwan, M. Carmen Romano, M. Thiel, J. Kurths, Recurrence plots for the analysis of complex systems, Physics Reports 438 (5-6) (2007) 237–329.

[118] J. Eckmann, S. Kamphorst, D. Ruelle, Recurrence plots of dynamic systems, Europhys. Lett 4 (9) (1987) 973–977.

[119] J. Theiler, Spurious dimension from correlation algorithms applied to limited time-series data, Physical Review A 34 (3) (1986) 2427–2432.

[120] J. Theiler, Estimating fractal dimension, Optical Society of America, Journal, A: Optics and Image Science 7 (1990) 1055–1073.

[121] A. Provanzale, L. Smith, R. Vio, G. Murante, Distinguishing between low-dimensional dynamics and randomness in measured time series, in: Conference proceedings on Interpretation of time series from nonlinear mechanical systems, Elsevier North-Holland, Inc. New York, NY, USA, 1992, pp. 31–49.

[122] H. Schuster, W. Just, Deterministic Chaos an Introduction, Wiley–Vch, Weinheim, Germany, 1988.

[123] J. Sprott, Chaos and Time-Series Analysis, Oxford Univ Pr, Great Britain, 2003.

[124] P. Berenson, Film boiling heat transfer from a horizontal surface, J. Heat Transfer 83 (3) (1961) 351–358.

[125] S. van Stralen, R. Cole, Boiling Phenomena, Hemisphere, Washington, 1979.

[126] K. Kreider, D. Ripple, D. DeWitt, Calibration of thin-film thermocouples on silicon wafers, in: 7 th International Symposium on Temperature and Thermal Measurements in Industry and Science TEMPMECO 99, 1999, pp. 1–3.

[127] M. Arik, A. Bar-Cohen, Effusivity-based correlation of surface property effects in pool boiling CHF of dielectric liquids, International Journal of Heat and Mass Transfer 46 (20) (2003) 3755–3764.

[128] S. Glenn, Effects of carbon nanotube coating on bubble departure diameter and frequency in pool boiling on a flat, horizontal heater, Master's thesis, Texas A&M University, College Station, TX, Dept. of Mechanical Engineering (2009).

[129] F. Moon, Chaotic Vibrations, Wiley, New York, 1987.

[130] B. Mandelbrot, The Fractal Geometry of Nature, W. H Freeman and Company, New York, 1982.

[131] L. Chai, X. Peng, B. Wang, Nonlinear aspects of boiling systems and a new method for predicting the pool nucleate boiling heat transfer, International Journal of Heat and Mass Transfer 43 (1) (2000) 75–84.

APPENDIX A

EXPERIMENTAL DATA - BARE SILICON SURFACE

Temperature time-series record:

The temperature time-series record for all tests and functioning TFT for the bare silicon surface is summarized below. All signals were recorded for a duration of 18 seconds upon attainment of quasi-steady state conditions. Non-linear noise reduction was performed to reduce the noise-level in the signals. The magnitude of surface temperature fluctuations is observed to increase with an increase in the heat flux input. No single dominant periodicities are visible. The dominance of noise diminishes progressively from the convective regime to ONB, PNB, FDNB, CHF and film boiling.

While both functioning TFT were located within a 100 μm distance from one another, the signals at high heat fluxes do not appear to be strongly correlated. This is indicative of difference in spatial dynamics. A spatiotemporally chaotic system may spatially chaotic temporally regular, spatially regular temporally chaotic, spatially and temporally chaotic, spatially random temporally chaotic or spatially chaotic temporally random. The temperature time-series record shows the necessity for development of an array of sensors.

The magnitude and frequency of temperature fluctuations decreases with subcooling. It is reasonable to expect subcooling to limit the temperature excursions on the surface as a result of the cooler bulk fluid coming in contact with the heater surface during bubble departure. Additionally, at low heat fluxes the population density of the bubbles could be lower compared to saturated pool boiling.

Fourier Spectra

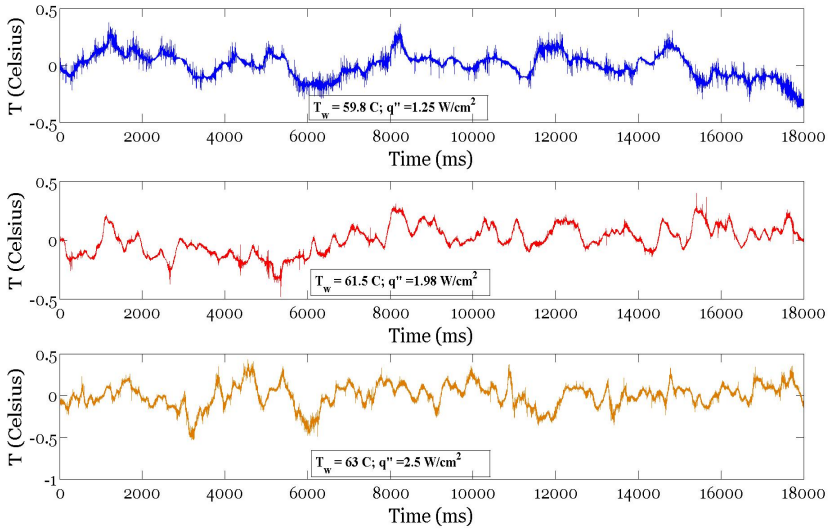

(a) Temperature fluctuation for a total time of 18 seconds

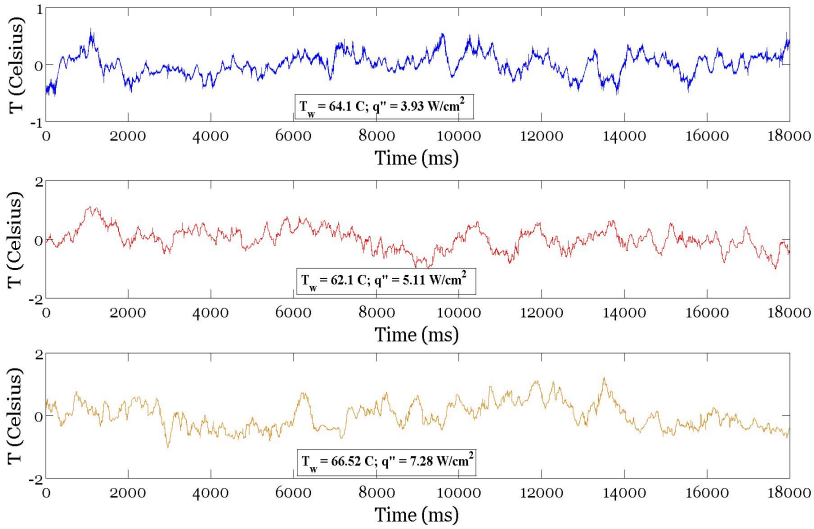

(b) Temperature fluctuation for a total time of 18 seconds

Fig. 70.: Surface temperature fluctuations recorded by TFT-3 (1000Hz), in saturated pool boiling (Run-I) 70(a) convective regime, ONB & 70(b) PNB, after noise-reduction.

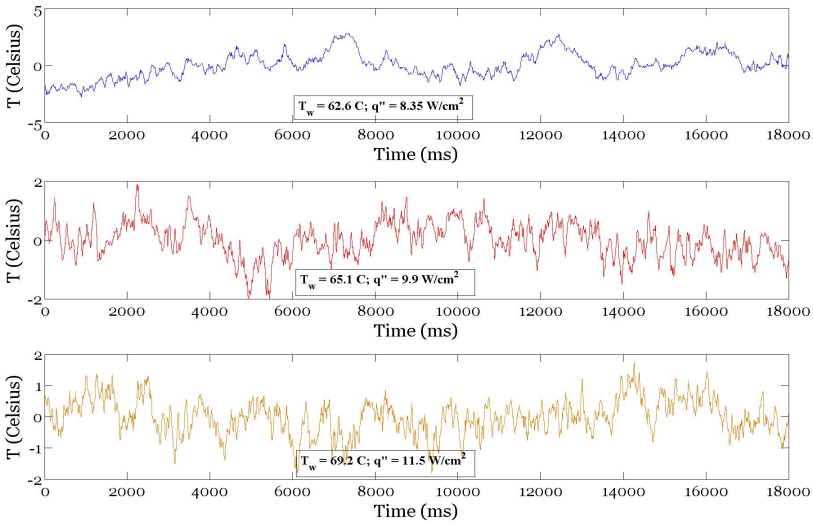

(a) Temperature fluctuation for a total time of 18 seconds

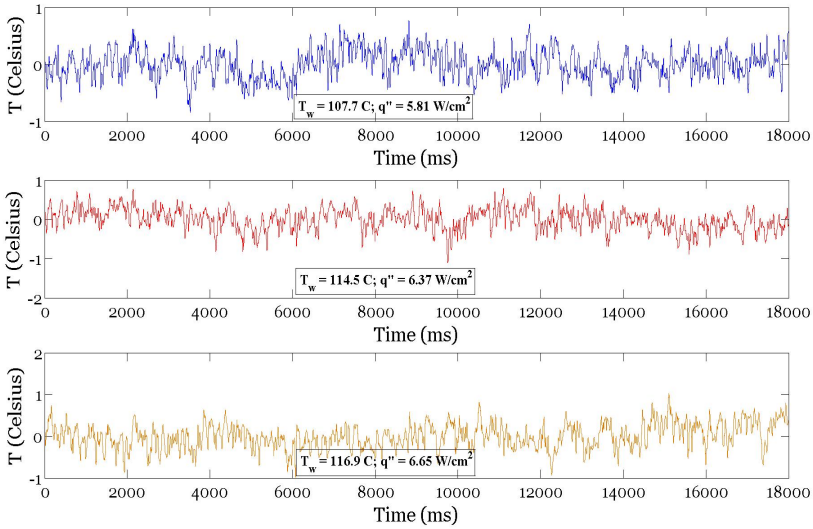

(b) Temperature fluctuation for a total time of 18 seconds

Fig. 71.: Surface temperature fluctuations recorded by TFT-3 (1000Hz), in saturated pool boiling (Run-I) 71(a) FDNB, CHF & 71(b) film boiling after noise-reduction.

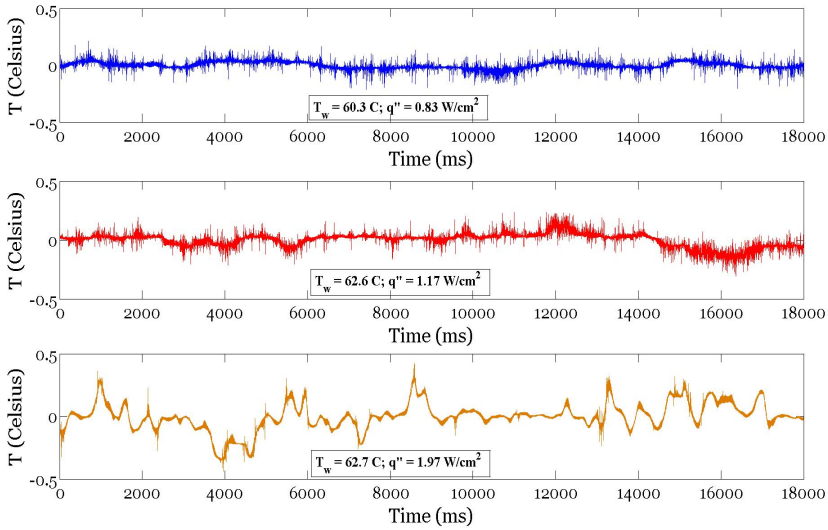

(a) Temperature fluctuation for a total time of 18 seconds

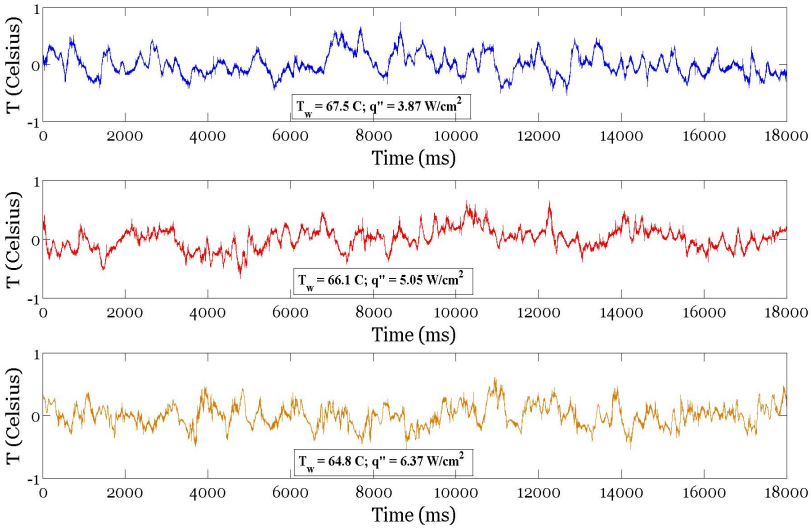

(b) Temperature fluctuation for a total time of 18 seconds

Fig. 72.: Surface temperature fluctuations recorded by TFT-1 (1000Hz), in saturated pool boiling (Run-II) 72(a) convective regime, ONB & 72(b) PNB, after noise-reduction.

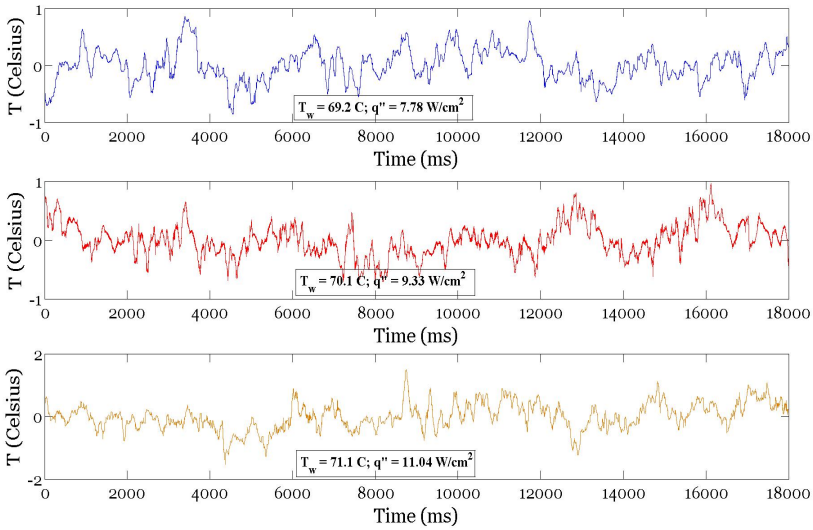

(a) Temperature fluctuation for a total time of 18 seconds

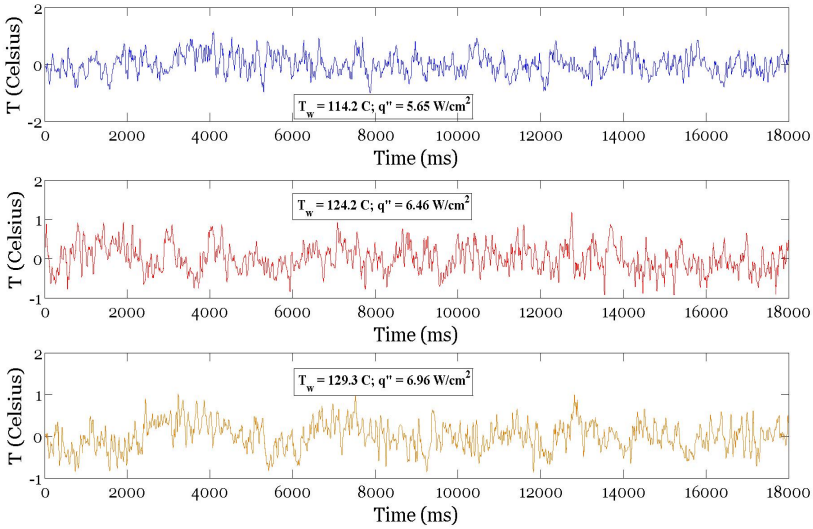

(b) Temperature fluctuation for a total time of 18 seconds

Fig. 73.: Surface temperature fluctuations recorded by TFT-1 (1000Hz), in saturated pool boiling (Run-II) 73(a) FDNB, CHF & 73(b) film boiling after noise-reduction.

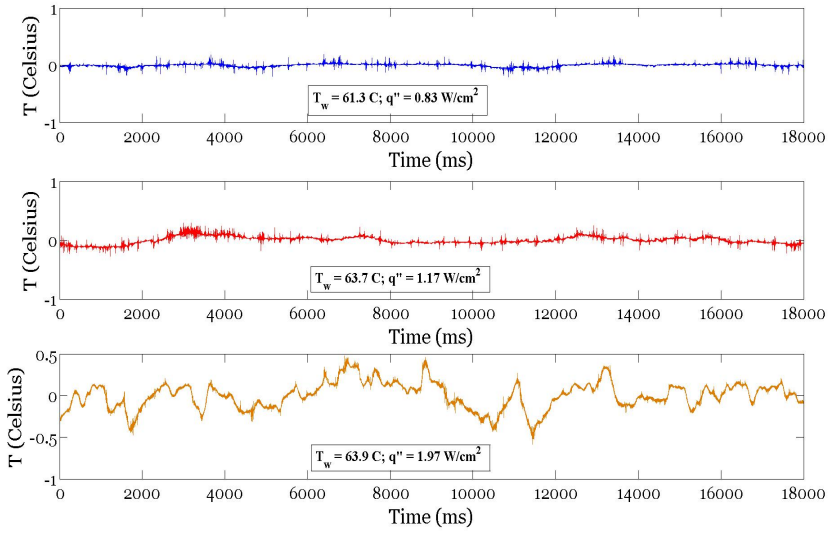

(a) Temperature fluctuation for a total time of 18 seconds

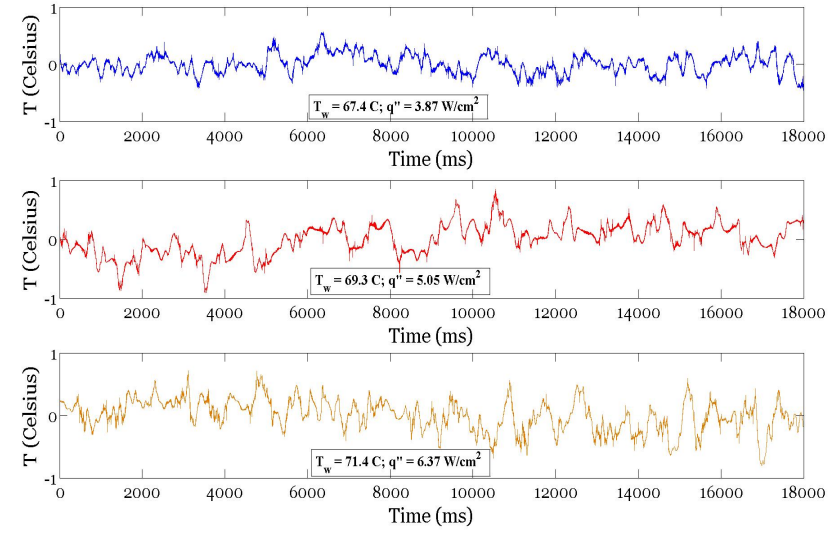

(b) Temperature fluctuation for a total time of 18 seconds

Fig. 74.: Surface temperature fluctuations recorded by TFT-3 (1000Hz), in saturated pool boiling (Run-II) 74(a) convective regime, ONB & 74(b) PNB after noise-reduction.

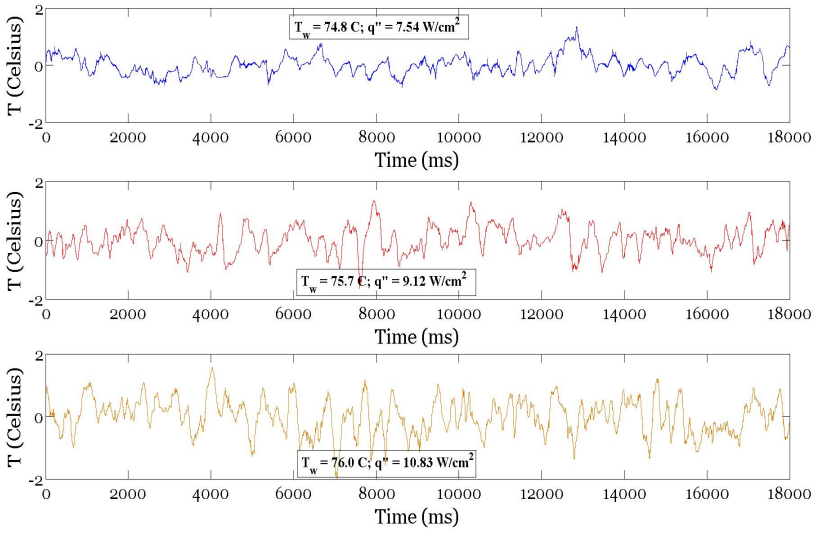

(a) Temperature fluctuation for a total time of 18 seconds

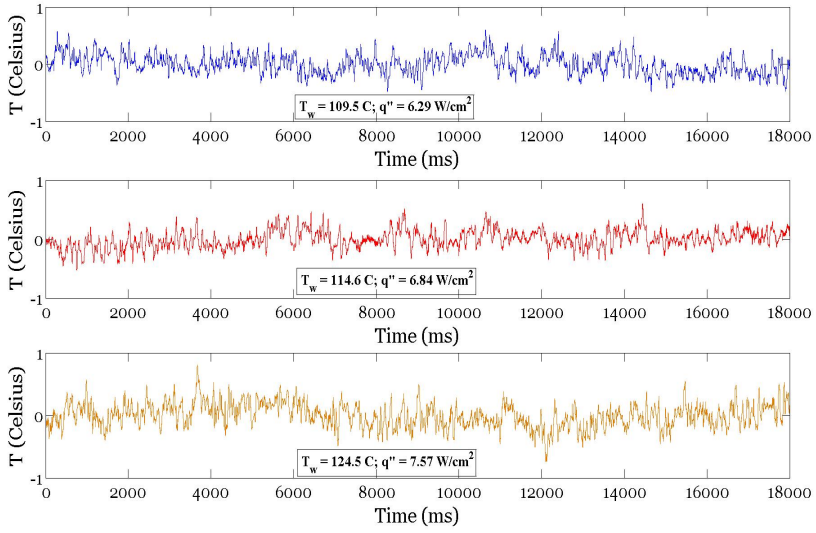

(b) Temperature fluctuation for a total time of 18 seconds

Fig. 75.: Surface temperature fluctuations recorded by TFT-3 (1000Hz), in saturated pool boiling (Run-II) 75(a) FDNB, at CHF & 75(b) film boiling after noise-reduction.

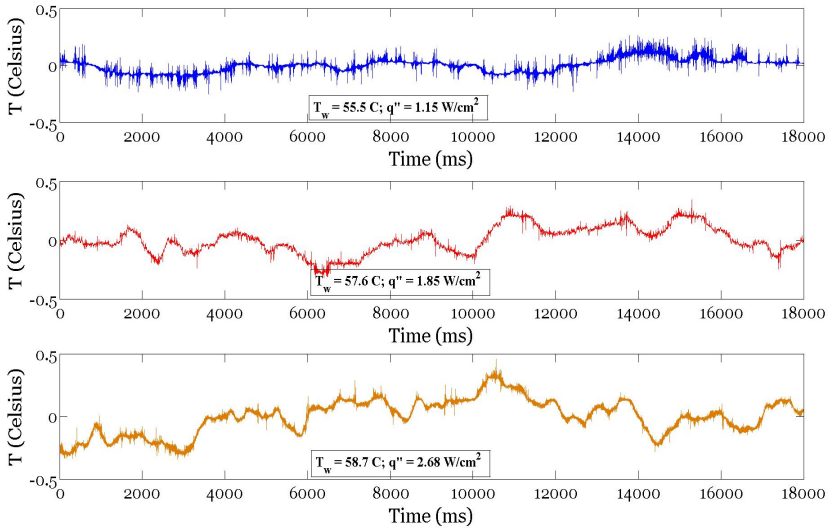

(a) Temperature fluctuation for a total time of 18 seconds

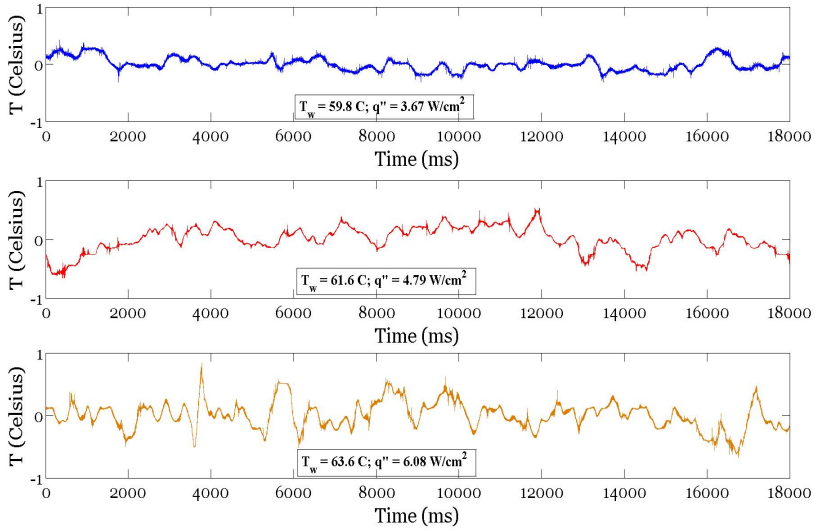

(b) Temperature fluctuation for a total time of 18 seconds

Fig. 76.: Surface temperature fluctuations recorded by TFT-1 (1000Hz), in 10 ℃ subcooled pool boiling (Run-I) 76(a) convective regime, ONB & 76(b) PNB after noise-reduction.

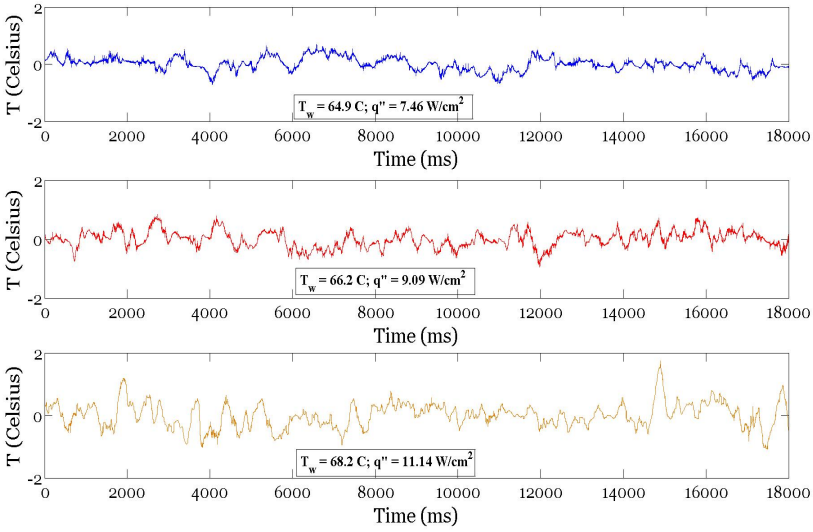

(a) Temperature fluctuation for a total time of 18 seconds

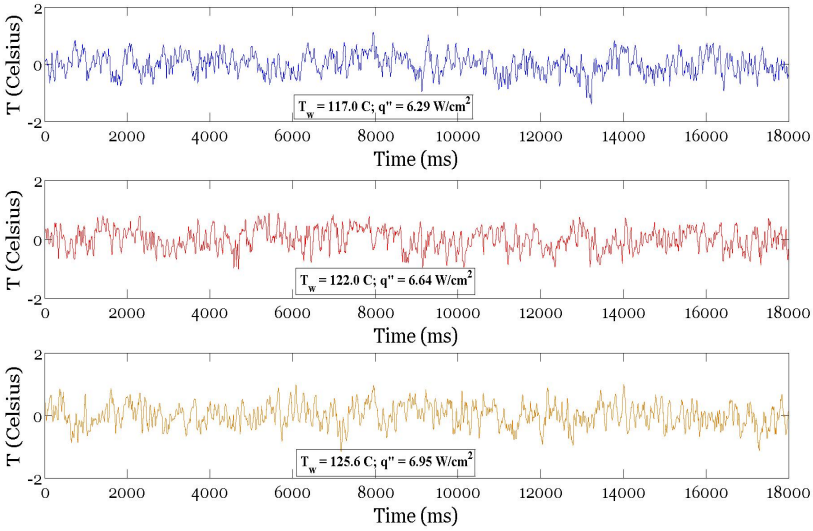

(b) Temperature fluctuation for a total time of 18 seconds

Fig. 77.: Surface temperature fluctuations recorded by TFT-1 (1000Hz), in 10 ℃ subcooled pool boiling (Run-I) 77(a) FDNB, at CHF & 77(b) in film boiling after noise-reduction.

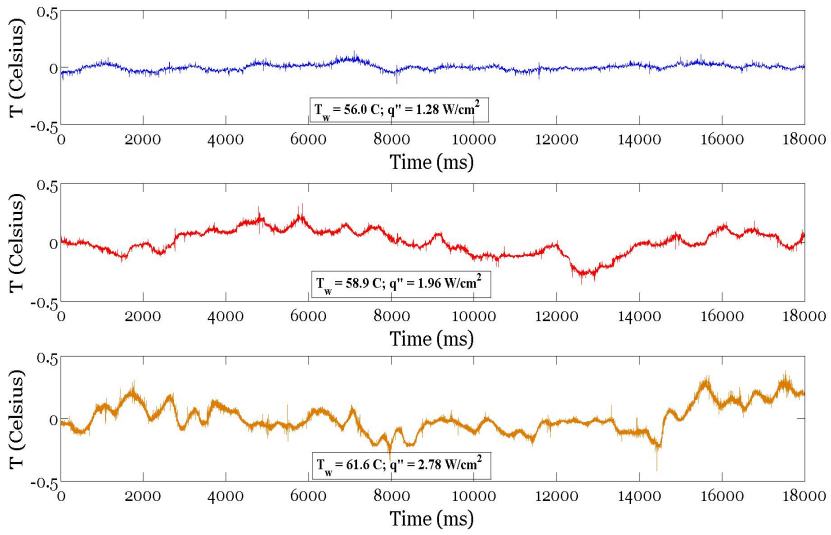

(a) Temperature fluctuation for a total time of 18 seconds

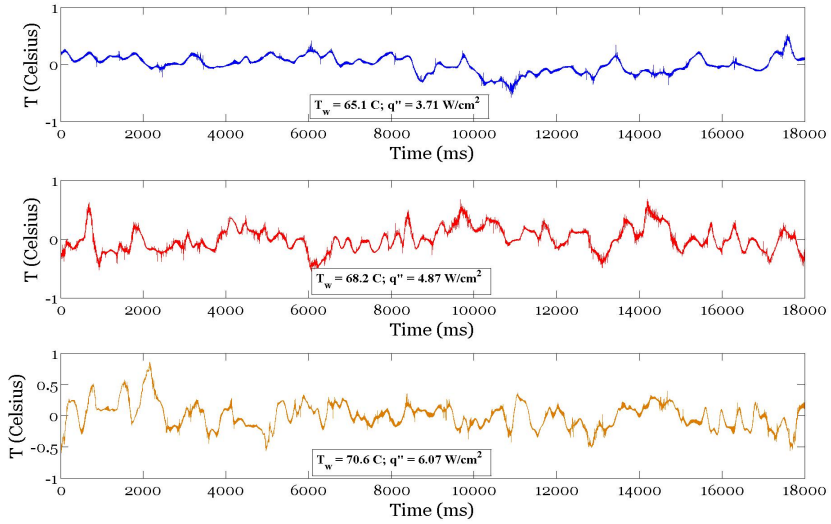

(b) Temperature fluctuation for a total time of 18 seconds

Fig. 78.: Surface temperature fluctuations recorded by TFT-1 (1000Hz), in 10 ℃ subcooled pool boiling (Run-II) 78(a) convective regime, ONB & 78(b) PNB after noise-reduction.

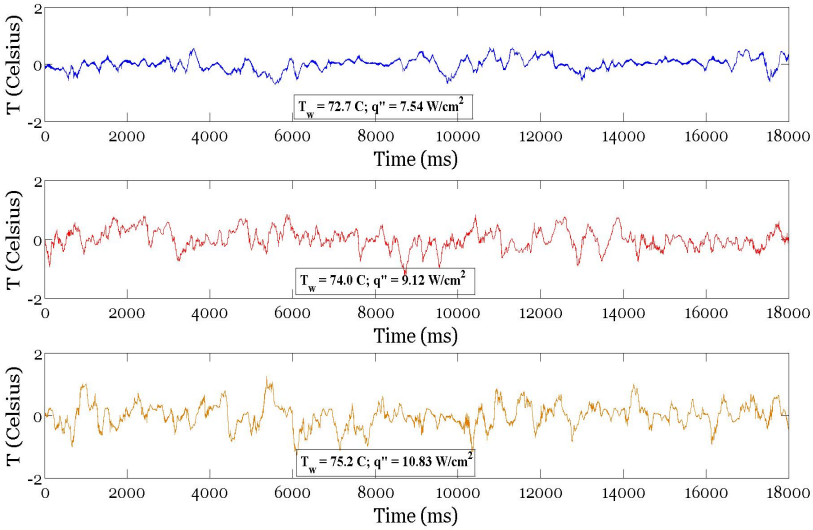

(a) Temperature fluctuation for a total time of 18 seconds

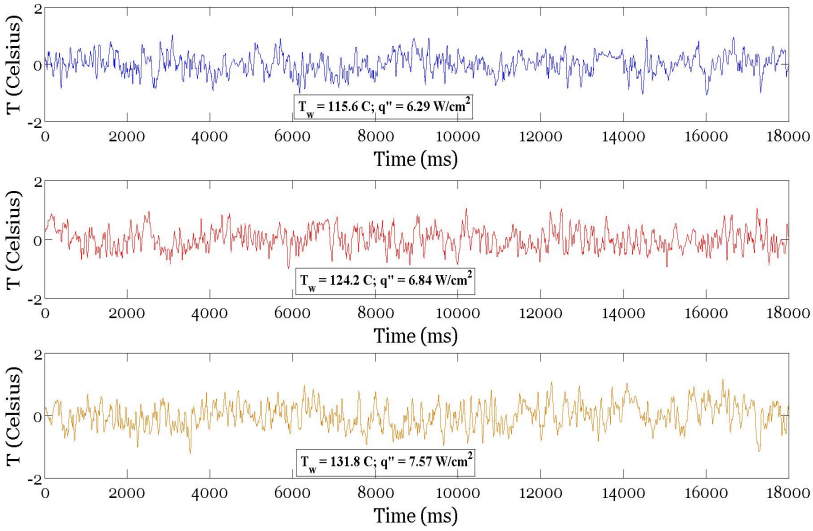

(b) Temperature fluctuation for a total time of 18 seconds

Fig. 79.: Surface temperature fluctuations recorded by TFT-1 (1000Hz), in 10 ℃ subcooled pool boiling (Run-II) in 79(a) FDNB, at CHF & 79(b) in film boiling after noise-reduction.

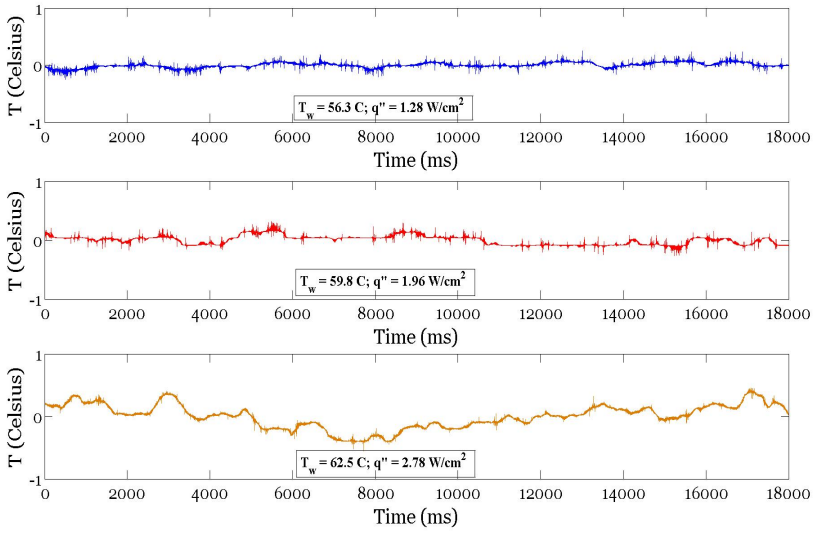

(a) Temperature fluctuation for a total time of 18 seconds

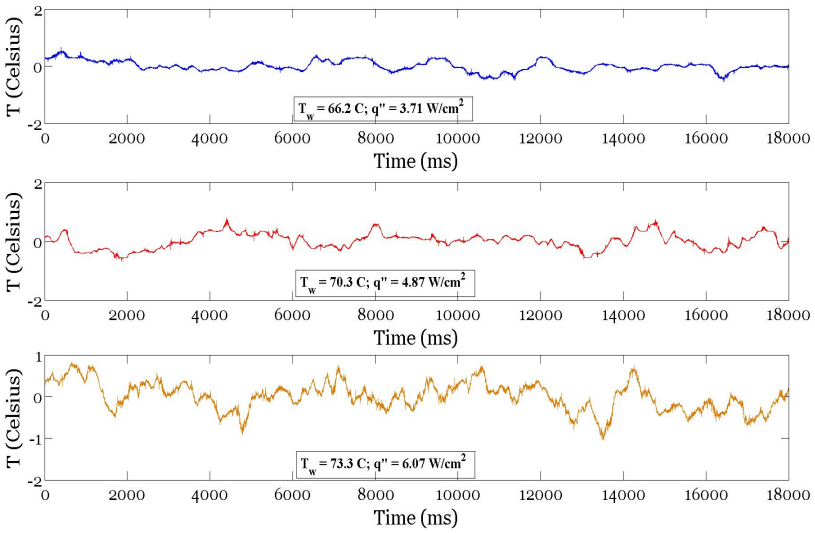

(b) Temperature fluctuation for a total time of 18 seconds

Fig. 80.: Surface temperature fluctuations recorded by TFT-3 (1000Hz), in 10 ℃ subcooled pool boiling (Run-II) in 80(a) convective regime, ONB & 80(b) PNB after noise-reduction.

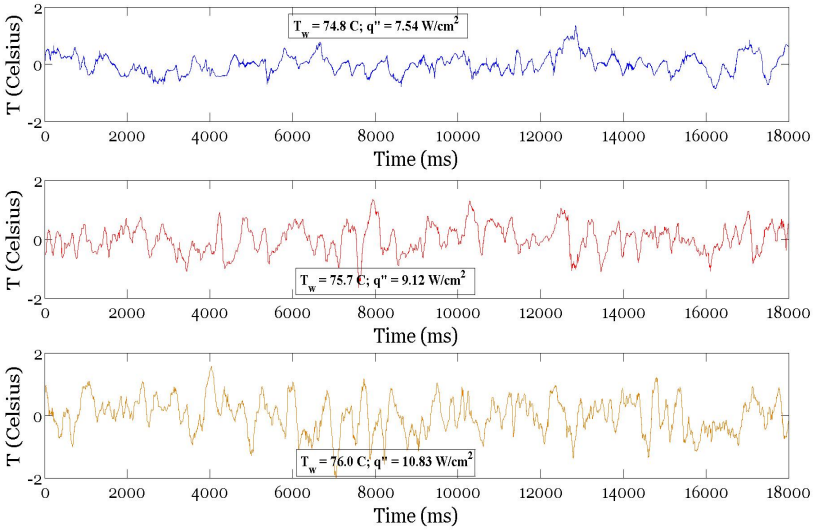

(a) Temperature fluctuation for a total time of 18 seconds

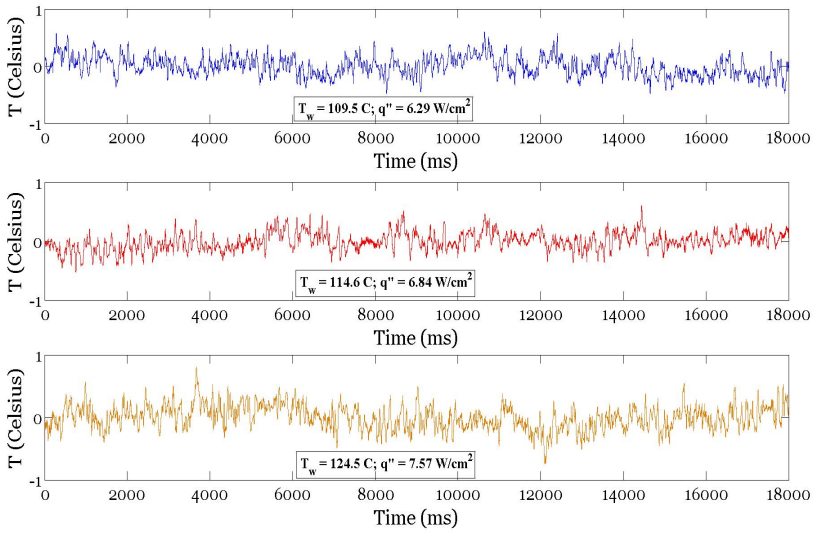

(b) Temperature fluctuation for a total time of 18 seconds

Fig. 81.: Surface temperature fluctuations recorded by TFT-3 (1000Hz), in 10 ℃ subcooled pool boiling (Run-II) in 81(a) FDNB, at CHF & 81(a) in film boiling after noise-reduction.

The results of spectrum analysis is shown below for the different tests. The number of active frequencies increases with an increase in the supplied heat flux. The dominant frequencies present in vicnity of both active TFT junctions is different. The spectra show an underlying broad-band structure indicative of chaotic dynamics. The number of dominant frequencies in subcooled pool boiling is lower than that in saturated pool boiling.

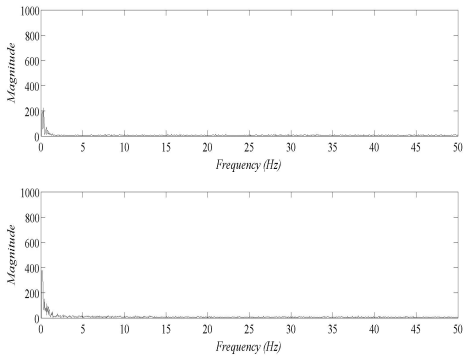

(a) Convective regime

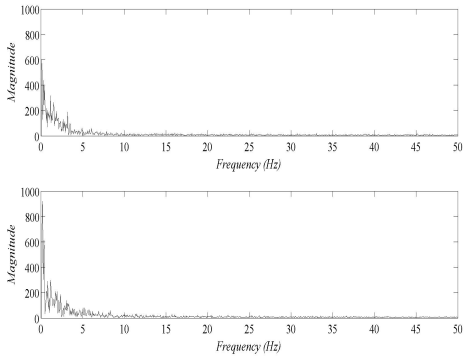

(b) ONB

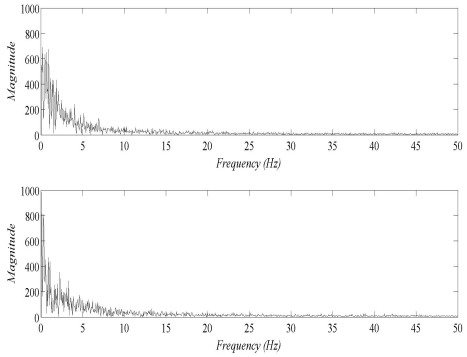

(c) PNB

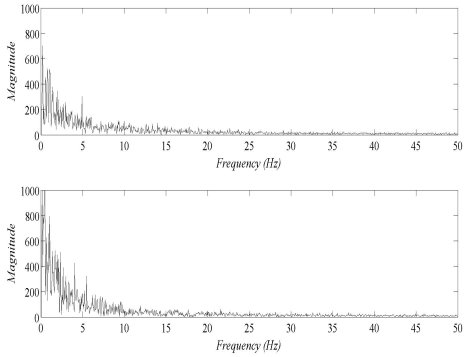

(d) FDNB

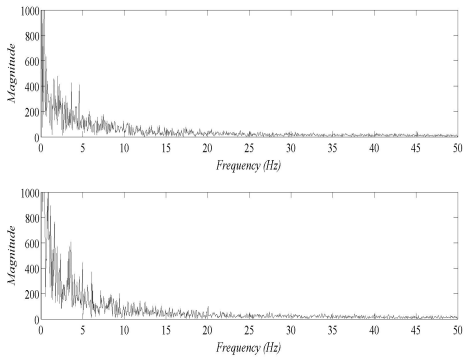

(e) CHF & Leidenfrost Point

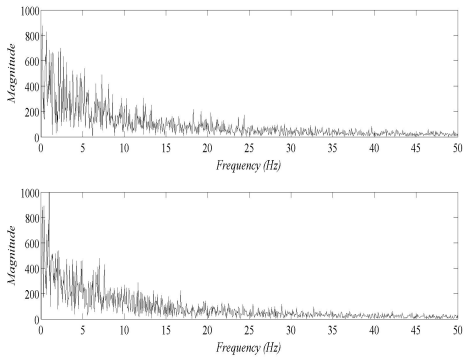

(f) Film Boiling

Fig. 82.: Fourier spectra for saturated pool boiling test-II corresponding to high frequency temperature measurements of TFT-1 after noise reduction.

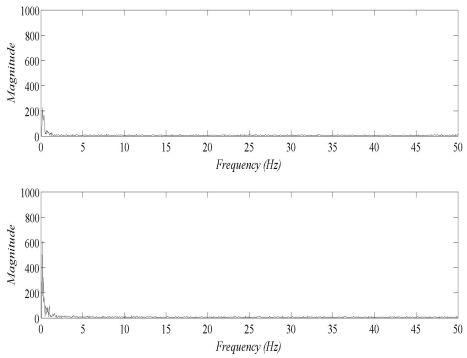

(a) Convective regime

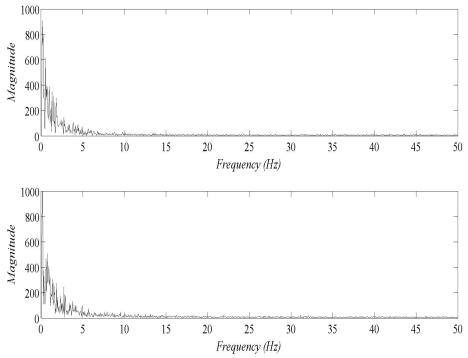

(b) ONB

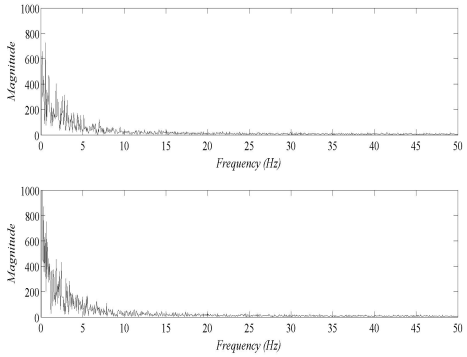

(c) PNB

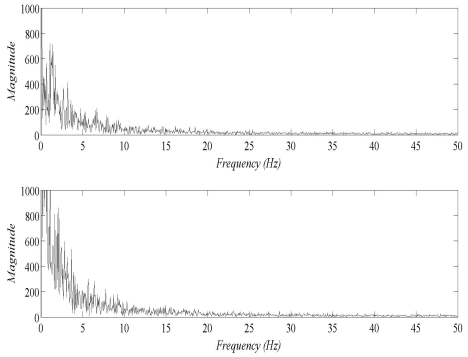

(d) FDNB

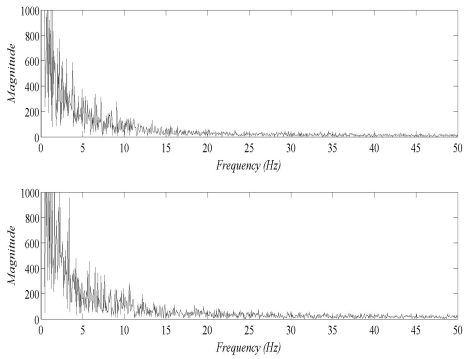

(e) CHF & Leidenfrost Point

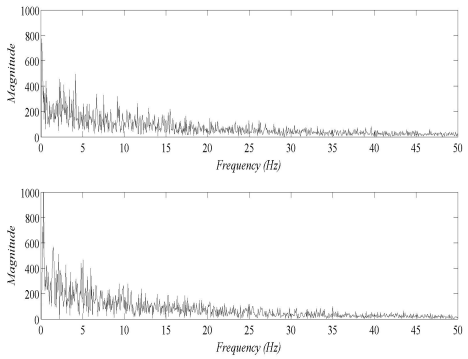

(f) Film Boiling

Fig. 83.: Fourier spectra for saturated pool boiling test-II corresponding to high frequency temperature measurements of TFT-3 after noise reduction.

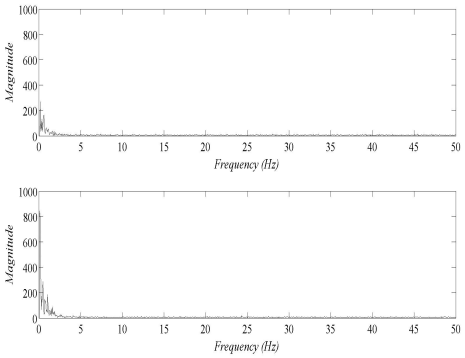

(a) Convective regime

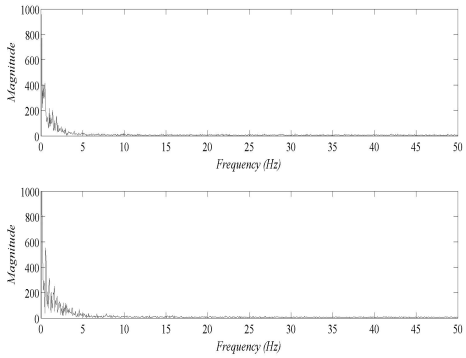

(b) ONB

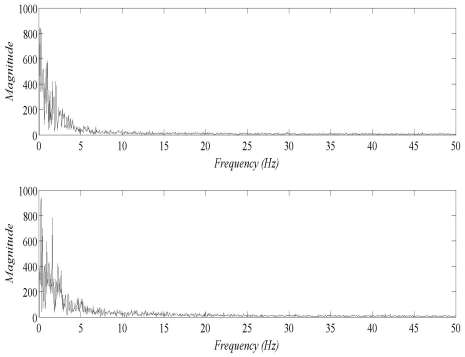

(c) PNB

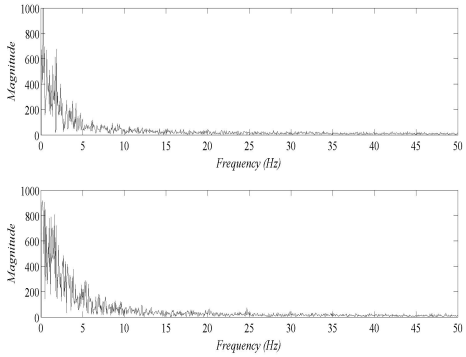

(d) FDNB

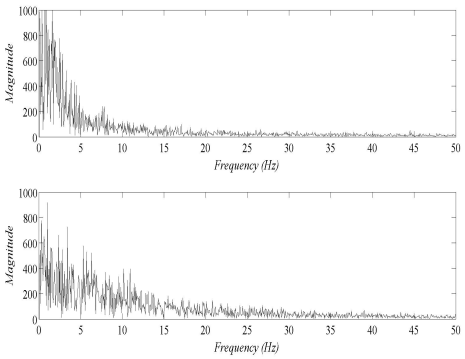

(e) CHF & Leidenfrost Point

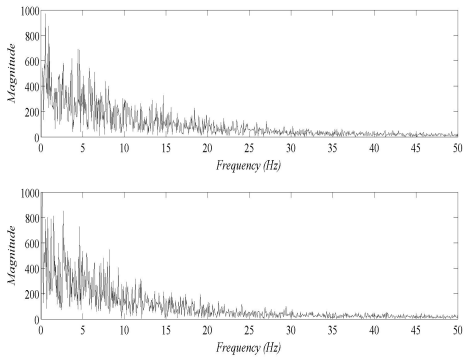

(f) Film Boiling

Fig. 84.: Fourier spectra for subcooled pool boiling test-II corresponding to high frequency temperature measurements of TFT-1 after noise reduction.

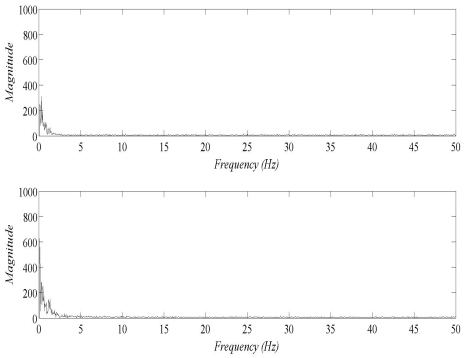

(a) Convective regime

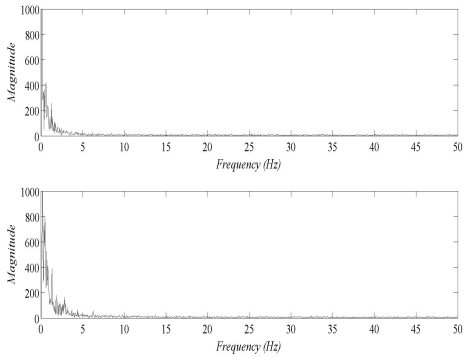

(b) ONB

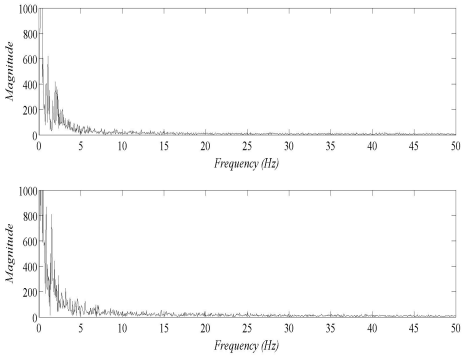

(c) PNB

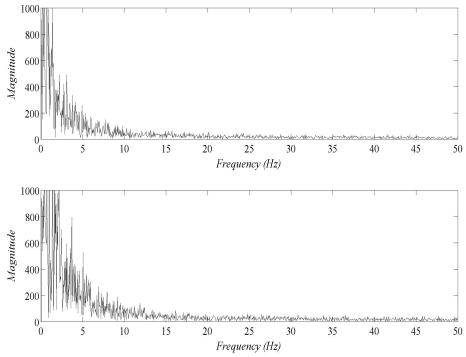

(d) FDNB

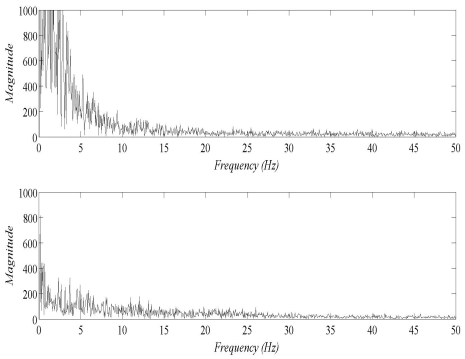

(e) CHF & Leidenfrost Point

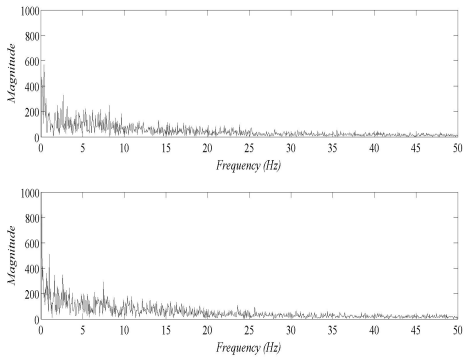

(f) Film Boiling

Fig. 85.: Fourier spectra for subcooled pool boiling test-II corresponding to high frequency temperature measurements of TFT-3 after noise reduction.

Principal Component Analysis

The results of principal component analysis is shown for all remaining test cases in different boiling regimes. The time-delay vectors are projected onto an Eigen basis to magnify the underlying geometry in phase space. No clear geometrical features are visible in the convective regime, near ONB and in some cases, in the PNB regime. Near FDNB and CHF however, clear structures appear and are present in film-boiling regime. This is indicative of dominance of chaotic dynamics.

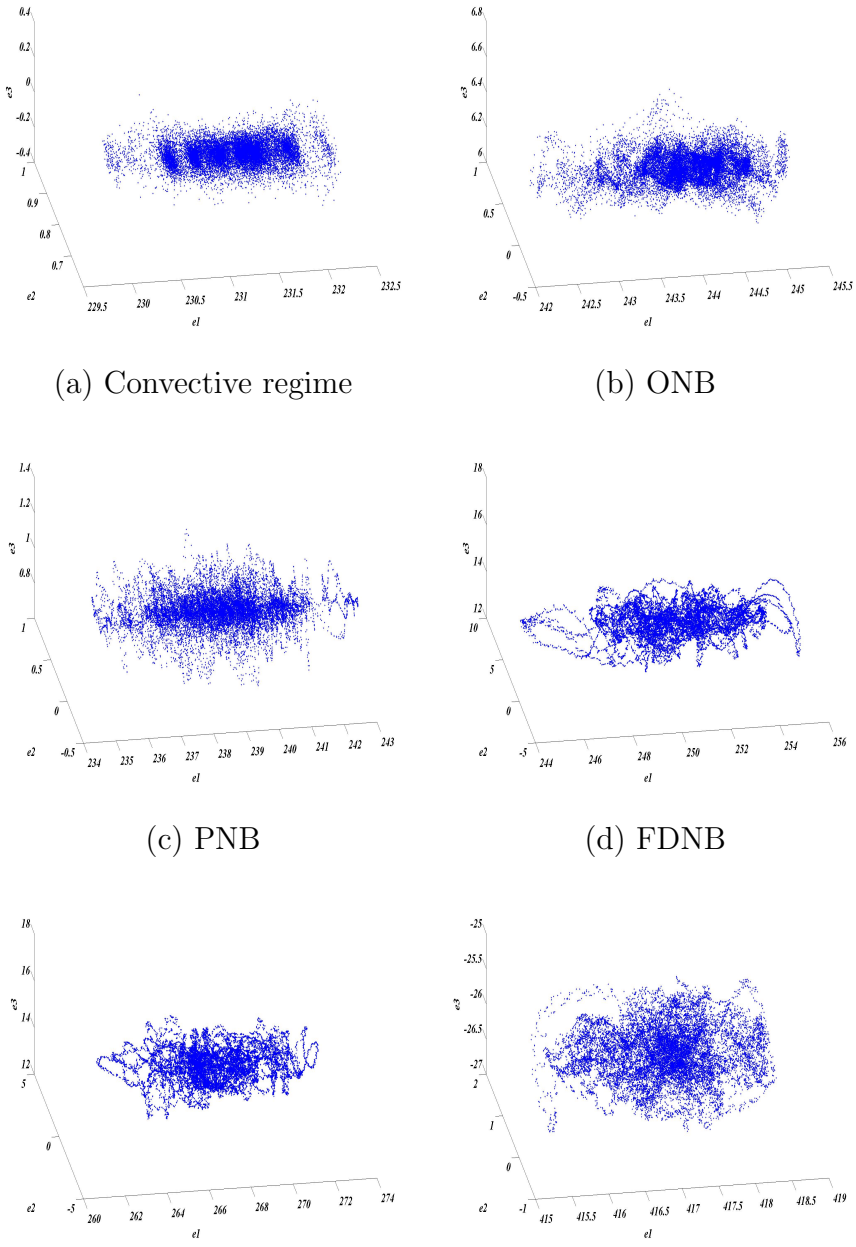

(a) Convective regime

(b) ONB

(c) PNB

(d) FDNB

(e) CHF

(f) Film Boiling

Fig. 86.: Phase plots for saturated pool boiling test-I corresponding to high frequency temperature measurements of TFT-3 after noise reduction.

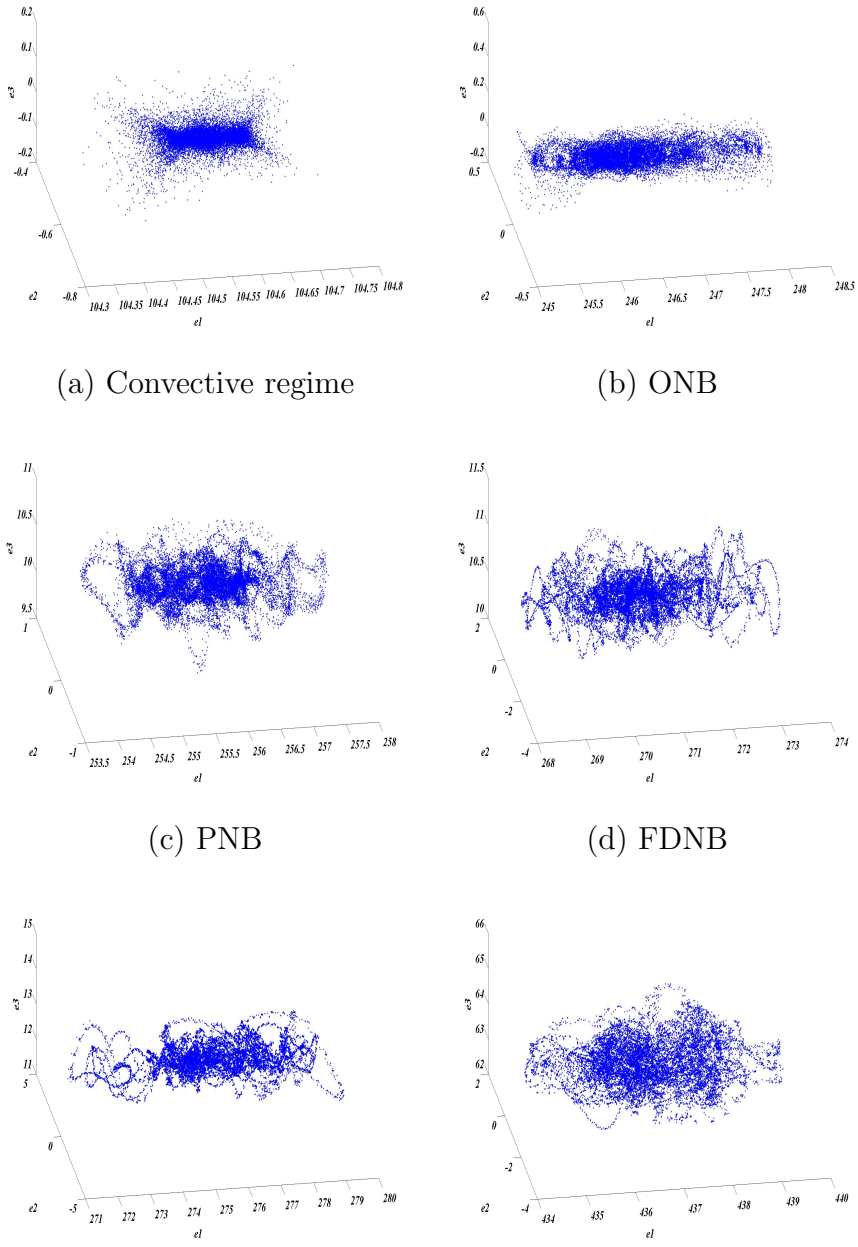

(a) Convective regime

(b) ONB

(c) PNB

(d) FDNB

(e) CHF

(f) Film Boiling

Fig. 87.: Phase plots for saturated pool boiling test-II corresponding to high frequency temperature measurements of TFT-1 after noise reduction.

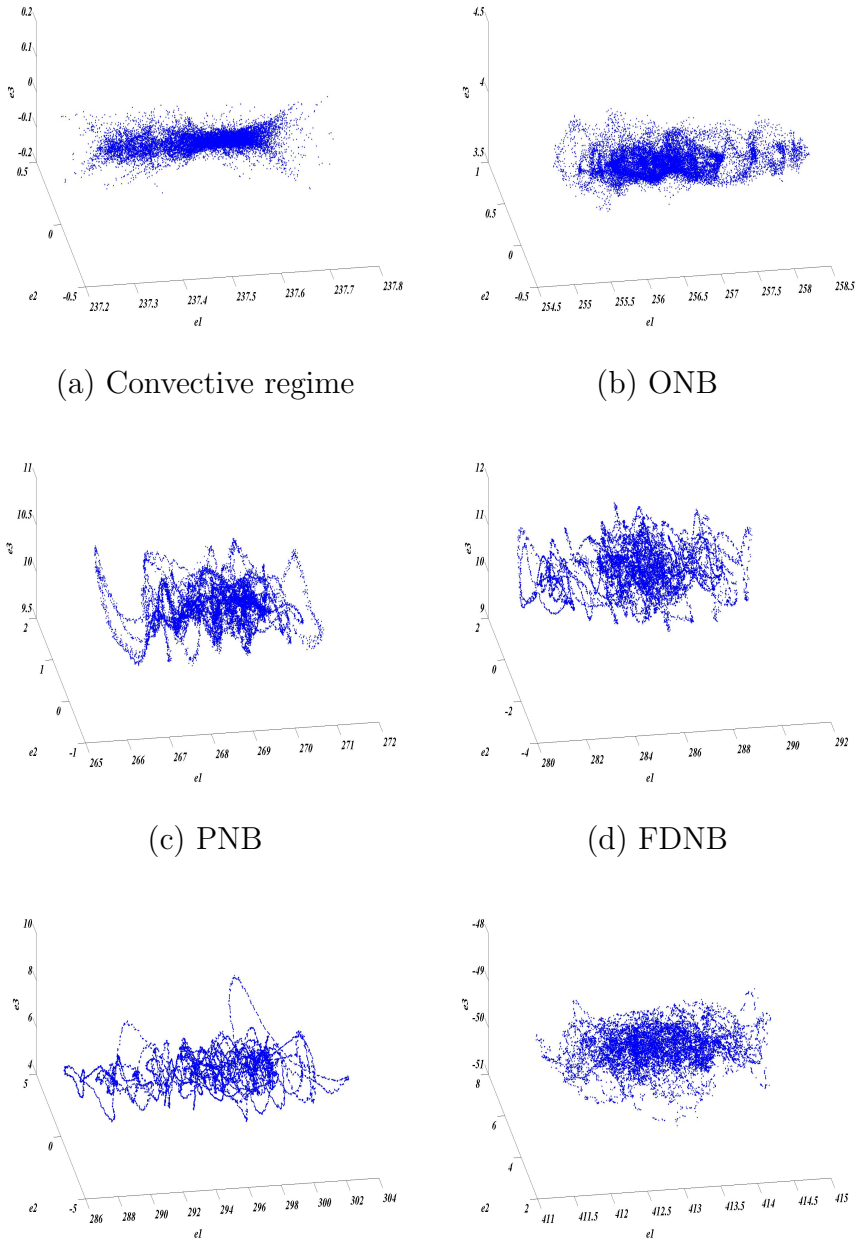

(a) Convective regime

(b) ONB

(c) PNB

(d) FDNB

(e) CHF

(f) Film Boiling

Fig. 88.: Phase plots for saturated pool boiling test-II corresponding to high frequency temperature measurements of TFT-3 after noise reduction.

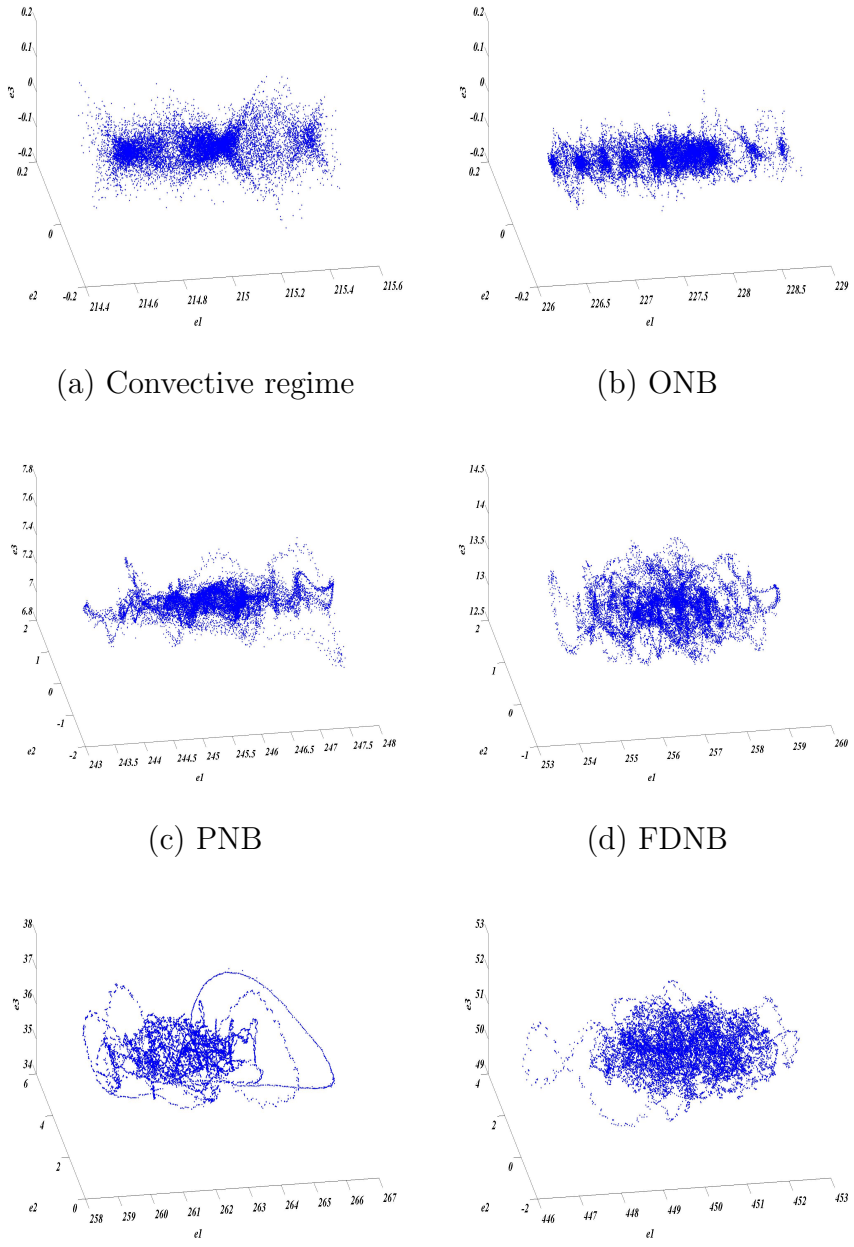

(a) Convective regime

(b) ONB

(c) PNB

(d) FDNB

(e) CHF

(f) Film Boiling

Fig. 89.: Phase plots for 10 ℃ subcooled pool boiling test-I corresponding to high frequency temperature measurements of TFT-1 after noise reduction.

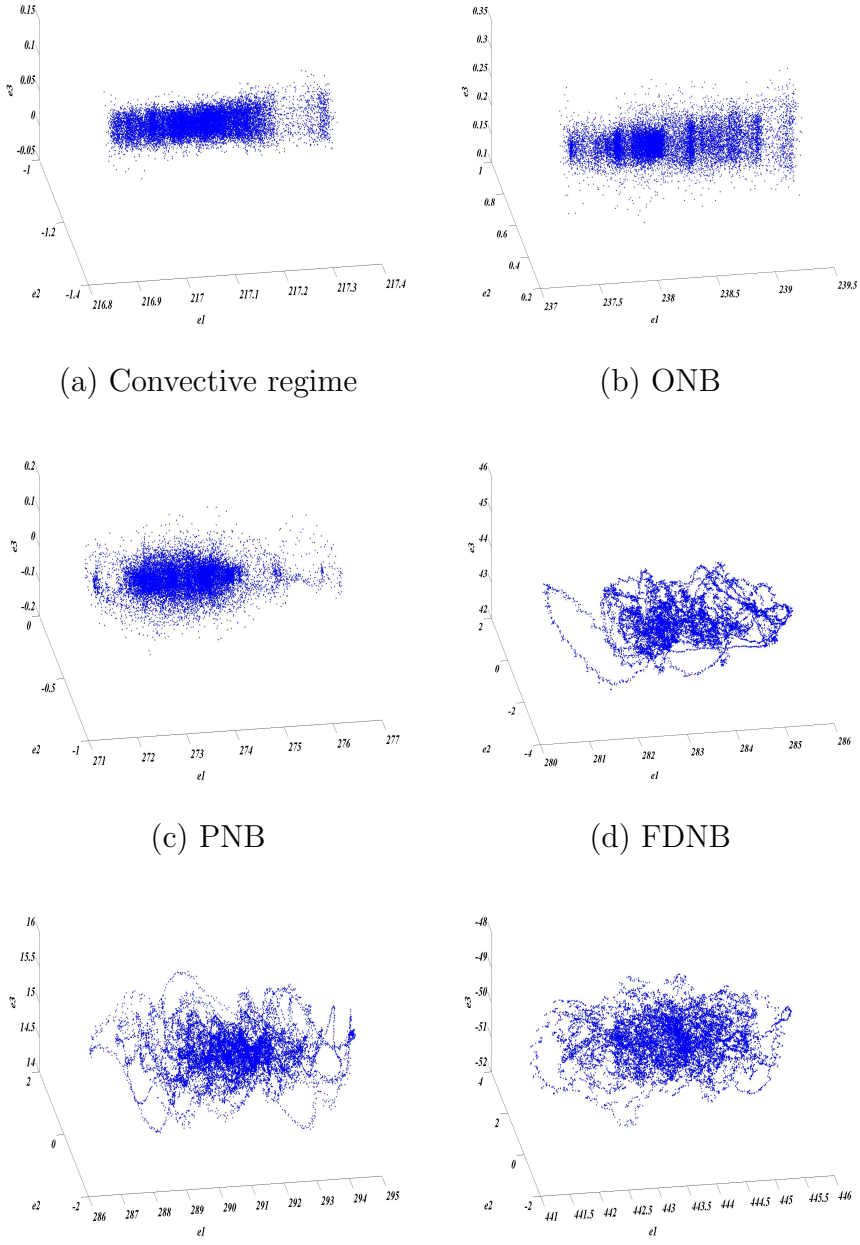

(a) Convective regime

(b) ONB

(c) PNB

(d) FDNB

(e) CHF

(f) Film Boiling

Fig. 90.: Phase plots for 10 ℃ subcooled pool boiling test-II, corresponding to high frequency temperature measurements of TFT-1 after noise reduction.

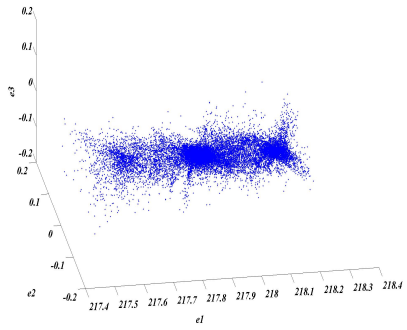

(a) Convective regime

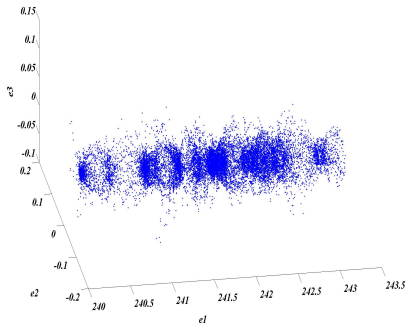

(b) ONB

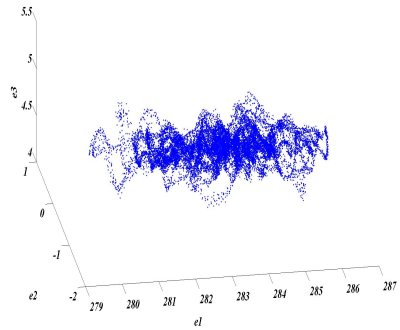

(c) PNB

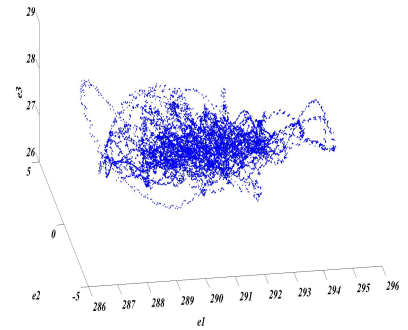

(d) FDNB

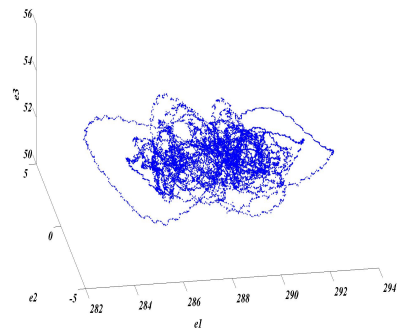

(e) CHF

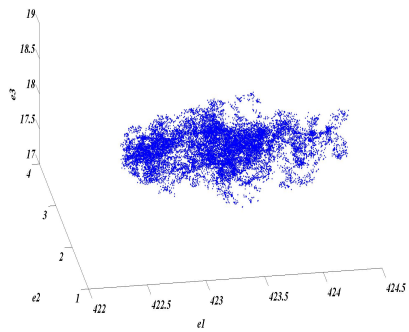

(f) Film Boiling

Fig. 91.: Phase plots for 10 ℃ subcooled pool boiling test-II, corresponding to high frequency temperature measurements of TFT-3 after noise reduction.

Space-Time Separation Plots

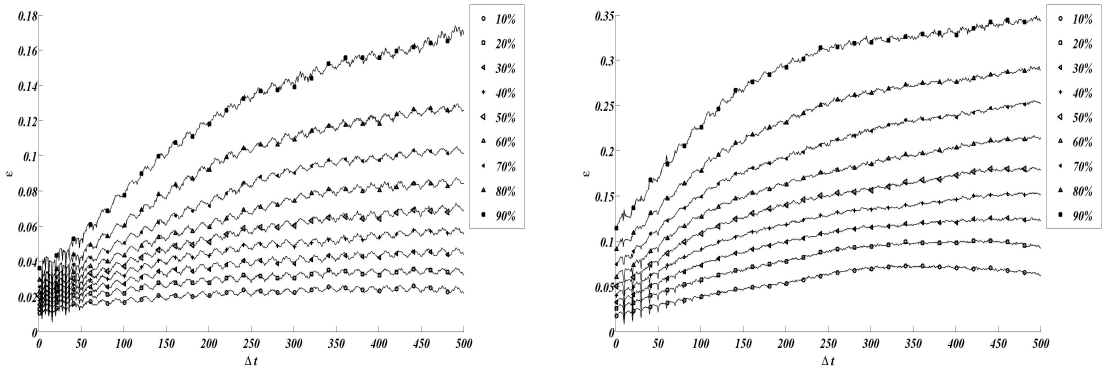

(a) Convective regime

(b) ONB

(c) PNB

(d) FDNB

(e) CHF

(f) Film Boiling

Fig. 92.: Space-time separation plot for an embedding dimension of 5, in saturated pool boiling test-I, TFT-1, at various wall superheat levels after noise reduction.

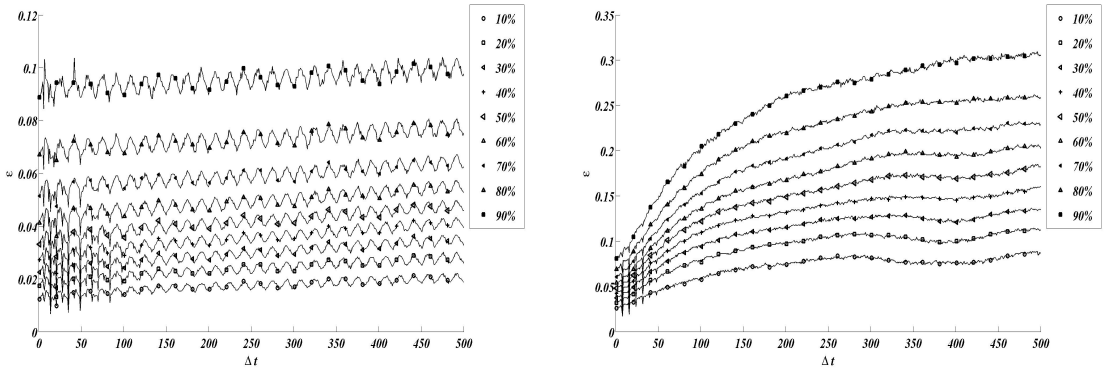

(a) Convective regime

(b) ONB

(c) PNB

(d) FDNB

(e) CHF

(f) Film Boiling

Fig. 93.: Space-time separation plot for an embedding dimension of 5, in saturated pool boiling test-I, TFT-3, at various wall superheat levels after noise reduction.

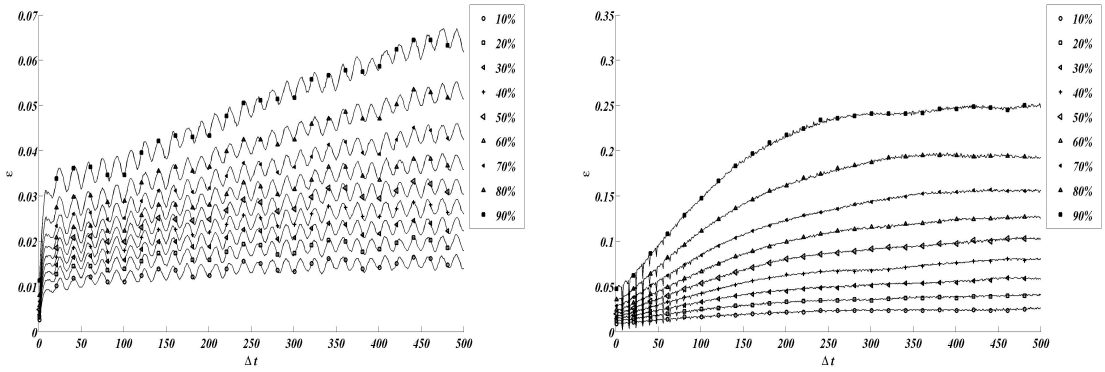

(a) Convective regime

(b) ONB

(c) PNB

(d) FDNB

(e) CHF

(f) Film Boiling

Fig. 94.: Space-time separation plot for an embedding dimension of 5, in saturated pool boiling test-II, TFT-1, at various wall superheat levels after noise reduction.

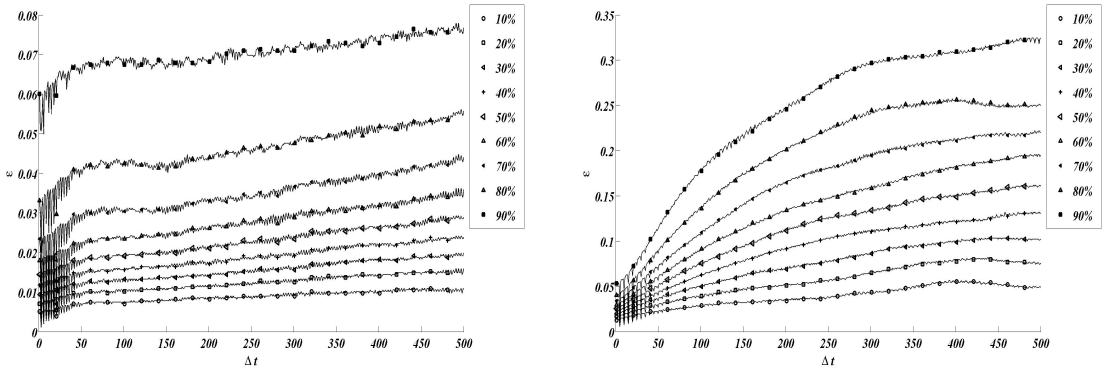

(a) Convective regime (b) ONB

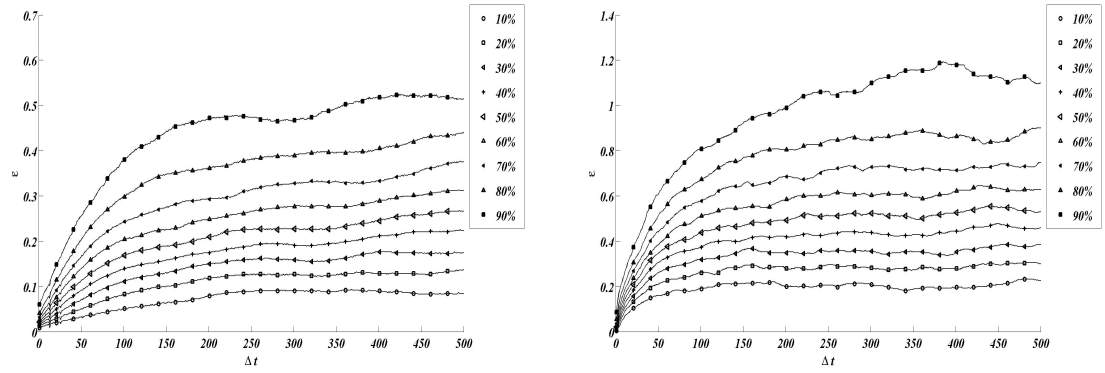

(c) PNB (d) FDNB

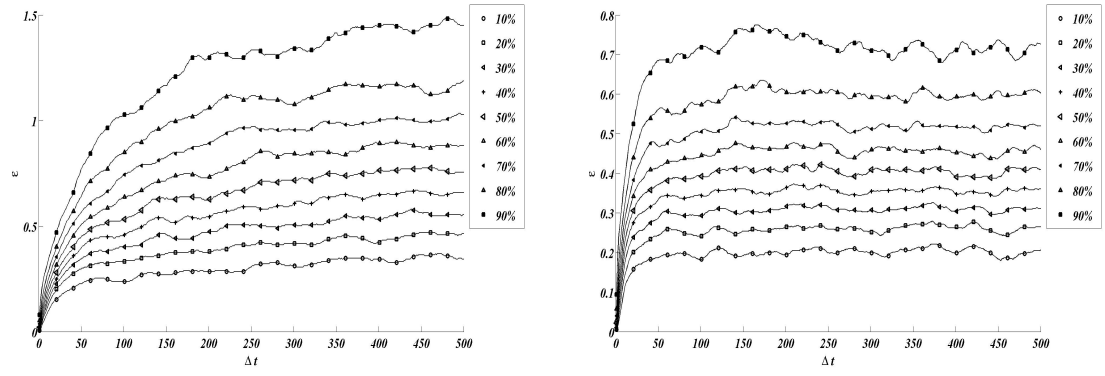

(e) CHF (f) Film Boiling

Fig. 95.: Space-time separation plot for an embedding dimension of 5, in saturated pool boiling test-II, TFT-3, at various wall superheat levels after noise reduction.

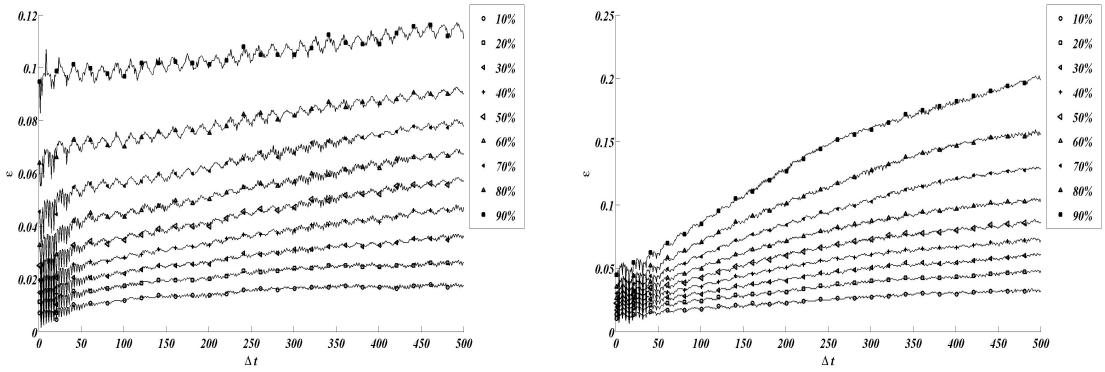

(a) Convective regime

(b) ONB

(c) PNB

(d) FDNB

(e) CHF

(f) Film Boiling

Fig. 96.: Space-time separation plot for an embedding dimension of 5, in 10 ℃ sub-cooled pool boiling test-I, TFT-1, at various wall superheat levels after noise reduction.

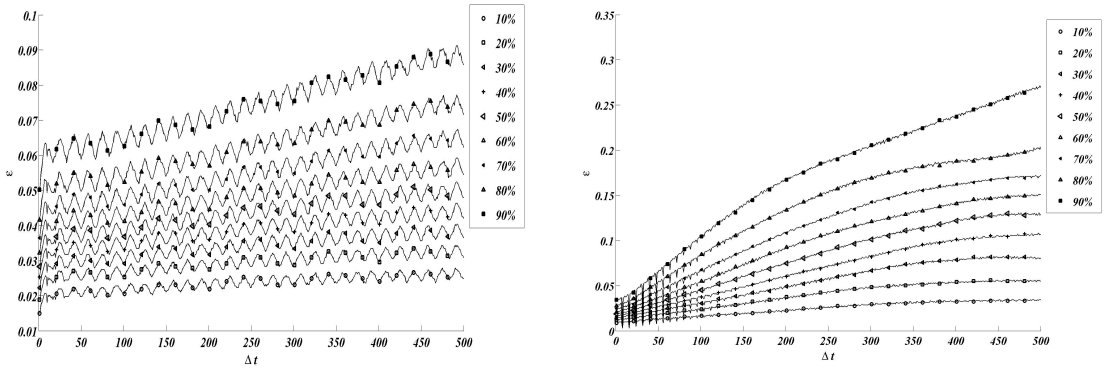

(a) Convective regime

(b) ONB

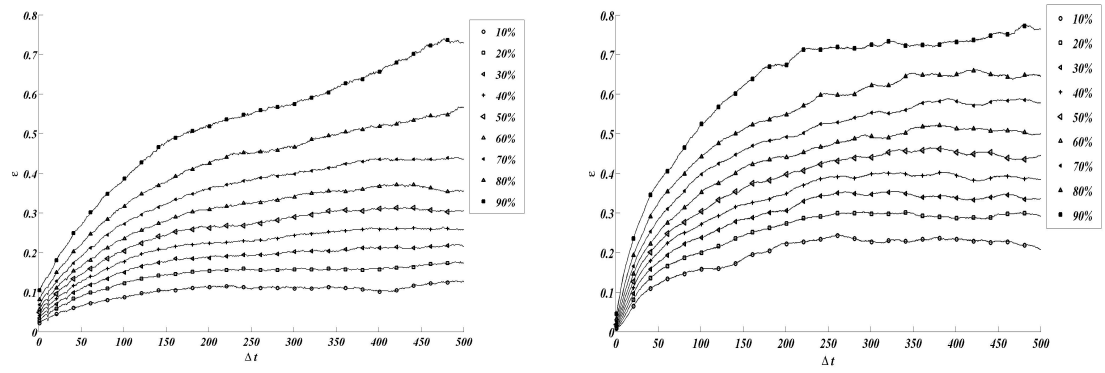

(c) PNB

(d) FDNB

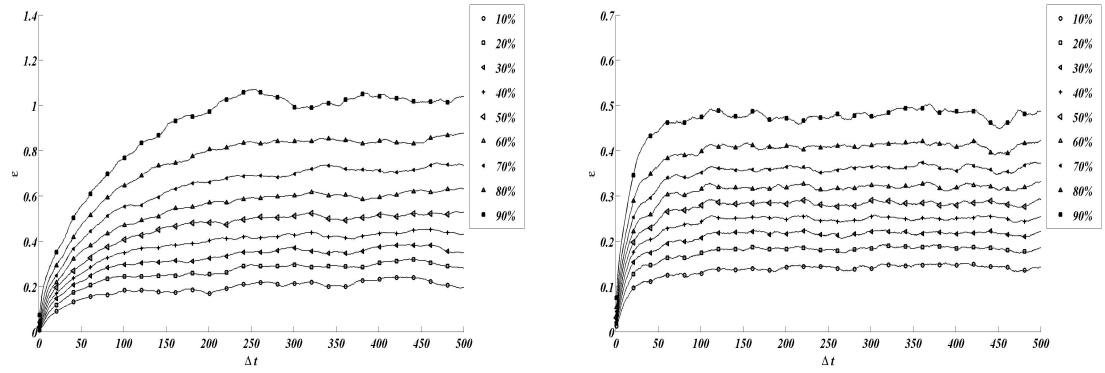

(e) CHF

(f) Film Boiling

Fig. 97.: Space-time separation plot for an embedding dimension of 5, in 10 ℃ sub-cooled pool boiling test-I, TFT-3, at various wall superheat levels after noise reduction.

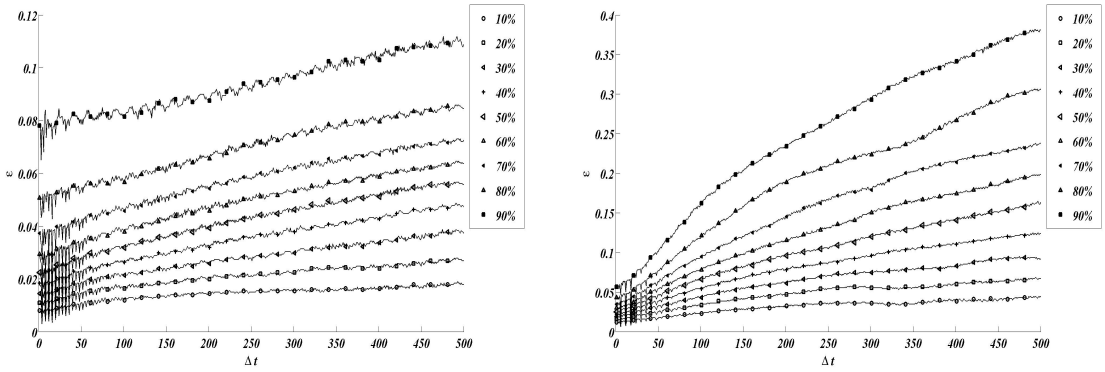

(a) Convective regime (b) ONB

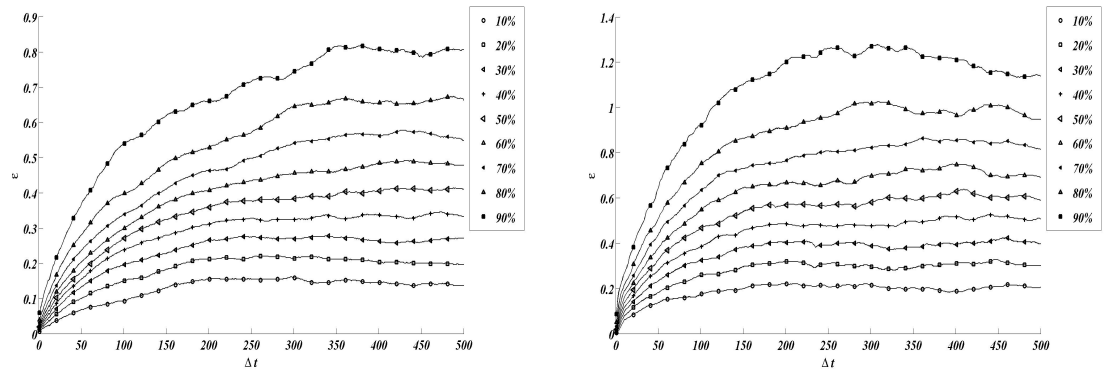

(c) PNB (d) FDNB

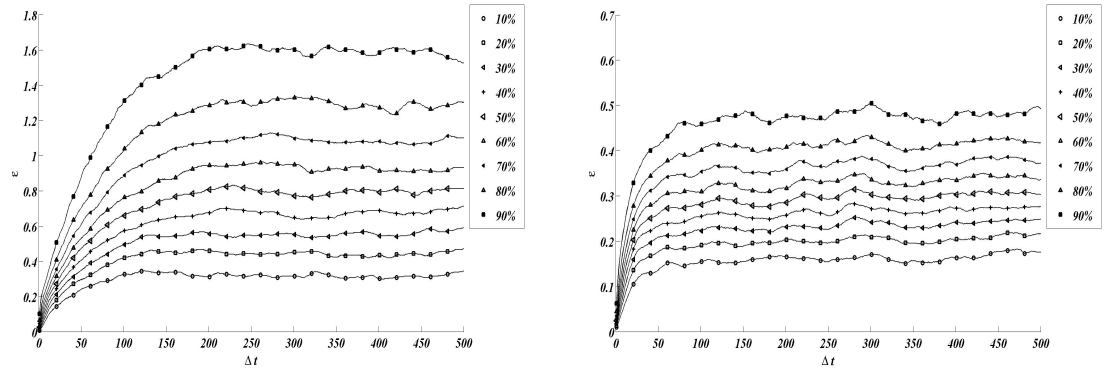

(e) CHF (f) Film Boiling

Fig. 98.: Space-time separation plot for an embedding dimension of 5, in 10 ℃ subcooled pool boiling test-II, TFT-3, at various wall superheat levels after noise reduction.

Lyapunov Exponents Summary

Table XI.: Saturated pool boiling Run-1 TFT-3 - Exponents & dimension estimates for noise-reduced data.

$\Delta\ T_w(℃)$	$q"(W/cm^2)$	λ_{robust}	K-Y	$D_C{}^{\dagger}$	*Dynamics*	*T.R.A*
59.76	1.25	-0.06 ± 0.01, -0.62 ± 0.05, -0.92 ± 0.05,-1.63 ± 0.2,	0	8.47	Fixed point	×
61.54	1.98	-0.04 ± 0.01, -0.01 ± 0.01, -0.16 ± 0.03	0	7.16	Fixed point	×
63.00	2.90	-0.04 ± 0.02, -0.9 ± 0.05, -1.64 ± 0.12	0	9.29	Fixed point	P
64.07	3.93	-0.03 ± 0.02, -0.18 ± 0.02, -0.27 ± 0.03, -1.73 ± 0.34	0	5.98	Fixed point	×
62.08	5.11	0.03 ± 0.02, -0.07 ± 0.02, -0.23 ± 0.03, -1.28 ± 0.09	> 2	6.99	Possibly chaotic	×
66.52	7.28	0.02 ± 0.02, -0.03 ± 0.01, -0.07 ± 0.01, -0.14 ± 0.03, -0.26 ± 0.05	1 or > 2	5.77	Possibly Chaotic	×
62.56	8.35	0.01 ± 0.01, -0.03 ± 0.01, -0.07 ± 0.01, -0.12 ± 0.01, -0.16 ± 0.02	1, $>$ 2	6.16	Possibly chaotic	×
65.11	9.90	0.02 ± 0.01, 0 ± 0, -0.03 ± 0.01, -0.06 ± 0.01, -0.11 ± 0.01	> 2	9.9	Chaotic	×
69.16	11.52	0.02 ± 0.01, -0.04 ± 0.01, -0.07 ± 0.01, -0.12 ± 0.01	1, >2	9.21	Chaotic	×

Table XI. Continued.

$\Delta\ T_w(℃)$	$q"(W/cm^2)$	λ_{robust}	*K-Y*	$D_C{}^{\dagger}$	*Dynamics*	*T.R.A*
107.68	5.81	0.02 ± 0.01, 0.03 ± 0.01, -0.06 ± 0.01	>2	9.7	Chaotic	P
114.51	6.37	0.02 ± 0.01, 0.01 ± 0.02, -0.02 ± 0, -0.04 ± 0.01, -0.07 ± 0.01, -0.13 ± 0.04	>2	7.28[c]	Chaotic	×
116.94	6.65	0.03 ± 0.02, -0.03 ± 0.01, -0.07 ± 0.01, -0.15 ± 0.06	>2	7.88	Chaotic	×
119.05	6.91	0.02 ± 0.01, 0.07 ± 0.02, -0.04 ± 0.01, -0.13 ± 0.03, -0.07 ± 0.02	>2	7.23[c]	Chaotic	P

[b]Estimate Converged

Table XII.: Saturated pool boiling Run-2 TFT-1 - Exponents & dimension estimates noise reduced data.

$\Delta\ T_w(℃)$	$q"(W/cm^2)$	λ_{robust}	*K-Y*	D_C[†]	*Dynamics*	*T.R.A*
60.32	0.83	-0.09 ± 0.04, -0.91 ± 0.08, -1.34 ± 0.2	0	7.35	Fixed point	×
62.61	1.17	-0.53 ± 0.02, -0.64 ± 0.03, -1.38 ± 0.2	0	8.05	Fixed point	×
62.66	1.97	0.02 ± 0.02, -0.04 ± 0.03, -0.35 ± 0.03, -0.83 ± 0.05	0 or 1	7.35	Fixed point/ Periodic	×
63.64	2.86	-0.07 ± 0.02, -0.24 ± 0.02, -0.16 ± 0.03, -0.34 ± 0.02	≥1	8.05	Fixed point	×
64.82	3.87	0.02 ± 0.02, -0.02 ± 0.01, -0.79 ± 0.05, -1.12 ± 0.12, -1.68 ± 0.21	0	8.9	Fixed point/Periodic	×
66.09	5.05	-0.03 ± 0.01, -0.59 ± 0.06, -1.70 ± 0.2	0	7.23	Fixed point	×
67.52	6.37	0.02 ± 0.03, -0.03 ± 0.02, -1.54 ± 0.16	> 2	5.36[c]	Possibly Chaotic	P
69.21	7.78	0.02 ± 0.01, -0.02 ± 0.01, -0.07 ± 0.01, -0.14 ± 0.02	> 2	5.93[c]	Chaotic	×
70.06	9.33	-0.14 ± 0.03, -0.02 ± 0.01, -1.6 ± 0.11	0	9.39	Periodic	×
71.12	11.04	0.02 ± 0.02, -0.04 ± 0.01, -0.08 ± 0.01, -0.12 ± 0.02, -0.18 ± 0.01	> 2	8.1	Chaotic	×

Table XII. Continued.

$\Delta\ T_w(℃)$	$q"(W/cm^2)$	λ_{robust}	*K-Y*	D_C[†]	*Dynamics*	*T.R.A*
114.12	5.68	0.02 ± 0.01, -0.03 ± 0.01, -0.07 ± 0.02, -0.13 ± 0.03	> 2	7.65	Chaotic	×
124.17	6.46	0.03 ± 0.02, -0.02 ± 0.01, -0.07 ± 0.01, -0.14 ± 0.03	> 2	11.12	Chaotic	P
129.29	6.96	0.02 ± 0.02, 0.01 ± 0.01, -0.02 ± 0.01, -0.04 ± 0.01, -0.07 ± 0.01	> 2	12.03	Possibly hyper-chaotic	P

[b]Estimate Converged

Table XIII.: Saturated pool boiling Run-2 TFT-3 - Exponents & dimension estimates for noise reduced data.

$\Delta\ T_w(℃)$	$q"(W/cm^2)$	λ_{robust}	K-Y	$D_C{}^{\dagger}$	*Dynamics*	*T.R.A*
61.28	0.83	0.04 ± 0.02, -0.14 ± 0.03, -1.43 ± 0.23	0 or 1	9.03	Fixed point/ Periodic	×
63.73	1.17	0.03 ± 0.03, -0.05 ± 0.03, -0.26 ± 0.03	0 or 1	8	Fixed point Periodic	×
63.87	1.97	-0.03 ± 0.02, -0.27 ± 0.04, -1.25 ± 0.24	0	5.58[c]	Fixed point	×
66.28	2.86	-0.04 ± 0.02, -0.96 ± 0.05, -1.45 ± 0.11	0	7.85	Fixed point	P
67.44	3.87	-0.05 ± 0.03, -0.16 ± 0.13, -0.25 ± 0.02, -1.19 ± 0.21	0	6.44	Fixed point	×
69.26	5.05	0.0 ± 0.01, -0.05 ± 0.03, -1.41 ± 0.05	1 or ≥ 2	4.75[c]	Periodic/ Chaotic	×
71.42	6.37	0.01 ± 0.01, -0.07 ± 0.02, -1.51 ± 0.26	> 2	4.17[c]	Chaotic	P
72.06	7.78	0.02 ± 0.01, -0.03 ± 0.01, -0.07 ± 0.02	> 2	4.49[c]	Chaotic	×

Table XIII. Continued.

$\Delta\ T_w(℃)$	$q"(W/cm^2)$	λ_{robust}	K-Y	$D_C{}^{\dagger}$	*Dynamics*	*T.R.A*
73.68	9.33	0.02 ± 0.01, -0.07 ± 0.02, -0.13 ± 0.02, -0.18 ± 0.02, -0.25 ± 0.03	> 2	7.95	Chaotic	×
75.65	11.04	0.02 ± 0.01, -0.01 ± 0.01, -0.02 ± 0.01, -0.05 ± 0.01, -0.14 ± 0.02	> 2	6.27	Chaotic	×
107.64	5.68	0.02 ± 0.01, -0.04 ± 0.01, -0.09 ± 0.06	> 2	10.46[c]	Chaotic	P
114.23	6.46	0.01 ± 0.01, -0.02 ± 0.01, -0.04 ± 0.01, -0.13 ± 0.03	> 2	9.84	Chaotic	×
123.35	6.96	0.01 ± 0, 0 ± 0, -0.01 ± 0, -0.02 ± 0.01, -0.04 ± 0.02	> 2	11.79	Chaotic	×

[b]Estimate Converged

Table XIV.: Subcooled pool boiling Run-1 TFT-1 - Exponents & dimension estimates for noise reduced data.

$\Delta\ T_w(℃)$	$q"(W/cm^2)$	λ_{robust}	*K-Y*	D_C†	*Dynamics*	*T.R.A*
55.52	1.15	0.04 ± 0.03, -0.13 ± 0.04, -0.25 ± 0.04, -0.39 ± 0.06, -1.34 ± 0.18	0 or >2	2.8	Fixed point/ chaotic	×
57.56	1.85	-0.02 ± 0.01, -0.08 ± 0.01, -0.12 ± 0.01, -0.24 ± 0.03	0	7.95	Fixed point	×
58.74	2.68	-0.04 ± 0.02, -0.15 ± 0.03, -0.46 ± 0.03, -1.4 ± 0.26	0	4.32	Fixed point	×
59.79	3.67	-0.06 ± 0.02, -0.59 ± 0.08, -1.03 ± 0.12, -1.63 ± 0.19	0	6.6	Fixed point	×
61.58	4.79	0.02 ± 0.02, -0.02 ± 0.01, -0.14 ± 0.03, -1.22 ± 0.41	> 2	2.83[c]	Chaotic	×
63.57	6.08	0.03 ± 0.03, -0.04 ± 0.03, -0.24 ± 0.03, -0.35 ± 0.03, -1.05 ± 0.1	> 2	3.06[c]	Chaotic	P
64.89	7.46	0.03 ± 0.03, -0.03 ± 0.02, -1.03 ± 0.11, -1.54 ± 0.17	> 2	3.15[c]	Chaotic	P

Table XIV. Continued.

$\Delta\ T_w(℃)$	$q"(W/cm^2)$	λ_{robust}	K-Y	$D_C{}^{\dagger}$	*Dynamics*	*T.R.A*
66.15	9.09	0.03 ± 0.03, -0.03 ± 0.02, -0.14 ± 0.03, -1.44 ± 0.16	> 2	3.81[c]	Chaotic	×
68.21	11.14	0.03 ± 0.02, -0.01 ± 0.01, -0.06 ± 0.02, -0.14 ± 0.03	> 2	5.09	Chaotic	×
117.02	6.29	0.01 ± 0.01, 0.06 ± 0.02, -0.01 ± 0.01, -0.03 ± 0.01, -0.05 ± 0.01, -0.12 ± 0.02	> 2	7.87	Chaotic	×
122.01	6.64	0.02 ± 0.01, -0.01 ± 0.01, -0.03 ± 0, -0.06 ± 0.01, -0.13 ± 0.04	> 2	7.37	Chaotic	×
125.59	6.95	0.02 ± 0.02, 0 ± 0.01, -0.01 ± 0.01, -0.03 ± 0.02, -0.05 ± 0.02	> 2	11.27	Chaotic	×
132.26	7.48	0.01 ± 0, -0.03 ± 0.01, -0.05 ± 0.01, -0.13 ± 0.03	> 2	9.27	Chaotic	×

[b]Estimate Converged

Table XV.: Subcooled pool boiling Run-2 TFT-1 - Exponents & dimension estimates for noise reduced data.

$\Delta\ T_w(℃)$	$q"(W/cm^2)$	λ_{robust}	K-Y	D_C[†]	*Dynamics*	*T.R.A*
56.03	1.28	0.01 ± 0.02, -0.01 ± 0.01, -0.03 ± 0.01, -0.13 ± 0.03	0	10.89	Periodic	×
58.85	1.96	-0.02 ± 0.01, -0.08 ± 0.02, -0.13 ± 0.03	0	6.35	Fixed point	×
61.63	2.78	-0.06 ± 0.02, -0.98 ± 0.08, -1.58 ± 0.15	0	10.24	Fixed point	×
65.05	3.71	0.01 ± 0.02, -0.35 ± 0.03, -0.46 ± 0.02, -0.97 ± 0.1	1	7.42[c]	Periodic	×
68.24	4.87	-0.03 ± 0.02, -0.96 ± 0.09, -1.47 ± 0.18	0	7.7	Fixed point	×
70.63	6.07	-0.05 ± 0.03, -1.1 ± 0.13, -1.55 ± 0.19	0	6.33[c]	Fixed point	×
72.74	7.54	-0.03 ± 0.02, -0.14 ± 0.03, -1.42 ± 0.13	0	7.55	Fixed point	×
74.03	9.12	0.01 ± 0.01, -0.02 ± 0.01, -0.07 ± 0.02, -0.13 ± 0.02	> 2	9.26	Chaotic	×
75.2	10.83	0.01 ± 0.02, -0.04 ± 0.02, -0.14 ± 0.03, -1.35 ± 0.15	> 2	3.73[c]	Chaotic	×

Table XV. Continued.

$\Delta\ T_w(℃)$	$q"(W/cm^2)$	λ_{robust}	K-Y	$D_C{}^{\dagger}$	$Dynamics$	$T.R.A$
115.58	6.29	0.01 ± 0.01, -0.02 ± 0.01, -0.04 ± 0.02	> 2	6.06^c	Chaotic	P
124.22	6.84	0.02 ± 0.01, 0 ± 0.01, -0.02 ± 0.01, -0.04 ± 0.01, -0.06 ± 0.02, -0.14 ± 0.03	> 2	9.7	Chaotic	P
131.81	7.57	0.01 ± 0, 0 ± 0, -0.01 ± 0, -0.03 ± 0.01, -0.05 ± 0.03	> 2	10.48	Chaotic	×

Table XVI.: Subcooled pool boiling Run-2 TFT-3 - Exponents & dimension estimates for noise reduced data.

$\Delta\ T_w(℃)$	$q"(W/cm^2)$	λ_{robust}	K-Y	D_C[†]	*Dynamics*	*T.R.A*
56.27	1.28	-0.03 ± 0.02, -0.25 ± 0.03, -1.46 ± 0.24	0	7.55	Fixed point	×
59.75	1.96	0.05 ± 0.02, -0.06 ± 0.02, -0.14 ± 0.03, -0.24 ± 0.04	0	2.03[c], -1.48 ± 0.32	Fixed point/Chaotic	×
62.5	2.78	-0.01 ± 0.01, -0.05 ± 0.01, -0.13 ± 0.03	0 or 1	7.05	Fixed point/ Periodic	×
66.22	3.71	-0.04 ± 0.02, -1.08 ± 0.1, -1.41 ± 0.09	≥1	5.08	Fixed point	×
70.29	4.87	0.03 ± 0.02, -0.02 ± 0.01, -0.14 ± 0.03, -1.02 ± 0.31	0	2.63[c]	Chaotic	×
73.32	6.07	-0.02 ± 0.02, -1.02 ± 0.07, -1.34 ± 0.16	0	6.71	Fixed point	×
74.76	7.54	0.02 ± 0.02, -0.03 ± 0.01, -1.49 ± 0.23	> 2	4.05[c]	Chaotic	P
75.71	9.12	0.03 ± 0.02, -0.02 ± 0, -0.07 ± 0.01, -0.13 ± 0.02, -0.23 ± 0.03	> 2	7.41	Chaotic	P
75.98	10.83	0.02 ± 0.01, -0.03 ± 0.01, -0.09 ± 0.01, -0.05 ± 0.01, -0.14 ± 0.02	> 2	8.44	Chaotic	×

Table XVI. Continued.

$\Delta\ T_w(℃)$	$q"(W/cm^2)$	λ_{robust}	K-Y	$D_C{}^{\dagger}$	$Dynamics$	$T.R.A$
109.5	6.29	0.03 ± 0.02, 0 ± 0, -0.04 ± 0.02, -0.07 ± 0.04	> 2	10.29	Chaotic	×
114.6	6.84	-0.02 ± 0, -0.04 ± 0.01, -0.07 ± 0.02, -0.14 ± 0.03	> 2	7.08^{c}	Chaotic	×
124.45	7.57	0.03 ± 0.01, 0 ± 0, -0.02 ± 0.01, -0.06 ± 0.02, -0.05 ± 0.02, -0.12 ± 0.02	> 2	8.29	Chaotic	P

APPENDIX B

PROGRAM LISTING

Program to locate TFT data from raw file and convert to binary float format

```
% FILE PREPARATION FOR MUTUAL INFORMATION COMPUTATION-CONVERT
% TEXT FILE TO
% BINARY
%%OBTAIN THE DIRECTORY LOCATION \& FILE NAME
clc;
clear all;
dir_con= input('Enter the full path of the directory containing...
        ...the files: ');
nam = input('Enter the File name :');
fil_nam=strcat(dir_con,'\',nam,'.xls');

%%LOCATE TFT READINGS
l=0;
y1=18000;
s=22+y1;
s=int2str(s);
for m=75:1:90
  x=strcat(char(m),'22');
  [p,q]=xlsread(fil_nam,1,x);
% Checks for appropriate column containing TFT temperature data
% in Excel file
```

```
  if strncmpi('TFT-4',q,5)==1
       l=l+1;% Structure to store the TFT temperature data
% Range of cells to pick from excel.
       y=strcat(':',char(m),s);
       z=strcat(x,y);
% Structure to store the TFT temperature data
       TFTd0(l).temp=xlsread(fil_nam,1,z);
   end;                                                % END OF IF
end;                                                   % END OF FOR
%[time,T3]=xlsread(fil_nam,1,z);
%temp=dlmread('F:\BOILING DATA\Boiling-PHD-2007\phD 2007 tft...
data analysis\bare Si TFT-1 1000\65_1000');

%%WRITE BINARY FILE
fid = fopen(strcat(dir_con,'\Binary files\',nam),'w');
fwrite(fid,TFTd0(l).temp(1:18000),'float')
fclose(fid);

%%WRITE SINGLE COLUMN TEXT FILES
%fid = fopen(strcat(dir_con,nam,'nr2'),'wt');
%fprintf(fid,'%7.4f\n',TFTd0(l).temp(1:18000));
%fclose(fid);
```

Program to generate phase plots for given Delay

```
% PROGRAM TO GENERATE RETURN MAPS WITH VARIABLE DELAY PERIODS
% PROGRAM READS THE EXCEL FILE SPECIFIED BY USER,
```

```
%IMPORTS THE REQUISITE
% TFT DATA COLUMNS UPTO A SPECIFIED RANGE AND PLOTS
% POINCARE SECTIONS
%
%  DATE          AUTHOR             REVISIONS
% ======      ==========          ============
% 12/17/06    S.VIJAYKUMAR
%
% VARIABLE DEFINITIONS:-

%% Block to clear workspace and command screen
clc;
clear all;

%% Block to obtain the path and filename from user
%dir_con= input('Enter the full path of the directory ...
containing the files: ');

%nam ='65_1000';% input('Enter the File name :');

fil_nam='C:\Users\Vijay\Desktop\phD 2007 tft ...
data analysis-latesr\Bare Si TFT-2-10-1000\...
Text files-3\205_1000';%strcat(dir_con,'\',nam);

%% Enter the Desired delay and calulcate ...
the frequency of data acquisition
```

```
% Reads The Time instants from the data file
%[time,T1]=xlsread(fil_nam,1,'B23:B24');
taui=0;
tauact=input('ENTER THE DESIRED DELAY IN MILLISECONDS: ');
freq=1000;
%n=ceil(tauact*freq);
%y1=input('ENTER THE NUMBER OF POINTS TO PLOT: ');
%del_per=input('ENTER THE MAXIMUM NUMBER OF DELAY PERIODS
% (1,2,3...): ');

%% Block to read the TFT temperature data only from the excel file
 % Structure to store the TFT temperature data
TFTd0.temp=dlmread(fil_nam);

%% Block to Store the delayed temperature data in structures
scrsz = get(0,'ScreenSize');
t1= TFTd0.temp(1:4001,1);
t2= TFTd0.temp(tauact:(4000+tauact),1);
t3= TFTd0.temp(2*tauact:(4000+2*tauact),1);
% Create figure
figure1 = figure('Color',[1 1 1],'Position',...
           ...[1 scrsz(4) scrsz(3) scrsz(4)]);

% Create axes
axes('Parent',figure1,'FontWeight','demi','FontSize',20,...
    'FontName','Times New Roman',...
```

```
    'FontAngle','italic');
view([322.5 30]);
hold('all');

% Create plot3
%plot3(t1,t2,t3,'Marker','.','LineStyle','none');
plot3(t1,t2,t3,'MarkerFaceColor',[0 0 0],'MarkerEdgeColor',[0 0 0],...
    'Marker','.',...
    'Color',[0 0 1]);

% Create ylabel
ylabel('t+\tau','FontWeight','demi','FontSize',20,'FontAngle','italic');

% Create zlabel
zlabel('t+2\tau','FontWeight','demi','FontSize',20,'FontAngle','italic');

% Create xlabel
xlabel('t','FontWeight','demi','FontSize',20,'FontName',...
          'Times New Roman','FontAngle','italic');

%% Print figure
set(gcf,'PaperPositionMode','auto','PaperType', 'A4')
print -djpeg 'C:\Users\Vijay\Desktop\phD 2007 tft data...
     ...analysis-latesr
\Bare Si TFT-2-10-1000\Text files-3\205_pp';
```

Program to generate Space-Time Separation Plots

```
% PROGRAM TO READ TEXT FILES AND GENERATE SPACE-TIME
% SEPARATION PLOTS

%% Block to clear workspace and command screen
clc;
clear all;

%% Block to obtain the path and filename from user
%input('Enter the full path of the directory containing
% the files: ');
dir_con='F:\IJHMT\job_chaos\1118\TFT_Rth111806\analysis\space-time_tft4';
nam = '247_stp5';%input('Enter the File name :');
fil_nam=strcat(dir_con,'\',nam);

%% Read dataset
lev=5;
k=0;
b=dlmread(fil_nam,'',[0 0 4999 1]);
a1= b(1:500,2);
a2= b(501:1000,2);
a3= b(1001:1500,2);
a4= b(1501:2000,2);
a5= b(2001:2500,2);
a6= b(2501:3000,2);
```

```
a7= b(3001:3500,2);

a8= b(3501:4000,2);

a9= b(4001:4500,2);

a10= b(4501:5000,2);

c=[1:1:500]';


%% Plot

scrsz = get(0,'ScreenSize');

figure1 = figure('Color',[1 1 1],'Position',...

             ...[1 scrsz(4) scrsz(3) scrsz(4)]);

axes('Parent',figure1,'FontWeight','bold','FontSize',15,...

    'FontName','Calibri',...

    'FontAngle','italic');

hold('all');


% Create xlabel

xlabel('\Delta t','FontWeight','bold','FontSize'...

      ...,20,'FontAngle','italic');


% Create ylabel

ylabel('\epsilon','FontWeight','bold','FontSize'...

    ...,20,'FontName','Calibri','FontAngle','italic');


% Create title

title('Space-time separation plot for dimension 5',...

       'FontWeight','bold',...
```

```
    'FontSize',24,...
    'FontName','Calibri',...
    'FontAngle','italic');
hold('all');
plot(c,a1,'DisplayName','10%','LineWidth',2);
plot(c,a2,'DisplayName','20%','LineWidth',2,'Color',[0 0.498 0]);
plot(c,a3,'DisplayName','30%','LineWidth',2,'Color',[1 0 0]);
plot(c,a4,'DisplayName','40%','LineWidth',2,'Color',[0 0 0]);
plot(c,a5,'DisplayName','50%','LineWidth',2,'Color',...
      [0.03922 0.1412 0.4157]);
plot(c,a6,'DisplayName','60%');
plot(c,a7,'DisplayName','70%','Color',[0 0.498 0]);
plot(c,a8,'DisplayName','80%','Color',[1 0 0]);
plot(c,a9,'DisplayName','90%','Color',[0 0 0]);
plot(c,a10,'DisplayName','100%','Color',[0.03945 0.1418 0.4137]);
%legend('show','Location',[0.01019 0.648 0.08047 0.2823]);
hold off;

%% Print figure
set(gcf,'PaperPositionMode','auto','PaperType', 'A4')
print -djpeg 'F:\IJHMT\job_chaos\1118\TFT_Rth111806\analysis\space-time_tft4\247_5';
```

Program to compare the spectra of original and noise reduced signals

```
% PROGRAM TO COMPARE SPECTRA OF ORIGINAL AND NOISE REDUCED SIGNALS
%
```

```
%  DATE          AUTHOR            REVISIONS
% ======      ==========         ============
% 12/17/06    S.VIJAYKUMAR
%
% VARIABLE DEFINITIONS:-
%
%
%
%
%
%

%% Block to clear workspace and command screen
clc;
clear all;

%% Block to obtain the path and filename from user
dir_con= 'C:\Documents and Settings\Lab\Desktop\...
        phD 2007 tft data analysis-new...
\Bare Si TFT-1-10-1000\Text files';

nam = '88';

fil_nam=strcat(dir_con,'\',nam,'_1000');
fil_nam2=strcat(dir_con,'\Noise Reduced','\',nam,'_1000nr.2');
```

```
%% Block to read the Top of the copper block ...
   ...temperature from the excel file
% Structure to store the TFT temperature data
 TFT_o=dlmread(fil_nam);
 TFT_nr1=dlmread(fil_nam2);

%% Fast Fourier Transform of TFT-4 Signals
surtemp4=TFT_o;
fftw('planner','patient');
Fou1 = fft(surtemp4,5900);
Pyy1 = Fou1.* conj(Fou1)/5900;
f1= 1000*(0:5899)/5900;



%% FFT of noise reduced signals
surtemp5=TFT_nr1;
fftw('planner','patient');
Fou2 = fft(surtemp5,5900);
Pyy2 = Fou2.* conj(Fou2)/5900;
f2= 1000*(0:5899)/5900;

%% PLOT
scrsz = get(0,'ScreenSize');

% Create figure
```

```
figure1 = figure('Color',[1 1 1],'Position',[1 scrsz(4)...
 scrsz(3) scrsz(4)]);

% Create axes
axes1 = axes('Parent',figure1,'FontWeight','demi','FontSize',20,...
    'FontName','Calibri',...
    'FontAngle','italic');
box('on');
hold('all');

% Create multiple lines using matrix input to plot
plot1(1)= plot(f1,Pyy1(1:5900));
plot1(2)=plot(f2,Pyy2(1:5900));
set(plot1(1),'DisplayName','Original Signals',...
'LineWidth',1,'Color',[1 0 0]);
set(plot1(2),'DisplayName','Signal after noise reduction',...
'LineWidth',2,'LineStyle',':','Color',[0 0 0]);

% Create title
%title('Signals before after non-linear noise reduction',...
'FontWeight','bold','FontSize',20,'FontAngle','italic');

% Create xlabel
xlabel('Frequency (Hz)','FontWeight','bold','FontSize',20);

% Create ylabel
```

```
ylabel('Power','FontWeight','bold','FontSize',20,...
   'FontAngle','italic');

% Create legend
legend(axes1,'show');
xlim([0 30]);
ylim([0 25]);

%% WRITE JPEG file
set(gcf,'PaperPositionMode','auto','PaperType', 'A4')
print -djpeg 'C:\Documents and Settings\Lab\Desktop...
\phD 2007 tft data analysis-new\Bare Si TFT-1-10-1000\Text files
...\Noise Reduced\88_2_m15';
```

VITA

Vijaykumar Sathyamurthi graduated with a B.E in Mechanical Engineering with distinction from Nagpur University in August 2003. Upon completion of his B.E. program, he ranked 9^{th} in the university. He joined Texas A&M University in Fall-2004 and graduated with an M.S. in Mechanical Engineering in December 2006. Subsequently, he enrolled at Texas A&M for the Ph.D. program in Mechanical Engineering in Spring-2007. His Ph.D. research focussed on the application of time series analysis algorithms to discern the presence of chaos in pool boiling. His research interests include phase-change heat transfer, applied fluid mechanics and chaos theory. He is currently employed as a Research Engineer at Heat Transfer Research Inc. His current address is: 3123, TAMU, Department of Mechanical Engineering, College Station, TX-77843.

The typist for this dissertation was Vijaykumar Sathyamurthi.